UNIVERSITY OF SOUTHAMPTON

FACULTY OF NATURAL AND ENVIRONMENTAL SCIENCES

School of Chemistry

X-ray and Electrochemical Studies of Bimetallic Pt-based Oxygen Reduction Electrocatalysts

by

David Warwick Inwood

Thesis for the degree of Doctor of Philosophy

August 2017

Academic Thesis: Declaration of Authorship

I, **David Warwick Inwood**, declare that this thesis entitled **X-ray and Electrochemical Studies of Bimetallic Pt-based Oxygen Reduction Electrocatalysts** and the work presented in it are my own and have been generated by me as the result of my own original research.

I confirm that:

1. This work was done wholly or mainly while in candidature for a research degree at this University;
2. Where any part of this thesis has previously been submitted for a degree or any other qualification at this University or any other institution, this has been clearly stated;
3. Where I have consulted the published work of others, this is always clearly attributed;
4. Where I have quoted from the work of others, the source is always given. With the exception of such quotations, this thesis is entirely my own work;
5. I have acknowledged all main sources of help;
6. Where the thesis is based on work done by myself jointly with others, I have made clear exactly what was done by others and what I have contributed myself;
7. None of this work has been published before submission.

Signed: ……

Date: ……

Acknowledgements

Firstly, I would like to thank my supervisor Andrea Russell for the opportunity to study for my PhD and for her support throughout. Thanks also to my academic supervisors Alex Martinez Bonastre and Jonathan Sharman for the useful discussions and helping me with my work at JMTC.

I'd also like to thank:

- Steve Thompson and Waldemir Paschoalino for showing me the ropes in the lab and giving me the rite of passage that is the synchrotron night shift, complete with leaky *in situ* cell.
- Steve Price for assistance with the EXAFS data collection and analysis.
- Andrew Leach, Turgut Sonmez, Colleen Jackson and Penny Whalley for assisting with the synchrotron experiments.
- Pete Mardle, Jake Lawrie-Ashton and Sam Fisher for assisting and guiding my research as part of their undergraduate projects and for doing the experiments that I didn't want to do!
- The rest of the Russell group past and present, Scott Gorman, Danai Panagoulia, Alex Keeler and Howard Huang for being friendly, helpful and always happy to bounce ideas around.
- Various employees of JMTC including Emily Brooke for the TEM/EDX measurements, Tugce Eralp Erden for XPS measurements and Chris Zalitis for advice on the GDE and RDE experiments.

Finally, thanks to my family for their continual support, encouragement and advice.

Abstract

University of Southampton

Faculty of Natural and Environmental Sciences

School of Chemistry

Doctor of Philosophy

X-ray and electrochemical studies of bimetallic Pt-based oxygen reduction electrocatalysts

By David Warwick Inwood

Dealloying carbon supported Pt alloy nanoparticles has been shown to particles with a Pt rich outer shell surrounded by an alloy rich core that are highly active electrocatalysts for the oxygen reduction reaction, which is of interest for use in fuel cell cathodes. The structure of these materials as well as how the size, elemental distribution and composition changes during fuel cell operation is important.

The catalysts were subjected to an accelerated stability test under similar conditions to those experienced in fuel cell cathodes. At various points throughout the test, the ECSA was recorded and samples taken for *ex situ* analysis. A variety of x-ray based spectroscopic techniques including XPS, XRD and XAS were used to investigate how the catalyst structure has been affected by the test. TEM will also be used. The 5 nm Pt/C and equivalent alloy catalysts were shown to be stable under these conditions with no significant change in structure or surface area. This shows that the protocol used here does not fully represent the conditions experienced in the fuel cell where degradation is observed. In comparison, the ECSA of 2 nm Pt/C sample was greatly decreased. Further testing for either a longer duration or using higher acid concentration is required to differentiate between the stability of the 5 nm nanoparticle samples.

Additionally, as measurements of the electrocatalytic activity made using the RDE technique differ significantly to the performance obtained in an MEA an alternative method was proposed. The GDE combines the advantages of the RDE system in terms of speed of testing and the quantity of catalyst required, with a more accurate representation

of the conditions experienced in a fuel cell *i.e* ability to access the high current density regime. This method was shown to compare favourably with other electrode configurations from the literature such as floating electrodes in terms of ease of use and similarity to results from testing in PEMFC MEAs. Several issues remain with the system, notably quantifying the amount of the catalyst actually utilised, although this does also allow the study of fuel cell related phenomena such as flooding of catalyst layers.

Contents

1.1 Aims 1
1.2 Fuel Cells and the Oxygen Reduction Reaction (ORR) 1
1.3 Pt Alloys as ORR Electrocatalysts 3
1.4 Activity Measurements 7
1.5 Accelerated Stability Testing (AST) 8
1.6 X-ray Absorption Spectroscopy (XAS) 9
1.7 Thesis Structure 13
1.8 References 14
2.1 Materials and Reagents 19
2.2 Sample Preparation 20
2.2.1 Catalyst Powders 20
2.2.2 Electrode Preparation 20
2.2.3 Electrochemical Methods 21
2.2.3.1 Electrochemical Cell Design 21
2.2.3.2 Cyclic Voltammetry (CV) 25
2.3 X-ray Absorption Spectroscopy 29
2.4 X-ray Photoelectron Spectroscopy (XPS) 30
2.4.1 Sample Preparation and Analysis 31
2.5 Transmission Electron Microscopy (TEM) and Energy Dispersive X-ray (EDX) Spectroscopy 31
2.5.1 Sample Preparation and Analysis 32
2.6 X-ray Diffraction (XRD) 33
2.6.1 Sample Preparation and Analysis 34
2.7 References 34
3.1 Data Pre-processing in Athena 38
3.1.1 Calibration and Alignment 38
3.1.2 Merging 39
3.1.3 Background Removal 39
3.1.4 Fourier Transform 41
3.2 EXAFS Analysis in Artemis 43
3.2.1 Analysis of Pt Foil 44
3.2.2 EXAFS Analysis of Pt/C – Introducing Degeneracy as a Variable 50
3.3 References 57

4.1 Introduction 59
4.2 Experimental 63
4.2.1 RDE Methodology and Ink Characterisation 63
4.2.2 Accelerated Stability Testing Procedure 64
4.2.3 XAS Measurements 65
4.2.4 Other Techniques 66
4.3 Results and Discussion 67
4.3.1 Thin film Electrodes 67
4.3.1.1 Ink Characterisation 67
4.3.1.2 Film Characterisation 68
4.3.1.3 Activity 71
4.3.2 Catalyst Coated Button Electrodes 74
4.3.2.1 TEM 75
4.3.2.2 XPS 78
4.3.2.3 XRD 83
4.3.2.4 *Ex situ* XAS 83
4.3.2.3 *In situ* XAS 92
4.3.3 Poisoned Electrodes 98
4.4 Conclusions 101
4.5 References 102
5.1 Introduction 109
5.2 Experimental 110
5.3 Results and Discussion 111
5.3.2.1 TEM 111
5.3.2.2 XPS 113
5.3.2.3 XRD 115
5.3.2.4 XAS 116
5.4 Conclusions 131
5.5 References 132
6.1 Introduction 137
6.2 Experimental 139
6.3 Results and Discussion 140
6.3.1 Thin film Electrodes 140
6.3.1.1 Ink Characterisation 140

6.3.1.2 Film Characterisation 141
6.3.1.3 Activity 142
6.3.1.4 Oxide Growth 146
6.3.2 Catalyst Coated Button Electrodes 148
6.3.2.1 TEM 149
6.3.2.2 XPS 155
6.3.2.3 XAS 157
6.4 Conclusions 168
6.5 References 170
7.1 Introduction 175
7.2 Experimental 178
7.2.1 RDE 178
7.2.2 Button electrodes 178
7.2.3 GDE 179
7.3 Results and Discussion 186
7.3.1 Catalyst Activity 186
7.3.1.1 MEA 186
7.3.1.2 RDE 188
7.3.1.3 GDE 188
7.3.1.4 Discussion 189
7.3.2 ECSA determination in the GDE 193
7.4 Conclusions 202
7.5 References 203
8.1 Original Aims 207
8.2 Conclusions 208
8.2.1 Characterisation 208
8.2.2 Activity Measurements 212
8.3 Future Work 214
8.4 References 215

Chapter 1: Introduction

1.1 Aims

The project set out to study the impact of an accelerated stability test on the structure of Pt and Pt alloy nanoparticles, specifically de-alloyed PtCo/C and PtNi/C catalysts alongside a Pt/C standard with comparable particle size. Various samples were prepared and tested, then characterised using several *in* and *ex situ* techniques including X-ray absorption spectroscopy (XAS), in particular the extended X-ray absorption fine structure (EXAFS), as well as X-ray photoelectron spectroscopy (XPS), X-ray diffraction (XRD) and microscopy. Samples were also characterised at intermediate points throughout the AST. Enhancing the surface sensitivity of XAS by poisoning the exposed Pt surfaces with iodine was also investigated.

A second aim of the project was to establish and validate a method for testing oxygen reduction reaction (ORR) electrocatalysts for use in the cathode of H_2-O_2 proton exchange membrane fuel cells (PEMFCs) that yields activity values that are more consistent with measurements in operating fuel cells, but that can still be easily achieved in a research laboratory setting. A gas diffusion electrode (GDE) setup was chosen for this. The results obtained in the GDE were compared to the activity measured in both the more typical rotating disk electrode (RDE) and realistic fuel cell membrane electrode assembly (MEA) experiments.

1.2 Fuel Cells and the Oxygen Reduction Reaction (ORR)

Fuel cells, in particular low temperature H_2-O_2 PEMFCS, are one of the technologies able to replace the internal combustion engine used to power cars and other forms of transport whilst potentially emitting little to no pollutants in terms of CO_2 as well as CO, NO_x and particulate species. The efficiency of fuel cell systems can also be greater than the conventional internal combustion engine as the thermodynamics associated with the Carnot cycle are avoided.

PEMFCs convert chemical energy directly into electrical energy and do so continuously as long as fuel is available. The H_2-O_2 PEMFC operates at 60-80 ^{o}C and consists of two catalyst coated electrodes separated by a solid, electrically insulating and gas impermeable Nafion

membrane, a diagram of which is shown in Figure 1. In brief, H_2 is supplied to the anode where it is oxidised, catalysed typically by carbon supported Pt nanoparticles (Pt/C), to form protons and electrons. Protons can diffuse through the Nafion membrane down the concentration gradient, whilst electrons must flow around the external circuit. At the cathode, O_2, either pure or taken from the air, is reduced by the protons and electrons to form H_2O. This reaction can also be catalysed by Pt/C, although is kinetically much slower than H_2 oxidation.

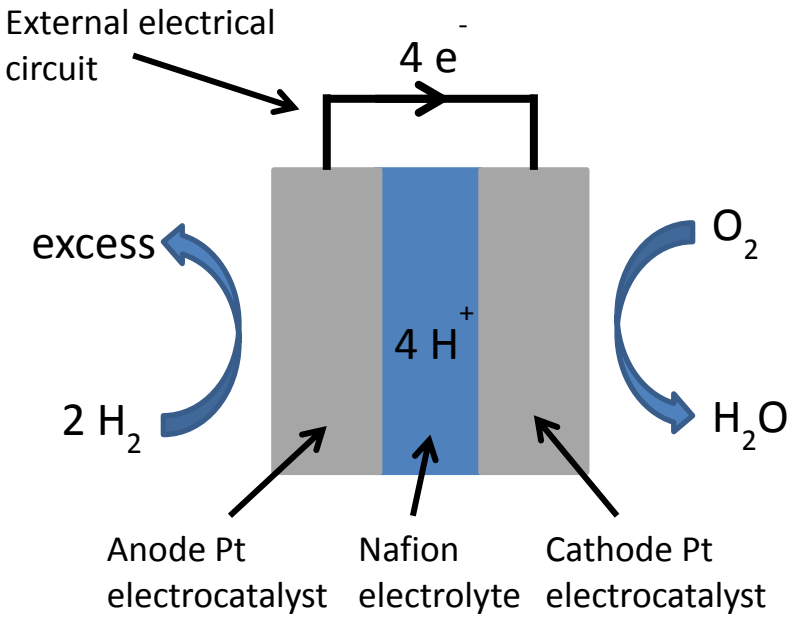

Figure 1 Schematic showing the membrane electrode assembly (MEA) of a H_2-O_2 PEMFC. The gas diffusion layers and current collectors are not shown.

Due to the slow kinetics of the oxygen reduction reaction (ORR), much research has been done on the mechanism of the reaction as well as finding the most active and cost efficient electrocatalysts.

The complicated reaction mechanism is commonly simplified to the reaction scheme given by Wroblowa *et al.*,[1] which is shown in Figure 2 and consists of three main pathways which are a direct 4 e^- reduction from O_2 to H_2O, two lots of 2 e^- reduction steps with H_2O_2 as an intermediate or finally, chemical disproportionation of the H_2O_2 intermediate. The rate of each of these reactions is determined by various factors including the catalyst used, the surface structure of the catalyst as well as the electrode potential[2].

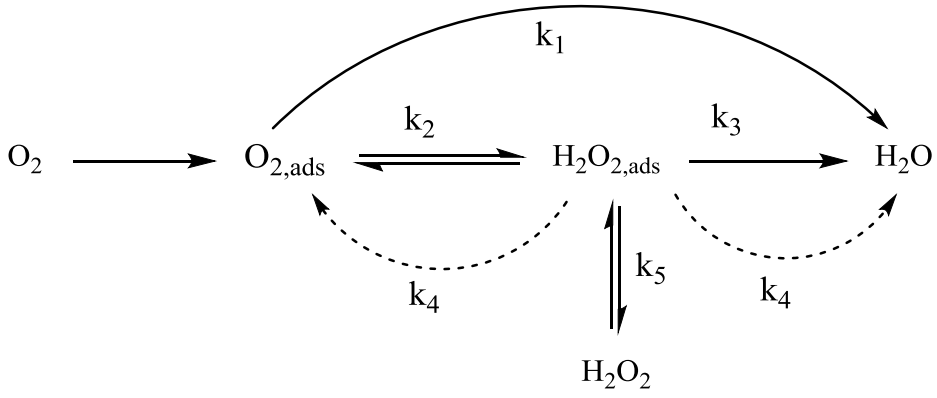

Figure 2 Simplified reaction scheme for the ORR according to Wroblowa *et al.*[1] showing the electrochemical steps as filled arrows and the chemical pathway as dotted lines.

Whilst the exact mechanism for the ORR on Pt is uncertain, it is generally accepted that a 'series' 4 e^- reduction pathway is dominant on Pt and Pt alloys.[2,3] This mechanism, known as the 'associative' mechanism, involves protonation of the adsorbed O_2 molecule to form a peroxy-intermediate, which is then protonated once more, breaking the O-O bond and yielding an H_2O molecule and adsorbed O on the surface. The O_{ads} is then sequentially protonated to produce the final H_2O molecule. Alternatively, the O-O bond in the peroxide species can be cleaved and the resulting OH_{ads} and O_{ads} species are protonated separately, which is known as the dissociative mechanism.

1.3 Pt Alloys as ORR Electrocatalysts

Carbon supported Pt alloy nanoparticles have been widely investigated as promising ORR electrocatalysts. DFT calculations by Nørskov *et al.*[4] have been able to define and describe the changes in the free energy of the intermediates involved throughout the ORR mechanism at different potentials. They found that the stability of adsorbed oxygen and hydroxyl species was responsible for the large overpotential required to drive the ORR, are roughly linearly correlated, and the exact point of O-O bond cleavage in the mechanism is unimportant. Pt and Pd are shown to be the best monometallic catalysts based on oxygen adsorption energy, but that by weakening the M-O bond slightly, higher activities are expected. This agrees with experimental work and invoking *d* band theory allows the decrease in adsorption strength caused by adding the second metal to be explained.[5,6,7] Alloying Pt, often with third row transition metals, has been shown to result in close to optimal oxygen adsorption strength as shown in Figure 3, a magnified view of the top of the volcano plot of activity *vs.* O adsorption strength.[8] Pt binds O and OH species too strongly such that the protonation and removal of these species from the catalyst surface

limits the rate. For Pt alloy surfaces, which adsorb O containing species less strongly than Pt, the paper suggests that dissociation of O_2 and/or transfer of protons and electrons to adsorbed O_2 is rate limiting. The two mechanistic possibilities result in the fine structure of the slope to the right hand side of Figure 3. There is a small discrepancy between the theoretical and experimental data, which is thought to be down to differences in the surface structure of the alloy used in the calculation to the structure present in the experiments, *i.e.* segregation effects. Various other alloying metals have also been considered including lanthanides,[9] yttrium,[10] and ruthenium.[11]

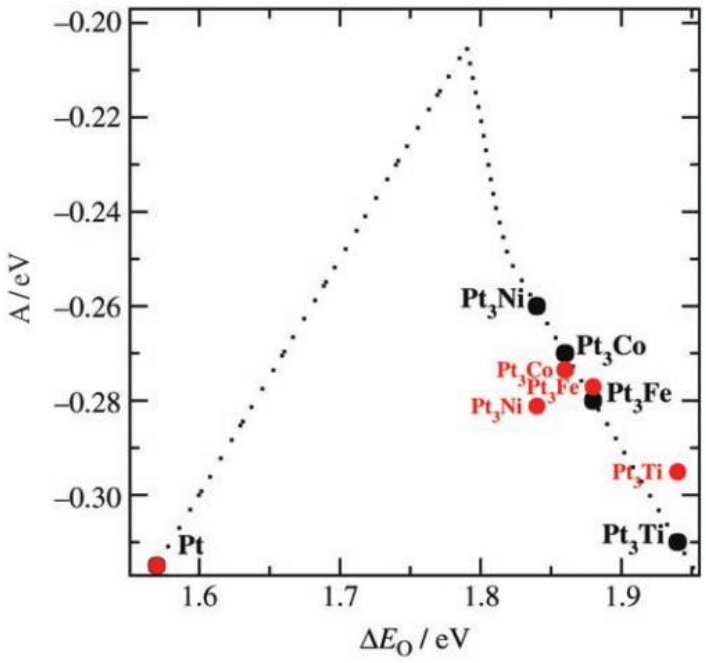

Figure 3 Reproduced from work by Stamenkovic *et al.*[8] and modified to define regions based on the rate limiting step. Region i) is where O and OH species are bound too tightly to the surface so their desorption is rate limiting, in region ii) O_2 dissociation and for region iii) the protonation of adsorbed O_2 become the rate limiting steps respectively. The activity is modelled at 0.9 V as a function of the O adsorption energy on Pt(111) and on Pt(111) monolayers on transition metal slabs, and denoted by the black dashed line and the black data points. Red points are experimentally measured data. The theoretical data defines the activity as, $A = k_bT\ln(r)$, with r being the rate per surface atom per second for the model, and for the experimental data, $A = k_bT\ln(r)+A_{Pt}$, where $r = i/i_{Pt}$, the current density relative to Pt. The number of active sites per surface area and the coverage of O species were both assumed to be constant for all materials. Full details are in the paper.

RDE testing (briefly described below) of these alloy materials have confirmed the increased activity typically resulting in a several fold enhancement over pure Pt nanoparticle catalysts, for example as shown in Figure 4 in work by Stamenkovic *et al.*,[12] as well as by many others. This figure also illustrates the importance of the surface structure and composition of the

catalyst, as significant differences can be observed in the activity of Pt skin compared to Pt skeleton type structures. The Pt skin structure is defined as a non-porous Pt shell around the PtM alloy core, typically formed through annealing, and the Pt skeleton structure is a porous structure usually resulting from acid leaching of the base metal from the near surface region. The formation of these structures is linked to the rate of diffusion of Pt atoms across the metal surface compared with the rate of dissolution of the other metal, which are affected by particle size,[13,14] alloy composition,[15] and electrode potential[16]. When surface diffusion of Pt atoms is fast compared to dissolution of the non-noble metal, the non-porous skin structure forms, when it is slower, nanoporosity ensues. Other experimental methods can also be used to control porosity such as presence of O_2.[17]

Thermal annealing typically results in the segregation of Pt atoms to the surface of Pt alloy nanoparticles, whilst the second layer becomes rich in the non-Pt element in order to maintain the overall stoichiometry.[18] This occurs based on the thermodynamics of the system where the element that segregates to the surface has the larger atomic radius and the lower surface energy. In some cases, the presence or absence of adsorbates can be used to influence this, *e.g.* CO strongly favours Pt surface segregation,[19] and Gan *et al.*[17] showed that the presence of O_2 favoured Ni segregation to the surface, which was subsequently dissolved to leave a porous skeletal Pt skin structure. This work also illustrates that Pt skin structures can be formed via chemical leaching of the base metal out of the near surface region of the alloy nanoparticles. The Pt skin is typically thicker, up to several monolayers, when using chemical leaching or de-alloying than when using thermal treatments, where the bulk composition is maintained by increased concentration of the non-Pt metal in the second layer.[18]

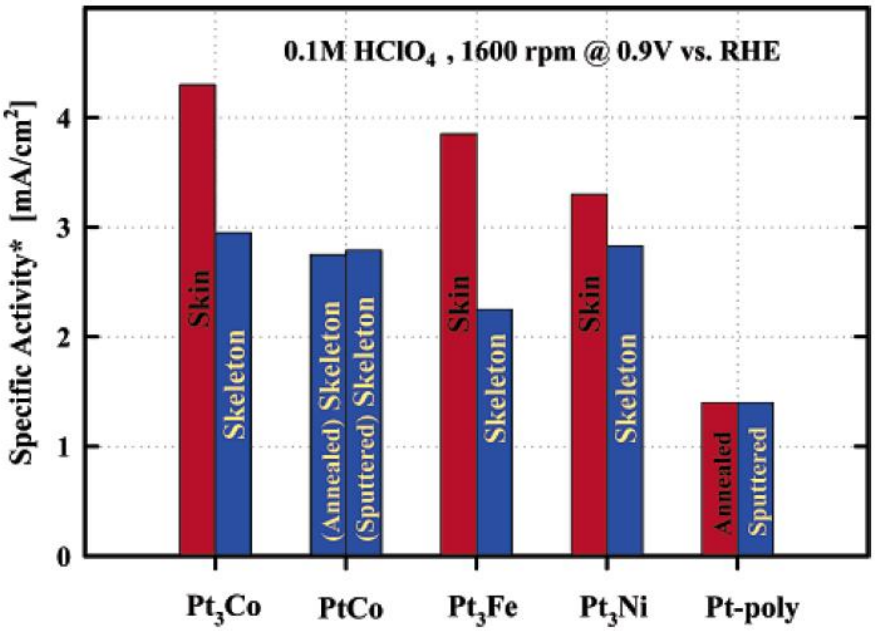

Figure 4 The graph shows the specific activity of several PtM/C catalysts measured at 50 mV s^{-1} at 0.9 V *vs.* RHE using the RDE technique at 1600 RPM in 0.1 M $HClO_4$ at 333 K. The experiments in this paper heat treated the catalysts to give a Pt skin structure, whilst dissolution, or in this case removal by sputtering, of non-Pt atoms from the surface leaves a skeleton type structure. Full details of the characterisation and preparation are in the paper. This graph was reproduced from work by Stamenkovic *et al.*[12]

The mechanism for the enhanced activity shown by Pt alloys has been attributed to a combination of factors such as strain effects, *e.g.* from a mismatch in atomic sizes,[20,21] and ligand effects, *e.g.* the effect of nearby transition metal atoms on the occupancy of the *d*-band, example relationship shown in Figure 5.[18] It is difficult to separate these effects entirely as both affect the electronic structure and consequently the binding strength of O-containing intermediates.[22]

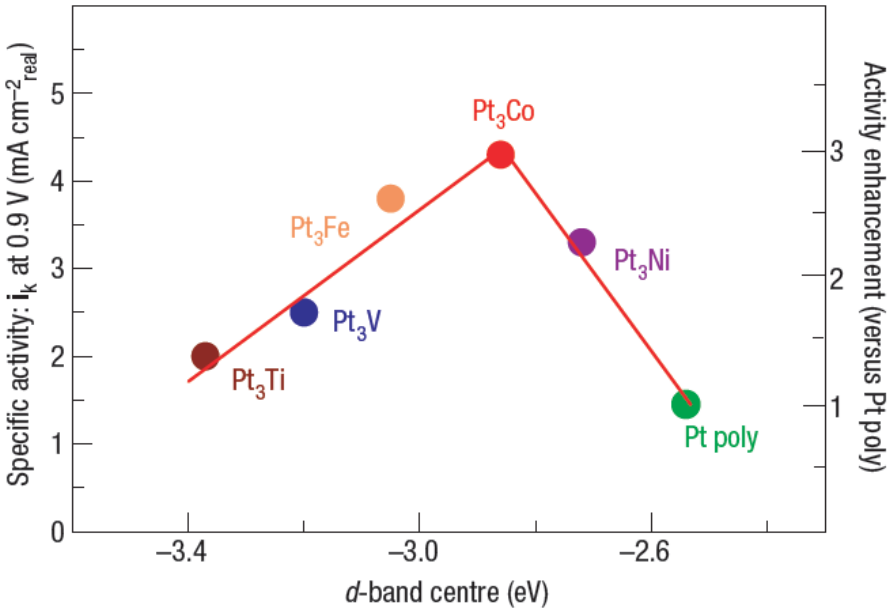

Figure 5 Graph comparing the relationship between specific activities measured at 50 mV s^{-1} at 333 K using RDE experiments at 1600 RPM in 0.1 M $HClO_4$ and experimentally determined *d*-band centres. The alloys used all have Pt skin type structures. Reproduced from work by Stamenkovic et al.[18]

1.4 Activity Measurements

When measuring the activity of ORR electrocatalysts on a laboratory scale, one of the most common techniques is the RDE.[23–26] Typically, perchloric or sulfuric acids are used and mass transport of O_2 to the catalyst surface is controlled via the rotation speed of the electrode and the concentration of O_2 that can dissolve in the electrolyte. In commercial PEMFCs, the liquid electrolyte is replaced by Nafion, a proton conducting polymer consisting of a fluorinated carbon backbone with side chains containing ether spacers and sulfonic acid groups, and gaseous reactants are used rather than dissolved species. The difference in conditions leads to discrepancies when comparing the electrocatalytic activity measured by RDE and in a fuel cell.[27] Additionally, the mass transport limited current density in the RDE is many times smaller than the current densities achieved in a fuel cell.

Other measurements have also been used to determine the ORR activity. One example is Zalitis *et al.*[28] where a floating electrode system was used, which allows the testing of catalysts at extremely low loadings under similar conditions to that of a PEMFC *i.e.* at high current density facilitated by use of a gaseous O_2 supply. In a similar manner to the RDE, the mass transport of O_2 to the electrode surface can also be controlled using a microdisk, flow cell or wall jet electrodes, where O_2 is dissolved in the electrolyte and the mass transport rate can be defined mathematically.

A recent, novel approach by Perry *et al.*[29,30] on microdisk electrodes following a rigorous potential pre-treatment and a sampled current voltammetry methodology has shown that at millisecond timescales an additional oxygen reduction charge is observed, above that predicted from theory. This has been shown to have potential as a sensitive descriptor for both oxygen adsorption strength and catalytic activity through comparison with theory, and could be used to draw up a calibration curve able to predict ORR activity. The additional reduction charge is thought to be caused by adsorbed atomic oxygen. This phenomenon is observed at neutral and alkaline pH, but not under the acidic conditions used in fuel cells, since the potential at which the oxygen species are formed overlaps with the potential window for oxide formation. However, currently when similar measurements are done using state of the art PtM/C materials, complications arise due to the carbon support as a variety of oxygen containing groups are present on the support.

In this work, a GDE was chosen, similar to the one used by Price *et al.*,[31] although modified to be suitable for work in acidic environments by replacement of the Ni components with Au or Pt. Measurements were also carried out using the RDE technique, and data from testing in a fuel cell system was obtained from Johnson Matthey for comparison purposes.

1.5 Accelerated Stability Testing (AST)

A vital remaining challenge for supported Pt nanoparticle catalysts is their durability in the harsh fuel cell conditions, particularly in the highly oxidising environment present at the cathode. As a result, catalysts are subjected to an AST in an attempt to mimic the stresses experienced during operation over a short period of time and determine whether the performance of the catalyst can be maintained over a reasonable lifetime. The factors contributing to the decrease in catalytic activity are losses in electrochemically active surface area (ECSA) via dissolution, re-deposition and coalescence of Pt to form larger particles and corrosion of the support material. This results in gradual growth in the diameter of the average Pt nanoparticle or loss of electrical contact with nanoparticle. It has been found that the various degradation pathways are affected by conditions such as the potential limits and scan rate used for the cycling, and temperature. The US Department of Energy has covered this topic extensively, with much of the information summarised by authors such as Kocha[23,24,32] and Garsany[33,34], including standard protocols for performing ASTs for thin film catalyst layers in RDE experiments.

The DOE recommended AST protocol for the RDE consists of 30000 cycles between 0.6 and 1.0 V *vs.* RHE at 50 mV s^{-1}, at 25 ^{o}C in 0.5 M H_2SO_4 or 0.57 M $HClO_4$, with the ECSA and ORR activity measured after 10, 100, 1000, 3000, 10000, 20000, and 30000 cycles. To test the durability of the catalyst support, a protocol consisting of fewer cycles and a more positive potential window is used, but as different catalyst support materials have not been studied, this will not be addressed here. In this work, the stability testing was primarily carried out on catalyst coated carbon paper electrodes in order to allow *ex situ* analysis by XPS, XRD, XAS and microscopy techniques. The protocol was modified to reduce the length of the experiments by increasing the harshness of the conditions used, and the work here was used to establish whether these conditions can be used to model the degradation observed in fuel cells. Instead, 1000 cycles over the same potential window and at the same scan rate were carried out in 1 M $HClO_4$ at 80 ^{o}C.

1.6 X-ray Absorption Spectroscopy (XAS)

X-ray absorption spectroscopy is one of the techniques that will be extensively employed in the work presented in this thesis. XAS has been previously used to study Pt ORR catalysts both *in* and *ex situ*, and is a synchrotron-based bulk averaging technique that can be used to determine properties such as coordination environments, interatomic distances, and oxidation states determined by developing a structural model and fitting calculated spectra to the experimentally obtained data. The experimental spectrum is separated into the XANES region, which is area within 100 eV of the absorption edge, and the EXAFS region, which stretches from around 100 eV to ~1000 – 2000 eV above the absorption edge, as shown in Figure 3. Factors, such as sample quality and experimental conditions, may limit the amount of usable data to less than this. More information, including the way in which the EXAFS data presented in this thesis was analysed, is detailed in chapter 3.

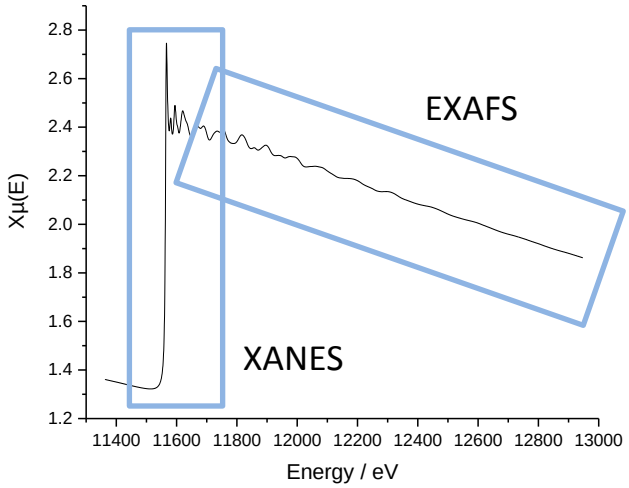

Figure 6 XAS spectra of a Pt reference foil. Single measurement recorded at B18, Diamond Light Source at room temperature. The XANES and EXAFS regions are highlighted.

Before analysing EXAFS it is useful to have information about the sample garnered from other techniques to provide a starting place for the model, which also helps to break the correlations between the terms in the EXAFS equation. For example, this can be in the form of particle size and shape from transmission electron microscopy (TEM) images, lattice parameters from XRD, chemical intuition from synthesis procedure and electrochemical measurements or from simply knowing the bulk composition of the material.

For Pt, the L_3 edge is most commonly used, but if the L_2 edge is also measured, information about the *d*-band occupancy can be determined as shown by Mansour *et al*.,[35] which has been used by Mukerjee *et al*. to analyse PtM/C materials.[36] This is possible as for Pt L_3 edge XANES, there is an allowed transition from the Pt 2*p*3/2 state to the partially filled 5*d*5/2 state so a large white line is observed, whereas at the L_2 edge, the only allowed transition is from the 2*p*1/2 state to the 5*d*3/2 state, which is fully occupied so no white line is observed.[37] In Pt alloys, charge transfer between the metals takes place, which affects the occupancy of the *d*-band. This may lead to the creation of available states for the 2*p* to 5*d* transition, thereby increasing the white line intensity at the L_2 edge. Also, when metals are oxidised, holes in the *d*-band are created leading to an increase in the intensity of the white line at the L_3 edge.

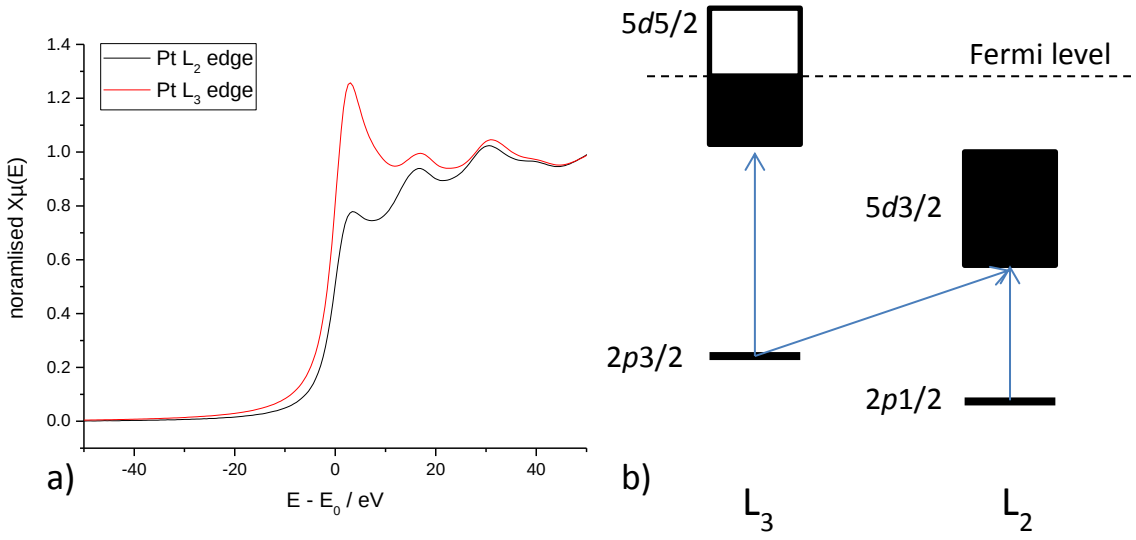

Figure 7 a) XANES region at the Pt L_3 and L_2 edges plotted with respect to the edge position. b) Energy level diagram showing the allowed transitions at the L_3 and L_2 edges. Following the selection rule, $\Delta j = \pm 1$, there are no empty final states for the L_2 edge so the observed intensity is low. For the L_3 edge, the 5*d*5/2 orbital can be occupied, meaning that a larger white line is measured.

When looking at alloy materials, XAS spectra can be obtained at several absorption edges thereby increasing the information available to build up the structural model of the system. This also allows various assumptions and constraints to be imposed, for example, interatomic distances will be equivalent regardless of the absorbing atom.

The $\Delta\mu$ method whereby the difference between XANES spectra taken at several potentials has been used to gain information about the formation of Pt oxides,[38] although the assumptions involved must be carefully considered as all changes must be shown to be due to adsorption rather than the metal nanoparticle itself undergoing a shape change. Previously published work has shown that nanoparticles can undergo shape changes in a potential controlled environment,[39] which calls into question the assumptions behind the $\Delta\mu$ method. The EXAFS region can be used to establish structural information about the catalyst based on the interatomic distances and the degeneracy of scattering paths obtained once a calculated spectrum is fit to the experimental data. When considering single scattering paths, where only the absorbing atom and one other are involved, the degeneracy is equal to the coordination number or the partial coordination number if multiple elements are present in the material. The coordination numbers, and the ratio between certain pairs of them, can be used to determine average particle size and shape, as has been shown by Benfield,[40] Jentys[41] , Beale and Weckhuysen,[42] as well as Glasner and Frenkel.[43] This relationship is shown for small nanoparticles/clusters in Figure 8, which also

highlights the need to fit the EXAFS spectra over multiple atomic shells in order to achieve good resolution and accuracy.

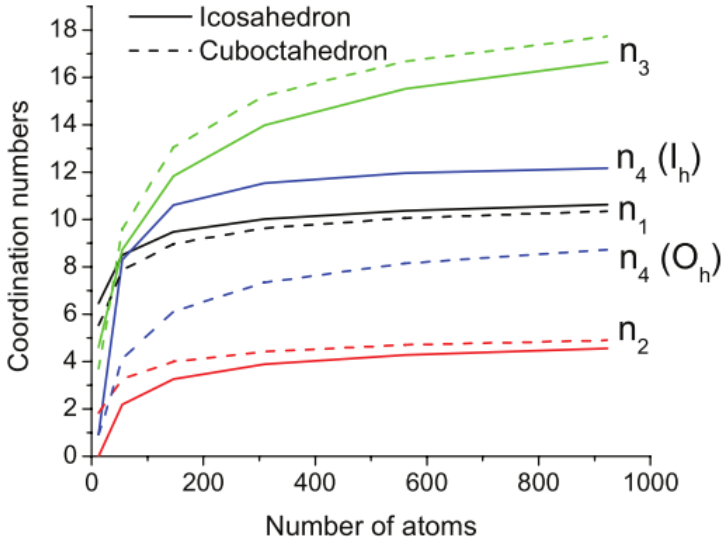

Figure 8 The effect of increasing particle size on the expected coordination number for the first 4 atomic shells in icosahedral and cuboctahedral clusters. Reproduced from work by Glasner and Frenkel.[43]

A significant strength of the technique lies in the ability to perform *in situ* measurements over a wide range of conditions as there is no need for the sample to be crystalline or show long range order. This is particularly useful for the type of segregated alloy nanoparticle catalysts studied in this work as other techniques often cannot distinguish the core and shell. Several examples of where XAS and specifically EXAFS has been used to study alloy nanoparticles include work by Nashner *et al.*[44] who showed that during PtRu nanoparticle synthesis, the initial structure starts out as a Pt core surrounded by Ru, but later on in the procedure undergoes inversion. Price *et al.*[39] looked at the completeness of Cu underpotential deposition on Au cores. Hansen *et al.*[45] worked on PtPd core shell structures in nanoparticles and through comparison of the homo-metallic coordination numbers concluded that, under the conditions of the study, Pd segregated to the surface, leaving a Pt rich core.

EXAFS studies typically observe that the coordination number of the element present at the core of the nanoparticle is higher than for the element at surface due to termination effects, *i.e.* the undercoordination of atoms at the surface. A method based on the ratios of the various partial and total coordination numbers obtained when fitting EXAFS data from multiple absorption edges for alloy samples has been developed to quantify segregation effects. This is known as the Cowley short range order parameter and is based on early

work by Cowley[46] and later shown to be applicable to nanoparticle alloy systems by Frenkel *et al*.[47] Another similar method was described by Hwang *et al*.[48] and was demonstrated using PtRu/C nanoparticles. These will both be covered in more detail in a later chapter and applied during the analysis of the PtCo/C and PtNi/C alloys used in this work.

1.7 Thesis Structure

The remainder of the thesis is separated into 6 chapters.

The next chapter provides an overview of the materials and chemicals used, electrode preparation methods and experimental techniques used throughout the work. Extra details are given in the relevant chapters.

Chapter 3 outlines the way in which the EXAFS analysis was carried out including the way in which the degeneracy (or coordination number), Debye-Waller like disorder terms and bond lengths are assigned parameters during the fitting process. Use of previously published fitting models yields similar results, but requires more parameters.

The first results chapter, Chapter 4, concerns the characterisation of two Pt/C catalysts with particle size distributions nominally centred on 2 and 5 nm respectively. Results obtained from RDE measurements are presented, accompanied by XAS, XRD, TEM and XPS analysis. XAS measurements were used to determine the particle sizes and quantify the expected increase in size once samples were aged in the electrochemical environment. This also acted as the control response for the durability testing to which the alloy samples can be compared.

In a similar manner to chapter 4, the Pt alloy catalysts, PtCo/C and PtNi/C, were characterised and these results are presented in chapters 5 and 6. Chapter 5 focusses on the characterisation of the as-prepared catalyst powders and electrodes, highlighting how the EXAFS fitting model was adapted to include the contributions from the Ni and Co. Chapter 6 aims to study how the structure of the Pt alloy samples changes upon exposure and aging in the electrochemical environment and whether the structure determined in chapter 5 is maintained.

The final results chapter, Chapter 7, concerns the comparison of activity measurements obtained using the RDE and GDE configurations, which were compared to realistic results gathered in an MEA under real-world fuel cell operating conditions. The hypothesis is that as the GDE configuration employs an electrode configuration and loadings similar to that of

an MEA, the activity measurements will better correlate with catalyst performance in fuel cells. Due to the scale of the experiments, the method also retains the advantages of the RDE in terms of speed and the requirement of small quantities of catalyst powder, but also allows access to higher current densities.

1.8 References

(1) Wroblowa, H. S.; Yen-Chi-Pan; Razumney, G. Electroreduction of Oxygen. *J. Electroanal. Chem. Interfacial Electrochem.* **1976**, *69*, 195–201.

(2) Markovic, N. M.; Schmidt, T. J.; Stamenkovic, V.; Ross, P. N. Oxygen Reduction Reaction on Pt and Pt Bimetallic Surfaces: A Selective Review. *Fuel Cells* **2001**, *1*, 105–116.

(3) Stamenković, V.; Schmidt, T. J.; Ross, P. N.; Marković, N. M. Surface Segregation Effects in Electrocatalysis: Kinetics of Oxygen Reduction Reaction on Polycrystalline Pt3Ni Alloy Surfaces. *J. Electroanal. Chem.* **2003**, *554–555*, 191–199.

(4) Nørskov, J. K.; Rossmeisl, J.; Logadottir, A.; Lindqvist, L.; Kitchin, J. R.; Bligaard, T.; Jónsson, H. Origin of the Overpotential for Oxygen Reduction at a Fuel-Cell Cathode. *J. Phys. Chem. B* **2004**, *108*, 17886–17892.

(5) Hammer, B.; Norskov, J. K. Theoretical Surface Science and Catalysis — Calculations and Concepts. *Adv. Catal.* **2000**, *45*, 71–129.

(6) Hammer, B.; Nørskov, J. K. Electronic Factors Determining the Reactivity of Metal Surfaces. *Surf. Sci.* **1995**, *343*, 211–220.

(7) Nilsson, A.; Pettersson, L. G. M.; Hammer, B.; Bligaard, T.; Christensen, C. H.; Norskov, J. K. The Electronic Structure Effect in Heterogeneous Catalysis. *Catal. Letters* **2005**, *100*, 111–114.

(8) Stamenkovic, V.; Mun, B. S.; Mayrhofer, K. J. J.; Ross, P. N.; Markovic, N. M.; Rossmeisl, J.; Greeley, J.; Nørskov, J. K. Changing the Activity of Electrocatalysts for Oxygen Reduction by Tuning the Surface Electronic Structure. *Angew. Chemie Int. Ed.* **2006**, *45*, 2897–2901.

(9) Escudero-Escribano, M.; Malacrida, P.; Hansen, M. H.; Vej-Hansen, U. G.; Velazquez-Palenzuela, A.; Tripkovic, V.; Schiotz, J.; Rossmeisl, J.; Stephens, I. E. L.; Chorkendorff,

I. Tuning the Activity of Pt Alloy Electrocatalysts by Means of the Lanthanide Contraction. *Science* **2016**, *352*, 73–76.

(10) Malacrida, P.; Sanchez Casalongue, H. G.; Masini, F.; Kaya, S.; Hernández-Fernández, P.; Deiana, D.; Ogasawara, H.; Stephens, I. E. L.; Nilsson, A.; Chorkendorff, I. Direct Observation of the Dealloying Process of a Platinum–yttrium Nanoparticle Fuel Cell Cathode and Its Oxygenated Species during the Oxygen Reduction Reaction. *Phys. Chem. Chem. Phys.* **2015**, *17*, 28121–28128.

(11) Jackson, A.; Viswanathan, V.; Forman, A. J.; Larsen, A. H.; Nørskov, J. K.; Jaramillo, T. F. Climbing the Activity Volcano: Core-Shell Ru@Pt Electrocatalysts for Oxygen Reduction. *ChemElectroChem* **2014**, *1*, 67–71.

(12) Stamenkovic, V. R.; Mun, B. S.; Mayrhofer, K. J. J.; Ross, P. N.; Markovic, N. M. Effect of Surface Composition on Electronic Structure, Stability, and Electrocatalytic Properties of Pt-Transition Metal Alloys: Pt-Skin versus Pt-Skeleton Surfaces. *J. Am. Chem. Soc.* **2006**, *128*, 8813–8819.

(13) Oezaslan, M.; Heggen, M.; Strasser, P. Size-Dependent Morphology of Dealloyed Bimetallic Catalysts: Linking the Nano to the Macro Scale. *J. Am. Chem. Soc.* **2012**, *134*, 514–524.

(14) Snyder, J.; McCue, I.; Livi, K.; Erlebacher, J. Structure/Processing/Properties Relationships in Nanoporous Nanoparticles As Applied to Catalysis of the Cathodic Oxygen Reduction Reaction. *J. Am. Chem. Soc.* **2012**, *134*, 8633–8645.

(15) Erlebacher, J.; Aziz, M. J.; Karma, A.; Dimitrov, N.; Sieradzki, K. Evolution of Nanoporosity in Dealloying. *Nature* **2001**, *410*, 450–453.

(16) Sieradzki, K.; Dimitrov, N.; Movrin, D.; McCall, C.; Vasiljevic, N.; Erlebacher, J. The Dealloying Critical Potential. *J. Electrochem. Soc.* **2002**, *149*, B370.

(17) Gan, L.; Heggen, M.; O'Malley, R.; Theobald, B.; Strasser, P. Understanding and Controlling Nanoporosity Formation for Improving the Stability of Bimetallic Fuel Cell Catalysts. *Nano Lett.* **2013**, *13*, 1131–1138.

(18) Stamenkovic, V. R.; Mun, B. S.; Arenz, M.; Mayrhofer, K. J. J.; Lucas, C. A.; Wang, G.; Ross, P. N.; Markovic, N. M. Trends in Electrocatalysis on Extended and Nanoscale Pt-Bimetallic Alloy Surfaces. *Nat. Mater.* **2007**, *6*, 241–247.

(19) Mayrhofer, K. J. J.; Juhart, V.; Hartl, K.; Hanzlik, M.; Arenz, M. Adsorbate-Induced Surface Segregation for Core-Shell Nanocatalysts. *Angew. Chemie Int. Ed.* **2009**, *48*, 3529–3531.

(20) Strasser, P.; Koh, S.; Anniyev, T.; Greeley, J.; More, K.; Yu, C.; Liu, Z.; Kaya, S.; Nordlund, D.; Ogasawara, H.; Toney, M. F.; Nilsson, A. Lattice-Strain Control of the Activity in Dealloyed Core–shell Fuel Cell Catalysts. *Nat. Chem.* **2010**, *2*, 454–460.

(21) Mavrikakis, M.; Hammer, B.; Nørskov, J. K. Effect of Strain on the Reactivity of Metal Surfaces. *Phys. Rev. Lett.* **1998**, *81*, 2819–2822.

(22) Jiang, K.; Zhang, H.-X.; Zou, S.; Cai, W.-B. Electrocatalysis of Formic Acid on Palladium and Platinum Surfaces: From Fundamental Mechanisms to Fuel Cell Applications. *Phys. Chem. Chem. Phys.* **2014**, *16*, 20360–20376.

(23) Shinozaki, K.; Zack, J. W.; Richards, R. M.; Pivovar, B. S.; Kocha, S. S. Oxygen Reduction Reaction Measurements on Platinum Electrocatalysts Utilizing Rotating Disk Electrode Technique. *J. Electrochem. Soc.* **2015**, *162*, F1144–F1158.

(24) Kocha, S. S.; Garsany, Y.; Myers, D. Testing Oxygen Reduction Reaction Activity with the Rotating Disc Electrode Technique http://energy.gov/eere/fuelcells/downloads/testing-oxygen-reduction-reaction-activity-rotating-disc-electrode (accessed Sep 14, 2016).

(25) Paulus, U. A.; Schmidt, T. J.; Gasteiger, H. A.; Behm, R. J. Oxygen Reduction on a High-Surface Area Pt/Vulcan Carbon Catalyst: A Thin-Film Rotating Ring-Disk Electrode Study. *J. Electroanal. Chem.* **2001**, *495*, 134–145.

(26) Mayrhofer, K. J. J.; Strmcnik, D.; Blizanac, B. B.; Stamenkovic, V.; Arenz, M.; Markovic, N. M. Measurement of Oxygen Reduction Activities via the Rotating Disc Electrode Method: From Pt Model Surfaces to Carbon-Supported High Surface Area Catalysts. *Electrochim. Acta* **2008**, *53*, 3181–3188.

(27) Debe, M. K. Electrocatalyst Approaches and Challenges for Automotive Fuel Cells. *Nature* **2012**, *486*, 43–51.

(28) Zalitis, C. M.; Kramer, D.; Kucernak, A. R. Electrocatalytic Performance of Fuel Cell Reactions at Low Catalyst Loading and High Mass Transport. *Phys. Chem. Chem. Phys.* **2013**, *15*, 4329–4340.

(29) Perry, S. C.; Denuault, G. Transient Study of the Oxygen Reduction Reaction on Reduced Pt and Pt Alloys Microelectrodes: Evidence for the Reduction of Pre-Adsorbed Oxygen Species Linked to Dissolved Oxygen. *Phys. Chem. Chem. Phys.* **2015**, *17*, 30005–30012.

(30) Perry, S. C.; Denuault, G. The Oxygen Reduction Reaction (ORR) on Reduced Metals: Evidence for a Unique Relationship between the Coverage of Adsorbed Oxygen Species and Adsorption Energy. *Phys. Chem. Chem. Phys.* **2016**, *18*, 10218–10223.

(31) Price, S. W. T.; Thompson, S. J.; Li, X.; Gorman, S. F.; Pletcher, D.; Russell, A. E.; Walsh, F. C.; Wills, R. G. A. The Fabrication of a Bifunctional Oxygen Electrode without Carbon Components for Alkaline Secondary Batteries. *J. Power Sources* **2014**, *259*, 43–49.

(32) Takahashi, I.; Kocha, S. S. Examination of the Activity and Durability of PEMFC Catalysts in Liquid Electrolytes. *J. Power Sources* **2010**, *195*, 6312–6322.

(33) Garsany, Y.; Baturina, O. A.; Swider-Lyons, K. E.; Kocha, S. S. Experimental Methods for Quantifying the Activity of Platinum Electrocatalysts for the Oxygen Reduction Reaction. *Anal. Chem.* **2010**, *82*, 6321–6328.

(34) Garsany, Y.; Singer, I. L.; Swider-Lyons, K. E. Impact of Film Drying Procedures on RDE Characterization of Pt/VC Electrocatalysts. *J. Electroanal. Chem.* **2011**, *662*, 396–406.

(35) Mansour, A. N.; Cook, J. W.; Sayers, D. E. Quantitative Technique for the Determination of the Number of Unoccupied D-Electron States in a Platinum Catalyst Using the L2,3 X-Ray Absorption Edge Spectra. *J. Phys. Chem* **1984**, *88*, 2330–2334.

(36) Mukerjee, S.; Srinivasan, S.; Soriaga, M. Role of Structural and Electronic Properties of Pt and Pt Alloys on Electrocatalysis of Oxygen Reduction. *J. Electrochem. Soc.* **1995**, *142*, 1409–1422.

(37) Bare, S. XANES Measurements and Interpretation. *EXAFS Data Collect. Anal. Course, APS* **2005**, 1–51.

(38) Jia, Q.; Caldwell, K.; Ziegelbauer, J. M.; Kongkanand, A.; Wagner, F. T.; Mukerjee, S.; Ramaker, D. E. The Role of OOH Binding Site and Pt Surface Structure on ORR

Activities. *J. Electrochem. Soc.* **2014**, *161*, F1323–F1329.

(39) Price, S. W. T.; Speed, J. D.; Kannan, P.; Russell, A. E. Exploring the First Steps in Core–Shell Electrocatalyst Preparation: In Situ Characterization of the Underpotential Deposition of Cu on Supported Au Nanoparticles. *J. Am. Chem. Soc.* **2011**, *133*, 19448–19458.

(40) Benfield, R. E. Mean Coordination Numbers and the Non-Metal-Metal Transition in Clusters. *J. Chem. Soc., Faraday Trans* **1992**, *88*, 1107–1111.

(41) Jentys, A. Estimation of Mean Size and Shape of Small Metal Particles by EXAFS. *Phys. Chem. Chem. Phys.* **1999**, *1*, 4059–4063.

(42) Beale, A. M.; Weckhuysen, B. M. EXAFS as a Tool to Interrogate the Size and Shape of Mono and Bimetallic Catalyst Nanoparticles. *Phys. Chem. Chem. Phys.* **2010**, *12*, 5562.

(43) Glasner, D.; Frenkel, A. I. Geometrical Characteristics of Regular Polyhedra: Application to EXAFS Studies of Nanoclusters. In *AIP Conference Proceedings*; AIP, 2007; 882, 746–748.

(44) Nashner, M. S.; Frenkel, A. I.; Somerville, D.; Hills, C. W.; Shapley, J. R.; Nuzzo, R. G. Core Shell Inversion during Nucleation and Growth of Bimetallic Pt/Ru Nanoparticles. *J. Am. Chem. Soc.* **1998**, *120*, 8093–8101.

(45) Hansen, P. L.; Molenbroek, A. M.; Ruban, A. V. Alloy Formation and Surface Segregation in Zeolite-Supported Pt-Pd Bimetallic Catalysts. *J. Phys. Chem. B* **1997**, *101*, 1861–1868.

(46) Cowley, J. M. An Approximate Theory of Order in Alloys. *Phys. Rev.* **1950**, *77*, 669–675.

(47) Frenkel, A. I.; Wang, Q.; Sanchez, S. I.; Small, M. W.; Nuzzo, R. G. Short Range Order in Bimetallic Nanoalloys: An Extended X-Ray Absorption Fine Structure Study. *J. Chem. Phys.* **2013**, *138*, 64202-1-64202–64207.

(48) Hwang, B. J.; Sarma, L. S.; Chen, J. M.; Chen, C. H.; Shin, S. C.; Wang, Q. R.; Liu, D. G.; Lee, J. F.; Tang, M. T. Structural Models and Atomic Distribution of Bimetallic Nanoparticles as Investigated by X-Ray Absorption Spectroscopy. *J. Am. Chem. Soc.* **2005**, *127*, 11140–11145.

Chapter 2: Experimental Methods and Techniques

This chapter will cover the materials, reagents and techniques used to prepare and analyse the catalyst samples.

2.1 Materials and Reagents

The materials and reagents used in this work are listed in Table 1 along with their supplier.

Table 1 List of materials used and corresponding supplier.

Material or Reagent	Supplier
Water (18 MΩ cm)	Obtained from Pur1te system
Perchloric acid (70%), $HClO_4$	Merck (Suprapur)
Carbon paper (teflonated, with C baselayer)	Johnson Matthey
Pt/C, PtNi/C, and PtCo/C	Proprietary material of Johnson Matthey Technology Centre[1–3]
Nafion (11.92 wt% in water), (0.5% in water:IPA, 20:80)	Proprietary material of Johnson Matthey Technology Centre. Nafion obtained from Dupont.
Isopropyl alcohol	Sigma Aldrich (puriss, ACS reagent)
Potassium iodide, KI	Fisher (analytical reagent grade)
Potassium permanganate, $KMnO_4$	Fisher (analytical reagent grade)
Hydrogen peroxide (30%), H_2O_2	VWR chemicals (AnalaR Normapur)
Sulfuric acid (<95%), H_2SO_4	Fisher (analytical reagent grade)
Perchloric acid, $HClO_4$	Fischer (analytical reagent grade)
Oxygen, O_2	BOC
Oxygen free nitrogen, N_2	BOC
Carbon monoxide, CO	BOC (CP grade)
3% CO, balance N_2	BOC, made to order
Boron nitride (98%), BN	Sigma Aldrich

The electrochemical work was carried out using the SP-150 potentiostat made by Bio-Logic, and the PGSTAT128N made by Metrohm Autolab and running EC-lab and NOVA software respectively. The RDE work was carried out using equipment and electrodes from Pine.

2.2 Sample Preparation

2.2.1 Catalyst Powders

Catalyst powders were prepared at the Johnson Matthey Technology Centre (JMTC) in Sonning Common by borohydride reduction of aqueous precursors in the presence of high surface area carbon support material,[1–3] which were then supplied for the project. The metal assays for the catalysts, along with extra preparation details are listed in Table 2. The catalysts will be referred to as 2 or 5 nm Pt/C, PtCo/C and PtNi/C respectively.

Table 2 Summary of catalyst powders used.

Catalyst Material Code	Pt Assay / wt%	Ni or Co Assay / wt%	Other Treatments
13/176 – Pt/C	29.7	n/a	Annealed, ~5 nm particles
13/300 – Pt_3Ni/C	29.1	6.7	De-alloyed in 1 M H_2SO_4 at 80 ^{o}C for 24 hrs in N_2.
13/412 – Pt/C	28.0	n/a	Untreated, ~2 nm particles
14/16 – Pt_3Co/C	29.1	3.4	De-alloyed in 1 M H_2SO_4 at 80 ^{o}C for 24 hrs in N_2.

2.2.2 Electrode Preparation

Electrode samples for testing were prepared on site at JMTC.

The respective catalyst powders (~0.5 g) were mixed with Nafion solution (11.92 wt% in water, ~2.9 g) such that there was an equal ratio of Nafion to carbon. A small amount of water (18 MΩ cm, ~0.3 g) was added to improve consistency of the suspension and to maintain the amount of solid material in the ink at 23 wt%. The ink was mixed for 10 minutes using a dual asymmetric centrifuge (SpeedMixer™ DAC 150.1 FV-K, Synergy Devices Ltd) with 5 yttria stabilised zirconia mixing balls at 3000 RPM, pausing after 2, 5, and 8 minutes to prevent overheating of the catalyst sample. This ink was then brush-coated onto carbon paper discs (teflonated, with carbon baselayer, diameter = 32 mm) that

had been pre-wetted by spraying with 35% IPA in water solution. After each coating, the layer was dried at 85°C using a hotplate, and weighed to determine catalyst loading. Typical loadings used in this work were 0.2 and 0.5 mg_{Pt} cm^{-2}.

Before use, the catalyst coated carbon paper was hot-pressed at 177 °C under a weight of 4 kg for 3 minutes. A smaller disk with a diameter of 1.1 cm was cut from the larger sample and used as the working electrode for the electrochemical measurements. Due to the hydrophobicity of the catalyst coated disk, the disk was usually flooded before use as the electrode by immersion in water under vacuum for 10-15 minutes or until the disk no longer floats.

2.2.3 Electrochemical Methods

Pt/C, PtNi/C, and PtCo/C are all active electrocatalysts for the ORR, and electrochemical techniques allow the activity of the catalysts to be determined as well as providing information on the ECSA and other key properties.

Since absolute potential cannot easily be measured directly, the potential difference between a fixed, stable reference point and the working electrode (WE) made up of the carbon paper coated with the catalyst of interest is used instead. In this work, experiments typically used homemade mercury/mercurous sulfate (MMS) reference electrode (RE), which has a potential of 0.70 V *vs.* RHE, the reversible hydrogen electrode, measured in H_2 saturated 1 M $HClO_4$. A homemade RHE was also utilised when carrying out the RDE experiments and consisted of a Pt wire in a glass bulb sealed at the top end and open at the other to allow contact with electrolyte. Before use as a RE, the Pt wire was temporarily used as the WE in a 2 electrode set up with a negative current (0.05 A, 15 mins) to generate a large bubble of H_2 that was trapped within the glass bulb. The counter electrode (CE) used for all experiments was a Pt wire and gauze.

2.2.3.1 Electrochemical Cell Design

The cell design plays an important role in electrochemistry, particularly when investigating electrocatalytic activity for the ORR. This is due to way in which the oxygen is supplied to the electrode and the primary mode of mass transport taken. Depending on whether oxygen can be supplied directly to the electrode as a gas or must be bubbled through the electrolyte and then diffuse to the electrode surface defines the current regime under study. This can lead to varying mass activity estimates.

2.2.3.1.1 Conventional Three Electrode Cell

The accelerated stability testing was carried out in a conventional three electrode cell surrounded with a water jacket to allow temperature control. The glass cell facilitates optimal electrode geometry with the luggin for the RE close to the WE and has a volume of 150 mL. A loop of gold wire was used to hold the catalyst coated carbon paper disc submerged in the electrolyte.

A schematic of the cell is shown in Figure 1.

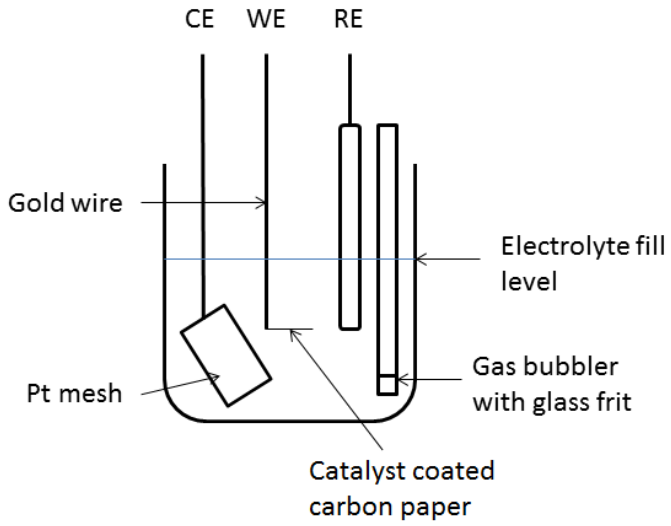

Figure 1 Schematic of the three electrode cell used. The counter electrode is a Pt mesh with a high surface area, the reference electrode is MMS that has been calibrated against the RHE, and the working electrode consists of carbon paper that has been coated with the catalyst and attached to a coil of gold wire.

2.2.3.1.2 Rotating Disk Electrode (RDE)

Cleanliness of glassware is of great importance when using the RDE technique because contaminants quickly build up on the electrode surface due to the forced convection of electrolyte. As a result, all glassware, including the electrochemical cell, bubbler, luggin capillaries, and volumetric flask, were first soaked in acidified $KMnO_4$ (25 mL conc. H_2SO_4 in 5 L of 1 M $KMnO_4$) for at least 8 hours, before rinsing 6 times with ultrapure water, and once with freshly prepared dilute piranha solution (0.2 M H_2O_2, 0.6 M H_2SO_4). The glassware was then boiled in ultrapure water for at least 1 hour, and rinsed and cleaned whilst still hot by rinsing a further 6 times with ultrapure water. Ideally, a specific activity for the ORR of 2 mA cm^{-2} should be achieved on a polished Pt RDE as a test for a contamination free system[4]. In this work, around 1.2 mA cm^{-2} was achieved in part due to the lower purity of O_2 used and the cleanliness and length of the O_2 pipework. Regardless,

activities comparable to previously published results were obtained for the 5 nm Pt/C catalyst.

The catalyst coated electrode is rotated at constant speed, setting up well-defined, calculable, convection dominated mass transport in the three electrode cell. Convection draws the electroactive species, in this case oxygen, to the electrode surface at a constant rate.

This technique can be performed rapidly on many catalysts, and whilst the results provide a good indication for trends in activity across a series of catalysts, there are some discrepancies between the activities measured by this method and under realistic fuel cell conditions.

2.2.3.1.3 Gas Diffusion Electrode (GDE)

The GDE used in this work is based on the design illustrated in Figure 2. This experimental set up was modified to make it appropriate for use in acidic media by swapping the nickel wire and contact loop to a platinum wire and foil respectively. Electrical contact is made by the O-ring (area = 0.5 cm^2) pushing the catalyst coated carbon paper disc WE on to the Pt foil, which is attached to the Pt wire. The gas inlet and outlet allow N_2 purging or supply of gas phase O_2 directly to the catalyst layer. A related design has been previously used to study low catalyst loadings at high current densities.[5]

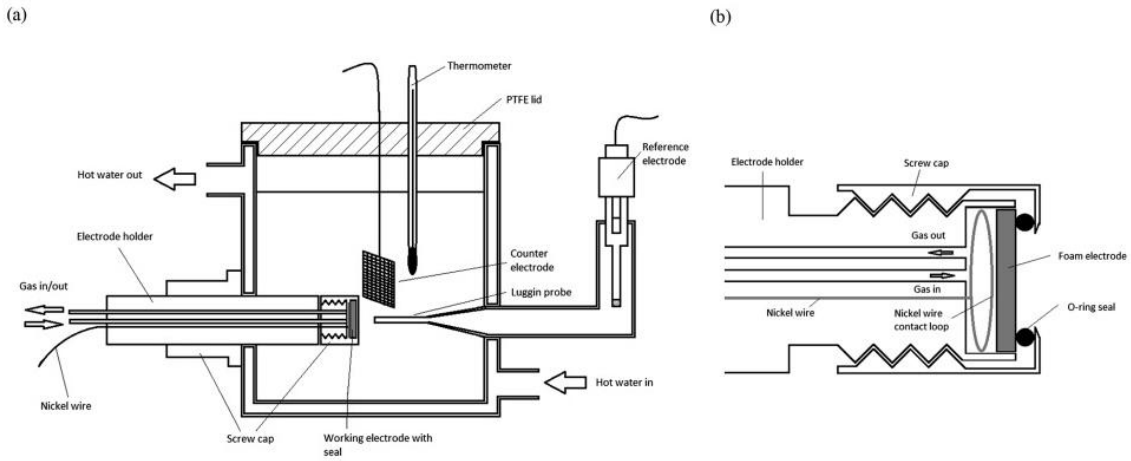

Figure 2 Schematic showing an example of the design for the cell employed when performing experiments with the gas diffusion electrode. This design in particular has been used to study bifunctional oxygen electrodes for use in alkaline secondary batteries, and is taken from the paper by Price *et al.*[6]

Unlike the RDE method, O_2 is supplied in the gas phase directly to the electrode allowing much higher current densities to be accessed as the concentration is not limited by

reactant solubility. However, other problems are encountered such as electrolyte leakage when the seal is incorrectly formed, and magnification of iR drop as a result of the higher currents involved.

When using the GDE, O_2 or N_2 was supplied to the reverse face of the electrode at approximately 3 cm^3 s^{-1} (0.2 LPM). N_2 was used during the conditioning cycles and ECSA determination procedure, and O_2 was used when looking at electrocatalytic activity.

2.2.3.1.4 In situ XAS cell

The cell shown in Figure 2 was used to mount the catalyst coated carbon paper electrodes on the beamline at the synchrotron in order to allow electrochemical control whilst also collecting the XAS data. The working electrode contact is established using a flattened gold wire, whilst a Pt wire is used as the counter. An electrolyte filled tube links to a separately mounted reference electrode holder and the other tubes enable the electrolyte to be pumped around the cell in order to remove any bubbles and maintain the electrolyte concentration at the bulk value. Kapton windows are used at both the front and rear faces with a thin layer of electrolyte flowing between the Kapton and the electrode to minimise any interaction with the x-ray beam and allow for transmission or fluorescence measurements to be taken. The cell is made watertight by using two O-rings (Viton) to seal against the Kapton windows, and each part was constructed from a single piece of 40% glass filled polyphenylene sulphide.

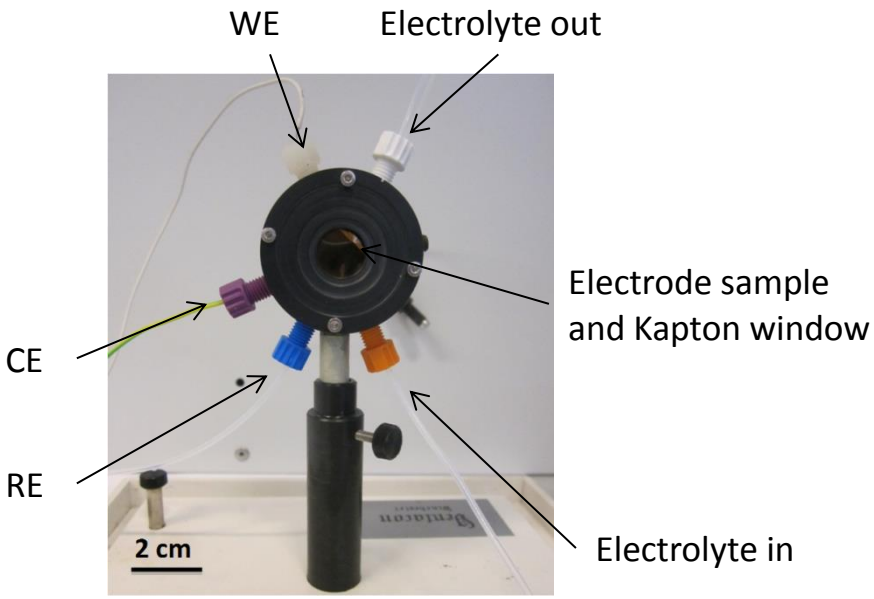

Figure 3 Photo of the *in situ* spectroelectrochemical cell.

2.2.3.2 Cyclic Voltammetry (CV)

2.2.3.2.1 Theory

Many of the experiments will rely on the CV technique, where the potential is repeatedly cycled between upper and lower potential limits in a saw tooth pattern, whilst the current is monitored. Modifications of this basic method give information on a variety of the electrocatalytic properties. For example, when determining the ORR activity, the cycle begins at the upper potential limit, where no reaction can occur, and is then scanned down to lower potentials where the reaction can proceed rapidly. The reverse direction scan is also collected. The scan rate, *i.e.* the rate at which the potential is changed, is also an important factor to investigate, *e.g.* allowing surface and solution based redox couples to be distinguished. Cyclic voltammetry provides an easy method for probing the nature of adsorbed species on the surface of electrodes and redox active species in the bulk electrolyte.

Polycrystalline Pt, in an ideal electrochemical experiment, gives a distinctive voltammogram, shown in Figure 4, because of the adsorption of hydrogen on the surface at low potentials, and oxide formation and reduction at higher potentials. The shape of Pt CV can often serve as a diagnostic tool for detecting non-ideal electrochemical behaviour, *e.g.* unusually high cell resistance or the presence of contaminants or O_2.

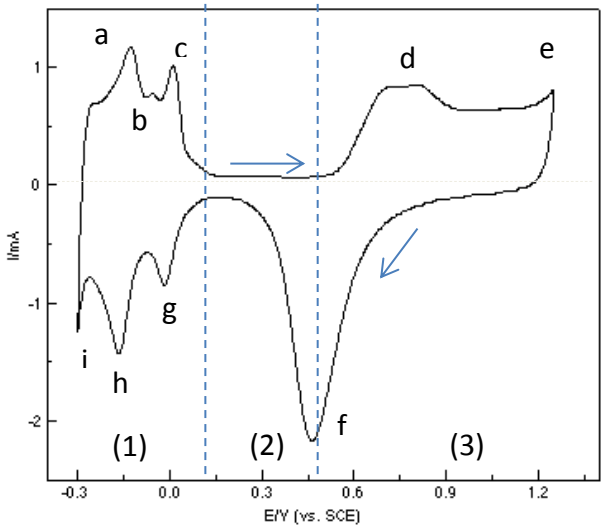

Figure 4 Cyclic voltammogram of a roughened platinum electrode in 0.5M H_2SO_4.[7] In region 1, hydrogen evolution, adsorption, and desorption features are observed, whilst at potentials above ~0.5 V *vs.* SCE in region 3 oxide growth, evolution and reduction can be seen. SCE is the saturated calomel electrode which has a potential of 0.24 V *vs.* RHE.

The unique shape is made up of three main features. Firstly, in the middle of the voltammogram, there is the double layer region (region 2), where only current due to the charging of the electrode surface (Pt nanoparticles and the C support) is observed. Moving from the region 2 in the negative going direction, the two cathodic peaks are due to the adsorption of strongly (peak g) and weakly bound hydrogen (peak h), with the strongly bound hydrogen adsorbing first. Peak i marks the onset of H_2 evolution. The first anodic peak, a, is assigned to the desorption of weakly bound hydrogen, as it is desorbed more easily than strongly bound hydrogen, the second anodic peak, c. If careful measurements are done in a clean system, a third H desorption peak b can be observed. This section is often called the H region. At potentials more positive than the double layer region, a broad anodic peak, d, is observed. This peak is actually made up of three overlapping peaks representing the stepwise formation of adsorbed OH species, Pt-O and PtO_2 on the Pt surface, with each step requiring a more positive potential to occur. If the potential was increased further, evolution of O_2 would be observed as a sharp increase in anodic current, the onset can be seen at point e. The main cathodic peak f shows the reduction of the oxide layer.

When looking at Pt/C, the voltammogram is typically not as well defined as this, see Figure 5, although the main features can be still be distinguished. This is because the Pt is dispersed as nanoparticles on a carbon support and then coated in Nafion. The nanoparticles are of a similar dimensions, but not monodisperse, which leads to inequivalent environments resulting in broadening of the characteristic peaks and other features. Additionally an extra feature is sometimes observed in the double layer charging region at around 0.5 V *vs.* RHE due to redox processes that occur on the surface of the carbon support.[8]

The majority of the work presented here is carried out in $HClO_4$ rather than H_2SO_4, which introduces several differences to the observed voltammetry. Song-Chen *et al.*[9] presented a detailed comparison of the voltammetry measured in both electrolytes on Pt single crystal and polycrystalline nanoparticles. In $HClO_4$, the lack of a specifically adsorbing anion causes a broadening of the peaks in the low potential region (1) compared to the same measurements made in H_2SO_4. Additionally it was observed that on stepped sites *i.e.* Pt(100), a broad peak in the double layer charging region is present and they proposed that this was due to OH adsorption at these sites based on similar observations on single crystal electrodes.

Van der Niet *et al.*[10] put forward a similar suggestion based on anomalous results obtained across the pH scale obtained on Pt(111), (553) and (533) single crystal electrodes in $HClO_4$ and NaOH. They suggest that at step sites, Pt(110) and (100), water is not stable and disassociates spontaneously due to the strong interaction with OH and O species resulting in a peak in the 0.3-0.4 V *vs.* RHE range. This does not occur on the Pt(111) terrace as the interaction is weaker. As a result van der Niet *et al.*[10] propose a model invoking co-adsorption of H and OH species on step sites at potentials in the so called hydrogen region, although they do admit that there has been no direct observation of these species via spectroscopy.

2.2.3.2.2 ECSA Determination

The ECSA of the electrode can be determined by either of two methods. The first method involves using the charge associated with the adsorption or desorption of an H monolayer that spontaneously forms on Pt surfaces at potentials approaching 0 V *vs.* RHE. Hydrogen adsorption on Pt follows the Langmuir isotherm, and as a result, will have a maximum coverage of up to a monolayer.[11] This is a single electron process described by Equation 1. The area highlighted region from the CV of a Pt/C sample, shown in Figure 5, integrated and divided by the scan rate used (10 mV s^{-1}) to give the charge. This value is then divided by 210 µC cm^{-2}, which is an empirically determined value reported for polycrystalline Pt and happens to be close to the theoretical H ad/desorption charge on low index crystal faces, to give the ECSA of Pt contained in the sample.[12] This conversion factor is a good approximation for Pt nanoparticle samples, however, when considering ideal Pt surfaces, factors such as the dominant crystal face and the presence of anions will affect the exact value.[9]

$$\boldsymbol{Pt - H \rightarrow Pt + H^{+} + e^{-}}$$

Equation 1

Equally, the ECSA can be calculated from the charge associated with the reverse process, the adsorption of H on the Pt surface, in the same way. This area is represented by the cathodic peaks between 0.05 V and ~0.4 V *vs.* RHE. Care must be taken with the potential limits because if the lower limit is set incorrectly significant H_2 evolution can occur, which will distort the ECSA calculation if this extra area is included.

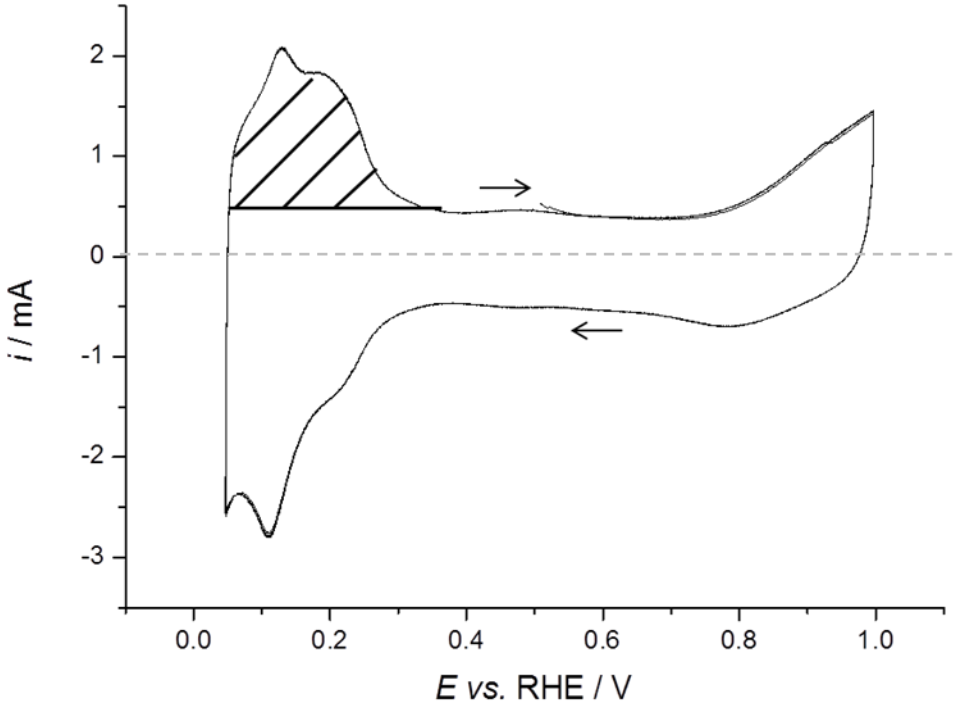

Figure 5 Cyclic voltammetry of a carbon disk coated with Pt/ C catalyst to a loading of 0.2 mg_{Pt} cm^{-2} carried out at 10 mV s^{-1} with the electrode submerged in N_2 purged 1 M H_2SO_4. The electrode has been electrochemically pre-treated by cycling 50 times at 50 mV s^{-1} between 0.05 and 1 V *vs.* RHE in the same electrolyte. The integral of the highlighted area was used to calculate the ECSA of the Pt in the catalyst.

The second method follows a similar logic to the first; the Pt surface is coated with a monolayer of CO, which strongly binds to Pt. This can be easily achieved experimentally by bubbling CO through the electrolyte whilst holding the potential of the working electrode at 0.15 V *vs.* RHE, and then any excess CO is removed by purging with N_2. Holding the potential at this value ensures that CO is not oxidised, and that there are no strongly bound anions present on the Pt surface. CO is typically bubbled through the solution for 15 minutes, and then the solution is purged with N_2 for at least 30 minutes. The CO monolayer is then oxidatively stripped by cycling the potential from 0.15 to 1.0 to 0.05 V *vs.* RHE for several cycles to ensure that the CO has been completely removed and to obtain a background CV. The background CV is subtracted from the CV showing the CO oxidation, and the remaining area is converted to charge as before. The charge is then treated in the same way as with the hydrogen method, but accounting for the fact that CO oxidation to CO_2 is a two electron reaction, as shown in Equation 2, *i.e.* the charge is divided by 420 µC cm^{-2} rather than 210 µC cm^{-2}.

$$Pt - CO + H_2O \rightarrow Pt + CO_2 + 2H^+ + 2e^-$$

Equation 2

There is some debate about the advantages and drawbacks to each of these methods. For example, it is often found that when considering Pt alloy surfaces the ECSA determined by each of these methods differs considerably. This can be explained by the electronic effect of the additional metal, which, in the case of transition metals, weakens the Pt-H bond strength, and correspondingly, the equilibrium surface coverage. The theory behind this observation is known as d-band theory and was explained previously.[13,14] Additionally, H does not specifically adsorb on some metals to an appreciable extent. Other points for discussion include the actual coverage achieved, especially in the case of CO where a coverage of 0.7 – 0.8 is sometimes quoted. The adsorption of a CO monolayer has also been shown to cause a restructuring of the Pt surface.[15] The issue of which method is best for ECSA determination, in particular when looking at Pt alloy catalysts is discussed in detail by Rudi *et al*.[16] and by Van der Vliet *et al*.[17]

2.3 X-ray Absorption Spectroscopy

At the synchrotron, measurements can be taken in either transmission or fluorescence mode depending on the concentration of the element of interest within the sample. The position of the detectors in both modes is illustrated in Figure 6.

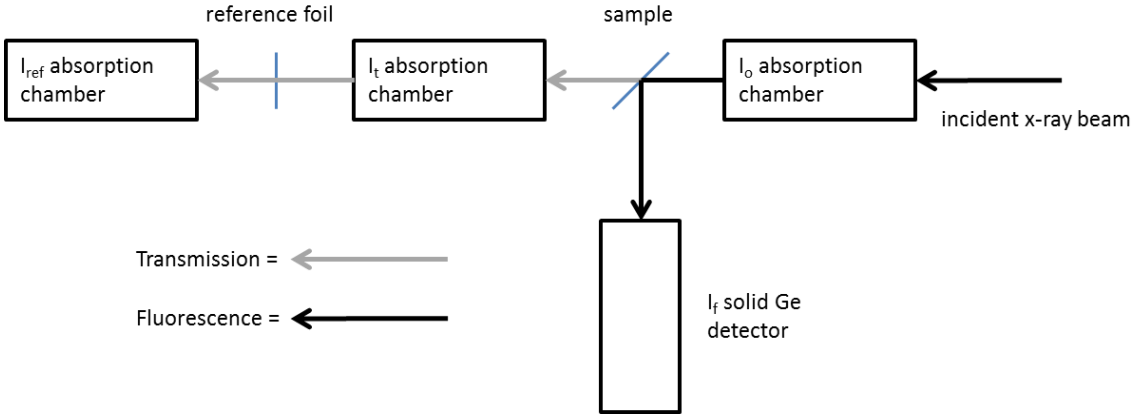

Figure 6 Sketch showing the positioning of the sample and detectors in the synchrotron experimental hutch.

In both modes, the intensity of the incident x-ray beam is first measured using an ionisation detector filled with a mixture of gases. The beam then passes through and hits the sample, which absorbs a proportion of the photons, depending on the exact photon energy and

elements present in the sample. A second absorption chamber then records the intensity of the transmitted beam. The XAS of a reference sample can also be measured simultaneously in the same way. Alternatively, for more dilute samples, the fluorescence mode can be used. In this case, the absorption of the sample is measured by detecting the intensity of the photoelectrons produced when outer shell electrons relax into the core hole produced by the initial x-ray absorption.

Samples were primarily the electrodes used as prepared for the electrochemical experiments, and were analysed both *ex situ* after washing with H_2O and drying, as well as *in situ* under potential control. XAS spectra for Pt, Ni and Co metal foils were also obtained in addition to boron nitride pellets containing each of the Pt/C, PtNi/C, and PtCo catalyst powders.

All XAS measurements were carried out during two sessions at the B18 Core XAS beamline at Diamond Light Source synchrotron (Harwell, UK), and the beamline scientists were Giannantonio Cibin and Stephen Parry. The measurements were carried out by Andrew Leach, Turgut Sonmez (two sessions, all from the University of Southampton, UK), Penny Whalley (one session, from University of Southampton, UK), and Colleen Jackson (one session, University of Cape Town, South Africa). The synchrotron operates at a ring energy of 3 GeV, and the current is maintained at 300 mA. The beamline uses a water-cooled double Si 111 crystal monochromator, and focuses the photon beam to a 250 by 200 µm spot. In transmission, ionisation chambers are used to measure intensity, before and after the sample, and after the reference foil and fluorescence is measured by a Ge solid state detector.[18]

2.4 X-ray Photoelectron Spectroscopy (XPS)

XPS is a surface sensitive technique, which can be used to determine elemental composition in the near surface region, as well as the oxidation state of each element. This is achieved by calculating the electron binding energy from the incident photon energy ($h\nu$), the work function (ϕ) and the kinetic energy (KE) of the emitted photoelectrons using Equation 3.

$$\boldsymbol{BE = h\nu - KE - \phi}$$

Equation 3

The intensity of emitted electrons at each energy is measured leading to a series of peaks along with a broad background signal where electrons have lost kinetic energy through collisions or other loss mechanisms. Surface sensitivity arises because electrons must escape from the material in order to reach the detector, which is exponentially related to the depth at which they are produced. As a result, the signal obtained from the near surface region is much larger than that from deeper within the sample. In terms of looking at the nanoparticle catalysts, it is likely that photoelectrons will be detected from the whole particle since the mean free path length of electrons is comparable to or larger than the diameter of the Pt alloy nanoparticles.

2.4.1 Sample Preparation and Analysis

XPS equipment was operated by Tugce Eralp Erden of JMTC. Tugce also assisted with using the XPS software (Thermo Scientific Avantage) to analyse the spectra.

The samples were prepared by attaching a segment of the aged catalyst coated electrode to the sample holder stub using conducting adhesive carbon tape. Multiple samples were attached to the stub and their positions noted to allow automatic operation of the XPS machine. For powder samples, a small amount was dusted onto the adhesive tape and attached to the stub.

A fast, lower resolution, survey spectrum was obtained for each sample, and then regions containing the peaks of interest were selected for longer, higher resolution scans.

2.5 Transmission Electron Microscopy (TEM) and Energy Dispersive X-ray (EDX) Spectroscopy

The resolution of optical microscopy is limited by diffraction, which depends on the wavelength of the light used. Through use of high energy electrons, which have a smaller wavelength than optical photons, the resolution can be increased sufficiently to allow individual nanoparticles and their lattice structure to be imaged. However, due to the high energy of these photons, care must be taken to avoid damaging the sample. TEM uses the transmission of electrons through a thinly sliced sample to build up a 2D image based on the transmitted intensity to produce a ‘bright-field’ image. Consequently, denser and/or thicker regions of the sample appear darker, as fewer electrons penetrate through, so in relation to this project, Pt would appear dark compared to the carbon support material.

Alternatively, in 'dark-field' mode, back scattered electrons hitting an annular detector are used to build up the image, and as a result, the light and dark regions would be inverted.

Operation in Scanning Tunnelling Electron Microscope (STEM) mode allows a small, specific region of the sample to be analysed more closely by focussing the electron beam into a spot of 1 nm diameter and scanning this spot over the region of interest. This is used in conjunction with EDX to analyse the elemental composition of the sample, and of nanoparticles within. The high energy electrons used in the STEM are sufficient to excite inner core electrons, creating a hole near the nucleus of atoms. When an outer electron fills this hole, an x-ray photon is emitted, and based on the characteristic energy of the photon, the atom in question can be identified. Using this technique, an elemental map of an interesting region can be built up, or the EDX probe can be scanned in a line, across a particle, for example, and used to analyse the compositional change.

2.5.1 Sample Preparation and Analysis

Samples were prepared by Emily Brooke of JMTC, who also was responsible for operation of the JEM 2800 (Scanning) Transmission Electron Microscope, and for assisting in processing the images. The instrumental conditions used were: voltage 200 kV; C2 aperture 40 µm, condenser aperture 3; spot size 2 in TEM mode; camera length 4 m, probe size 1 nm for STEM mode; bright-field and high magnification lattice resolution imaging modes using CCD; dark-field imaging in scanning mode using an off-axis annular detector. The secondary electron signal was collected simultaneously with the other STEM images to provide topological information. Compositional analysis using x-ray emission detection was done in the scanning mode.

Samples were prepared by two methods. For the first method, a segment of the aged catalyst coated electrode was embedded in resin and allowed to set. The resin was then sliced into ~50 µm wafers using a microtomer, which were collected in a pool of water, and then transferred onto a holey carbon coated Cu mesh. Since it was difficult to locate the catalyst material amongst the relatively large amount of additional material from the carbon paper, the catalyst was instead scraped off the carbon paper surface and dusted directly onto the holey Cu grids. The untreated catalyst powders were also dusted directly onto holey carbon grids.

SEM, bright field and dark field TEM images were taken for each sample, and used to determine particle size distribution based on at least 100 particles. TEM-EDX images and

linescans were also acquired to show the composition and distribution of elements in the samples.

2.6 X-ray Diffraction (XRD)

XRD is a bulk averaging technique that requires long range order to produce diffraction patterns that can give information on crystallite size, often comparable to particle size, lattice parameters, and identification of phases present in the material.

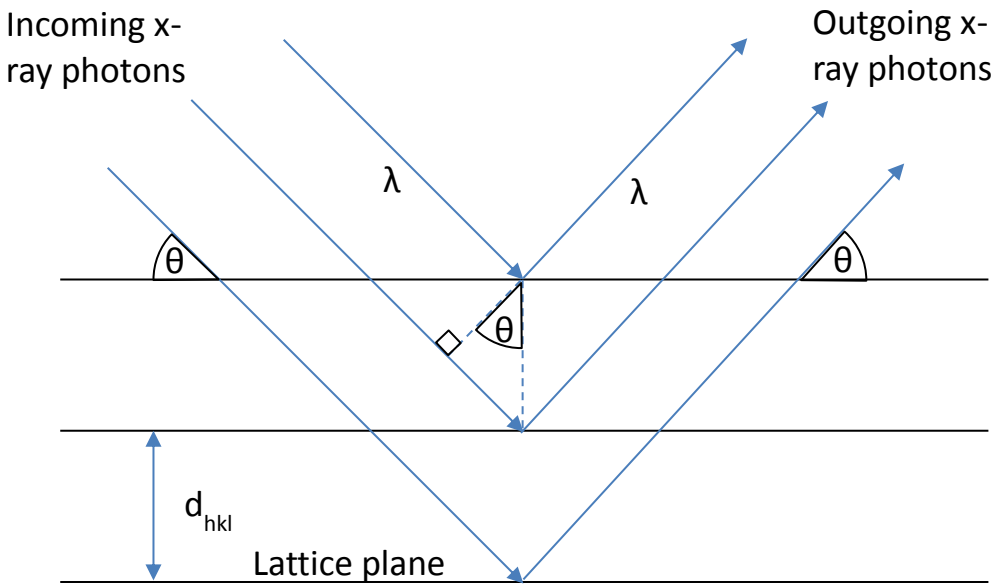

Figure 7 Diagram illustrating Bragg's law, the principle behind XRD.

The wavelength of x-ray photons is in the Å range and is comparable to the spacing between atomic lattice planes, which allows them to act as a diffraction grating for the photons. The incident angle of the x-ray beam, θ, is scanned through a range of values and the intensity of outgoing photons is measured resulting in a pattern of maxima and minima. The maxima arise when constructive interference occurs, i.e. when Bragg's law (see Figure 7 and Equation 4) is satisfied, and all other conditions result in destructive interference.

$$n\lambda = 2dsin\theta$$

Equation 4

Where λ is the x-ray wavelength, d is the lattice spacing, θ is the angle between the lattice plane and incident beam as shown in Figure 7, and n is the order of reflection.

2.6.1 Sample Preparation and Analysis

Aged catalyst coated electrodes, and the untreated catalyst powders were used as prepared in the Rigaku Smartlab XRD machine. Diffraction spectra were acquired between 2θ angles of 10 and 90^{o} at a speed of 3^{o} min^{-1}, and 3 scans were averaged together to produce the spectra.

2.7 References

(1) Buchanan, J. S.; Potter, R. J.; Ralph, T. R. Johnson Matthey Public Limited Company, London , England. US Patent 5759944, 1998.

(2) Keck, L.; Buchanan, J.; Hards, A. Johnson Matthey Public Limited Company, London , England. US Patent 5068161, 1991.

(3) Buchanan, J.; Hards, G. A.; Cooper, S. J. Johnson Matthey Public Limited Company, London , England. GB Patent 2242203, 1991.

(4) Shinozaki, K.; Zack, J. W.; Richards, R. M.; Pivovar, B. S.; Kocha, S. S. Oxygen Reduction Reaction Measurements on Platinum Electrocatalysts Utilizing Rotating Disk Electrode Technique. *J. Electrochem. Soc.* **2015**, *162*, F1144–F1158.

(5) Zalitis, C. M.; Kramer, D.; Kucernak, A. R. Electrocatalytic Performance of Fuel Cell Reactions at Low Catalyst Loading and High Mass Transport. *Phys. Chem. Chem. Phys.* **2013**, *15*, 4329–4340.

(6) Price, S. W. T.; Thompson, S. J.; Li, X.; Gorman, S. F.; Pletcher, D.; Russell, A. E.; Walsh, F. C.; Wills, R. G. A. The Fabrication of a Bifunctional Oxygen Electrode without Carbon Components for Alkaline Secondary Batteries. *J. Power Sources* **2014**, *259*, 43–49.

(7) Ren, B.; Yao, J. L.; Li, X. Q.; Cai, W. B.; Mao, B. W.; Tian, Z. Q. A New Progress in Surface Raman Spectroscopy of Platinum Electrode Surfaces. *Int. J. Vib. Spect.* **1996**, *1*.

(8) Kangasniemi, K. H.; Condit, D. A.; Jarvi, T. D. Characterization of Vulcan Electrochemically Oxidized under Simulated PEM Fuel Cell Conditions. *J. Electrochem. Soc.* **2004**, *151*, E125.

(9) Chen, Q.-S.; Solla-Gullón, J.; Sun, S.-G.; Feliu, J. M. The Potential of Zero Total Charge

of Pt Nanoparticles and Polycrystalline Electrodes with Different Surface Structure: The Role of Anion Adsorption in Fundamental Electrocatalysis. *Electrochim. Acta* **2010**, *55*, 7982–7994.

(10) Van Der Niet, M. J. T. C.; Garcia-Araez, N.; Hernández, J.; Feliu, J. M.; Koper, M. T. M. Water Dissociation on Well-Defined Platinum Surfaces: The Electrochemical Perspective. *Catal. Today* **2013**, *202*, 105–113.

(11) Christenson, P. A.; Hamnet, A. *Techniques and Mechanisms in Electrochemistry*; Springer, 1994.

(12) Chen, S.; Sheng, W.; Yabuuchi, N.; Ferreira, P. J.; Allard, L. F.; Shao-Horn, Y. Origin of Oxygen Reduction Reaction Activity on "Pt 3 Co" Nanoparticles: Atomically Resolved Chemical Compositions and Structures. *J. Phys. Chem. C* **2009**, *113*, 1109–1125.

(13) Hammer, B.; Nørskov, J. K. Electronic Factors Determining the Reactivity of Metal Surfaces. *Surf. Sci.* **1995**, *343*, 211–220.

(14) Nilsson, A.; Pettersson, L. G. M.; Hammer, B.; Bligaard, T.; Christensen, C. H.; Norskov, J. K. The Electronic Structure Effect in Heterogeneous Catalysis. *Catal. Letters* **2005**, *100*, 111–114.

(15) Chen, D.; Tao, Q.; Liao, L. W.; Liu, S. X.; Chen, Y. X.; Ye, S. Determining the Active Surface Area for Various Platinum Electrodes. *Electrocatalysis* **2011**, *2*, 207–219.

(16) Rudi, S.; Cui, C.; Gan, L.; Strasser, P. Comparative Study of the Electrocatalytically Active Surface Areas (ECSAs) of Pt Alloy Nanoparticles Evaluated by Hupd and CO-Stripping Voltammetry. *Electrocatalysis* **2014**, *5*, 408–418.

(17) van der Vliet, D. F.; Wang, C.; Li, D.; Paulikas, A. P.; Greeley, J.; Rankin, R. B.; Strmcnik, D.; Tripkovic, D.; Markovic, N. M.; Stamenkovic, V. R. Unique Electrochemical Adsorption Properties of Pt-Skin Surfaces. *Angew. Chemie Int. Ed.* **2012**, *51*, 3139–3142.

(18) Dent, A. J.; Cibin, G.; Ramos, S.; Parry, S. A.; Gianolio, D.; Smith, A. D.; Scott, S. M.; Varandas, L.; Patel, S.; Pearson, M. R.; Hudson, L.; Krumpa, N. A.; Marsch, A. S.; Robbins, P. E. Performance of B18, the Core EXAFS Bending Magnet Beamline at Diamond. *J. Phys. Conf. Ser.* **2013**, *430*, 12023.

Chapter 3: XAS Data Collection and Analysis

This chapter details how XAS spectra, collected at the B18 Core EXAFS beamline at Diamond Light Source, were analysed using the freely available Demeter software package,[1] which consists of the Athena and Artemis programs. The process of background subtraction and extraction of parameters, including coordination numbers and interatomic distances, is illustrated using a Pt foil, and 5 nm Pt/C nanoparticle catalyst sample in the form of a boron nitride pellet as model examples. The spectrum for the Pt/C pellet, used as an example here, consists of the equally weighted average of 3 sequentially obtained spectra of the same sample to improve signal to noise ratio.

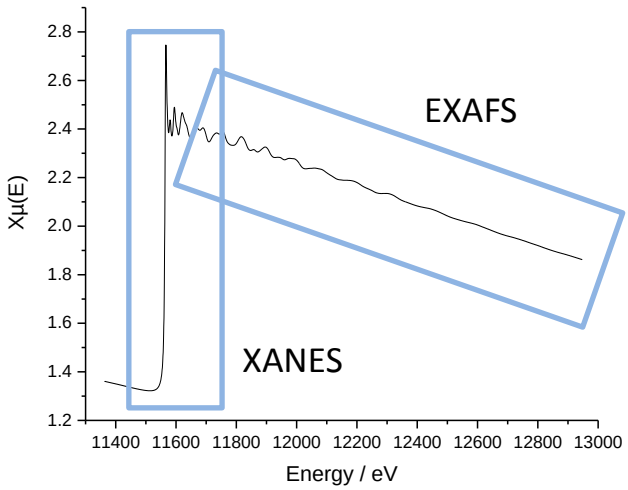

Figure 1 XAS spectra of a Pt reference foil. Single measurement recorded at B18, Diamond Light Source at room temperature. The XANES and EXAFS regions are highlighted.

XAS provides information about the local chemical environment of a specific element, which provides information on coordination number, oxidation states and interatomic distances. The energy of the incident x-ray photons is used to select the absorption edge, which is specific to a certain element, *e.g.* for this work the Pt L_3 edge was used, which requires photon energy of more than 11564 eV to eject a 2*p* electron from the core of the atom to an available *d* state. This photoelectron can scatter between surrounding atoms and return to the original absorber atom. The presence of the scattered electron at the

absorbing atom alters its absorption coefficient resulting in constructive or destructive interference, which gives rise to the EXAFS oscillations.

3.1 Data Pre-processing in Athena

Before EXAFS analysis of XAS spectra can commence, the data must be carefully processed to ensure consistency and accuracy of the spectra. When collecting sample data in transmission mode, as done with this sample, a spectrum of a reference material can be measured simultaneously and is important throughout the analysis. A single data file output from the synchrotron consists of both the sample data and the reference data, and any operation carried out on the reference spectrum will also be performed on the sample spectrum, but not *vice versa*.

In the fluorescence configuration, simultaneous collection of reference data is often not possible, so this data must be obtained in separate measurements. However, the principles behind the data treatment remain the same.

3.1.1 Calibration and Alignment

The first step is to correct for any variations in energy of the monochromator at the beamline by calibrating the edge step of the data to the literature value. The energy value for the energy step, E_0, is often chosen based on the peaks observed in the 1st derivative of the spectrum. Typically, the energy at the 1st large peak is selected as the E_0 value, as in Figure 2, the objective being the selection of equivalent peaks in all other spectra. E_0 acts as a reference point for defining the pre- and post-edge ranges and the normalisation range when looking at background removal, and is set to the literature value, *e.g.* in the case of the Pt L_3 edge, this value is 11564 eV.

Consistent E_0 values should be chosen for each spectrum, *e.g.* all values are taken at the same point on the spectra *i.e.* points E_0 1 and 2 in Figure 2 are at the top of the first peak in the derivative spectrum. Then, at least one of the reference spectra is calibrated to the literature value and the remaining data sets are aligned to this 'standard' by shifting the spectra along the x-axis until the E_0 values match. The corresponding sample spectra will be shifted in energy accordingly. In Figure 2, E_0 1 has been calibrated to the literature value of 11564 eV, and the second spectrum has not yet been aligned to the first.

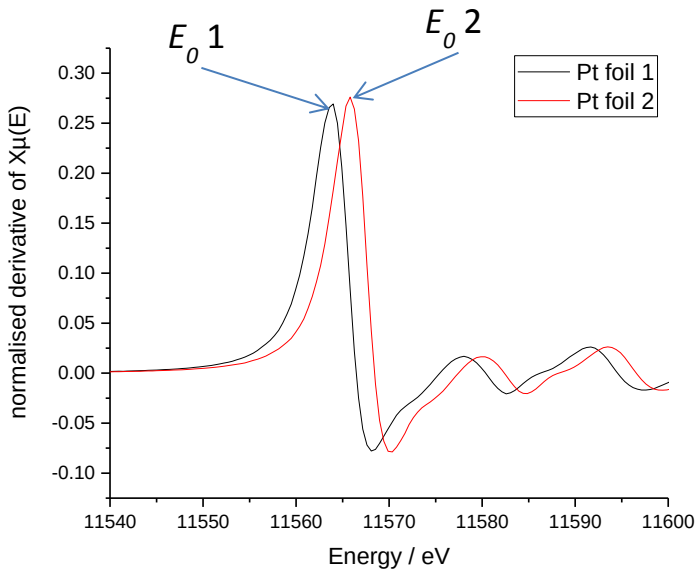

Figure 2 The normalised derivative χμ(*E*) spectra collected for the same Pt foil on separate occasions. The position of E_0 has been highlighted, and the misalignment between the 2 measurements has been exaggerated in this example.

3.1.2 Merging

Typically, the XAS data quality of a single spectrum for a sample is insufficient in terms of the amount of noise, and as a result several spectra are collected of the sample under identical conditions. Once calibrated and aligned, these spectra are merged to form a single spectrum with a larger signal to noise ratio. Each scan was collected over a period of 5 minutes covering an energy range of 1400 eV starting from 200 eV below the expected energy for the absorption edge.

3.1.3 Background Removal

The next step is to remove the background, due to the scattering observed from a single atom of the element in question, from the XAS spectra to allow the isolation of the EXAFS. This is achieved by extrapolating lines for the pre- and post-edge regions, which enables the removal of the step function resulting from the absorption edge. The pre-edge line is chosen to be linear and passing through the points before the edge step between roughly E_0-200 eV and E_0-50 eV, whilst the post edge is a quadratic function designed to pass through the middle of the EXAFS oscillations typically in the range of E_0+150 eV stretching to 10 eV from the end of the data. The background function is then generated from a combination of these 2 lines, along with a polynomial spline function, see Figure 3 and Figure 4.

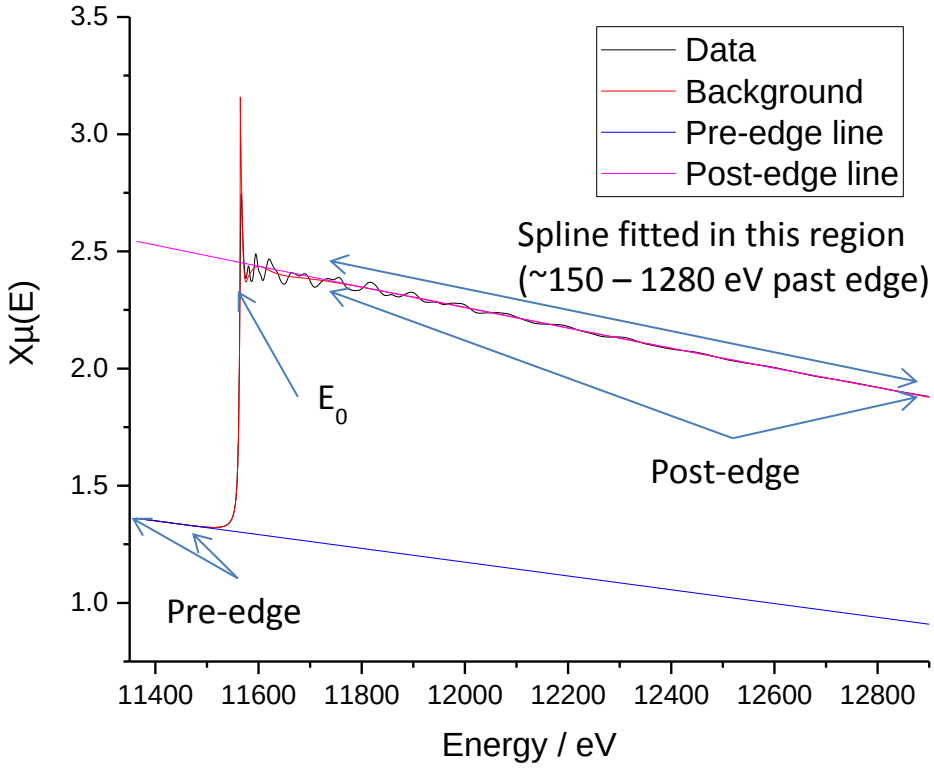

Figure 3 Example spectrum of a Pt foil illustrating how the background is modelled based on the pre- and post-edge regions.

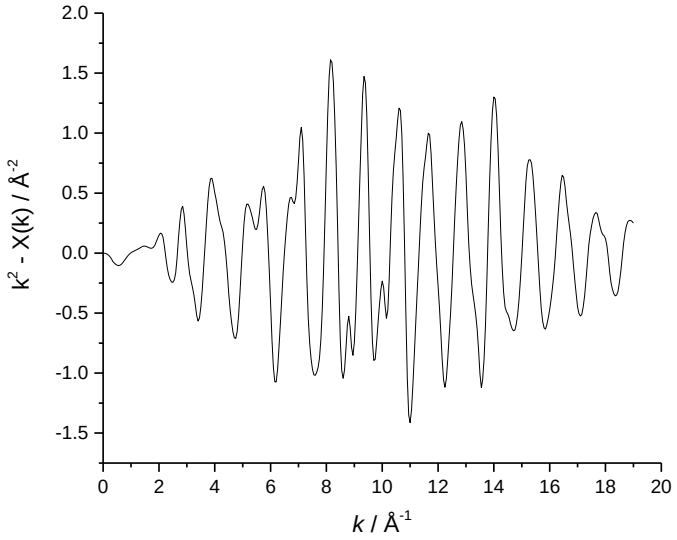

Figure 4 The EXAFS data isolated from the spectrum in Figure 3 by subtracting the background function. The data is k^2 -weighted.

When presenting EXAFS data, the units for the energy scale are converted from eV to $Å^{-1}$ to show the EXAFS in terms of the wave behaviour of the ejected photoelectron, in *k*-space, using Equation 1:

$$\boldsymbol{k = \sqrt{2m_e E/\hbar^2}}$$

Equation 1

The χ(*k*) data can be plotted as a function of k, k^2 or k^3 to emphasise the effect of different elements present in the sample. Light elements have the most impact on the low k end of the spectrum, whilst heavy elements contribute most significantly at higher k. Since the EXAFS oscillations become smaller at higher k, these signals must be amplified.

3.1.4 Fourier Transform

Artemis fits EXAFS data in *R*-space rather than k-space, so a Fourier transform is used over a subsection of the χ(*k*) data to convert it to a χ(*R*) signal. The first 1 or 2 oscillations in the 1-3 $Å^{-1}$ region of the χ(*k*) spectrum are distorted by the white line feature in the original χμ(*E*) spectrum, *i.e.* the sharp peak in intensity immediately after the absorption edge so can't be used for data fitting. Additionally, subject to data and sample quality, the χ(*k*) spectrum may become very noisy at high k, which marks the end of the usable data. These regions must be excluded from the Fourier transform.

The data shown in previous figures has been of Pt foil, which produces high quality data out to high k values. A more realistic example is presented in Figure 5, which shows the data collected from a Pt/C catalyst coated electrode plotted in k-space. The range selected for the Fourier transform for this example was 2.25 – 16.3 $Å^{-1}$, and the transform for this spectrum is shown in Figure 6. As part of the analysis procedure, several copies of the data were created, in each case the range of data used for the Fourier transform was changed to include or exclude an extra oscillation, and used to evaluate the robustness and stability of the fitting. If small changes to the fitting range result in large differences to the fitting parameters, it is often indicative of a problem with the model used.

The low *R* region of Figure 6 is excluded from the fitting window, because any signal here is left over from the background subtraction process and leads to bond lengths that are not physically possible in most systems. When bonds to oxygen are present however, there will be a peak in or near this low *R*-space region, which must be considered. *R*-space is not a radial distribution function, so bond distances can't be directly read from the graph.

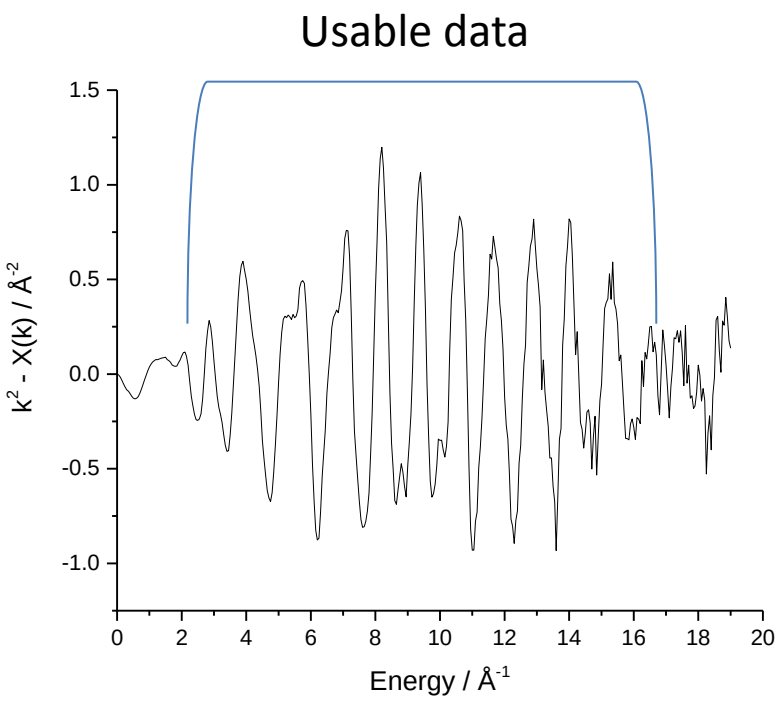

Figure 5 *k*-space data for a Pt/C catalyst coated electrode illustrating more typical data quality for a sample. The window showing the usable data for the Fourier transform is marked.

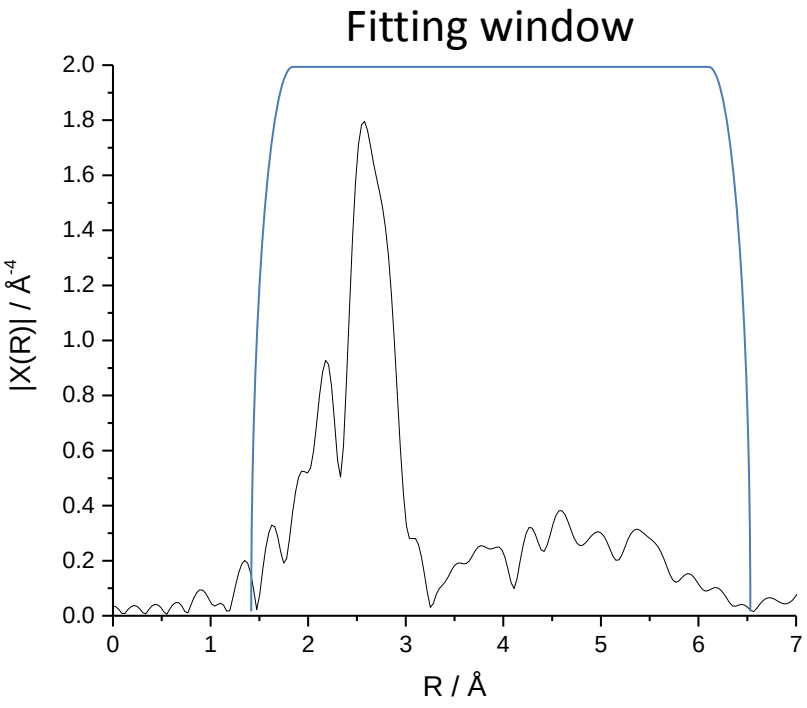

Figure 6 Fourier transform of the spectrum in Figure 5, with the data included in the fit highlighted. The low *R* region is excluded as any contribution here is left over from the background removal process because the corresponding length scale is too small to represent physically real bonds. Similarly the high *R* region is excluded because there is no signal above the noise level beyond around 6.5 Å.

3.2 EXAFS Analysis in Artemis

EXAFS analysis is carried out by comparing the difference between a theoretically modelled spectrum and the actual data collected for the sample and in Artemis the fit is carried out in *R*-space. A detailed guide for EXAFS analysis is presented in work by Ravel,[2] and a variety of ideas, principles and strategies commonly used in analysis of XAS are discussed. The calculated spectrum is generated based on Equation 2 - Equation 4, where the functions in blue are from theory (FEFF6), and the parameters in red are to be fitted based on chemical knowledge of the system being analysed.

$$\chi(k,\Gamma) = \sum_{\Gamma} \frac{(N_\Gamma S_0^2) F_\Gamma(k)}{2kR_\Gamma^2} \sin(2kR_\Gamma + \phi_\Gamma(k)) e^{-2\sigma_\Gamma^2 k^2} e^{-2R_\Gamma/\lambda(k)}$$

Equation 2

$$k = \sqrt{2m_e(E - E_0)/\hbar^2}$$

Equation 3

$$R_\Gamma = R_{cif} + \Delta R_\Gamma$$

Equation 4

The parameters involved are Γ, the number of the photoelectron scattering path in question, N_Γ, the degeneracy of path Γ, R_Γ, the effective photoelectron half path length of path Γ in Å, σ_Γ^2, the mean square disorder of path Γ in Å^2, S_0^2, the amplitude reduction factor, and E_0, an energy correction term that aligns the theory and data in eV. The theoretical functions are $F_\Gamma(k)$, the effective scattering amplitude of the photoelectron, $\phi_\Gamma(k)$, the phase shift of the photoelectron, and $\lambda_\Gamma(k)$, the mean free path of the photoelectron. This accounts for the local chemical environment around the absorbing atom. In the Artemis software, the parameters are defined as an expression containing one or more variables, which allows for complex models with multiple constraints between variables.

The theoretical functions in the EXAFS equation and initial values for degeneracy and path length are calculated for each possible scattering path based on a list of atom coordinates and identities. This coordinate list can be generated from CIF files of a material that contains similar structures and bonding to the sample. Constraints between the variables and additional single scattering (SS) and multiple scattering (MS) paths are incorporated

into the fitting model to improve the match with the experimental data. Examples of both SS paths, where the photoelectron scatters between the absorbing atom and one other neighbouring atom, and MS paths, where the photoelectron scatters between multiple surrounding atoms and the absorbing atom, are shown in Figure 7. Pt atoms at the same distance from the absorbing atom are considered to be part of the same shell, and are numbered sequentially outwards. The fit is built up by starting with the first shell and working outwards.

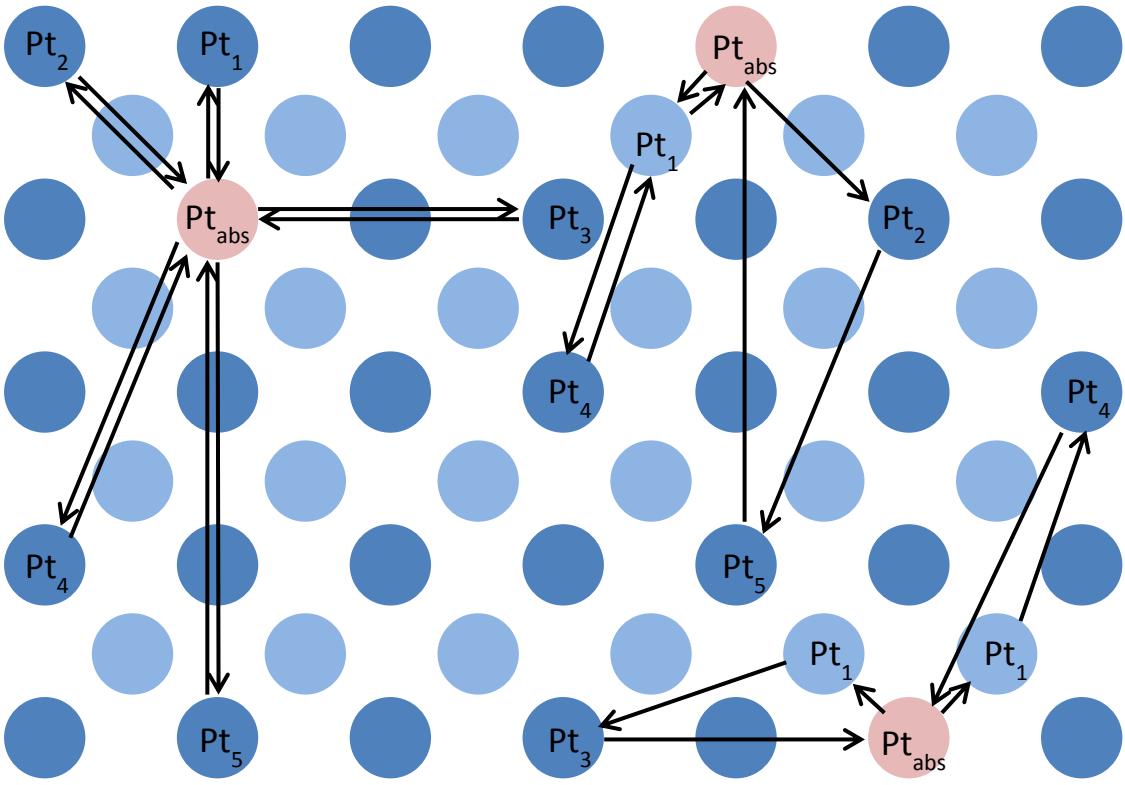

Figure 7 Examples of single (left hand side) and multiple scattering (right hand side) paths that can occur in a Pt sample. The pale red circles, labelled Pt_{abs} represent the absorbing atoms, the dark blue circles depict Pt atoms in the same plane as the absorbing atom, and the pale blue circles represent Pt atoms beneath the plane.

3.2.1 Analysis of Pt Foil

Before moving on to actual samples, analysis of a reference material, in this case a Pt foil, must be completed in order to break the correlation between the amplitude reduction factor and the degeneracy. In a Pt foil, the degeneracy for each scattering path is fixed to the expected value for the bulk material, allowing S_0^2 value to be determined, whereas for a Pt/C nanoparticle sample, bulk values for degeneracy are inaccurate due to surface termination effects arising from small particle sizes. By assuming that S_0^2 is chemically transferable, reasonable when looking at the same absorption edge at the same beamline,

the degeneracy of scattering paths in a Pt nanoparticle sample can now be floated as a guess variable and accurately determined. This is a common strategy when dealing with nanoparticles, for example as outlined in the review by Frenkel[3] and other authors.[4,5]

The 5 parameters, shown in red in Equation 2-Equation 4, must be defined for each scattering path, however the amount of information present in an EXAFS spectrum is limited and the number of variables introduced must be restricted. The Nyquist theorem can be used to place an upper limit on the number of independent points and therefore number of variables. This limit is proportional to the range of data used in k-space for the Fourier transform and to the range of data in *R*-space used for the fit and the relationship is shown in Equation 5. The number of variables should be no greater than 50-60% of the number of independent points because many of the assumptions required for the Nyquist theory are not strictly true when looking at EXAFS spectra. To be valid, the information content of the EXAFS signal must be uniform, have a known theoretical lineshape for the data with known, quantifiable sources of error in a normal distribution. The fits presented here typically have around 40 independent points.

$$N_{ind} \approx \frac{2\Delta k \Delta R}{\pi}$$

Equation 5

Addition of variables improves the fit to the data, but each additional variable must be physically reasonable. S_0^2 and E_0 are parameters that scale the theoretical spectrum along the amplitude and energy axes, respectively, to match the experimental spectrum and are influenced by the beamline. As a result these parameters can each be represented by a single variable for all scattering paths. This leaves 3 remaining parameters for each included path that need to be defined, *R*, σ^2 and *N*, which may or may not be known depending on the sample.

σ^2 in this work is constrained based on the photoelectron free path length, in a similar manner to work done by Price *et al*.[5] and differs from the simpler constraints used in older work such as by Frenkel.[6] A new σ^2 variable must be included for each SS path used in the fit. σ^2 for the MS paths are modelled in terms of the variables used for the SS paths. This is done by considering each leg of the scattering path and finding its equivalent in terms of SS paths. σ^2 for the SS path with the 1st nearest neighbouring Pt atom is called *SS1*, σ^2 for the SS path with the 2nd nearest neighbour is *SS2* and so on for the next nearest neighbouring

atoms. Taking the MS path, Pt_{abs}-Pt_1-Pt_3-Pt_{abs}, shown near the bottom of Figure 7, as an example, which consists of a Pt_{abs}-Pt_1 leg, a Pt_{abs}-Pt_3 leg and finally a Pt_1-Pt_3 leg, which is equivalent to the Pt_{abs}-Pt_1 leg by symmetry. The σ^2 for this MS path is then defined as *½ SS1 + ½ SS3 + ½ SS1*, thus avoiding the need for any further variables. A similar approach can be taken for most other MS paths; some differences must be accounted when considering colinear, focussed or 'rattle' MS paths, where the scattering angle is 180° or 360°.[7] A general scheme is outlined below in Figure 8 where the distance between the absorbing atom and shell 2 is assumed to be twice the distance to the first shell.

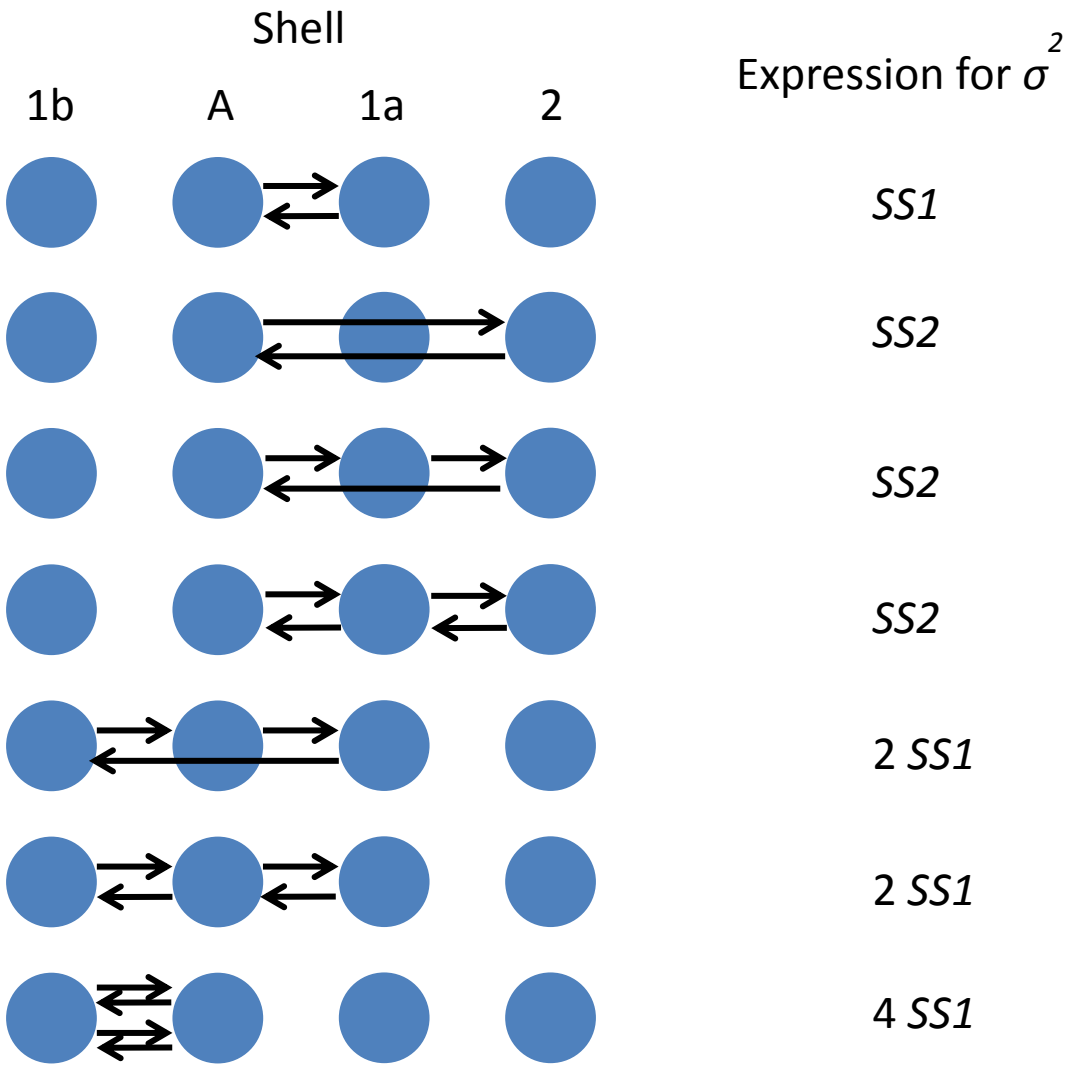

Figure 8 General scheme illustrating how the σ^2 values for each scattering path were defined. A denotes the absorbing atom, 1a and 1b denote 1st shell atoms on opposite sides of the absorbing atom, and 2 denotes the 2nd shell atoms. The interatomic distance between A and 1 is assumed to be half that between A and 2. Explanations for these relationships are given by Hudson *et al.*[7]

Other ways of modelling the σ^2 parameter include the correlated Debye, and Einstein models as described by Sevillano *et al.,*[8] however these models have their own limitations. The Einstein model is most useful when measurements have been taken at multiple temperatures, whilst the correlated Debye model is only applicable to monoatomic materials. Although the Debye model would work well for the reference materials and some of the catalyst samples, requiring only one variable to define σ^2 for all scattering paths, this work goes on to investigate Pt alloy nanoparticle catalysts, and Pt oxide species were expected so the model was avoided on this basis.

Since Pt and Ni both take the highly symmetrical cubic close packed (fcc) structure, *R*, the effective photoelectron scattering path length, can be defined by a single variable, an isotropic expansion coefficient, α. Due to the high symmetry of the structure, path lengths for all SS and MS paths expand or contract by the same percentage, so *R* can be defined as $R_{cif} * \alpha$ for all Pt and Ni samples.

The same does not apply for Co as it assumes the hexagonal close packed structure, so does not have a cubic unit cell. As a result of the lower symmetry, further variables are necessary to define R for the SS and MS paths. This can be achieved using the '*a*' and '*c*' variables, commonly used to define the unit cell, and trigonometry to define algebraically the distance between atoms and thereby the photoelectron path length.

A list of the various scattering paths used for the EXAFS fit for the Pt foil and how the parameters were defined is presented in Table 1. A total of 8 variables were used to define the parameters for the 15 scattering paths used, and the fit in *R*-space is shown in Figure 9, and shown in *k*-space at 3 different *k*-weights in Figure 10. The fitting range used was 3.00-17.06 $Å^{-1}$ in *k*-space, and 1.0-6.6 Å in *R*-space. The r-factor for the fit was 0.017.

The difference between the calculated spectrum and the experimental spectrum is minimised based on a non-linear least-squares method (Levenberg-Marquardt) to determine χ^2 and an r-factor as defined in Equation 6. Due to the way in which measurement uncertainty is determined in Artemis, along with other errors or approximations in the underlying theory, sample inhomogeniety and non-linearity of detectors, χ^2 is not calculated correctly. As a result, it can only be used when comparing different fits, where a good fit has a much lower χ^2, and is not a meaningful value on its own. For the r-factor, a great fit will have a value less than 0.02, whilst for good fits, the r-factor is less than 0.05. The fitting model must also make physical and chemical sense.

$$\mathbf{r} = \frac{\sum_{i=min}^{max}\left[\boldsymbol{Re}(\chi_d(r_i) - \chi_t(r_i))^2 + \boldsymbol{Im}(\chi_d(r_i) - \chi_t(r_i))^2\right]}{\sum_{i=min}^{max}\left[(\boldsymbol{Re}(\chi_d(r_i))^2 + \boldsymbol{Im}(\chi_d(r_i))^2\right]}$$

Equation 6

To obtain error bars for the fitted parameters, the diagonal of the covariance matrix is used and is scaled by $\sqrt{\chi_\nu^2}$ to ensure errors of the correct magnitude. This assumes a good fit.

Table 1 Summary of parameters and scattering paths included in the EXAFS fitting model for the Pt foil.

Scattering path	*N*	S_0^2	ΔE_0	ΔR	σ^2
Pt_{abs}-Pt_1-Pt_{abs}	12	*amp*	*enot*	α*reff	*SS1*
Pt_{abs}-Pt_2-Pt_{abs}	6	*amp*	*enot*	α*reff	*SS2*
Pt_{abs}-Pt_3-Pt_{abs}	24	*amp*	*enot*	α*reff	*SS3*
Pt_{abs}-Pt_4-Pt_{abs}	12	*amp*	*enot*	α*reff	*SS4*
Pt_{abs}-Pt_5-Pt_{abs}	24	*amp*	*enot*	α*reff	*SS5*
Pt_{abs}-Pt_{1a}-Pt_{1b}-Pt_{abs} (acute triangle)	48	*amp*	*enot*	α*reff	1.5 *SS1*
Pt_{abs}-Pt_{1a}-Pt_{1c}-Pt_{abs} (obtuse triangle)	48	*amp*	*enot*	α*reff	*SS1* + ½ *SS3*
Pt_{abs}-Pt_1-Pt_3-Pt_{abs} (obtuse triangle)	96	*amp*	*enot*	α*reff	*SS1* + ½ *SS3*
Pt_{abs}-Pt_{1a}-Pt_{1d}-Pt_{abs} (non-forward, linear)	12	*amp*	*enot*	α*reff	2 *SS1*
Pt_{abs}-Pt_1-Pt_4-Pt_{abs} (forward, linear)	24	*amp*	*enot*	α*reff	*SS4*
Pt_{abs}-Pt_{1a}-Pt_{1d}-Pt_{abs} (forward through absorber, linear)	12	*amp*	*enot*	α*reff	2 *SS1*
Pt_{abs}-Pt_{1a}-Pt_4-Pt_{1a}-Pt_{abs} (double forward, linear)	12	*amp*	*enot*	α*reff	*SS4*
Pt_{abs}-Pt_{1a}-Pt_4-Pt_{1a}-Pt_{abs} (dog-leg)	48	*amp*	*enot*	α*reff	4 *SS1*
Pt_{abs}-Pt_1-Pt_5-Pt_{abs} (obtuse triangle)	48	*amp*	*enot*	α*reff	½ (*SS1* + *SS2* + *SS5*)
Pt_{abs}-Pt_2-Pt_5-Pt_{abs} (obtuse triangle)	48	*amp*	*enot*	α*reff	½ (*SS1* + *SS2* + *SS5*)

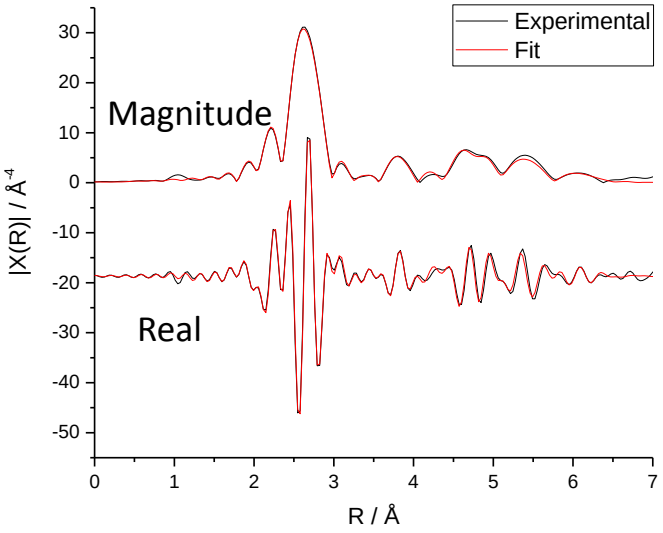

Figure 9 *R*-space spectra showing the fit to the experimental data for the Pt foil as both a magnitude and real plot. The fitting range used was 1.0-6.6 Å in *R*-space, and the r-factor for the fit was 0.017.

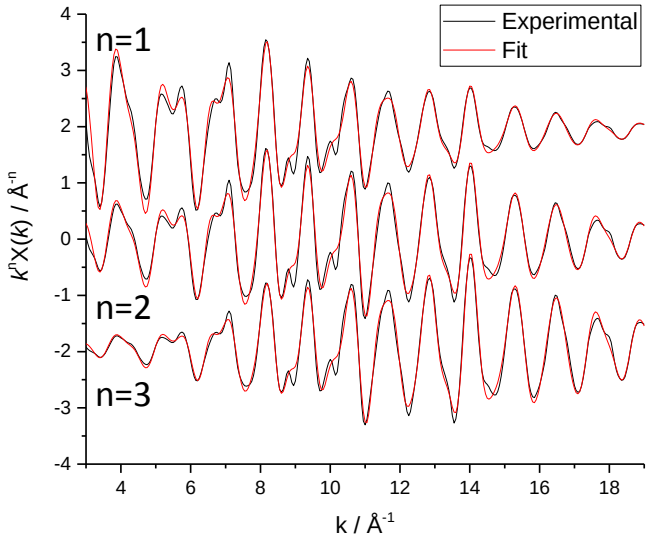

Figure 10 *k*-space plots for the Pt foil at different *k*-weights showing the experimental spectra compared to the calculated ones. The fitting range used for the fit was 3.00-17.06 Å^{-1} in *k*-space, and the r-factor was 0.017.

Table 2 Table showing the vales for the variables, calculated from the fit displayed in Figure 9 and Figure 10, along with their uncertainties. '*amp*' represents S_0^2, and '*enot*' denotes ΔE_0.

Variable	Value	Uncertainty
amp	0.84	0.03
enot / eV	7.05	0.30
α	-0.00375	0.00047
SS1 / Å^2	0.00488	0.00014
SS2 / Å^2	0.00691	0.00074
SS3 / Å^2	0.00721	0.00038
SS4 / Å^2	0.00835	0.00058
SS5 / Å^2	0.00851	0.00011

From the spectra shown in Figure 9 and Figure 10, the r-factor and from the values of the variables in Table 2, it is clear that a good fit to the experimental data has been achieved. The value determined for S_0^2 (*amp*) is close to previously published values[9]. In general, the r-factor should be less than 0.05, and preferably closer to 0.02, whilst the variables should all make physical sense. S_0^2 (=*amp*) is expected to be in the range 0.7-1.0, ΔR (*c.f.* α) is small, and σ^2 values are all definite positive and increase with path length. ΔE_0 (=*enot*) is less than 10 eV, although for some metals, including Pt, this value is overestimated when using the modelling program FEFF6 as done here. The later version, FEFF8, uses self-consistent potentials rather than overlapped atomic potentials. Fortunately, only ΔE_0 is affected, all other values do not change.

3.2.2 EXAFS Analysis of Pt/C – Introducing Degeneracy as a Variable

Pt/C nanoparticle catalyst sample with a particle size of around 5 nm and pressed into a pellet with boron nitride will be used as an example to explain how the degeneracy, or coordination number when looking at SS paths, can be determined using EXAFS. Due to the large number of under coordinated surface atoms in nanoparticles, and the fact that EXAFS analyses the average chemical environment of a given element, the assumption that degeneracy is the same as in the bulk material is invalid. This is known as the termination effect, and occurs because the probability of the existence of a complete scattering path decreases as the radial distance from the absorbing atom increases due to the finite size of

the nanoparticle. The important value previously calculated from analysing the Pt foil is the value for S_0^2 (or *amp*), which is assumed to be chemically transferable and is used to break the correlation with path degeneracy in the EXAFS equation. Comparison of the obtained values for degeneracy with values yielded from equations developed by authors such as Benfield,[10] Glasner and Frenkel[11] as well as numbers determined from computer modelling and simulation[12,13,14] allow the estimation of an average particle size for the sample.

Most of the parameters can be defined in the same as for the Pt foil *i.e.* σ^2 are modelled in the same way, isotropic expansion can still be assumed, and E_0 is still the same for each path. Some differences may be observed in terms of the magnitude of α and σ^2 due to the increased significance of surface relaxation effects, and increased disorder in the system due to the range of particle sizes present in the sample. Now S_0^2 is no longer a variable and is fixed at 0.84, whilst degeneracy, *N*, is an extra parameter for each path that must be defined, which can be done in several ways, imposing differing numbers of constraints between MS paths in particular.

Similar to the σ^2 values, each of the SS paths added to the fit require a separate degeneracy variable, and can be considered as the coordination number for this shell of atoms. Referring back to Table 1, some shells are expected to have the same degeneracy in bulk material, *e.g.* shells 1 and 4 have $N = 12$, and shells 3 and 5 have $N = 24$. In the case of nanoparticles a reasonable feasibility test is that the 1st shell coordination number, N_1, is more than N_4, the 4th shell coordination number, and likewise if available, N_3 is greater than N_5, because, as you move further away from the absorbing atom in a given direction, it is more likely that the surface has been reached and no scattering is possible from this direction. On the other hand, deciding whether a MS path requires a separate *N* variable, or can be expressed in terms of the existing variables from the SS paths is more difficult.

At one extreme, all 12 included SS and MS paths can be given a separate variable for degeneracy, giving a total of 19 parameters. This yields a very close fit to the experimental data, shown in Figure 11, with an r-factor of 0.0084, better than that achieved for the Pt foil. However looking more closely at the values used for the fit it becomes clear that this model is not sensible, see Table 3. Several degeneracies are negative, many are larger than the expected values for the bulk material, and many of the measurement uncertainties are considerable, which indicates that this model is not physically meaningful. Each individual variable is used only once in the calculation, which means that they are not robust. As a result, constraints between the degeneracies must be imposed.

Table 3 Summary of the values obtained from the fit shown in Figure 11 alongside reasonable values for a Pt/C sample.

Variable	Model	Typical values
amp[1]	0.84	0.7 – 1.0
enot / eV	7.10 ± 0.38	|*enot*| < 10
α	-0.00502 ± 0.00057	small, |α| < ~0.01
SS1 / Å^2	0.00528 ± 0.00016	0 ≤ *SS1* ≤ 0.010
SS2 / Å^2	0.00801 ± 0.00186	0 ≤ *SS2* ≤ 0.015, *SS2* ≥ *SS1*
SS3 / Å^2	0.00821 ± 0.00117	0 ≤ *SS3* ≤ 0.015, *SS3* ≥ *SS2*
SS4 / Å^2	0.00945 ± 0.00547	0 ≤ *SS4* ≤ 0.015, *SS4* ≥ *SS3*
N1	11.09 ± 0.45	0 ≤ *N1* ≤ 12
N2	5.70 ± 2.08	0 ≤ *N2* ≤ 6
N3	23.97 ± 10.45	0 ≤ *N3* ≤ 24
N4	26.71 ± 41.12	0 ≤ *N4* ≤ 12, *N4* ≤ *N1*
N11a	43.17 ± 41.61	0 ≤ *N1* ≤ 48
N11o	-69.13 ± 212.83	0 ≤ *N1* ≤ 48
N13	120.50 ± 163.36	0 ≤ *N1* ≤ 96
N11n	16.57 ± 105.57	0 ≤ *N1* ≤ 12
N14	21.14 ± 22.12	0 ≤ *N1* ≤ 24
N11f	-11.31 ± 100.02	0 ≤ *N1* ≤ 12
N141	10.27 ± 6.05	0 ≤ *N1* ≤ 12
N131	197.74 ± 384.46	0 ≤ *N1* ≤ 48

1 – *amp* not allowed to vary.

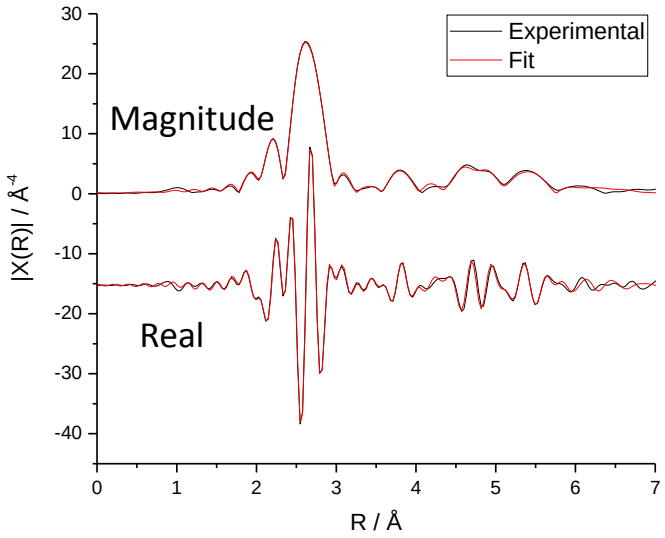

Figure 11 *R*-space spectra showing the fit to the experimental data for the 5 nm Pt/C as both a magnitude and real plot, where separate variables for the degeneracy for each scattering path have been used. The fitting range used was 1.0-6.6 Å in *R*-space, and the r-factor for the fit was 0.0084.

Previous EXAFS studies on Pt have used a model where each SS path has separate N and σ^2 variables, the triangular MS paths have another variable for each, and the SS variables for scattering off of the 4th nearest neighbour are used to describe the linear, focussed MS paths.[9,15] This model, summarised in Table 4, has been applied to the spectra generated in this work, although the σ^2 model has been altered so that physically reasonable values are obtained from the fit, and will be compared to the new more tightly constrained model.

Table 4 Summary of the model used by Frenkel *et al.*[15] modified to fit the Pt/C catalyst samples investigated in this work.

Scattering path	*N*	σ^2
Pt_{abs}-Pt_1-Pt_{abs}	*N1*	*SS1*
Pt_{abs}-Pt_2-Pt_{abs}	*N2*	*SS2*
Pt_{abs}-Pt_3-Pt_{abs}	*N3*	*SS3*
Pt_{abs}-Pt_4-Pt_{abs}	*N4*	*SS4*
Pt_{abs}-Pt_{1a}-Pt_{1b}-Pt_{abs} (acute triangle)	*TR1*	1.5 *SS1*
Pt_{abs}-Pt_{1a}-Pt_{1c}-Pt_{abs} (obtuse triangle)	*TR2*	*SS1*+ ½ *SS3*
Pt_{abs}-Pt_1-Pt_3-Pt_{abs} (obtuse triangle)	2 *TR2*	*SS1*+ ½ *SS3*
Pt_{abs}-Pt_{1a}-Pt_{1d}-Pt_{abs} (non-forward, linear)	*N1*	2 *SS1*
Pt_{abs}-Pt_1-Pt_4-Pt_{abs} (forward, linear)	2 *N4*	*SS4*
Pt_{abs}-Pt_{1a}-Pt_{1d}-Pt_{abs} (forward through absorber, linear)	*N1*	2 *SS1*
Pt_{abs}-Pt_{1a}-Pt_4-Pt_{1a}-Pt_{abs} (double forward, linear)	*N4*	*SS4*

The new more constrained model defines the degeneracy for all paths without including any new variables, which should make for a robust fit as all variables are used multiple times. Only 10 variables are used to fit the data including an extra shell, as opposed to the 12 required previously. The logic behind the model is that the degeneracy for the MS paths must be proportional to the coordination numbers for the associated shells of neighbour atoms, since if these shells contain fewer atoms, the number of complete MS paths, and thus the degeneracy, must decrease. The degeneracy for the MS paths is therefore modelled as the product of the coordination number of the atom shells involved. The proportionality constant is related to the 'importance' of an atom in each shell, *i.e.* the number of degenerate paths affected if an atom were to be removed from the shell, and the total number of atoms in the shell. If fully coordinated, the degeneracy will equate to the value expected for the bulk material. The parameters are defined in Table 5.

Table 5 Summary of the new constrained model with minimal usage of variables.

Scattering path	*N*	σ^2
Pt_{abs}-Pt_1-Pt_{abs}	*N1*	*SS1*
Pt_{abs}-Pt_2-Pt_{abs}	*N2*	*SS2*
Pt_{abs}-Pt_3-Pt_{abs}	*N3*	*SS3*
Pt_{abs}-Pt_4-Pt_{abs}	*N4*	*SS4*
Pt_{abs}-Pt_{1a}-Pt_{1b}-Pt_{abs} (acute triangle)	1/3 $N1^2$	1.5 *SS1*
Pt_{abs}-Pt_{1a}-Pt_{1c}-Pt_{abs} (obtuse triangle)	1/3 $N1^2$	*SS1*+ ½ *SS3*
Pt_{abs}-Pt_1-Pt_3-Pt_{abs} (obtuse triangle)	1/3 *N1* * *N3*	*SS1*+ ½ *SS3*
Pt_{abs}-Pt_{1a}-Pt_{1d}-Pt_{abs} (non-forward, linear)	1/12 $N1^2$	2 *SS1*
Pt_{abs}-Pt_1-Pt_4-Pt_{abs} (forward, linear)	1/6 *N1* * *N4*	*SS4*
Pt_{abs}-Pt_{1a}-Pt_{1d}-Pt_{abs} (forward through absorber, linear)	1/12 $N1^2$	2 *SS1*
Pt_{abs}-Pt_{1a}-Pt_4-Pt_{1a}-Pt_{abs} (double forward, linear)	1/12 *N1* * *N4*	*SS4*
Pt_{abs}-Pt_{1a}-Pt_3-Pt_{1a}-Pt_{abs} (dog-leg)	1/6 *N1* * *N3*	4 *SS1*

Both models give a good fit to the experimental data, with r-factors below 0.02, and yield sensible and comparable values for the various parameters, with the exception of the value for the coordination in the 4th shell of neighbouring atoms. Both fits are shown in Figure 12 and the parameter values are shown in Table 6. As a result, both models were considered when analysing the data.

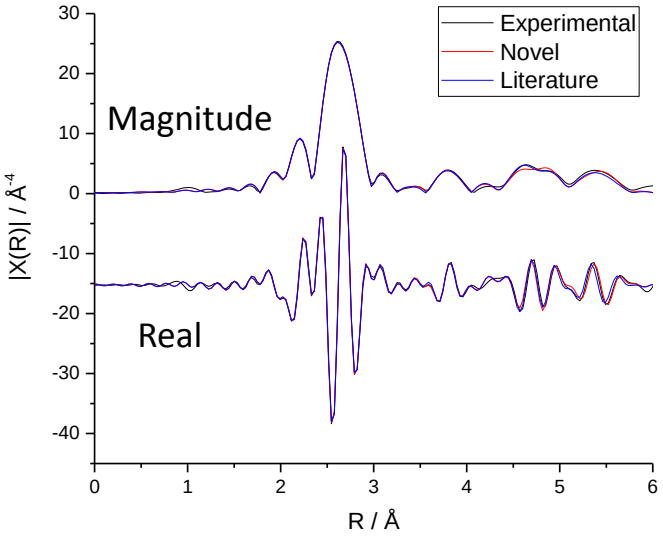

Figure 12 *R*-space spectra showing the fits to the experimental data for the 5 nm Pt/C as both a magnitude and real plot for the 2 models. The models are in close agreement and both reproduce the experimental data well, there is a small deviation in the novel model presented here at ~4.7 Å from the experimental data.

Table 6 Comparison of the values yielded by the fits shown in Figure 12 for the EXAFS data of the Pt/C pellet with each model.

Variable	Literature	Novel
amp[a]	0.84	0.84
enot / eV	7.00 ± 0.37	6.88 ± 0.29
α	-0.00490 ± 0.00056	-0.00507 ± 0.00048
SS1 / Å^2	0.00525 ± 0.00016	0.00521 ± 0.00014
SS2 / Å^2	0.00717 ± 0.00158	0.00769 ± 0.00149
SS3 / Å^2	0.00740 ± 0.00091	0.00812 ± 0.00095
SS4 / Å^2	0.00848 ± 0.00106	0.00851 ± 0.00097
N1	11.02 ± 0.44	10.86 ± 0.38
N2	4.83 ± 1.58	5.39 ± 1.53
N3	17.86 ± 3.83	22.18 ± 4.93
N4	9.06 ± 1.50	10.48 ± 1.63
TR1[b]	12.87 ± 15.03	-
TR2[b]	52.49 ± 18.86	-

a – *amp* not allowed to vary in either model, b – *TR1* and *TR2* only present in literature model.

3.3 References

(1) Ravel, B.; Newville, M. ATHENA , ARTEMIS , HEPHAESTUS : Data Analysis for X-Ray Absorption Spectroscopy Using IFEFFIT. *J. Synchrotron Radiat.* **2005**, *12*, 537–541.

(2) Ravel, B. Path Degeneracy and EXAFS Analysis of Disordered Materials. *J. Synchrotron Radiat.* **2014**, *21*, 1269–1274.

(3) Frenkel, A. I. Applications of Extended X-Ray Absorption Fine-Structure Spectroscopy to Studies of Bimetallic Nanoparticle Catalysts. *Chem. Soc. Rev.* **2012**, *41*, 8163–8178.

(4) Price, S. W. T.; Rhodes, J. M.; Calvillo, L.; Russell, A. E. Revealing the Details of the Surface Composition of Electrochemically Prepared Au@Pd Core@Shell Nanoparticles with in Situ EXAFS. *J. Phys. Chem. C* **2013**, *117*, 24858–24865.

(5) Price, S. W. T.; Speed, J. D.; Kannan, P.; Russell, A. E. Exploring the First Steps in Core–Shell Electrocatalyst Preparation: In Situ Characterization of the Underpotential Deposition of Cu on Supported Au Nanoparticles. *J. Am. Chem. Soc.* **2011**, *133*, 19448–19458.

(6) Frenkel, A. I. Solving the Structure of Nanoparticles by Multiple-Scattering EXAFS Analysis. *J. Synchrotron Radiat.* **1999**, *6*, 293–295.

(7) Hudson, E. A.; Allen, P. G.; Terminello, L. J.; Denecke, M. A.; Reich, T. Polarized X-Ray-Absorption Spectroscopy of the Uranyl Ion: Comparison of Experiment and Theory. *Phys. Rev. B* **1996**, *54*, 156–165.

(8) Sevillano, E.; Meuth, H.; Rehr, J. J. Extended X-Ray Absorption Fine Structure Debye-Waller Factors. I. Monatomic Crystals. *Phys. Rev. B* **1979**, *20*, 4908–4911.

(9) Frenkel, A. Solving the 3D Structure of Metal Nanoparticles. *Zeitschrift für Krist. - Cryst. Mater.* **2007**, *222*, 605–611.

(10) Benfield, R. E. Mean Coordination Numbers and the Non-Metal-Metal Transition in Clusters. *J. Chem. Soc., Faraday Trans* **1992**, *88*, 1107–1111.

(11) Glasner, D.; Frenkel, A. I. Geometrical Characteristics of Regular Polyhedra: Application to EXAFS Studies of Nanoclusters. In *AIP Conference Proceedings*; AIP, 2007; 882, 746–748.

(12) Beale, A. M.; Weckhuysen, B. M. EXAFS as a Tool to Interrogate the Size and Shape of Mono and Bimetallic Catalyst Nanoparticles. *Phys. Chem. Chem. Phys.* **2010**, *12*, 5562.

(13) Price, S. W. T.; Zonias, N.; Skylaris, C.-K.; Russell, A. E.; Ravel, B. The Application of Molecular Dynamics to Fitting EXAFS Data. *J. Phys. Conf. Ser.* **2013**, *430*, 12009.

(14) Price, S. W. T.; Zonias, N.; Skylaris, C. K.; Hyde, T. I.; Ravel, B.; Russell, A. E. Fitting EXAFS Data Using Molecular Dynamics Outputs and a Histogram Approach. *Phys. Rev. B - Condens. Matter Mater. Phys.* **2012**, *85*, 1–14.

(15) Frenkel, A. I.; Hills, C. W.; Nuzzo, R. G. A View from the Inside: Complexity in the Atomic Scale Ordering of Supported Metal Nanoparticles. *J. Phys. Chem. B* **2001**, *105*, 12689–12703.

Chapter 4: Degradation of Pt/C

4.1 Introduction

Pt/C nanoparticle materials are well known catalysts for both the hydrogen oxidation and oxygen reduction at fuel cell anodes and cathodes respectively. Of particular interest is the ORR due to the slower kinetics of the reaction and the harsh conditions experienced at the cathode during fuel cell operation. More recently, the focus of research in this area has shifted slightly and, rather than focussing on producing more active catalysts, is more concerned with their durability. One of the reasons for this is the poor correlation between activity measurements in typical laboratory scale experiments employing liquid half cells and the performance in fuel cell MEAs.[1] Additionally, recent hypotheses have suggested that, when operating in the high overpotential and high power regime, there is a limit on the achievable current density of around 0.1 A cm^{-2}, which calls into question the benefit of using very active catalysts rather than catalysts with a very high surface area.[2] As a result, durability of the catalysts in terms of maintaining a high electrochemically active surface area is vitally important.

This chapter will look at the effect of a potential cycling treatment *i.e.* an accelerating stability test (AST), on the structure and activity of two Pt/C catalyst samples with nominal particle size distributions centred on 2 and 5 nm respectively. The activity has been measured using the RDE method, and the structure of the catalyst nanoparticles has been analysed using a variety of techniques. Pt/C samples were first studied to provide a baseline to which the Pt alloy nanoparticle catalysts will be compared in the next chapter. Two particle sizes were chosen in order to test less conventional methods by which the nanoparticle diameters can be measured as well as for comparison purposes. These testing procedures were designed to be comparable to experiments and standards outlined in published literature by Kocha *et al*.[3] and represent conditions which should lead to degradation of the core-shell PtNi/C and PtCo/C catalysts used later on in this work. Higher acid concentration was used to enhance the amount of dissolution[4] and reduce the time required for the AST.

One of the pathways for the degradation of Pt alloy catalysts is the gradual, selective leaching of the less noble metal alloyed with the Pt. This selective de-alloying occurs based on three main factors; a large difference in standard reduction potential of the component

metals,[5] the parting limit, *i.e.* a minimum percentage composition of the less noble element,[6] and the critical potential for the material must be reached through chemical or electrochemical means.[7] An atomistic view of this selective dissolution process is presented by Hoshi *et al.,*[8] which also highlights the instability of the Ni and Co components under these conditions. The conditions chosen in this work, scans of 0.6 – 1.0 V *vs.* RHE in 1 M $HClO_4$ at 80 ^{o}C, are expected to be typical during normal operation of a commercial fuel cell. Significant Pt dissolution is not expected according to results by Topalov *et al.*,[9] who use experiments employing a flow cell coupled to ICP-MS to show that minimal Pt dissolution occurs when the potential is kept below 1.05 V *vs.* RHE. Us e of higher potentials also damages the carbon support as evidenced by identical location TEM experiments.[10,11]

Another typical degradation pathway is growth of the nanoparticles, which reduces available Pt surface area and may lead to decreased catalytic performance. The particle size distribution of nanoparticle catalysts is typically determined using TEM, where a number of particles are directly imaged and can be measured individually.[12] This method relies on imaging and counting a statistically significant number of particles, which can be laborious and time consuming, but also is routinely available and will also provide additional information such as particle dispersion, shape and morphology. TEM can also be coupled to other techniques such as EDX, EELS and HAADF to increase resolution further and to provide extra information on chemical distribution and composition, for example as done in work by Dubau *et al.*[12] XRD patterns can also be used to determine nanoparticle size by measuring the breadth of peaks, employing the Scherrer equation and assuming that the calculated crystallite size is equivalent to the particle size. This technique gives a bulk measurement of the average particle size, although is limited to slightly larger crystallite/particle sizes so provides lower resolution than obtainable via TEM, and also requires the sample to have an ordered crystalline component. TEM is open to bias caused by the operator's choice of the sample area to image, and typically, when estimating particle sizes, only ~100s of particles are analysed.

The size of the Pt nanoparticles is an important factor when looking at the electrocatalysis of the ORR as it is indicative of the available surface area, or Pt dispersion, as well as the distribution of crystal faces on the catalyst surface. As a result, changing the particle size affects both the mass and specific activity of the catalyst, discussed in more detail in the review paper by Stephens *et al*.[13] Increasing the Pt dispersion, by moving from extended surfaces to nanoparticles of decreasing size, significantly improves the mass activity up to a

certain point, at approximately 3 nm, [14,15,16] where the low specific activity of the surface outweighs the increased surface area. However, the exact maximum in mass activity is somewhat controversial.[17] The decrease in specific activity has been explained using DFT calculations,[18,19] which show that the number of step sites increases as the particle size decreases. These undercoordinated sites bind the intermediates of the ORR, most importantly OH_{ads}, more strongly thereby increasing the required overpotential for the reaction. This particle size effect is neatly summarised in Figure 1, reproduced from the literature.[13]

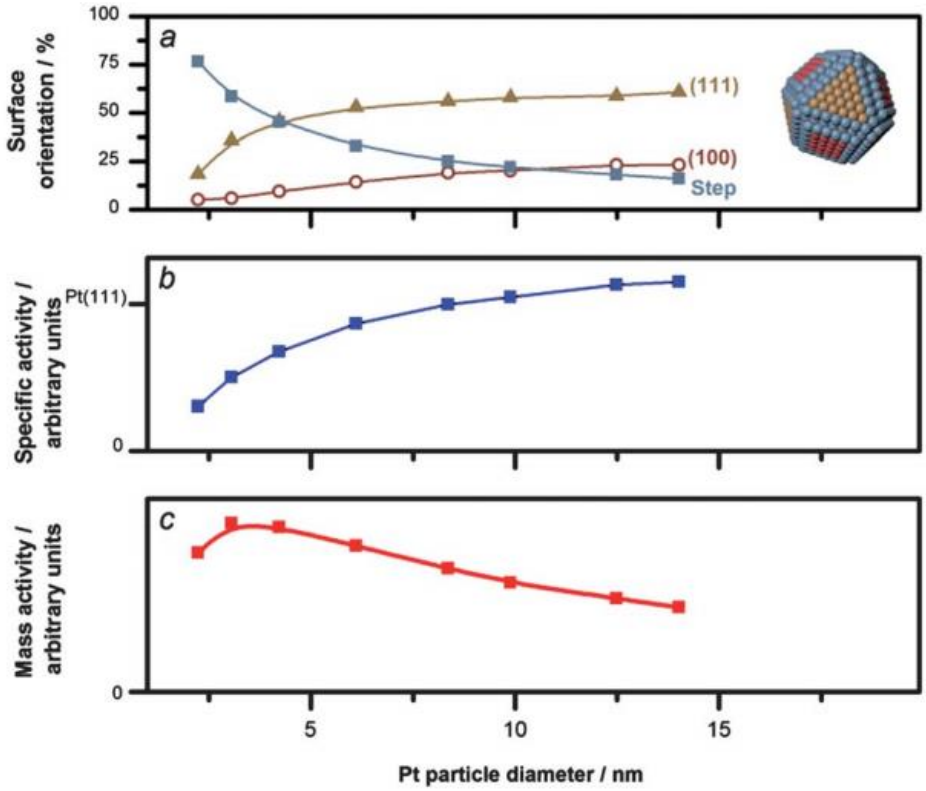

Figure 1 The theoretically determined effect of particle size on a) the distribution of crystal faces making up the nanoparticle surface of the type shown, b) the specific activity, and c) the mass activity, accounting for the proportions of crystal faces present, normalised to the activity of the Pt(111) surface. Reproduced from work by Stephens *et al.* [13]

In this work, the focus was to use XAS measurements to determine particle sizes for the catalyst powders and coated electrode samples. This was achieved by extracting the EXAFS signal from the spectrum and fitting the data as described in chapter 3. The coordination numbers determined from the fit can be compared to computationally modelled values thus indicating the particle size. An array of computational modelling has been done, examining the effect of particle as well as shape on the coordination numbers. Early studies

include those by Fritsche[20] and Benfield,[21] where the effect of geometry on the 1st shell coordination number was studied, as well as by Montejano *et al.*[22] who looked at cuboctahedral, icosahedral, body centred and primitive geometries. This work was built upon by Jentys who provided an equation allowing the estimation of coordination numbers for the first 5 shells of nearest neighbour atoms, and showed that the ratio of coordination numbers for shells 1 and 3 can be used to distinguish between spherical and flattened particles.[23] Glasner and Frenkel compute exact coordination numbers for the first 6 shells of cuboctahedron, icosahedron, truncated octahedron and hcp atom clusters ranging in size from 10-1000 atoms.[24] All studies show that the coordination number changes rapidly for small nanoparticles up to a couple hundred atoms, at which point the increase slows. This indicates that the EXAFS technique is most sensitive to particles of up to ~1000 atoms.

Additionally, laser scattering was used to determine the particle sizes within the RDE inks based on Mie theory, which is applicable when the diameter of the scattering particles is comparable to the wavelength of light used. Small particles cause larger angle scattering relative to the incident laser beam than larger particles.

Building upon this, KI will be used to poison the Pt surface, which will provide a heavy neighbouring atom for the surface Pt atoms with a distinctly different atomic number from any of the other elements involved in this work. Surface adsorbates, poisons and electrodeposition have been studied using EXAFS previously, examples include CO poisoned Pt/C,[25] O, S, and CO adsorption on Pt/C[26] and Cu electrodeposition on Au nanoparticles.[27] The shape and structure of Pt deposits on Rh(111) can be inferred through examination of the coordination numbers yielded from the EXAFS, whilst differences in the adsorption properties, caused by strain and ligand effects, can be seen in the XANES.[28,29] However, no attempt has been made to use these adsorbates to aid particle size determination. In this work, the coordination number of Pt-O and Pt-I will be investigated as a way differentiating between surface and bulk Pt atoms thereby allowing a measure of surface sensitivity. These measurements will be performed on commercial catalysts rather than ideal samples such as single crystals or highly monodisperse nanoparticles.

The aim of this chapter was to study the evolution of the structure and activity of Pt/C nanoparticles during an accelerated stability testing procedure. The potential cycling regime has been used before, *e.g.* by Jackson *et al.*,[30] although in this work, rather than room temperature 0.1 M $HClO_4$, more concentrated acid and higher temperatures were used in an attempt to enhance the observed degradation. The higher temperature is closer

to the expected operating temperature of a commercial PEMFC. The aforementioned study also primarily analysed the as-prepared supported Pt nanoparticle catalysts, whereas here the focus is on the changes occurring over the duration of the AST.

4.2 Experimental

4.2.1 RDE Methodology and Ink Characterisation

A polished glassy carbon RDE was coated with a thin film of the catalyst. An autopipette is used to dispense a 3 µL aliquot of catalyst suspension (~10 mg catalyst powder, 6.00 mL water:IPA mix, 25:75 ratio, 30 µL of 5.77% Nafion solution in IPA) onto the glassy carbon (GC) RDE tip (0.196 cm^2) at a rotation rate of 100 RPM, and dried at 600 RPM. An uncoated polished Pt RDE was also used.

100 conditioning scans (0 RPM) between 0.0 V and 1.0 V *vs.* RHE for catalyst samples (0.0 V and 1.5 V *vs.* RHE for poly. Pt RDE) are first carried out in N_2 purged 0.1 M $HClO_4$ electrolyte at 500 mV s^{-1}, and the ECSA is determined from cyclic voltammetry at 20 mV s^{-1} under the same conditions. The electrolyte was then purged with O_2 for 15 mins and the electrode was rotated at 1600 RPM whilst CV (3 scans) between 0.05 V – 1.05 V *vs.* RHE was carried out at 20 mV s^{-1}. The measurement was repeated 5 times on freshly prepared layers. Impedance was used to determine the uncompensated resistance of the electrode at 0.9 V *vs.* RHE, where the potential was modulated based on a sine wave with amplitude of 10 mV. The frequency range used was between 100 mHz and 100 kHz, and 15 points per decade were recorded. The high frequency intercept on the Nyquist plot was used as the uncompensated resistance. Activity measurements were typically carried out at 25 ^{o}C with the temperature being maintained by a circulating water bath. Measurements made during the accelerated stability test were done at 80 ^{o}C.

Before testing the catalyst samples, the procedure was carried out on a Pt RDE in order to check the cleanliness of the system, and was also periodically tested between measurements of the catalyst samples. An initial specific activity for the polished Pt RDE of above 1.0 mA cm^{-2} was considered clean, and if the specific activity measured on subsequent occasions dropped below 1 mA cm^{-2}, the glassware and other equipment was washed according to the previously outlined procedure. Despite this, the activity values obtained for the 5 nm Pt/C sample are comparable to published results for similar catalysts,[31,15,32,33] taking into consideration differences in experimental procedures and

methods. As a result, the cleanliness of the system was deemed adequate. An activity for the polished Pt RDE of above 2 mA cm^{-2} measured at 1600 RPM in O_2 saturated 0.1 M $HClO_4$ at 20 mVs^{-1} was not possible[34] to achieve due to sub-optimal cleanliness of O_2 pipework and/or O_2 gas, as well as possible contaminants present in the catalyst inks, particularly on the C support.

Based on the mass transport limited current measured at 0.5 V *vs.* RHE, the kinetic current measured at 0.9 V *vs.* RHE for each rotation rate, and accounting for the roughness factor, the specific activity and mass activity of the catalyst layers can be determined. The activity was determined at 1600 RPM.

X-ray fluorescence (XRF) (Fischerscope-XDV-SDD, Fischer) was used to determine the Pt loading on the glassy carbon RDE tip. Loadings were measured at the µg cm^{-2} level with an error estimated to be ± 0.3 µg cm^{-2} by repeating the measurement on the same catalyst layer. XRF measurement points were selected at the centre of the electrode, and at concentric rings with radii of 0.75 and 1.75 mm, taking 3 and 7 points respectively. The loading was taken as the average of these 11 points to account for any coffee-ring type structure of the catalyst layer. An optical microscope was used to examine the deposited layers to assess film quality.

The layer thickness was estimated from the particle size distribution within the catalyst suspensions. This was measured by using red and blue laser scattering (Mastersizer 2000, Malvern Instruments) to determine the diameters of particles within the ink. The dispersant used was a water:IPA mix (25:75 ratio), with the refractive index for the dispersant and the carbon support set to 1.38 and 2.42 respectively. Approximately 4 mL of the RDE ink was added to the dispersant such that a laser obscuration of around 10% was achieved. The catalyst suspension was then mixed at 800 RPM and 10 measurement scans were taken. The mixing speed was then increased to 1200 RPM, in order to check for agglomeration of particles, and five more measurements were taken. Mixing of the suspension was then stopped, and five further measurements were recorded at 10 s intervals to determine whether significant sedimentation of the catalyst ink occurred. Unusually large particles of above 1000 µm were considered to be air bubbles.

4.2.2 Accelerated Stability Testing Procedure

Accelerated stability testing was carried out in the water-jacketed three-necked cell in 1 M $HClO_4$ at 80 ^{o}C, on 2 nm and 5 nm Pt/C catalyst coated electrodes at a loading of

0.2 mg_{Pt} cm^{-2} for the *ex situ* synchrotron experiments and 0.5 mg_{Pt} cm^{-2} for the *in situ* synchrotron experiments. The electrochemical procedure consisted of three cycles at 10 mV s^{-1} between 0.05 and 1.0 V *vs.* RHE in N_2 purged electrolyte, then a potential hold at 0.15 V *vs.* RHE for 45 minutes, whilst the solution was purged with CO for 15 minutes and then N_2 for 30 minutes. The potential was then cycled four times from 0.15 to 1.0 to 0.05 V *vs.* RHE at 10 mV s^{-1}, and then multiple times between 0.6 and 1.0 V at 50 mV s^{-1}. ECSA measurements were taken at 0 cycles, and then after 50, 100, 200, 500, 750 and 1000 cycles had been completed. The number of cycles has been calculated excluding the cycles required for measuring the ECSA. These aged catalyst samples were washed with water, dried and stored for analysis by a variety of techniques.

A duplicate set of electrodes were also prepared, and treated with the same electrolyte, 1 M $HClO_4$ poisoned with 0.001 M KI. The electrodes were immersed in the KI solution and the potential was held at 0.3 V *vs.* RHE for one minute in order to reduce any oxide layer and to allow adsorption of I_2/I/I^- species onto the surface.[35,36] Yaraliev states that I^-, the most strongly adsorbing of the 3 species, can't adsorb on Pt oxide. A surface coverage of I-containing species of around 33% - 44%, corresponding to (3 x 3), (√3 x √3) and (√7 x √7)R19.1° adlayer structures, and at relevant potentials the (√3 x √3) structure is expected.[36,37]

4.2.3 XAS Measurements

Each of the aged catalyst coated carbon paper electrodes was analysed *ex situ* using the samples as-prepared during the electrochemical testing, along with a Pt reference foil, a PtO_2 sample, and pellets consisting of boron nitride and a sample of the catalyst powder. For the PtO_2 sample, a few mg of material were smeared onto Kapton and folded into a pouch, which was then mounted onto the holder along with the electrode samples, shown in the centre of Figure 2a.

Figure 2 Photo of a) the sample holder and beamline B18 at Diamond Light Source, and b) the gas cell used to mount the pellets.

To form the pellets, approximately 10 mg of the catalyst powder was added to sufficient boron nitride powder to make a total of 150 mg of the mixture. The amount of catalyst powder added was calculated based on the amount of Pt required to cause an absorption edge jump of approximately 1.This was ground for several minutes, or until homogeneous, using a mortar and pestle, the mixture was packed into a pellet cast and then pressed for two minutes at a pressure of 10 tons. The pellet was mounted inside an airtight 'gas cell', reduced using a 5% H_2 in N_2 gas stream for 30 minutes and then flushed through with and sealed in an inert atmosphere of N_2 whilst the XAS measurements were taken. A photo of the gas cell is shown in Figure 2b. Similarly, once measured *ex situ*, the freshly painted, un-cycled electrode was reduced under H_2 and mounted in the same way.

Several electrodes at the higher Pt loading (0.5 mg_{Pt} cm^{-2}) were mounted in the *in situ* cell, to allow control over the electrochemical environment during the XAS measurements. First, two CVs between 0.05 – 1.0 V vs. RHE at 5 mV s^{-1} were carried out to check any problems with connections or contamination in the cell. The XAS measurements, taken at the Pt L_3 and L_2 edges, were obtained at open circuit potential (approximately 0.9 V *vs.* RHE) and whilst doing chronoamperometry sequentially at 0.2, 0.5, 0.7 and 0.9 V *vs.* RHE. The potential was held for around 45 minutes at each value. N_2 purged 1 M $HClO_4$ was flowed around the cell throughout the experiments.

4.2.4 Other Techniques

TEM images (by Emily Brooke of JMTC), XPS spectra (by Tugce Eralp Erden of JMTC, samples prepared by me) and XRD patterns were obtained for a range of the electrode samples. For the TEM samples, the catalyst coating had to be scraped off the carbon paper

electrodes and dusted onto holey carbon grids. For the XPS analysis, a small section of the electrode was cut, attached to the stub and analysed as prepared.

4.3 Results and Discussion

4.3.1 Thin film Electrodes

Thin films of the catalyst sample were freshly deposited on the polished GC RDE tip before each measurement.

4.3.1.1 Ink Characterisation

The particle size distribution of the Nafion containing catalyst inks was measured in the liquid phase using red and blue laser scattering. This allows the thickness of the thin film deposited onto the GC RDE to be estimated. This measurement was performed for the 5 nm Pt/C catalyst only.

The measurements showed that the 5 nm Pt/C catalyst had a d(0.9) of 11.41 µm, a d(0.5) of 3.66 µm and a d(0.1) of 0.097 µm, and the complete particle size distribution is shown in Figure 3. The d(0.9), d(0.5) and d(0.1) values indicate that 90, 50, and 10% of the particles are at or below the given size respectively. Figure 3a shows the average of the measurements, and shows that the ink has particle sizes centred around 0.1 µm and 1 – 10 µm in diameter. From Figure 3b, which shows the measurements in the order they were taken, it is clear that some agglomeration of particles is occurring because the peak at 0.1 µm is reducing over the course of the 10 measurements whilst the broad peaks at 1 – 10 µm are increasing in height. However, the measurements taken afterwards whilst mixing at 1200 RPM and without mixing show little change over the measurement period of 5 scans in each case. These measurements indicate that the catalyst layer deposited on the RDE tip is around 10 µm thick since there are particles which have a diameter of this value. This compares with a Pt nanoparticle size of 6 ± 3 nm by TEM.

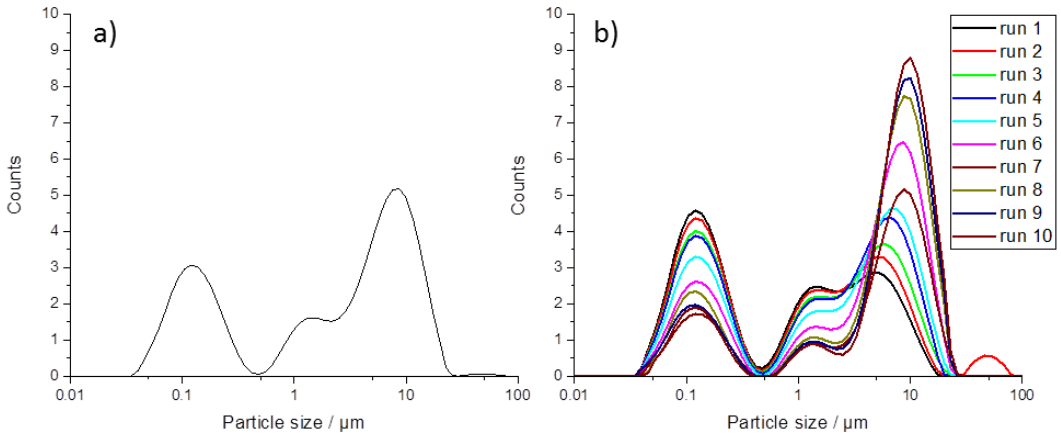

Figure 3 Liquid phase particle size distributions obtained using laser light scattering, a) the average distribution across all 10 measurements, b) the individual measurements in sequential order. The measurements were carried out whilst mixing the catalyst ink in dispersant (75:25 IPA:water mix) at 800 RPM.

4.3.1.2 Film Characterisation

The quality of the thin film catalyst layer has a significant effect on the electrochemical behaviour of the catalyst sample. Potential problems include non-uniform layers caused by capillary flow occurring when the layer is dried,[38] leading to incomplete coverage of the glassy carbon disk. Film quality was assessed using an optical microscope and an attempt was made to quantify surface coverage, thereby allowing error estimation. Not all layers could be examined. Drying catalyst layers whilst rotating the RDE tip is one way of controlling this problem,[34] whilst drying in an alcohol rich atmosphere has also been shown to disrupt formation of a coffee ring structure.[38]

Figure 4 shows images of the clean glassy carbon RDE tip and the same tip coated with the Nafion containing solvent. This shows that the electrodes could be polished and cleaned to a high standard with no visible defects, scratches or dust particles, and allows the assignment of all observable features to the catalyst rather than impurities or leftover alumina polishing powder. In Figure 4c and d, measurements have been taken to quantify the coverage achieved by the Nafion film. This film reaches to an average of 85.56 µm from the edge of the glassy carbon disc, which equates to a coverage of 93.3%, assuming that the disc is 5000 µm in diameter.

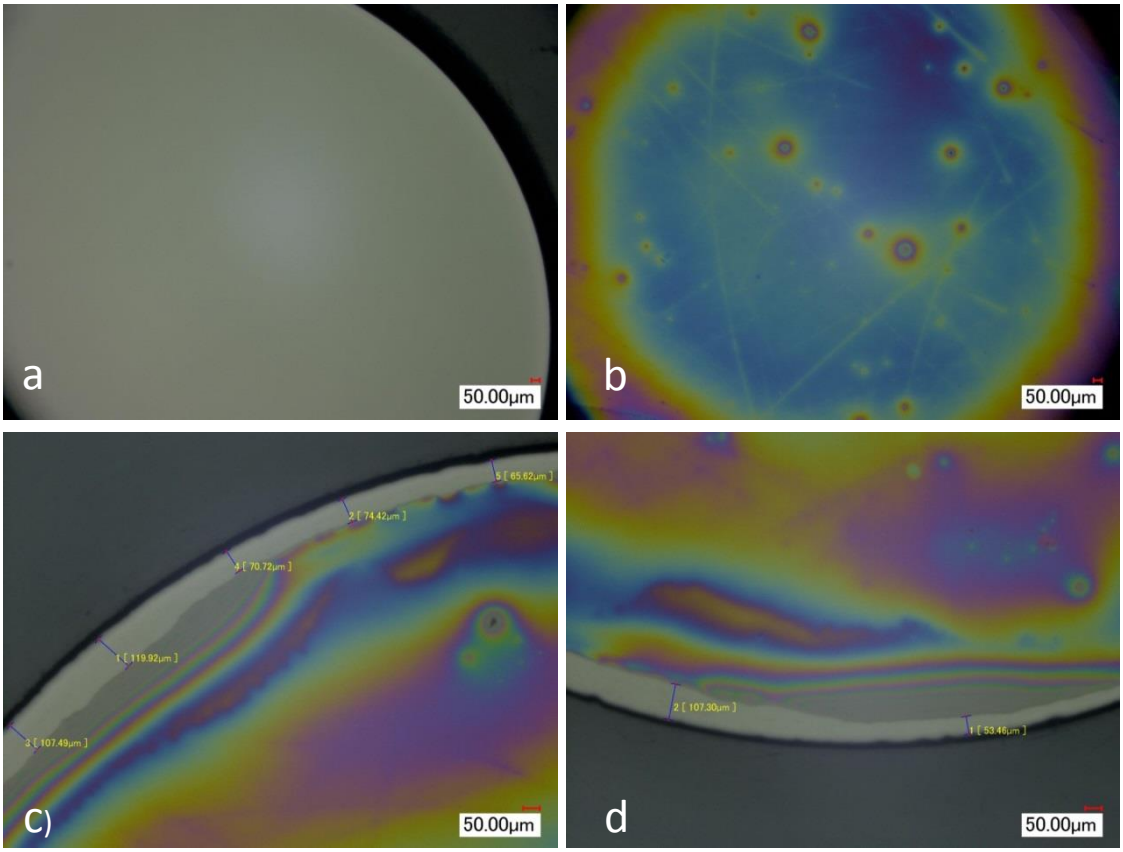

Figure 4 Optical microscope image of a) the polished glassy carbon electrode, and b) the glassy carbon electrode coated with 3 µL Nafion containing water/IPA solvent. On average, there is a gap of 85.56 µm between the edge of the Nafion film and the electrode edge as shown in panels c and d.

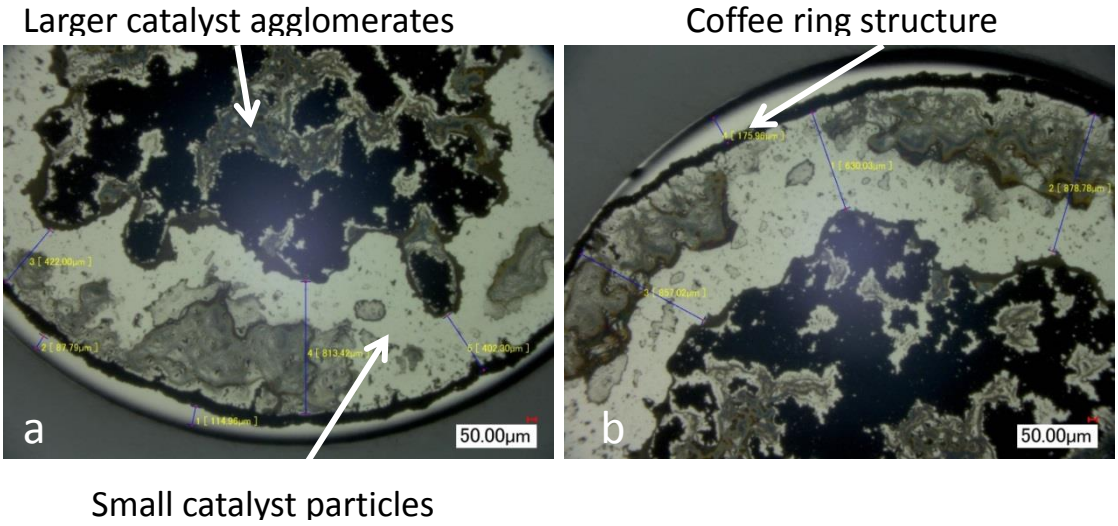

Figure 5 Optical microscope images of a GC RDE tip coated with 3 µL Pt/C (5 nm) Nafion containing ink dried whilst rotating the tip at 600 RPM. On average the catalyst film reaches 131.43 µm from the edge of the electrode.

Figure 5 shows optical microscope images of the 5 nm catalyst layer and some measurements to quantify how much of the electrode is covered by catalyst. Clearly from the images, the film coverage is patchy, with large agglomerates towards the centre of the electrode, a ring of thicker material near the edge of the GC, with a region with a fine coating of small catalyst particles in between. A homogeneous thin film would be optimal, however there is catalyst material across most of the electrode surface. The coverage can be estimated as before, by taking the average distance between the edge of the catalyst layer and the edge of the GC electrode, which in this instance was 131.43 µm resulting in a coverage of 89.8% of the total electrode area.

The non-uniformity of the films was also evident from the catalyst loading measurements taken using XRF by the large variations in catalyst loading between points on the electrode. The number and location of the points selected was chosen such that the average loading was weighted equally based on surface area and could account for a likely radial concentration gradient. Table 1 shows the individual measurements made at each point and generally it is observed that towards the edge of the electrode, points 5-11, the loading is higher than towards the electrode centre.

Table 1 Pt loading in µg cm^{-2} measured at each point on the GC RDE tip for the 5 nm Pt/C catalyst. Positions of the points are detailed in Figure 6. Error was estimated to be ±0.3 µg cm^{-2}.

Point	Layer 1	Layer 2	Layer 3	Layer 4	Layer 5
1	7.0	7.5	7.4	8.0	6.0
2	6.2	5.9	8.0	7.0	5.6
3	7.1	5.3	6.5	6.3	5.1
4	5.4	5.9	5.6	7.8	5.6
5	7.6	5.6	10.5	9.1	9.8
6	9.2	5.3	10.6	9.8	7.8
7	11.1	4.8	11.1	9.1	8.0
8	7.7	5.6	10.6	10.0	7.3
9	7.6	5.7	10.7	11.8	5.9
10	6.2	4.5	5.5	8.4	5.8
11	7.4	4.9	7.6	8.2	8.2
average	7.5	5.6	8.6	8.7	6.8

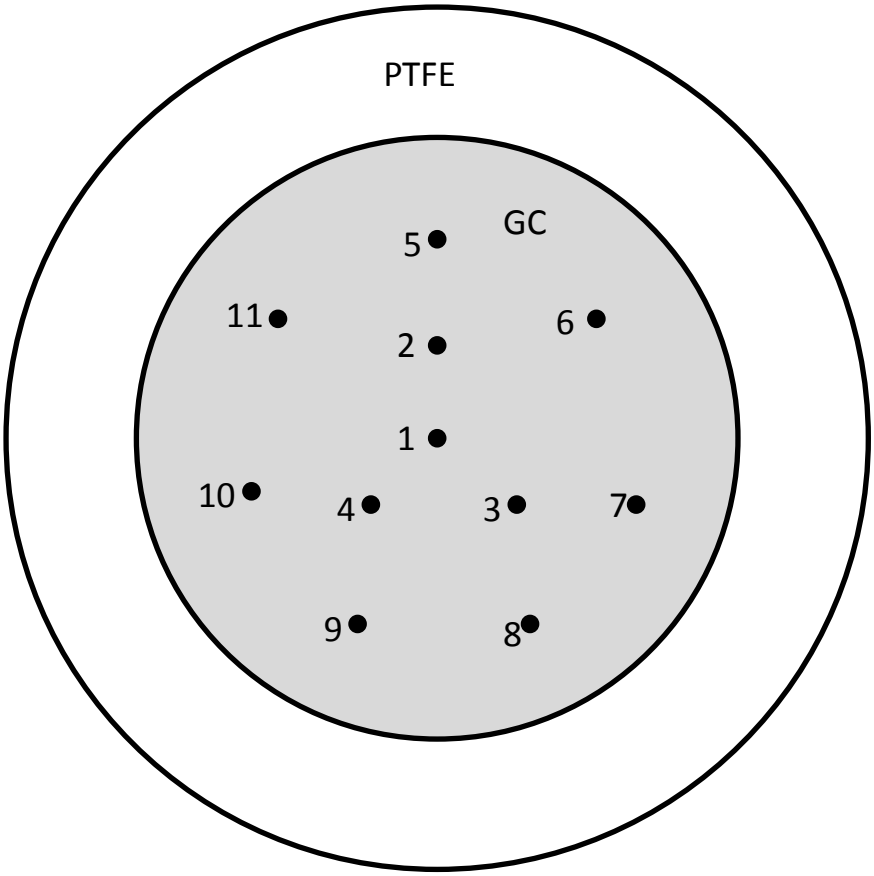

Figure 6 Diagram showing the points on the GC RDE at which the XRF measurements were performed.

4.3.1.3 Activity

The specific and mass activity of the 5 nm Pt/C catalyst was measured using the RDE method and calculated based on the average result of 5 repeats using freshly prepared catalyst layers. The specific activity of a polished polycrystalline Pt RDE was also measured before, after layer 2, and at the end of the set of measurements on the catalyst coated GC RDE, as a control. Looking at the results shown in Table 2, the specific activity of the Pt RDE was consistent throughout the duration of the experiments at 1242 ± 19 μA cm^{-2}, where the error was taken as the standard deviation of the 3 measurements. This indicates that there were no problems with build-up of contamination during the experiments.

Table 2 Activity measurements at 0.9 V *vs.* RHE for the Pt RDE and the catalyst coated GC RDE in O_2 saturated 0.1 M $HClO_4$ at 1600 RPM at 20 mV s^{-1}. The error is given as the standard deviation of the set of measurements.

RDE type	ECSA / $m^2\ g_{Pt}^{-1}$	Specific activity / $\mu A\ cm^{-2}$	Mass activity / $A\ g_{Pt}^{-1}$
Pt (start)	-	1241	-
Pt (middle)	-	1219	-
Pt (end)	-	1266	-
Pt average	-	1242 ± 19	-
Pt/C (layer 1)	44.6	269	120
Pt/C (layer 2)	57.3	307	176
Pt/C (layer 3)	38.2	297	113
Pt/C (layer 4)	39.2	310	121
Pt/C (layer 5)	49.1	311	152
Pt/C average	45.7 ± 7.0	299 ± 16	137 ± 24

The specific and mass activity calculated for the 5 nm Pt/C sample falls within the range of published results,[31,15,32,33] bearing in mind differences in metal content, particle size and dispersion of the Pt/C samples themselves, as well as probable discrepancies in ink composition and preparation and procedures used to correct for various effects. Figure 7 shows the iR corrected, background subtracted, positive going potential sweeps used to calculate the activity, and Table 2 shows the calculated specific and mass activities for the Pt/C catalyst along with an error taken as the standard deviation of the set of results. In reality, the error for the specific activity is approximately 10% and the error for the mass activity is approximately 15% based on the film coverage of the electrode, and the coverage in combination with the error in the Pt loading respectively.

There is some variation in the potential sweeps between the 5 layers, likely resulting from differences in the catalyst film quality. Since each layer was thoroughly conditioned before the experiment (100 cycles between 0.0-1.0 V *vs.* RHE at 500 mV s^{-1}), and the CVs became reproducible after around 50-60 cycles, this was not thought to be an issue. A detailed review of the RDE literature covering conditioning or 'break-in' procedures is presented by Shinozaki *et al.*[34] where it is suggested that a higher upper limit of 1.2 V or 1.5 V for conditioning scans is desirable, however this would also affect Pt/C, and particularly carbon-supported Pt alloy catalysts through possible carbon corrosion and leaching of base

metals. At high overpotentials, *ca.* 0.2 V *vs.* RHE, the magnitude of the limiting current decreases slightly, which is related to the onset of H_2O_2 formation.[32] RRDE measurements to confirm this were not carried out as part of this work.

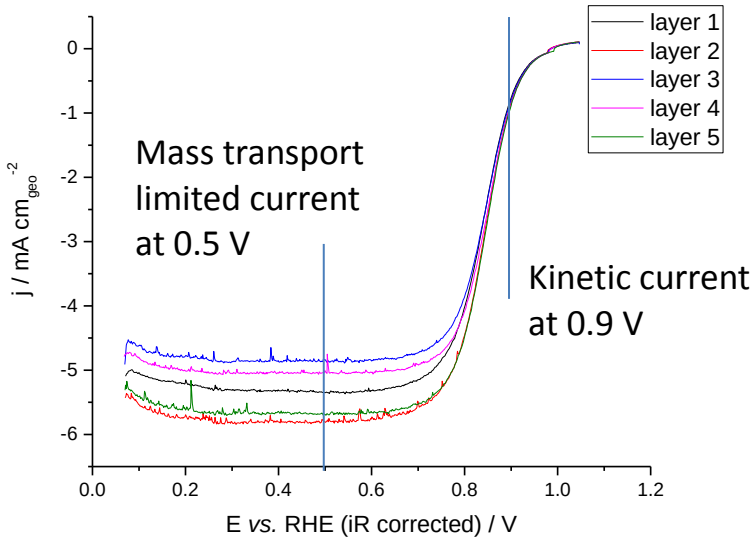

Figure 7 Positive going potential sweeps in O_2 purged 0.1 M $HClO_4$ at 20 mV s^{-1} at 1600 RPM for the 5 nm Pt/C catalyst coated GC RDE. 5 separate layers were used after re-polishing the RDE tip. The potential has been corrected for iR losses for which the resistance was measured using impedance to find the high frequency intercept on the Nyquist plot. A CV was recorded in N_2 purged electrolyte and subtracted from the raw data.

Figure 8 shows how the ECSA, specific and mass activities of a single Pt/C thin film modified GC RDE change over the course of the AST. The thin film was deposited and dried whilst rotating the electrode, and then conditioned before starting the test. CVs were recorded in N_2 purged 1 M $HClO_4$ to establish the ECSA and ORR activity was measured in O_2 saturated 0.1 M $HClO_4$ from the positive going potential sweep . These measurements were all done at 80°C, and recorded after the conditioning scans, and then after 50, 100, 200, 500, 750, 1000 cycles. The ECSA of the 2 nm Pt/C decreases rapidly over the first 200 cycles and then stabilises, similar to a 1/x function, x being the number of cycles. The ECSA of the 5 nm catalyst changes negligibly. This is similar to the results obtained by Sheng *et al*.[39] following a similar potential protocol to the present work, where they found that there was a steep loss in ECSA for a 2 nm Pt/C sample and no loss in ECSA for the 5 nm sample. In contrast to the results presented in Figure 8a, in their results, the ECSA of the 2 nm catalyst decayed until it reached the same level as the 5 nm sample with the inference being growth in the average nanoparticle diameter from 2 to 5 nm. There is a discrepancy between the activities presented in Figure 7 and Figure 8 because they were carried out using different RDE equipment, measurement temperatures and chemical source at separate locations.

The main factor was temperature, as significantly decreased O_2 partial pressure is observed above 60 °C.[32] Additionally, coverage of H on the Pt surface will be lower at 80 °C leading to a reduction in the measured ECSA. For reference, a polycrystalline Pt RDE had a specific activity of 943 µA cm^{-2} at 25 °C, as opposed to 1242 ± 19 µA cm^{-2} measured previously.

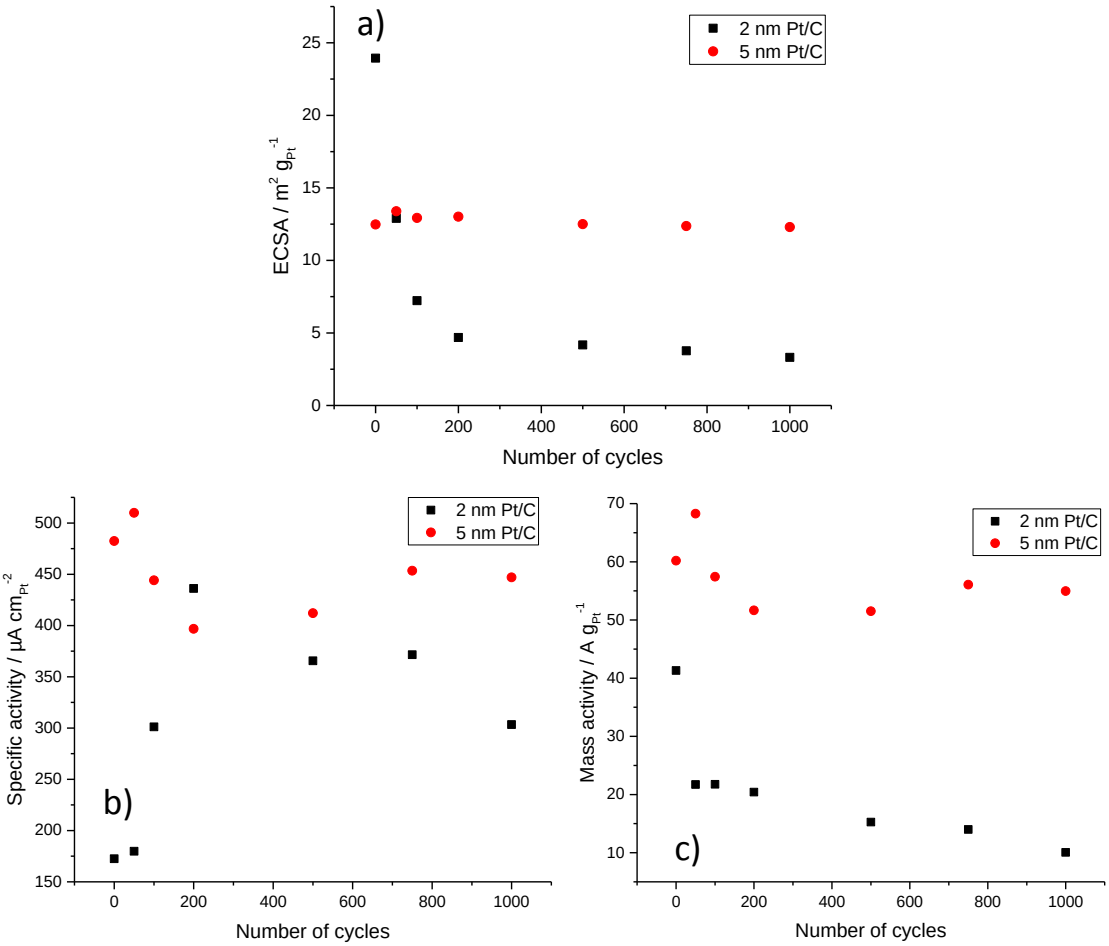

Figure 8 The evolution of a) ECSA over the course of the accelerated stability test, b) and c) associated changes in specific and mass activity of the 2 and 5 nm Pt/C catalysts with the ECSA. A single film (3.0 µL ink, ~8 µg catalyst) was deposited onto the polished GC RDE and dried in air under rotation. The film was conditioned and the ECSA determined in N_2 purged 1 M $HClO_4$ at 80 °C (stationary), and then transferred to O_2 saturated 0.1 M $HClO_4$ at 80 °C and the ORR activity was calculated from the iR corrected, background subtracted, positive going (0.1 – 1.05 V *vs.* RHE) sweep whilst rotating at 1600 RPM. Impedance spectroscopy was carried out at 0.5 and 0.9 V *vs.* RHE to allow for iR correction, taking the value for R as the high frequency intercept of the x-axis.

4.3.2 Catalyst Coated Button Electrodes

These electrodes all consist of carbon paper discs loaded with a known amount of Nafion coated Pt/C catalyst sample. Electrodes were hot pressed and flooded with purified water (18 MΩ cm) before use.

4.3.2.1 TEM

TEM was used as a conventional method to directly measure the average particle size of the Pt/C samples based on a reasonable number of particles. The particle size distribution was determined from a dark field image, an example is shown below in Figure 9 for the 5 nm Pt/C sample, from which the area of a number of particles can be automatically measured. By assuming that the particles are spherical, or circular from the point of view of the TEM, the radius, and hence diameter, was calculated from the measured areas.

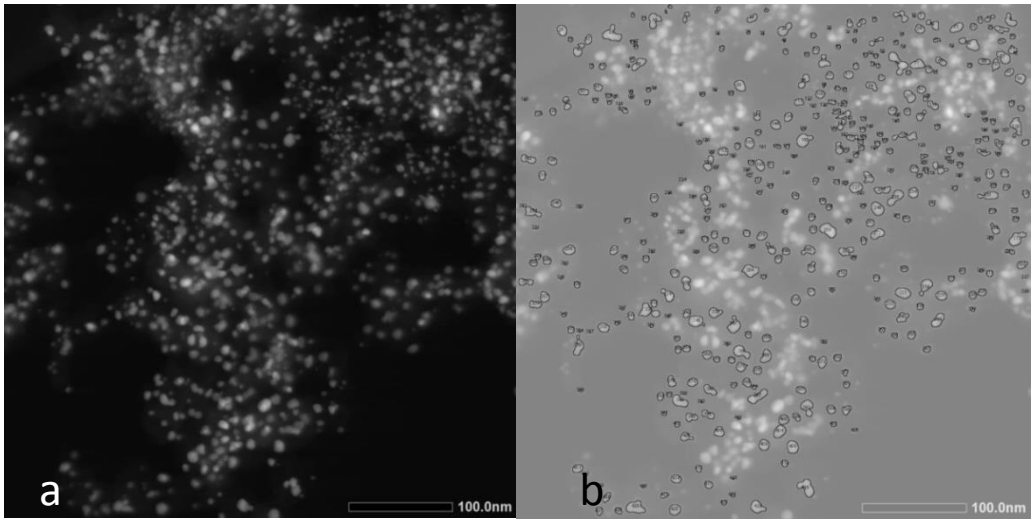

Figure 9 Image processing example for particle size determination for the 5 nm Pt/C. a) dark field image of the catalyst sample, and b) selection used to measure particle areas.

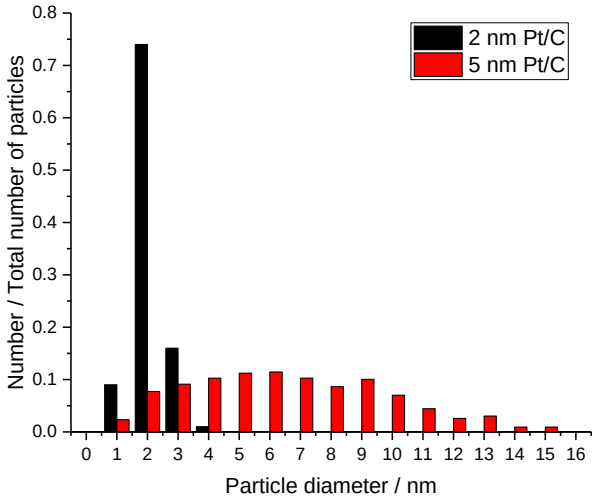

Figure 10 Comparison of the PSD for the 2 nm and 5 nm Pt/C catalyst samples. 100 and 428 particles were imaged respectively, and the diameter was calculated based on the assumption that the particles were spherical. The y-axis shows the number of particles at each diameter normalised by the total number of particles imaged. The TEM image used for the 5 nm Pt/C catalyst can be seen in Figure 9. Average particle sizes: 1.53 ± 0.48 nm (2 nm Pt/C) and 6.07 ± 3.18 nm (5 nm Pt/C).

Figure 10 shows a histogram detailing the particle size distribution in each catalyst. There is a considerable range of sizes; the standard deviation is ± 0.48 nm and ± 3.18 nm for the 2 and 5 nm Pt/C respectively. This range of sizes will increase the disorder present in the EXAFS fits for these samples as this technique measures the entire sample so will see the average particle rather than the small subsection of particles shown in the TEM image. Additionally, the particles shown in the TEM are not all spherical, some particles have agglomerated or are not far enough apart to be resolved by TEM at this angle and by the software used to pick out particles.

The average particle size can be used to calculate the number of atoms present in an average Pt nanoparticle from each of the catalyst samples. This was done by dividing the volume of an average particle by the volume of the fcc unit cell. Since the number of Pt atoms present in the unit cell is known to be 4, the total number of atoms in the average spherical particle can be calculated. From the sizes reported above, the 2 nm Pt/C contains an average of 124 atoms per particle, and the 5 nm Pt/C samples contains 7751 atoms per particle. There is a large error on these numbers due to the range in measured particle size.

Figure 11 shows a series of high resolution TEM images taken of the two catalyst powders, and the range of sizes can be seen. Figure 11a and d show a large number of particles, including a reasonable number of agglomerates or overlapping particles, which are noticeably darker than the separated particles. In Figure 11c and f, the crystal lattice and atomic planes of the particles can be made out. The highlighted particle in Figure 11f enlarged and sharpened and the fast Fourier transform of the image is shown Figure 12. The Fourier transform yields a diffraction pattern from which the distance between lattice planes can be estimated by measuring the distance between local maxima.

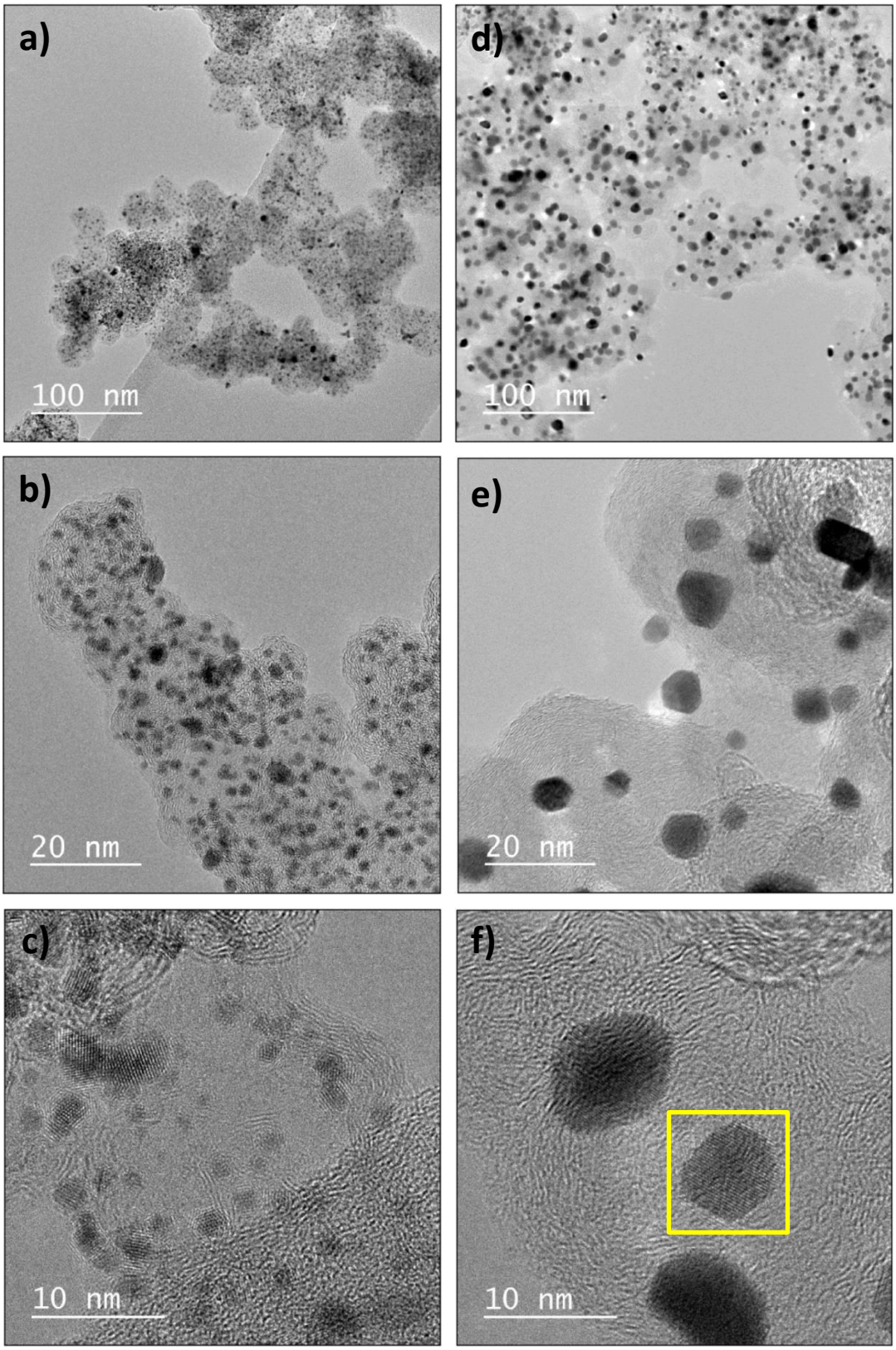

Figure 11 High resolution TEM images showing a-c) the 2 nm, and d-f) the 5 nm Pt/C catalyst powders.

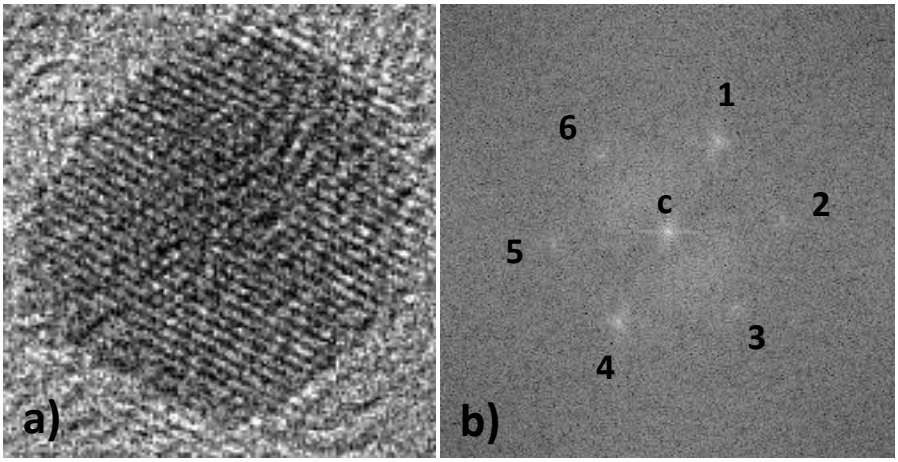

Figure 12 a) Sharpened and enlarged image of the particle highlighted in Figure 11f and b) fast Fourier transform of a), where the scale has been calibrated and set using the scale bar in Figure 11f - 19.6 pixels nm^{-1}. The distances between the local bright maxima, 1-6, and the central maxima, c, have been measured and shown in Table 3. The image processing, fast Fourier transform and measurements were done using the ImageJ software.

Table 3 Distances between local bright maxima of the fast Fourier transform in Figure 12b.

Local bright maxima	Distance to c / nm
1	2.95
2	3.32
3	2.92
4	2.94
5	3.32
6	2.90
Average (1, 3, 4, 6)	2.93
Average (2, 5)	3.32

4.3.2.2 XPS

XPS data for the 2 catalysts along with the aged electrode samples were collected. Figure 13 and Figure 14 show a comparison of the survey spectra collected for these samples. All spectra were calibrated such that the C1s peak position was 284.8 eV. The C1s, Pt4f, Pt4d, and O1s peaks were also collected at higher resolution, as well as the F1s and S2p peaks for the electrode samples. The C1s peak was fit according to the paper by Assumpção *et al.*[40] whereby 5 singlets with the GL(30) lineshape corresponding to C-C, C-H, C-O, C=O and O-C=O interactions were used and the C-C peak was used to calibrate the spectra.

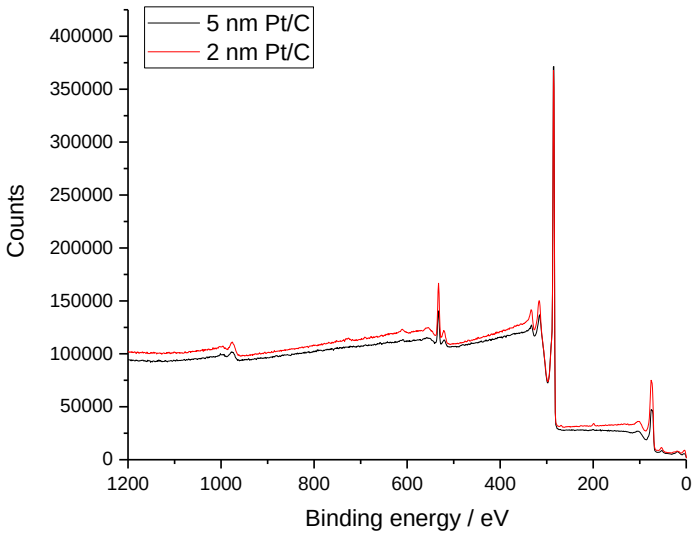

Figure 13 XPS survey spectra of the 2 and 5 nm Pt/C catalysts. The main observable peaks are the Pt4f peak at 72 eV, the C1s peak at 284.8 eV (calibrated), the Pt4d peak at 315 eV and the O1s peak at 532 eV.

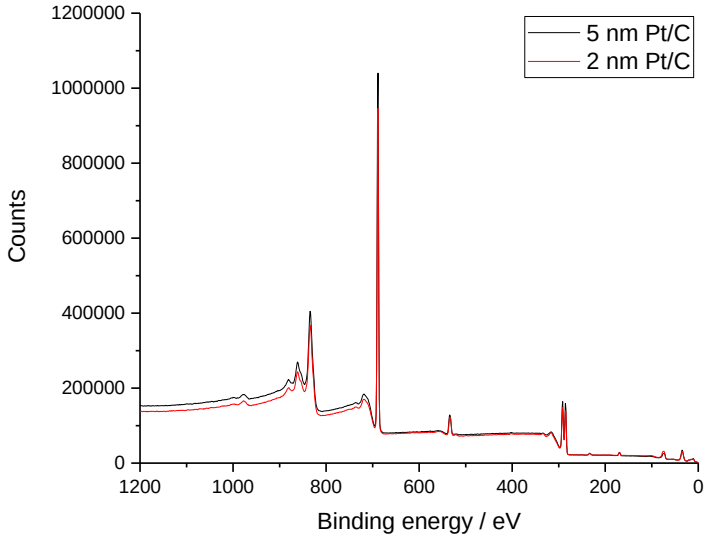

Figure 14 XPS survey spectra of the 2 and 5 nm Pt/C catalyst coated carbon paper electrodes. The additional peaks at 690 eV and 800 – 900 eV are due to the F1s transition and an Auger related process respectively. There is also a peak at around 165 eV due to the S2p transition. These additional peaks are caused by the Nafion ionomer used to make the catalyst layers. The strongly withdrawing F atoms also result in the splitting of both the O1s and C1s singlets into 2 peaks.

The presence of Nafion, used as the ionomer in the catalyst coated electrodes, results in the observation of the intense F1s peak just below 700 eV, along with a multiplet due to F Auger processes at 850 eV, and the small S2p peak at around 50 eV. Two O1s and C1s peaks, see Figure 15, are also observed as a result of highly fluorinated moieties in the Nafion structure.

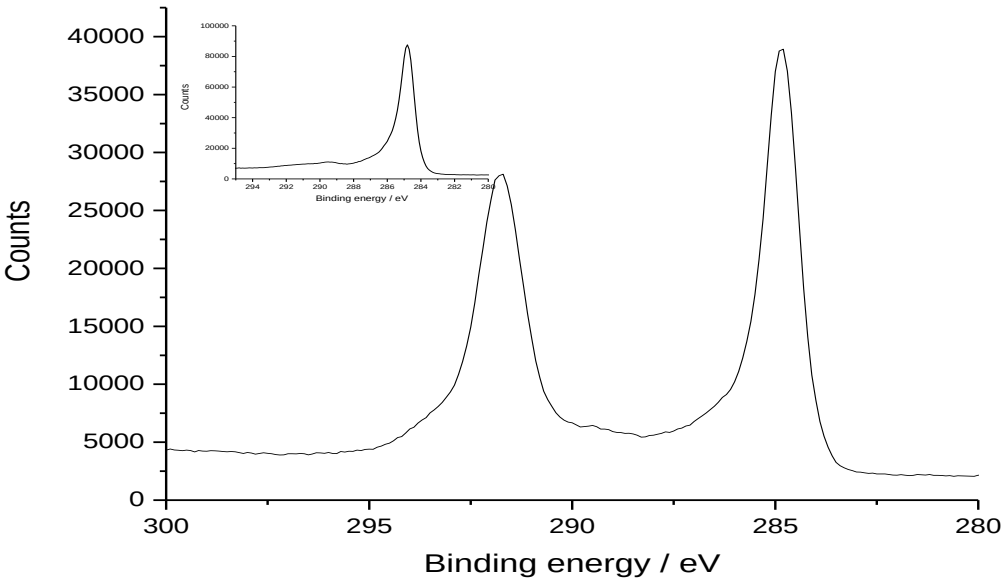

Figure 15 The main graph shows the two C1s peaks from the 5 nm Pt/C catalyst coated electrode sample caused by the presence of highly fluorinated carbon atoms in the Nafion ionomer. The inset shows the C1s peak from the untreated 5 nm Pt/C catalyst powder sample. This can also be observed to a lesser extent in the O1s region.

The Pt4f regions for the catalyst powder and electrode samples are compared in Figure 16-Figure 18. In both cases, the Pt4f peaks for the 2 nm particles are shifted to slightly higher binding energy, which has been observed previously on carbon nanotube supported Pt nanoparticles.[41] Due to the lack of potential control, this observation could also be caused by differences in the degree of oxidation between the samples. There is also a small shift observed between the catalyst powders and the electrode samples that may be caused by the highly electron withdrawing nature of the fluorine in the Nafion.

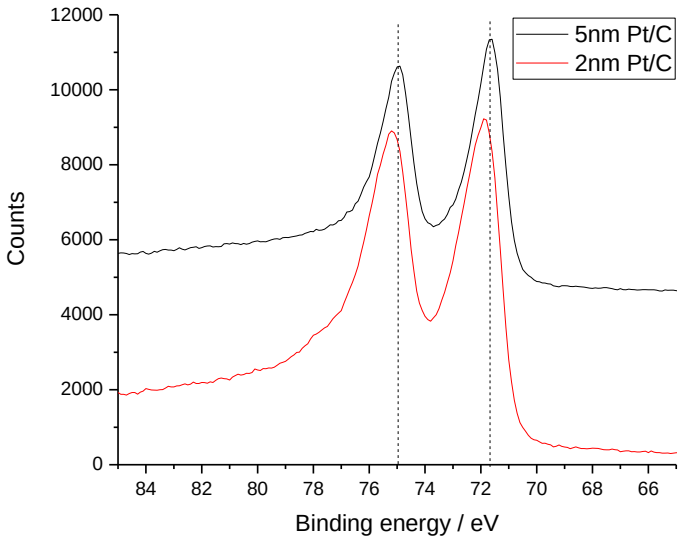

Figure 16 High resolution XPS spectra of the Pt4f region of the 5 nm and 2 nm Pt/C powders. The black line is offset by 4000 and the red line is offset by -500. There is a shift to higher binding energies for the smaller diameter nanoparticles.

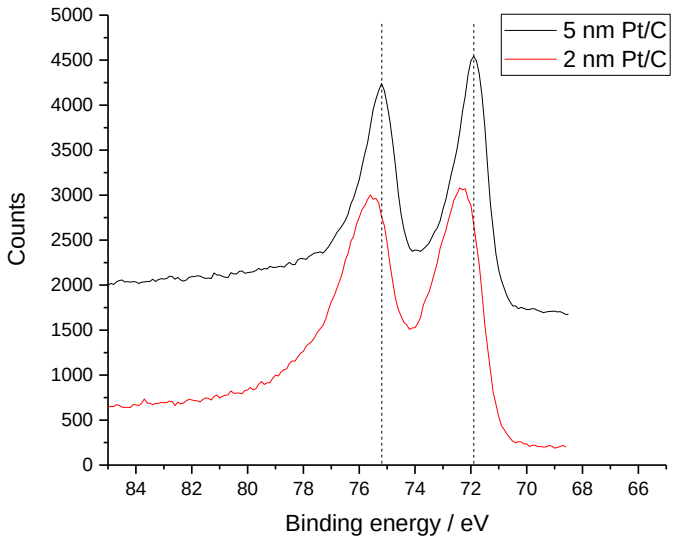

Figure 17 Pt4f region in high resolution for the catalyst coated electrodes. Again, there is a shift to higher binding energies for the 2 nm Pt/C sample. The black line is offset by 750 and the red line is offset by -750.

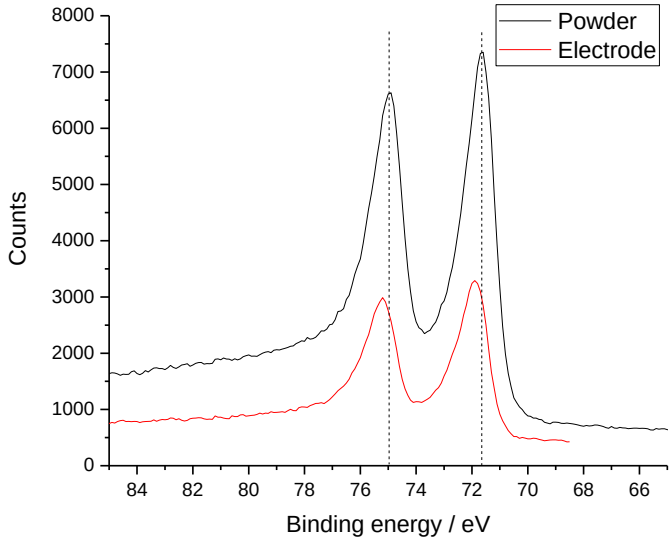

Figure 18 Comparison of the high resolution Pt4f region of the XPS spectra of the 5 nm Pt/C powder and electrode, no offsetting. There is a slight shift in binding energy for the electrode sample, which could result from interaction with the ionomer, or down to small errors in the calibration of the equipment and spectra, although the shift is also observed for the 2 nm Pt/C powder and electrode samples.

Table 4 Calculated atomic percentages determined from XPS fitting. Relative sensitivity factors of the various transitions have been taken into account. Percentages for common impurities, namely Cl and N, have been included in the calculation but are not shown here. F and S percentages from the Nafion used in the electrode samples are also not shown.

Transition	2 nm Pt/C powder	5 nm Pt/C powder	2 nm Pt/C electrode	5 nm Pt/C electrode
C1*s*	93.3	95.0	46.3	47.3
O1*s*	5.5	4.2	4.9	4.4
Pt4*f*7	1.0	0.6	0.3	0.2

Table 4 shows the surface composition of the various catalyst samples as determined by XPS, although as the x-ray will penetrate ~nm into the substrate, most of the 2 nm Pt/C sample and a large part of the 5 nm Pt/C sample will be contributing to the recorded spectra. This is also evident from the percentage Pt compositions above as the 2 nm sample consistently contains a larger amount of Pt than the 5 nm sample despite both catalysts containing the same amount of Pt by weight to within 2% - the ratio of Pt in the two samples is just above 3:2 for both the powder and the electrode samples. Additionally, as indicated from the coordination numbers determined in the EXAFS analysis, there is a larger amount of oxide measured for the 2 nm sample as opposed to the 5 nm sample, as would be expected based on surface area.

4.3.2.3 XRD

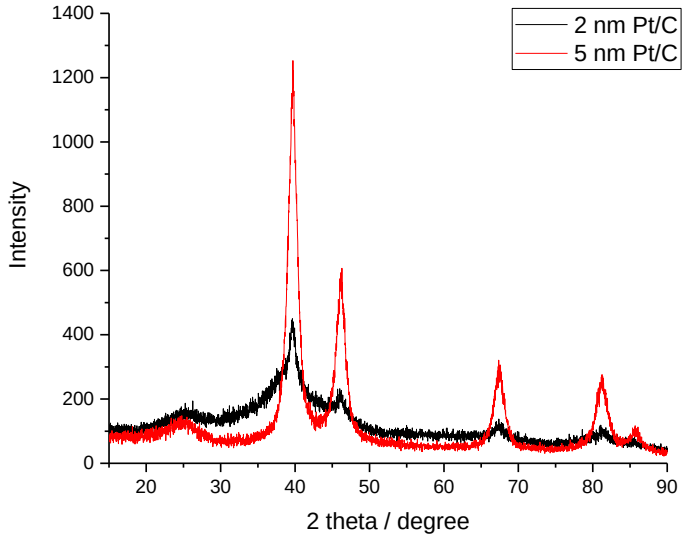

Figure 19 XRD patterns consisting of the average of 3 consecutive scans of the 2 nm and 5 nm Pt/C catalyst powder samples. The peaks at 39°, 46°, 67°, 81° and 86° have been indexed and are consistent with the fcc structure, *i.e.* the ratio of $\sin^2\theta$ values is 3:4:8:11:12, and the lattice constant was calculated to be 3.933 Å and 3.928 Å based on the peak positions of the 2 nm and 5 nm Pt/C catalyst powders respectively. The literature value is 3.924 Å. The peak at a 2θ angle of ~25° in both catalysts is attributed to the carbon support.[42,43] The 5 nm Pt/C sample was prepared by heat treatment of a 2 nm Pt/C catalyst, which may, in part, be the reason behind the well-defined peaks in the 5 nm sample as compared to the broader peaks and larger amorphous component for the 2 nm Pt/C sample, as well as the expected difference in peak width due to particle diameter.

XRD spectra of the two catalyst powders are shown in Figure 19 and the peak positions can be indexed according to the fcc structure, yielding lattice constants of 3.933 Å and 3.928 Å for the 2 nm and 5 nm Pt/C samples respectively, which is close to the expected value for Pt, 3.9242 Å. There is an additional peak at a 2θ angle of 25°, which has been attributed to the carbon support.[42,43] The peak width at half height for the 2 nm Pt/C is considerably wider than for the 5 nm sample as expected based on particle size. In addition, the 5 nm sample was synthesised via heat treatment of the 2 nm catalyst so is likely to have a larger degree of crystallinity and less amorphous content. The XRD spectra for the catalyst coated electrodes were all very similar to the ones presented here.

4.3.2.4 *Ex situ* XAS

As described in chapter 3, S_0^2 for Pt was established as 0.84 and will be set as a constant for all further fits at the Pt L3 edge. The fits for the 2 and 5 nm Pt/C pellet samples are presented below in Figure 20 and the values for the extracted parameters are shown in

Table 5. These pellets were reduced under a H_2 atmosphere at room temperature for 30 minutes before the *ex situ* measurements.

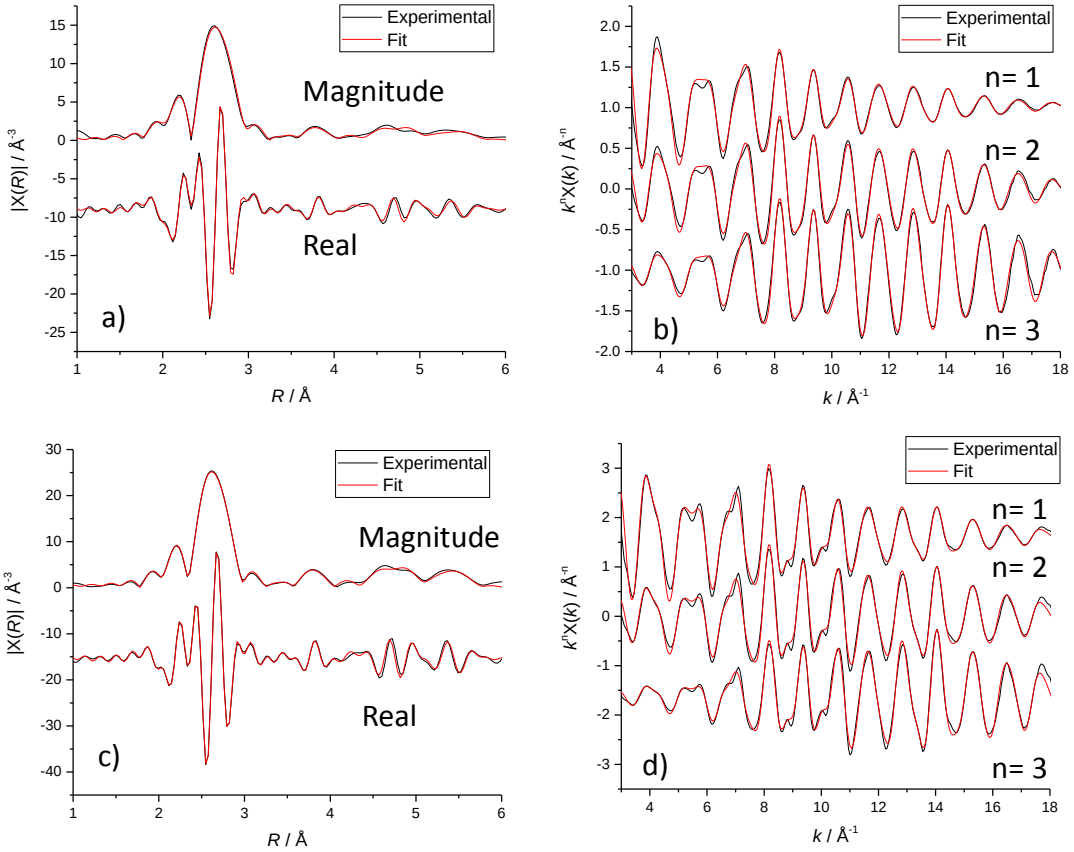

Figure 20 EXAFS fits for the 2 nm and 5 nm Pt/C catalyst pellets. a) k^2 weighted Fourier transform, and b) k^n weighted data for the 2 nm Pt/C. c) k^2 weighted Fourier transform, and d) k^n weighted data for the 5 nm Pt/C. Plots are not phase corrected.

Table 5 List of parameters calculated from the fits depicted in Figure 20. *α* is a % change in the Pt-Pt bond length defined in the CIF file used, which was 2.7748 Å.

Variable	2 nm Pt/C	5 nm Pt/C
amp[a]	0.84	0.84
enot / eV	6.40 ± 0.25	6.88 ± 0.29
α	-0.00619 ± 0.00053	-0.00507 ± 0.00048
SS1 / Å^2	0.00631 ± 0.00015	0.00521 ± 0.00014
SS2 / Å^2	0.00943 ± 0.00220	0.00769 ± 0.00149
SS3 / Å^2	0.00875 ± 0.00153	0.00812 ± 0.00095
SS4 / Å^2	0.01083 ± 0.00190	0.00851 ± 0.00097
N1	8.87 ± 0.27	10.86 ± 0.38
N2	3.60 ± 1.20	5.39 ± 1.53
N3	9.80 ± 3.12	22.18 ± 4.93
N4	7.71 ± 1.62	10.48 ± 1.63

a – not allowed to vary in fit.

The coordination numbers of the first 4 nearest shells of atoms were compared to computationally calculated values taken from literature, and displayed in Figure 21. The model by Jentys[23] is a way of estimating the expected coordination number for cuboctahedral particles of a given number of atoms, whilst the blue triangles and red circles are exact computationally modelled coordination numbers by Glasner and Frenkel.[24] In all cases the values obtained from the fits presented in this work are lower than predicted by the Jentys model, although generally agree considering the error. This is likely a combination of the model being an estimation as well as a symptom of the sensitivity of EXAFS to smaller particles, as the samples, particularly 5 nm Pt/C, have a broad distribution of particle sizes. Looking at the points calculated by Glasner and Frenkel for the 4th nearest neighbour coordination number provides a way of distinguishing between icosahedral and cuboctahedral particles. Computational modelling indicates that for small particles, the icosahedral geometry is most energetically favourable, and above a certain threshold number of atoms (~300-1000 atoms), the preferred geometry becomes the cuboctahedron.[44,45] The coordination numbers determined here are consistent with this, although the error bars do not exclude the possibility of small cuboctahedral particles.

The number of atoms in the average particle can be calculated from the coordination numbers determined by the EXAFS fit to provide a comparison to those values obtained

from the TEM images. This can be done by using equation from the paper by Jentys,[23] shown in Equation 1 for the 1st coordination shell and plotted for the first 4 shells in Figure 21.

$$N_1 = \frac{8.981 N_{at}}{9.640 + N_{at}} + \frac{3.026 N_{at}}{1462.61 + N_{at}}$$

Equation 1

For 2 nm Pt/C, this gives 198 ± 70 atoms, and for the 5 nm Pt/C, this works out as 2510 ± 1916 atoms. This calculation was only done for the 1st shell coordination number due to the larger errors in the values for the higher shells. Both values have a considerable error due to the assumptions of spherical particles with a complete outer shell of atoms and constant bond lengths, *i.e.* no contraction, relaxation or restructuring at the nanoparticle surface. There is also the error in the coordination number obtained during the EXAFS fitting process, which has been considered as well. These values differ significantly from the values obtained from the TEM images, particularly for the 5 nm sample, which may be down to the considerable particle size distribution, see Figure 10, adding to the disorder in the EXAFS fitting process.

Figure 21 presents the theoretically calculated data from work by Glasner and Frenkel,[24] and by Jentys[23] alongside the values determined using the fits in this work. Glasner and Frenkel explicitly generated metal clusters containing up to *ca.* 1000 atoms in several geometries and calculated coordination numbers for the first 6 atomic shells. The results for the icosahedral and cuboctahedral geometries are most relevant to this work and have been plotted below. In his paper, Jentys provided an empirical formula for calculating the expected coordination number for a cuboctahedral particle containing a given number of atoms. The equation fits the explicitly calculated data points for the cuboctahedron well, and here the equation has been used to extend the theoretical data up to values relevant to the 5 nm Pt/C sample studied here. The hyperbolic function, of the form shown by Equation 1, was generated for particles ranging from 13-7500 atoms.

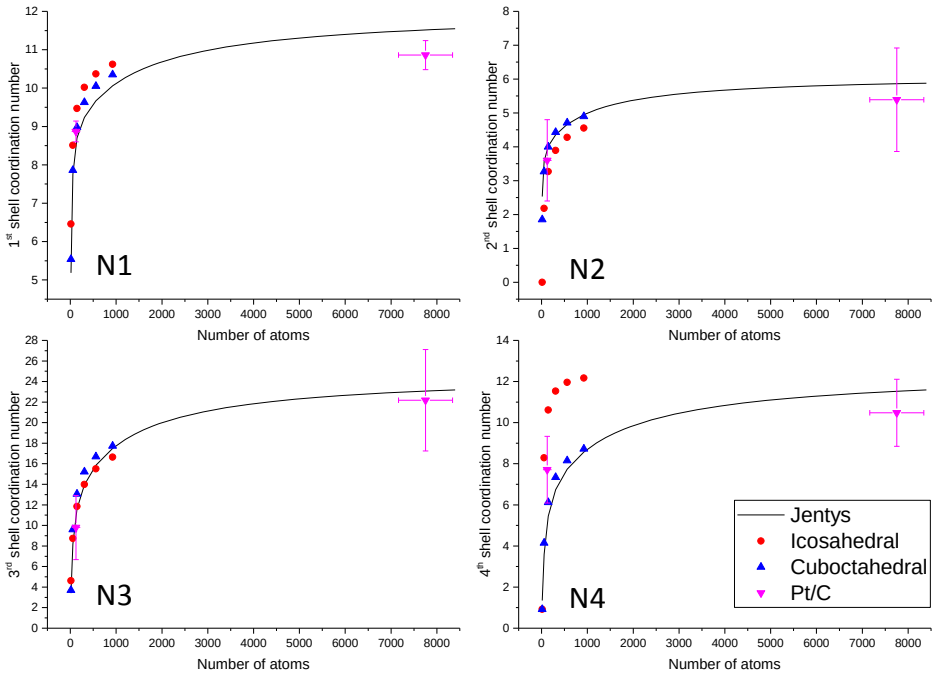

Figure 21 Coordination numbers modelled according to papers by Jentys[23] for spherical fcc metal particles, and by Glasner and Frenkel[24] for icosahedral and cuboctahedral geometries compared to the coordination numbers and particle sizes experimentally determined by the EXAFS and TEM results presented above.

The 5 nm Pt/C coated electrode samples were fitted in the same way as done for the pellets, although for a single sample the best fit value for the 2nd shell coordination number was forced to take a value of 6 or less to maintain physical viability of the model. The 2nd shell is typically harder to fit due to the small number of atoms and scattering paths involved, which makes the associated coordination parameter less robust.

Figure 22 shows that the accelerated stability test does not significantly affect the particle size of the catalyst, or the effect is below the resolution limit for EXAFS. There is little difference amongst the series of aged samples both in terms of coordination numbers and bond lengths, especially considering the error bars, see Figure 22. However, the electrode and pellet samples that were both reduced under H_2, each have higher 1st shell coordination numbers than for the aged and as-prepared samples, which suggests possible removal of oxygen from the outer atomic layers thereby increasing Pt-Pt coordination. The oxygen contribution to the EXAFS signal could not be unambiguously detected for this set of catalyst samples.

Additionally, as suggested by Figure 21, the sensitivity to particle size determined using EXAFS is increased for smaller particles, and the 5 nm sample is towards or above the upper limit of this range so the coordination numbers are tending towards the expected values in

the bulk. This arises due to the large proportion of under coordinated near-surface atoms relative to the number of bulk-like fully coordinated atoms in the nanoparticle core.

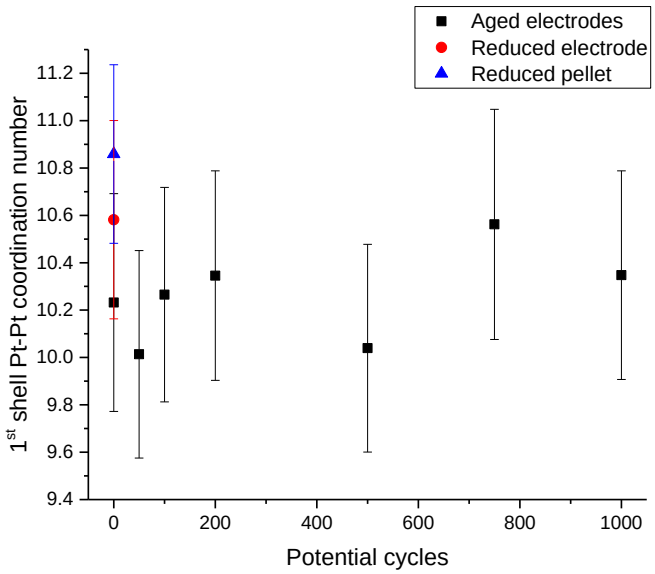

Figure 22 1st shell Pt-Pt coordination numbers for the series of aged 5 nm Pt/C coated electrode samples alongside a reduced electrode sample, and the pellet sample.

Table 6 Parameters obtained from the fits to the 5 nm Pt/C aged electrode samples, and pellet. The red value for *N2* was forced to be 6 or less to ensure the model was physically reasonable. The σ^2 disorder values are not shown. The reference Pt-Pt interatomic distances for the first 4 neighbouring shells were 2.7748, 3.9242, 4.8061, and 5.5497 Å respectively.

Sample	*enot / eV*	*a*	*N1*	*N2*	*N3*	*N4*
Pellet (reduced)	6.87 ± 0.29	-0.0051 ± 0.0005	10.9 ± 0.4	5.4 ± 1.5	22.2 ± 4.9	10.5 ± 1.6
Electrode (reduced)	7.46 ± 0.32	-0.0065 ± 0.0006	10.6 ± 0.4	5.6 ± 1.9	20.5 ± 5.4	9.9 ± 1.7
0 cycles	6.82 ± 0.37	-0.0063 ± 0.0008	10.2 ± 0.5	5.0 ± 2.0	18.0 ± 5.8	9.0 ± 2.1
50 cycles	7.06 ± 0.36	-0.0063 ± 0.0007	10.0 ± 0.4	4.5 ± 1.8	20.3 ± 6.2	10.2 ± 2.1
100 cycles	7.03 ± 0.36	-0.0064 ± 0.0007	10.3 ± 0.5	4.9 ± 1.9	19.4 ± 6.2	10.1 ± 2.2
200 cycles	6.92 ± 0.35	-0.0059 ± 0.0007	10.4 ± 0.4	4.5 ± 1.5	18.5 ± 5.4	9.6 ± 1.9
500 cycles	7.21 ± 0.35	-0.0057 ± 0.0007	10.0 ± 0.4	4.1 ± 1.5	19.8 ± 6.6	9.7 ± 1.9
750 cycles	7.07 ± 0.39	-0.0060 ± 0.0008	10.6 ± 0.5	6.00	20.8 ±7.5	9.1 ± 2.1
1000 cycles	7.44 ± 0.35	-0.0059 ± 0.0007	10.4 ± 0.4	5.2 ± 1.8	18.8 ± 5.7	8.9 ± 1.8

Table 6 shows the values extracted from the fit to the EXAFS spectra of the 5 nm Pt/C samples, and shows the similarities between the samples. This suggests that more cycles or harsher treatment is required during the stability test to degrade the catalyst. The ratio of *N3*:*N1* is close to 2 for all cases, which indicates that the nanoparticles are spherical. This validates the assumption of spherical particles used in several of the calculations.

The aged 2 nm Pt/C coated electrode samples were also analysed and have the added complication of possible O neighbours at the surface of the nanoparticles. This has a larger effect on the 2 nm Pt/C sample due to the greater proportion of surface atoms, around 60% of atoms as opposed to 20% for the 5 nm Pt/C catalyst, as has been observed previously.[26] The presence of Pt oxides has a noticeable effect on the EXAFS spectra and as a result a PtO_2 pellet was also prepared and analysed as a reference compound and for comparison purposes.

Since PtO_2 is less symmetric than fcc Pt, isotropic expansion can no longer be assumed, which necessitates additional variables to fit the interatomic distances. The scattering paths used, and the assignment of variables is displayed in Table 7, the fit in Figure 23, and the obtained values in Table 8.

Table 7 Scattering paths and assignment of variables used for the PtO_2 sample.

Scattering path	*N*	*R* / Å	σ^2 / Å^2
Pt_{abs}-O_1-Pt_{abs}	6	ΔRO_1	SSO_1
Pt_{abs}-Pt_1-Pt_{abs}	6	ΔRPt_1	$SSPt_1$
Pt_{abs}-O_2-Pt_{abs}	6	ΔRO_2	SSO_2
Pt_{abs}-O_1-Pt_1-Pt_{abs}	24	1.5*ΔRO_1	½ *(SSO_1 + $SSPt_1$ + SSO_3)
Pt_{abs}-O_3-Pt_{abs}	6	ΔRO_3	SSO_3
Pt_{abs}-O_1-O_1-Pt_{abs}	6	2*ΔRO_1	2*SSO_1
Pt_{abs}-Pt_2-Pt_{abs}	2	ΔRPt_2	$SSPt_2$
Pt_{abs}-Pt_1-O_3-Pt_{abs}	24	2*ΔRO_3	½ *(SSO_1 + $SSPt_1$ + SSO_3)
Pt_{abs}-O_4-Pt_{abs}	6	ΔRO_4	SSO_4

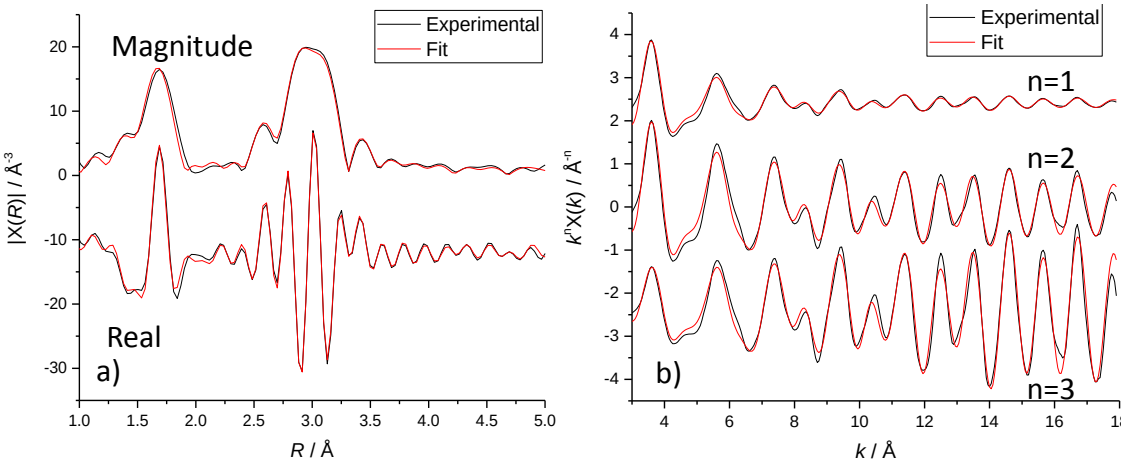

Figure 23 a) *R* and b) *k*-space fits for the PtO_2 pellet reference. 14 variables were used and an r-factor of 0.011 was obtained for the fit. Plots are not phase corrected.

Table 8 Values obtained from the fit for the PtO_2 pellet presented above, in Figure 23.

Scattering path	S_0^2	E_0 / eV	*R* / Å	σ^2 / Å^2
Pt_{abs}-O_1-Pt_{abs}	0.75 ± 0.03	9.8 ± 0.5	2.014 ± 0.004	0.0023 ± 0.0004
Pt_{abs}-Pt_1-Pt_{abs}			3.101 ± 0.002	0.0027 ± 0.0002
Pt_{abs}-O_2-Pt_{abs}			3.67 ± 0.03	0.006 ± 0.003
Pt_{abs}-O_3-Pt_{abs}			4.03 ± 0.05	0.011 ± 0.008
Pt_{abs}-Pt_2-Pt_{abs}			4.35 ± 0.08	0.009 ± 0.007
Pt_{abs}-O_4-Pt_{abs}			4.75 ± 0.06	0.004 ± 0.008

In addition to the large peak observed at 2.8 Å in *R*-space due to the Pt-Pt 1st shell scattering path, PtO_2 contains a peak at 1.6 Å due to the scattering by the nearest oxygen atom. This peak is particularly noticeable for the as prepared 2 nm Pt/C sample, and no significant Pt structure can be observed above the noise at higher values of *R*. The Fourier transforms for the as prepared 2 nm Pt/C electrode sample before and after reduction under H_2 are presented in Figure 24 to illustrate this point.

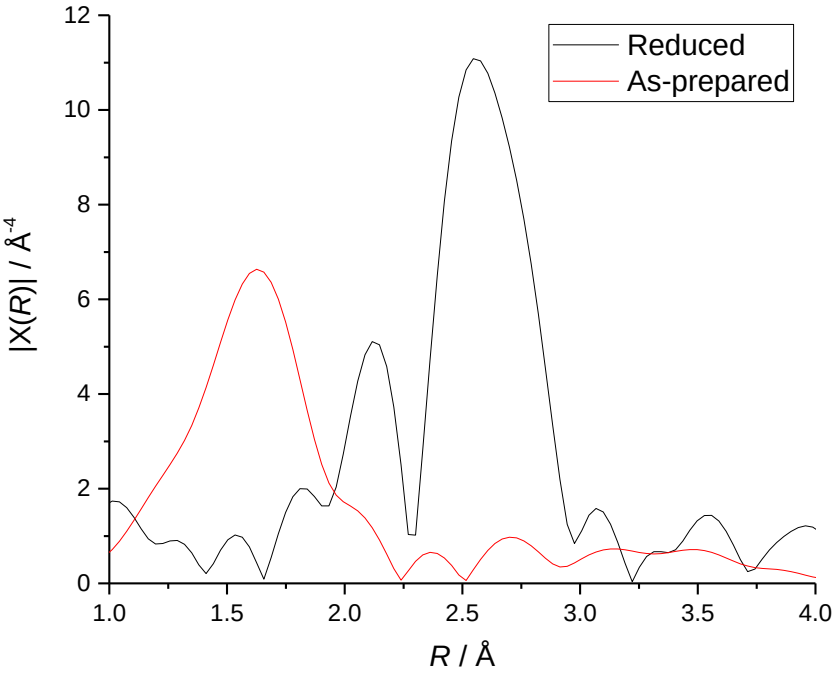

Figure 24 Fourier transform of the EXAFS data collected for the 2 nm Pt/C electrode sample before and after reduction under H_2 for 30 minutes. Plot is not phase corrected.

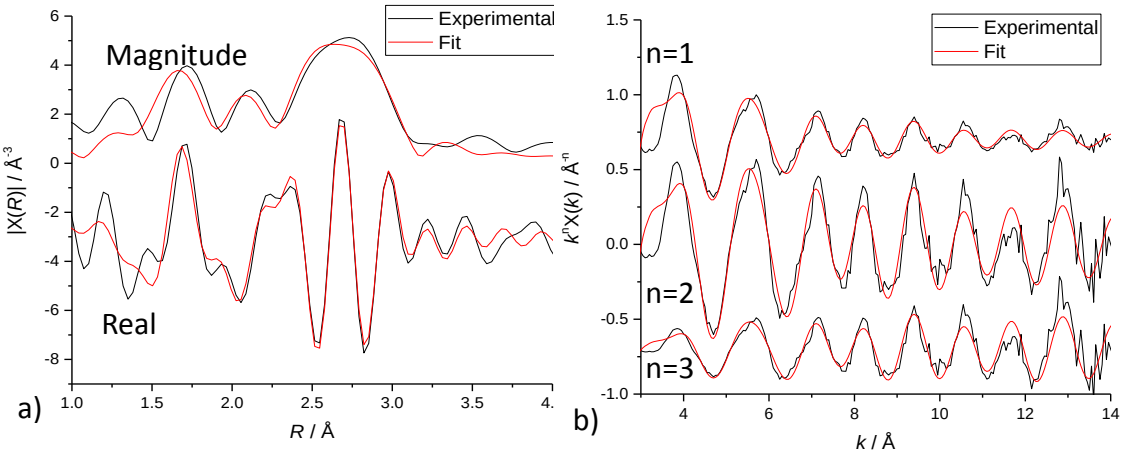

Figure 25 Example fit to one of the electrodes in the series of spectra collected for 2 nm Pt/C aged samples in a) *R* and b) *k*-space. Fit depicted is for the electrode sample that was electrochemically cycled 50 times in N_2 purged 1 M $HClO_4$ and measured *ex situ*. A smaller than normal range in both *k* and *R* space was used due to inherently large disorder in the sample. Plots are not phase corrected.

Due to the added complication of O neighbours alongside the inherent disorder expected for the EXAFS of 2 nm Pt/C particles, only 1st shell fits for these samples were possible. An example fit is shown in Figure 25.

The coordination number for the nearest O and Pt neighbours was plotted against the number of cycles performed as the accelerated stability test, and the trend shown in Figure 26 was observed. Electrochemical cycling of the electrode serves to reduce the amount of

surface oxide present as a hangover from the synthesis of the catalyst and preparation of the electrode. The number of both Pt and O neighbours reaches a stable value after 500 cycles, with about 8 and 1 neighbouring Pt and O atoms, respectively. This gives a total 1st shell coordination number similar to that obtained for the as prepared catalyst powder. The fits also indicate that the room temperature H_2 reduction treatment was not strong to reduce the oxide layer or was not carried out for sufficient time to reduce all of the surface oxide, as O scattering paths were required to obtain a good fit for the experimental data. ECSA data was taken from thin film modified GC RDE measurements performed at 80 °C in N_2 purged 1 M $HClO_4$ and follows an approximately linear trend with the 1st shell coordination numbers. RDE data was used to ensure that the catalyst loading was consistent throughout the measurements.

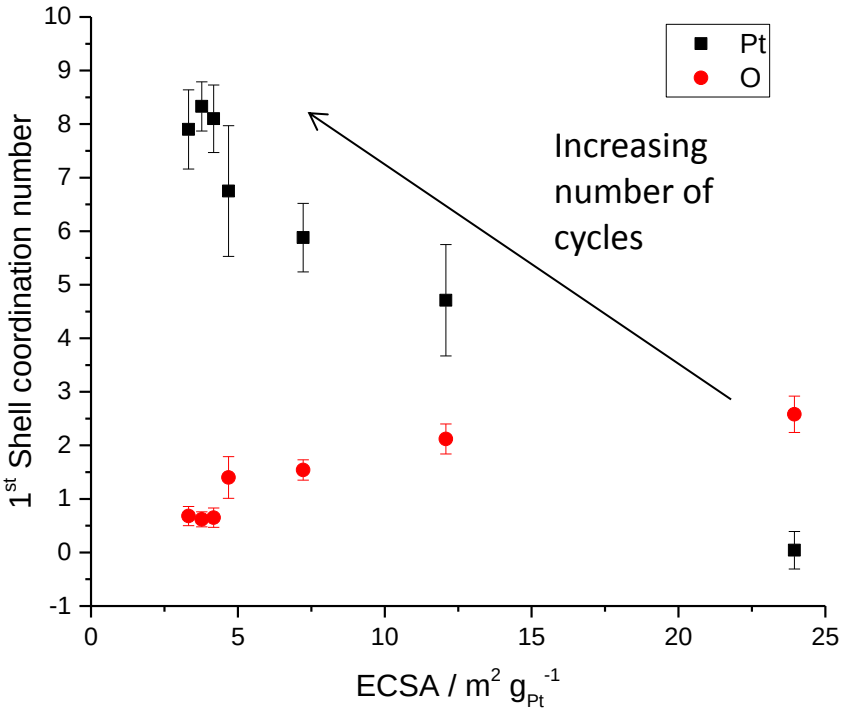

Figure 26 Pt and O nearest neighbour coordination numbers obtained from first shell fits of the 2 nm Pt/C data, example fit shown above in Figure 25. The electrode samples required the inclusion of a Pt-O scattering path. As a reference, the reduced pellet had a Pt nearest neighbour coordination number of 8.87 ± 0.27, with no O neighbours required in the fit, and the uncycled electrode that had been reduced under H_2 for 30 minutes had 7.53 ± 0.64 and 0.35 ± 0.15 Pt and O nearest neighbours respectively. The ECSA data was taken from RDE measurements using a thin film of the 2 nm Pt/C catalyst ink (3.0 µL) drop cast onto the polished GC tip and dried under rotation.

4.3.2.3 *In situ* XAS

As-prepared electrode samples coated with the Pt/C catalyst were mounted in the *in situ* EXAFS cell and mounted on the beamline, and supplied with N_2 purged 1 M $HClO_4$. XAS data

were collected at room temperature, in fluorescence mode whilst holding the potential at several points ranging from the H_{upd} through to the oxide formation regions. Before the XAS measurements were started, the electrode was allowed to equilibrate at the potential of interest for several minutes (~5 mins) until the current was small. Overall, the potential was held at each value for 45 minutes. The spectra were aligned based on the energy shift required to align a separately measured Pt film because the orientation of the *in situ* cell obscured the reference foil and the following ionisation chamber.

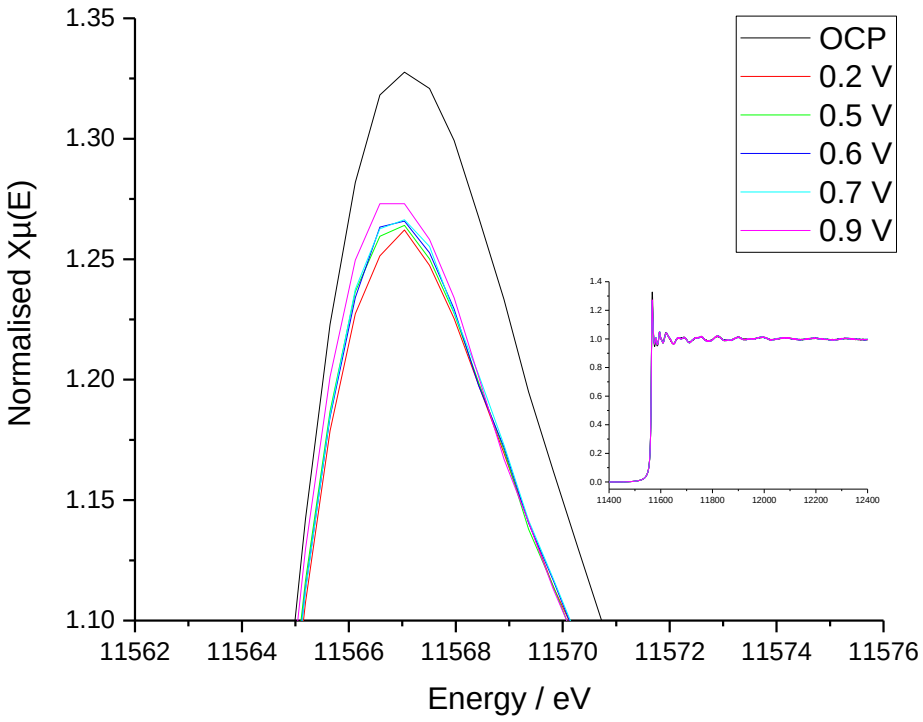

Figure 27 In situ XAS of the 5 nm Pt/C electrode taken at open circuit potential (OCP) and several other potentials *vs.* RHE. Main panel shows a zoomed in region of the XANES focussing on the white line. Inset: complete XAS spectra of the same samples.

Figure 27 shows the XAS collected at each potential for the 5 nm Pt/C electrode sample, whilst there is very little difference between the spectra, the white line intensity does increase as more oxidising potentials are reached. The measurement taken at OCP was done before any electrochemical treatment and shows more oxidation from sample preparation and storage than after potential control was established. OCP was typically slightly above 0.9 V *vs.* RHE. Some further small differences between the OCP scan and those under potential control are noticeable in the XANES region, but not in the EXAFS. The foil is very similar to the spectrum taken at 0.2 V *vs.* RHE.

Equivalent XAS spectra for the 2 nm Pt/C sample are shown in Figure 28, and larger differences between the spectra can be observed due to the increased surface area available for oxidation. The initial measurement at OCP shows that the sample is initially heavily oxidised as a result of the synthesis and preparation procedure, but quickly reduced to a more metallic phase under potential control. Again it can be observed that more oxidising potentials lead to larger white line intensity. The OCP measurement was repeated after the series of potential steps and shows that the catalyst particles are oxidised at OCP whilst immersed in $HClO_4$. Oxide formation can be identified in the EXAFS in the 0.9 V *vs.* RHE measurement and particularly at OCP, which may be in part due to the extended period of time spent at highly oxidising potentials.

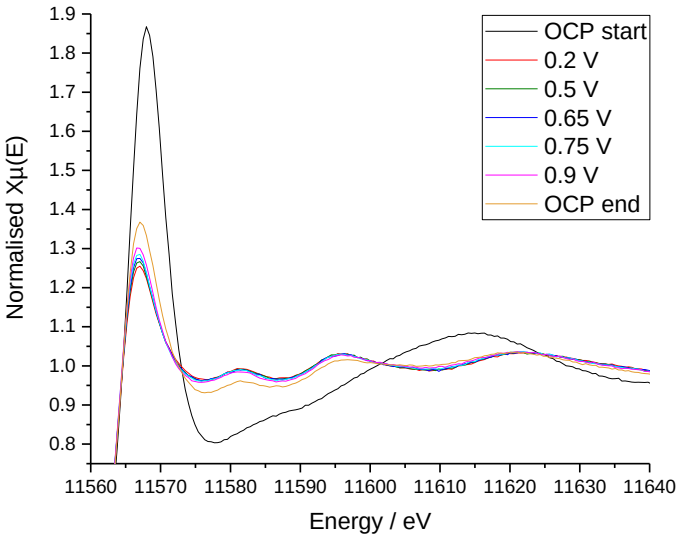

Figure 28 In situ XAS for the 2 nm Pt/C electrode at several potentials selected based on the position of the features of the cyclic voltammogram in 1 mM KI in 1 M $HClO_4$. Measurements at OCP were done both before and after the electrochemical treatment.

4.3.2.3.1 d-band occupancy

Work by authors such as Hammer and Norskov[46–48] show that *d*-band theory can be used to understand and explain observed trends in catalytic activity. The absorption strength of simple molecules such as hydrogen and oxygen fit these trends well, which makes the occupancy of *d*-states an interesting parameter when looking at fuel cell catalysts.

When using XAS at the Pt L_2 and L_3 edges, the transitions being probed are from $2p_{3/2}$ and $2p_{1/2}$ to unoccupied *d*-states, with the intensity of the white line related to the total angular momentum of the final state. These observations have been developed into a quantitative method, proposed by Mansour *et al.*,[49] for comparing the fractional change in d-band

occupancy (f_d) of a sample relative to a reference compound, according to Equation 2. The total density of unoccupied d-states compared to the reference is proportional to this value.

$$f_d = \frac{\Delta A_3 + 1.11\Delta A_2}{A_{3,ref} + 1.11A_{2,ref}} \qquad \Delta A_3 = A_{3,sample} - A_{3,ref} \qquad \Delta A_2 = A_{2,sample} - A_{2,ref}$$

Equation 2

A_i indicates the integral (between -10 and 40 eV) of the difference between the L_i XANES, i = 2 or 3, and the arc tangent background function for the sample and reference material (ref). Example background functions are shown in Figure 30. A larger value for f_d correlates with smaller d-state occupancy than the reference material, which, in this case, was a Pt foil.

The first step in the method[49] is the normalisation and flattening of the XAS spectrum, as outlined in chapter 3. The L_2 and L_3 edges are then aligned and placed on the same energy scale by subtracting the energy at the inflection point of the curve, which should result in spectra that differ in the XANES region close to the absorption edge, but match in the more distant EXAFS region, as shown in Figure 29. XANES spectra with intense white lines, commonly observed for Pt oxides, can complicate the alignment process since the energy at the inflection point can be significantly lowered compared to the reference sample.

The atomic background can then be fit to the spectra. This background was modelled as an arc tangent function passing through the inflection point and either the first or second local minima using the curve fitting software Eureqa[50] by adjusting Equation 3 to match the XANES spectra. The results of this process are shown in Figure 30.

$$\boldsymbol{y = A\ \tan^{-1}\left(B(x + C)\right) + D}$$

Equation 3

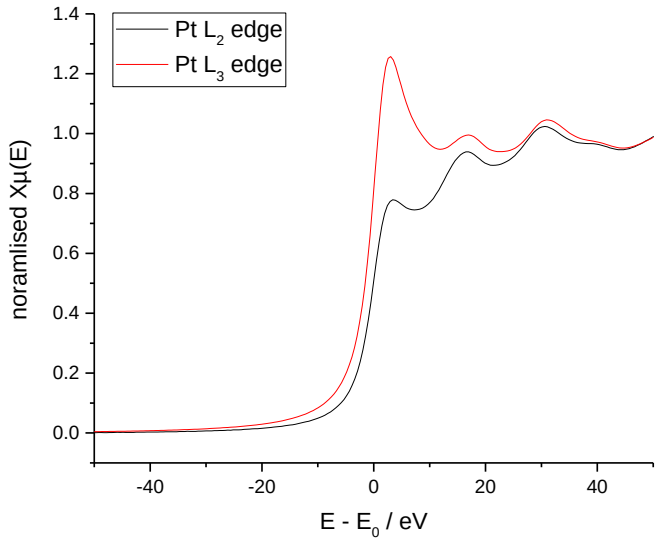

Figure 29 The Pt L_2 and L_3 edges for each sample (Pt foil data shown) are normalised and aligned by subtracting E_0, which, in this example, was 13273 and 11564 eV for the L_2 and L_3 edges respectively. The EXAFS region, further away from the edge, should match.

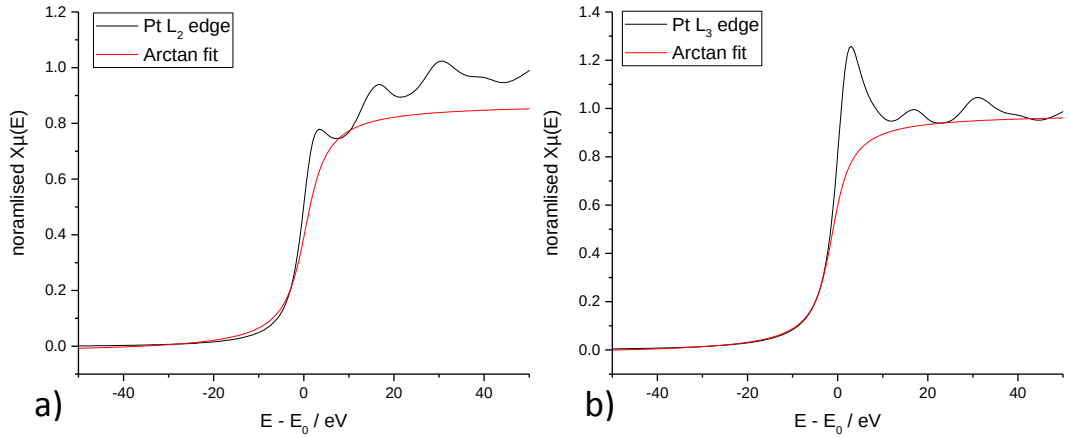

Figure 30 Normalised XANES spectra showing a) the L_2 and b) the L_3 edges of Pt foil with arc tangent functions fitted through the inflection point and the first and second local minima respectively. To determine f_d, the arc tangent is subtracted from the XANES spectrum, and the integral between -10 and 40 eV is calculated for each absorption edge and used in Equation 2.

The difference between the XAS data and the background can then be integrated between -10 eV and +40 eV and used as the relevant area in Equation 2.

The total density of the unoccupied *d*-state, h_s, can then be related to that of the reference foil, h_r, using Equation 4.

$$h_s = (1.0 + f_d)h_r$$

Equation 4

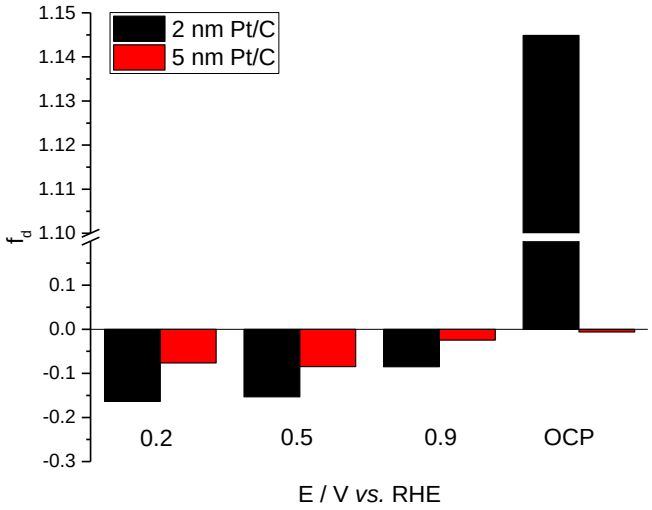

E / V *vs.* RHE	2 nm Pt/C	5 nm Pt/C
0.2	-0.20	-0.08
0.5	-0.18	-0.09
0.9	-0.09	-0.03
OCP	0.53	-0.006

Figure 31 Fractional change (f_d) in d-band occupancy relative to Pt foil for the 2 and 5 nm Pt/C catalysts at several potentials and at open circuit potential (OCP). A larger f_d value corresponds to smaller *d*-band occupancy. The 2 nm Pt/C sample was heavily oxidised before placing under potential control leading to a f_d large value at OCP.

Figure 31 displays the fractional change in *d*-band vacancy for the 2 and 5 nm Pt/C catalysts as function of potential. Due to the nature of the analysis process, the error in these values for f_d is likely to be around 10%, meaning that the 5 nm Pt/C sample has similar electronic structure to the Pt foil reference material, whilst the 2 nm Pt/C sample has a slightly more occupied *d*-band. This contradicts the result expected from theory and from published literature, which indicate that nanoparticles have larger *d*-band vacancies than the bulk material.[51] However, the integration in this paper was performed over a smaller range of -10 – 13 eV, which would approximately halve the values presented in Figure 31.

d-band theory states that as the Pt *d*-states become occupied, more of the antibonding orbitals get filled thereby weakening adsorption. Pt nanoparticles adsorb O more strongly than the bulk as the surface atoms are at higher energy due to undercoordination, whereas this result is consistent with the opposite case.

The method used by Friebel *et al.*[28] where the residual between the high energy resolution fluorescence detection (HERFD) XAS spectra at the Pt L_3 edge and an arctangent background was deconvoluted into contributions from metallic and oxide phases may have provided a more rigorous approach less susceptible to errors introduced during data analysis and fitting. HERFD XAS was not possible on the beamline used for this work.

4.3.3 Poisoned Electrodes

The additional set of prepared electrodes was poisoned by holding the electrode at 0.3 V *vs.* RHE in 1 mM KI in 1 M $HClO_4$ for 1 minute. Cyclic voltammetry for the catalyst coated electrode in acid and in the KI poisoned acid is presented in Figure 32. A noticeable decrease in both the H_{upd} and oxide formation regions is observed upon addition of the KI solid to the electrolyte, and further decreases are seen after successive potential cycles. Correspondingly, the peak at 0.45 V *vs.* RHE becomes apparent and increases in size with cycling. 0.3 V *vs.* RHE was chosen for the potential hold as it allows for reduction of surface oxides, known to prevent adsorption of I^-, whilst promoting I^- generation, the most strongly adsorbed I-containing species. Some Pt-I species may also be soluble in acid at anodic potentials.[35] On a Pt disc, a second pair of reduction and oxidation peaks is observed at 0.7 V *vs.* RHE, this is less clear on the Pt/C samples.

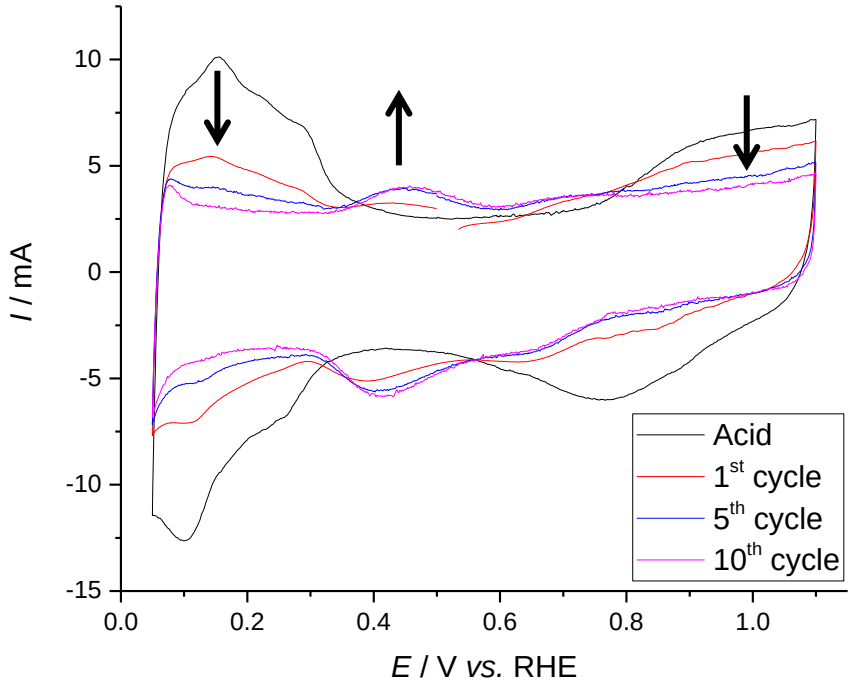

Figure 32 Cyclic voltammetry at 20 mV s^{-1} of the 5 nm Pt/C catalyst in N_2 purged 1 M $HClO_4$ (black), and the 1st, 5th and 10th cycles(red, blue and purple, respectively) in the same electrolyte after the addition of ~25 mg KI to make a 0.001 M KI solution.

Adsorption of I^- to the Pt surface provides a measure of surface sensitivity to the XAS measurements as Pt-I neighbours will only be observed for the outermost Pt atoms. I^- also adsorbs irreversibly and has an atomic number that is distinct from Pt, O and from Ni and Co, which will be introduced in the next chapter. This makes the analysis easier as elements

with similar atomic numbers are sometimes hard to distinguish using the calculations behind the EXAFS fitting software because the scattering effects are similar.

The number of Pt-I neighbours is expected to correlate with particle size based on the number of available atoms for adsorption, although this will not be a linear relationship since the number of surface atoms does not increase proportionally with the total number of atoms in a particle. This will lead to high size sensitivity for small nanoparticles and lower sensitivity when looking at larger nanoparticles. The surface coverage of I species is expected to be between 1/3 and 4/9 based on previous computational work supported by *in situ* STM experiments.[37]

Figure 33 shows a comparison of the number of 1st shell I and Pt atoms for the 2 sets of catalysts. There is some distinction between the 2 nanoparticle sizes, however the error bars are large, and for an unknown size sample it would be difficult to state with certainty a particle size range. These results do suggest that it would be possible, although it would probably be best to start with a series of samples with well-defined particle size distributions, to allow a calibration curve to be drawn up to which an unknown sample could be compared. The procedure for poisoning the samples with KI could also either be done for a longer period of time both to give time for better I coverage and to reduce any surface oxides present. Potential cycling in KI might be more effective than the potential hold used here.

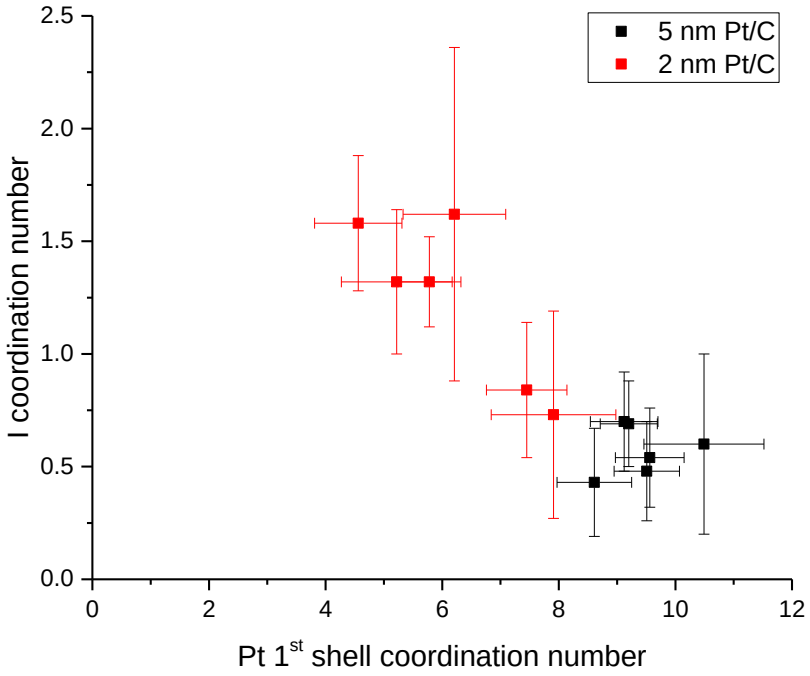

Figure 33 I coordination numbers plotted against the 1st shell Pt coordination numbers obtained from the EXAFS spectra for each of the KI poisoned electrodes. The as prepared samples (0 cycles) were not included due to the inhibition of iodine adsorption by the presence of significant surface oxides. The Pt/C samples were fitted using the same model as used previously with the addition of a Pt-I scattering path. The data points refer to the electrode samples taken throughout the accelerated degradation test. The Pt surface was poisoned with I-species by treatment in 0.1 M KI solution.

KI solutions have been used to leach and dissolve Pt out of Pt/C type materials present in fuel cells as an alternative to using more aggressive aqua regia based methods.[52] As a result, the use of KI as a surface probe may also corrode the Pt/C samples thereby affecting surface area. However, these methods employ much higher KI concentrations at high temperatures to achieve this. For example, in the work by Patel and Dawson,[52] the dissolution was measured at 4 M KI at 90 ^{o}C, although they concluded that increased concentration did not greatly affect the rate of dissolution. It is noted that small concentrations of dissolved iodine, *ca.* 5 mM level, accelerate the process, and that dissolution was limited by diffusion controlled processes and available surface area. As this work uses very low KI concentrations at room temperature under a N_2 atmosphere, which will supress aerobic oxidation of iodide ions to iodine, and for short timescales, dissolution effects are expected to be negligible.

4.4 Conclusions

The results shown here suggest that the 5 nm Pt/C catalyst was stable under the conditions used, whilst the 2 nm catalyst was unstable. Evidence of this comes from the electrochemical data, which showed that the ECSA for the 5 nm sample was near constant and the 2 nm catalyst lost a significant fraction of the original value. The mechanism for this loss was not directly observed, for example by TEM imaging of catalyst particles before and after the AST,[10,11] or from ICP-MS analysis of the electrolyte similar to Topalov *et al*.[9] However in this work, the typical EXAFS fitting model was further developed by relating the degeneracy parameters for single scattering paths to the multiple scattering paths thereby reducing the number of parameters required for the fit without affecting quality. This is of most use when analysing spectra with limited information, for example when it is necessary to include scattering paths to adsorbates such as oxygen or iodine as the number of parameters required quickly increases. The fitting model showed that the coordination number for the 2 nm Pt/C sample increased over the course of the stability test. From this result it can be inferred that the nanoparticle size was increasing, although this does not rule out other affects such as support degradation and particle detachment, which cannot be detected using the EXAFS measurements done here. Techniques such as FTIR, or ICP-MS could be coupled to a flow cell type system to analyse the exhaust for species such as CO_2 or metal atoms and ions indicative of support degradation and loss of Pt metal respectively. Identical location TEM experiments such as that done by Perez-Alonso *et al*.[53] could also be used to provide evidence for these degradation methods.

As a further experiment, samples of the electrolyte would be taken periodically throughout the AST to allow the quantification of dissolved or detached Pt. Ideally, the EXAFS measurements would be carried out *in situ* during the potential cycling treatment perhaps as a long duration experiment on the beamline, although this poses a number of practical problems and would not provide significantly improved data to that presented here.

The XPS spectra were significantly affected by the presence of Nafion in the catalyst layers, particularly the F 1*s* and F Auger transitions, which will obscure the expected binding energy region for the Co and Ni 2_p peaks, relevant for the subsequent work on the PtNi/C and PtCo/C catalysts. Slight shifts to higher binding energies can be observed for the 2 nm Pt/C and for the electrode samples, relative to the 5 nm Pt/C and powder samples.

The XRD spectra showed the crystalline nature of the 5 nm Pt/C arising from the heat treatment used during the synthesis process, whilst for the 2 nm Pt/C sample significant

peak broadening is observed consistent with the small crystallite size. Both spectra can be indexed to the fcc structure, and the calculated lattice parameter is close to the literature value.

The Pt/C samples were successfully coated with iodine/iodide, which is best achieved by reducing any oxide layer first. This can be easily via several potential cycles in N_2 purged 1 M $HClO_4$ + 1 mM KI solution, or through potential holds at a reducing potential followed by a mildly oxidising potential.

EXAFS analysis of the iodine poisoned samples resulted in observable differences in the Pt-I partial coordination for the 2 and 5 nm samples; negative correlation was found between the number of 1st shell Pt and I neighbours, which is consistent with nanoparticle surface area arguments. The improved EXAFS model used for the particle size determination could not be refined to include the contributions from the iodine neighbours.

This could serve as a supplementary method for particle size determination using EXAFS. However, the same flaws apply as when using the Pt coordination numbers, as the technique will remain most sensitive to smaller nanoparticles, and still requires accurate analysis of the EXAFS. With refinement and through use of ideal surfaces such as single crystals, iodine adsorption could possibly yield information about crystal faces present due to changes in partial Pt-I coordination number representing different coverages on each crystal face. Computational modelling of expected coordination numbers for various Iodine-adlayer structures would also be useful to compare with the experimentally obtained values. This would, however, be difficult for 'real world' catalyst samples.

4.5 References

(1) Stephens, I. E. L.; Rossmeisl, J.; Chorkendorff, I. Toward Sustainable Fuel Cells. *Science (80-.).* **2016**, *354*, 1378–1379.

(2) Kongkanand, A.; Mathias, M. F. The Priority and Challenge of High-Power Performance of Low-Platinum Proton-Exchange Membrane Fuel Cells. *J. Phys. Chem. Lett.* **2016**, *7*, 1127–1137.

(3) Takahashi, I.; Kocha, S. S. Examination of the Activity and Durability of PEMFC Catalysts in Liquid Electrolytes. *J. Power Sources* **2010**, *195*, 6312–6322.

(4) Furuya, Y.; Mashio, T.; Ohma, A.; Tian, M.; Kaveh, F.; Beauchemin, D.; Jerkiewicz,

G. Influence of Electrolyte Composition and pH on Platinum Electrochemical And/or Chemical Dissolution in Aqueous Acidic Media. *ACS Catal.* **2015**, *5*, 2605–2614.

(5) Pickering, H. W.; Wagner, C. Electrolytic Dissolution of Binary Alloys Containing a Noble Metal. *J. Electrochem. Soc.* **1967**, *114*, 698.

(6) Erlebacher, J. An Atomistic Description of Dealloying. *J. Electrochem. Soc.* **2004**, *151*, C614.

(7) Sieradzki, K.; Dimitrov, N.; Movrin, D.; McCall, C.; Vasiljevic, N.; Erlebacher, J. The Dealloying Critical Potential. *J. Electrochem. Soc.* **2002**, *149*, B370.

(8) Hoshi, Y.; Yoshida, T.; Nishikata, A.; Tsuru, T. Dissolution of Pt–M (M: Cu, Co, Ni, Fe) Binary Alloys in Sulfuric Acid Solution. *Electrochim. Acta* **2011**, *56*, 5302–5309.

(9) Topalov, A. A.; Cherevko, S.; Zeradjanin, A. R.; Meier, J. C.; Katsounaros, I.; Mayrhofer, K. J. J. Towards a Comprehensive Understanding of Platinum Dissolution in Acidic Media. *Chem. Sci.* **2014**, *5*, 631–638.

(10) Schlögl, K.; Mayrhofer, K. J. J.; Hanzlik, M.; Arenz, M. Identical-Location TEM Investigations of Pt/C Electrocatalyst Degradation at Elevated Temperatures. *J. Electroanal. Chem.* **2011**, *662*, 355–360.

(11) Meier, J. C.; Galeano, C.; Katsounaros, I.; Topalov, A. A.; Kostka, A.; Schüth, F.; Mayrhofer, K. J. J. Degradation Mechanisms of Pt/C Fuel Cell Catalysts under Simulated Start-Stop Conditions. *ACS Catal.* **2012**, *2*, 832–843.

(12) Dubau, L.; Lopez-Haro, M.; Castanheira, L.; Durst, J.; Chatenet, M.; Bayle-Guillemaud, P.; Guétaz, L.; Caqué, N.; Rossinot, E.; Maillard, F. Probing the Structure, the Composition and the ORR Activity of Pt3Co/C Nanocrystallites during a 3422h PEMFC Ageing Test. *Appl. Catal. B Environ.* **2013**, *142–143*, 801–808.

(13) Stephens, I. E. L.; Bondarenko, A. S.; Grønbjerg, U.; Rossmeisl, J.; Chorkendorff, I. Understanding the Electrocatalysis of Oxygen Reduction on Platinum and Its Alloys. *Energy Environ. Sci.* **2012**, *5*, 6744.

(14) Gasteiger, H. A.; Kocha, S. S.; Sompalli, B.; Wagner, F. T. Activity Benchmarks and Requirements for Pt, Pt-Alloy, and Non-Pt Oxygen Reduction Catalysts for

PEMFCs. *Appl. Catal. B Environ.* **2005**, *56*, 9–35.

(15) Mayrhofer, K. J. J.; Strmcnik, D.; Blizanac, B. B.; Stamenkovic, V.; Arenz, M.; Markovic, N. M. Measurement of Oxygen Reduction Activities via the Rotating Disc Electrode Method: From Pt Model Surfaces to Carbon-Supported High Surface Area Catalysts. *Electrochim. Acta* **2008**, *53*, 3181–3188.

(16) Shao, M.; Peles, A.; Shoemaker, K. Electrocatalysis on Platinum Nanoparticles: Particle Size Effect on Oxygen Reduction Reaction Activity. *Nano Lett.* **2011**, *11*, 3714–3719.

(17) Nesselberger, M.; Ashton, S.; Meier, J. C.; Katsounaros, I.; Mayrhofer, K. J. J.; Arenz, M. The Particle Size Effect on the Oxygen Reduction Reaction Activity of Pt Catalysts: Influence of Electrolyte and Relation to Single Crystal Models. *J. Am. Chem. Soc.* **2011**, *133*, 17428–17433.

(18) Tritsaris, G. A.; Greeley, J.; Rossmeisl, J.; Nørskov, J. K. Atomic-Scale Modeling of Particle Size Effects for the Oxygen Reduction Reaction on Pt. *Catal. Letters* **2011**, *141*, 909–913.

(19) Greeley, J.; Rossmeisl, J.; Hellmann, A.; Norskov, J. K. Theoretical Trends in Particle Size Effects for the Oxygen Reduction Reaction. *Zeitschrift für Phys. Chemie* **2007**, *221*, 1209–1220.

(20) Fritsche, H.-G.; Benfield, R. E. Exact Analytical Formulae for Mean Coordination Numbers in Clusters. *Zeitschrift für Phys. D Atoms, Mol. Clust.* **1993**, *26*, 15–17.

(21) Benfield, R. E. Mean Coordination Numbers and the Non-Metal-Metal Transition in Clusters. *J. Chem. Soc., Faraday Trans* **1992**, *88*, 1107–1111.

(22) Montejano-Carrizales, J. M.; Aguilera-Granja, F.; Morán-López, J. L. Direct Enumeration of the Geometrical Characteristics of Clusters. *Nanostructured Mater.* **1997**, *8*, 269–287.

(23) Jentys, A. Estimation of Mean Size and Shape of Small Metal Particles by EXAFS. *Phys. Chem. Chem. Phys.* **1999**, *1*, 4059–4063.

(24) Glasner, D.; Frenkel, A. I. Geometrical Characteristics of Regular Polyhedra: Application to EXAFS Studies of Nanoclusters. In *AIP Conference Proceedings*; AIP, **2007**; 882,746–748.

(25) Maniguet, S.; Mathew, R. J.; Russell, A. E. EXAFS of Carbon Monoxide Oxidation on Supported Pt Fuel Cell Electrocatalysts. *J. Phys. Chem. B* **2000**, *104*, 1998–2004.

(26) Gracia, F.; Guerrero, S.; Wolf, E.; Miller, J.; Kropf, A. Kinetics, Operando FTIR, and Controlled Atmosphere EXAFS Study of the Effect of Sulfur on Pt-Supported Catalysts during CO Oxidation. *J. Catal.* **2005**, *233*, 372–387.

(27) Price, S. W. T.; Speed, J. D.; Kannan, P.; Russell, A. E. Exploring the First Steps in Core–Shell Electrocatalyst Preparation: In Situ Characterization of the Underpotential Deposition of Cu on Supported Au Nanoparticles. *J. Am. Chem. Soc.* **2011**, *133*, 19448–19458.

(28) Friebel, D.; Viswanathan, V.; Miller, D. J.; Anniyev, T.; Ogasawara, H.; Larsen, A. H.; O'Grady, C. P.; Nørskov, J. K.; Nilsson, A. Balance of Nanostructure and Bimetallic Interactions in Pt Model Fuel Cell Catalysts: In Situ XAS and DFT Study. *J. Am. Chem. Soc.* **2012**, *134*, 9664–9671.

(29) Friebel, D.; Miller, D. J.; O'Grady, C. P.; Anniyev, T.; Bargar, J.; Bergmann, U.; Ogasawara, H.; Wikfeldt, K. T.; Pettersson, L. G. M.; Nilsson, A.; O'Grady, C. P.; Anniyev, T.; Bargar, J.; Bergmann, U.; Ogasawara, H.; Wikfeldt, K. T.; Pettersson, L. G. M.; Nilsson, A.; O'Grady, C. P.; Anniyev, T.; Bargar, J.; Bergmann, U.; Ogasawara, H.; Wikfeldt, K. T.; Pettersson, L. G. M.; Nilsson, A. In Situ X-Ray Probing Reveals Fingerprints of Surface Platinum Oxide. *Phys. Chem. Chem. Phys.* **2011**, *13*, 262–266.

(30) Jackson, C.; Smith, G. T.; Inwood, D. W.; Leach, A. S.; Whalley, P. S.; Callisti, M.; Polcar, T.; Russell, A. E.; Levecque, P.; Kramer, D. Electronic Metal-Support Interaction Enhanced Oxygen Reduction Activity and Stability of Boron Carbide Supported Platinum. *Nat. Commun.* **2017**, *8*, 15802.

(31) Jia, Q.; Caldwell, K.; Strickland, K.; Ziegelbauer, J. M.; Liu, Z.; Yu, Z.; Ramaker, D. E.; Mukerjee, S. Improved Oxygen Reduction Activity and Durability of Dealloyed PtCo X Catalysts for Proton Exchange Membrane Fuel Cells: Strain, Ligand, and Particle Size Effects. *ACS Catal.* **2015**, *5*, 176–186.

(32) Paulus, U. A.; Schmidt, T. J.; Gasteiger, H. A.; Behm, R. J. Oxygen Reduction on a High-Surface Area Pt/Vulcan Carbon Catalyst: A Thin-Film Rotating Ring-Disk Electrode Study. *J. Electroanal. Chem.* **2001**, *495*, 134–145.

(33) Guilminot, E.; Corcella, A.; Chatenet, M.; Maillard, F. Comparing the Thin-Film Rotating Disk Electrode and the Ultramicroelectrode with Cavity Techniques to Study Carbon-Supported Platinum for Proton Exchange Membrane Fuel Cell Applications. *J. Electroanal. Chem.* **2007**, *599*, 111–120.

(34) Shinozaki, K.; Zack, J. W.; Richards, R. M.; Pivovar, B. S.; Kocha, S. S. Oxygen Reduction Reaction Measurements on Platinum Electrocatalysts Utilizing Rotating Disk Electrode Technique. *J. Electrochem. Soc.* **2015**, *162*, F1144–F1158.

(35) Yaraliev, Y. A. Electrochemistry of Iodine. *Usp. Khim.* **1982**, *51*, 990–1016.

(36) White, J. H.; Abruna, H. D. Electrosorption of Iodide on Pt(111) Studied In Situ by X-Ray Absorption-Spectroscopy. *J. Phys. Chem.* **1988**, *92*, 7131–7134.

(37) Gossenberger, F.; Roman, T.; Groß, A. Equilibrium Coverage of Halides on Metal Electrodes. *Surf. Sci.* **2015**, *631*, 17–22.

(38) Deegan, R. D.; Bakajin, O.; Dupont, T. F.; Huber, G.; Nagel, S. R.; Witten, T. A. Capillary Flow as the Cause of Ring Stains from Dried Liquid Drops. *Nature* **1997**, *389*, 827–829.

(39) Sheng, W.; Chen, S.; Vescovo, E.; Shao-Horn, Y. Size Influence on the Oxygen Reduction Reaction Activity and Instability of Supported Pt Nanoparticles. *J. Electrochem. Soc.* **2012**, *159*, B96.

(40) Assumpção, M. H. M. T.; Moraes, A.; De Souza, R. F. B.; Reis, R. M.; Rocha, R. S.; Gaubeur, I.; Calegaro, M. L.; Hammer, P.; Lanza, M. R. V; Santos, M. C. Degradation of Dipyrone via Advanced Oxidation Processes Using a Cerium Nanostructured Electrocatalyst Material. *Appl. Catal. A Gen.* **2013**, *462–463*, 256–261.

(41) Huang, H.; He, Z.; Lin, X.; Ruan, W.; Liu, Y.; Yang, Z. Ultradispersed Platinum Nanoclusters on Polydopamine-Functionalized Carbon Nanotubes as an Excellent Catalyst for Methanol Oxidation Reaction. *Appl. Catal. A Gen.* **2015**, *490*, 65–70.

(42) Wang, J.; Yin, G.; Shao, Y.; Zhang, S.; Wang, Z.; Gao, Y. Effect of Carbon Black Support Corrosion on the Durability of Pt/C Catalyst. *J. Power Sources* **2007**, *171*, 331–339.

(43) Wang, H.; Da, H.; Wang, R.; Ji, S. Beef-Derived Mesoporous Carbon as Highly Efficient Support for PtRulr Electrocatalysts and Their High Activity for CO and

Methanol Oxidation. *South African J. Chem.* **2014**, *67*, 34–39.

(44) Myshlyavtsev, A. V.; Stishenko, P. V. Relative Stability of Icosahedral and Cuboctahedral Metallic Nanoparticles. *Adsorption* **2013**, *19*, 795–801.

(45) Svalova, A. I.; Stishenko, P. V. The Statistical Modeling of the Platinum Nanoparticles in the Transition Area from the Five-Fold Symmetry Structure to the Crystal Lattice. *Procedia Eng.* **2015**, *113*, 429–434.

(46) Hammer, B.; Norskov, J. K. Theoretical Surface Science and Catalysis — Calculations and Concepts. *Adv. Catal.* **2000**, *45*, 71–129.

(47) Hammer, B.; Nørskov, J. K. Electronic Factors Determining the Reactivity of Metal Surfaces. *Surf. Sci.* **1995**, *343*, 211–220.

(48) Nilsson, A.; Pettersson, L. G. M.; Hammer, B.; Bligaard, T.; Christensen, C. H.; Norskov, J. K. The Electronic Structure Effect in Heterogeneous Catalysis. *Catal. Letters* **2005**, *100*, 111–114.

(49) Mansour, A. N.; Cook, J. W.; Sayers, D. E. Quantitative Technique for the Determination of the Number of Unoccupied D-Electron States in a Platinum Catalyst Using the L2,3 X-Ray Absorption Edge Spectra. *J. Phys. Chem* **1984**, *88*, 2330–2334.

(50) Schmidt, M.; Lipson, H. Distilling Free-Form Natural Laws from Experimental Data. *Science (80-.).* **2009**, *324*, 81–85.

(51) Mukerjee, S.; Srinivasan, S.; Soriaga, M. Role of Structural and Electronic Properties of Pt and Pt Alloys on Electrocatalysis of Oxygen Reduction. *J. Electrochem. Soc.* **1995**, *142*, 1409–1422.

(52) Patel, A.; Dawson, R. Recovery of Platinum Group Metal Value via Potassium Iodide Leaching. *Hydrometallurgy* **2015**, *157*, 219–225.

(53) Perez-Alonso, F. J.; Elkjær, C. F.; Shim, S. S.; Abrams, B. L.; Stephens, I. E. L.; Chorkendorff, I. B. Identical Locations Transmission Electron Microscopy Study of Pt/C Electrocatalyst Degradation during Oxygen Reduction Reaction. *J. Power Sources* **2011**, *196*, 6085–6091.

Chapter 5: Characterisation of PtCo/C and PtNi/C Powders

5.1 Introduction

Whilst Pt is well known to be the best monometallic electrocatalyst for the ORR in acidic media with a Pt-O bond strength close to the optimal energy determined by theoretical calculations *e.g.* by Nørskov *et al.,*[1] alloying Pt with other transition metals can further increase the catalytic activity. Many carbon supported Pt alloy nanoparticle catalyst have been tested both in terms of the elemental composition as well as the structure of the nanoparticles themselves.[2,3,4] The mechanism for the improvement in catalytic activity has been linked to intertwined geometric and electronic effects such as lattice strain at the catalyst surface,[5,6] and modification of the *d*-band centre.[7,8] As a result the near surface structure and composition of the Pt alloy nanoparticles significantly affects the catalytic activity towards the ORR.

XAS is useful for studying the local coordination environment of specific elements in the catalyst sample. Previously, it was shown how changes in the Pt-Pt coordination numbers for specific shells can be used to determine particle size and provide shape information. When studying alloy catalyst nanoparticles, XAS information from both the Pt and the Ni/Co absorption edges can be utilised and the ratio of the number of intermetallic neighbours from each perspective can be used to determine atomic composition.[9] The total number of neighbouring atoms for each species can be used to indicate whether an element is most prevalent in the core or nearer the surface. Whilst several methods can be used to determine the distribution and ordering of elements within the nanoparticle alloy structure.[10,11]

XAS also allows for the determination of interatomic distances, which can be used as an indicator of the strain present in structure of the catalyst nanoparticles.[12] The strain can then be related to catalytic activity as well as composition, assuming that Vegard's law applies. This assumption has been made previously for both PtCo/C and PtNi/C catalysts.[13,14]

This chapter will focus on the characterisation of the de-alloyed PtNi/C and PtCo/C catalysts. These catalysts have a similar particle size and have been subjected to a similar heat treatment to the 5 nm Pt/C catalyst analysed previously, which will be used for comparison purposes. In this section, the initial structure of commercial PtCo/C and PtNi/C catalysts will be characterised, and will act as a reference point to which samples that have been further treated and degraded can be compared. These samples were analysed using TEM, EDX XPS, and XRD techniques in order to determine the elemental composition and distribution throughout the nanoparticles. The observations from these techniques were used to guide the development of a fitting model for the XAS spectra to account for the increased complexity and disorder resulting from the addition of Ni or Co into the Pt nanoparticle structure. Ideas and strategies from previous authors, such as Frenkel,[15] were incorporated into the model. Additionally for the PtNi/C catalyst, samples were obtained at several points in the synthesis procedure and analysed using the XAS fitting model.

5.2 Experimental

Characterisation of the PtCo/C and PtNi/C catalyst powders was carried out using TEM, XPS, XRD and XAS as done in the previous chapter with the Pt/C samples. More details of the atomic composition and de-alloying treatments are given in the experimental chapter. The TEM was operated by Emily Brooke, an employee at JMTC, who also assisted with the analysis. The XPS data was collected on my behalf by Tugce Eralp Erden, also of JMTC.

The XAS data was measured on catalyst samples that had been incorporated into boron nitride (BN) pellets. The pellets were formed by mixing each catalyst powder (~12 mg) with BN (~138 g) using a mortar and pestle. The mass of catalyst added was calculated to give an edge jump of approximately 1 using Equation 1, where the edge jump, μa, is given by Equation 2. For the alloy catalysts, the same pellet was used for both elements and absorption edges.

$$mass = \frac{(\mu a)(sample\ area)}{\mu_\rho}$$

Equation 1

$$\mu a = ln\left(\frac{I_0}{I_T}\right)$$

Equation 2

μ_ρ is the mass absorption coefficient of the element of interest, taken from the online Mucal program,[16] and I_0 and I_T are the intensities of the incident and transmitted X-rays. The sample area of the pellets used was 0.21 cm^2. The elemental composition of the catalyst powder must also be considered.

Once homogeneous, the mixture of the catalyst powder and BN was pressed into the pellet holder at a pressure of 5 tons for 1 minute. The pellet was mounted in an airtight container and reduced by passing H_2(g) through the cell for 30 minutes. N_2 was used to remove residual H_2 before the cell was placed on the beamline.

5.3 Results and Discussion

The characterisation data in this chapter were collected for the two Pt alloy nanoparticle powder samples and compared to equivalent data collected for the 5 nm Pt/C sample.

5.3.2.1 TEM

As before, TEM images were obtained for the catalyst powders and used to estimate the particle size distribution. Figure 1 shows a histogram of the PSDs of the three catalyst powders before incorporation into electrodes. The histogram shows that the average particle sizes of the catalysts are comparable, but different in terms of the range of diameters. The PtCo/C powder contains a larger proportion of smaller particles, with no or very few particles above 10 nm in diameter, unlike the other catalysts.

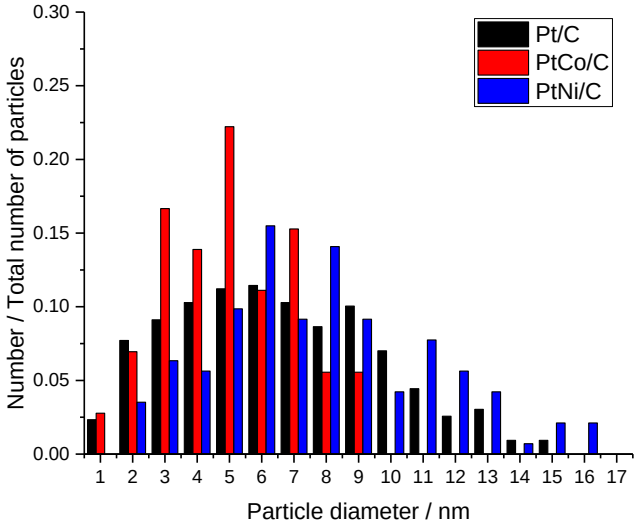

Figure 1 Comparison of the nanoparticle diameters of the Pt alloy catalysts compared to the standard Pt/C catalyst. 428, 72 and 142 particles were imaged at for the Pt/C, PtCo/C, and PtNi/C catalysts respectively, and the diameters were calculated based on the assumption that the nanoparticles were spherical. The number of particles at each diameter is expressed as a fraction of the total number of particles imaged.

TEM-EDX linescans across individual particles were also possible, and was done by monitoring the emission at the Pt L, and the Ni and Co K edges whilst bombarding the sample with high energy electrons. Ideally this analysis would be done for a number of particles within each sample to ensure that they are well represented, however only single particles were analysed due to time constraints. As these measurements were nearing the spatial resolution of the microscope and detectors, typically, nanoparticles towards the upper end of the size range were chosen. Measurement accuracy and precision were also limited by nanoparticles drifting, or becoming charged as a result of the electron beam, low x-ray photon counts and deliberate selection of isolated nanoparticles.

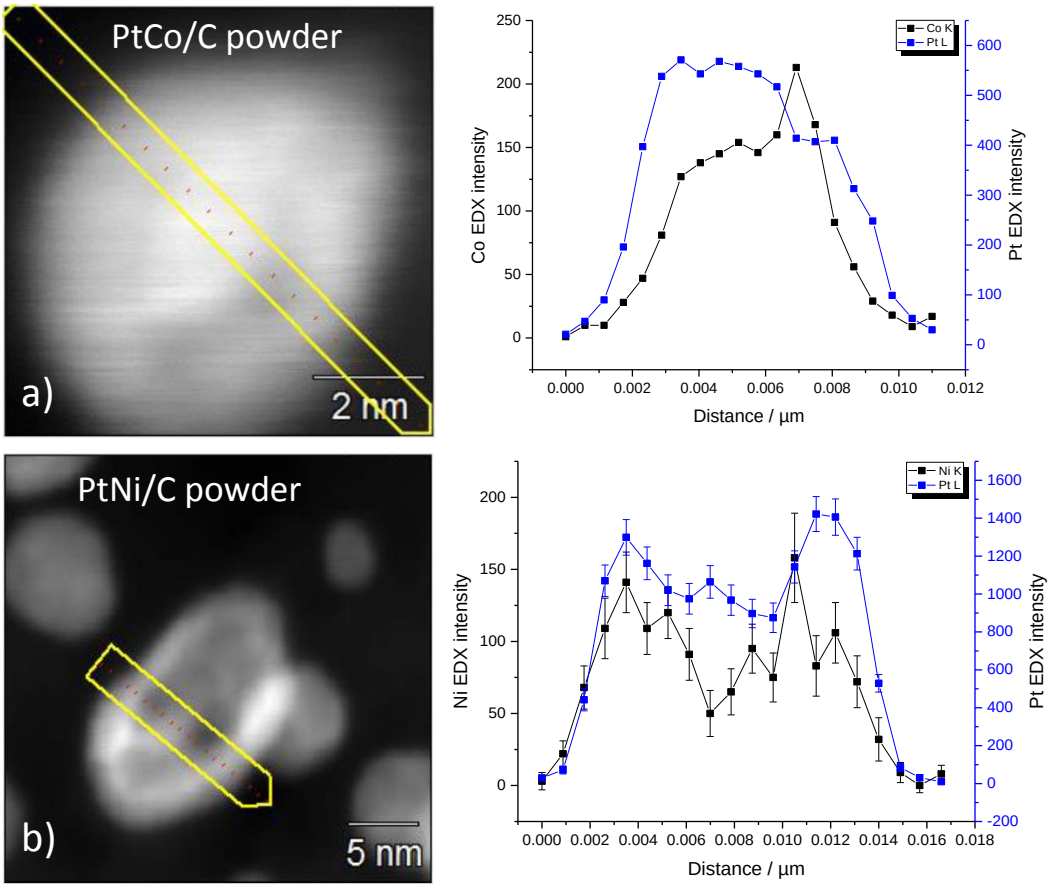

Figure 2 Dark field TEM images and corresponding EDX analysis of a) the PtCo/C and b) the PtNi/C nanoparticle.

Dark field TEM images along with EDX linescans across example nanoparticles in the PtCo/C and PtNi/C powders are shown in Figure 2. In the TEM images, variation in the contrast across the nanoparticle is observed. The contrast in dark field TEM images is roughly proportional to the average atomic number of species within each pixel due to the increased scattering of electrons from high atomic number atoms. As a result this can provide anecdotal evidence that there is less Pt in the core of the nanoparticles.

Figure 2a shows the EDX analysis of a PtCo/C nanoparticle and suggests that a core-shell type structure has formed as there is a 1 – 2 nm difference between the points on the linescan where Pt and Co are detected at both edges of the particle.

The image and EDX of the PtNi/C powder in Figure 2b shows a 'double hump' feature where there is a drop in emitted intensity for both the Pt and Ni edges. This could be indicative of the particles becoming hollow (seen previously[17]), porous[18] or changing shape in another way. Unlike with the PtCo/C, the EDX trace measured for the PtNi/C powder is not consistent with the desired core-shell structure. Qualitatively, the linescan also indicates a higher than expected Pt:Ni atomic ratio. From compositional analysis of the bulk PtNi/C powder, the expected ratio is 1.3 Pt atoms per Ni atom, whereas there as the observed intensity of the Pt emission is close to 10 times that of the Ni.

However, as these alloy catalysts have been acid-leached and annealed, it is possible that multiple structures exist, especially considering the range of particle sizes in the sample, which affects the leaching process.[19]

5.3.2.2 XPS

Figure 3a shows the survey XPS spectra collected for the 5 nm Pt/C, PtCo/C and PtNi/C catalyst powders. The main difference between the spectra are the small peaks that can be observed in Figure 3b at a binding energy of 785 eV and 855 eV, which are attributable to the Co2*p* and Ni2*p* transitions respectively.

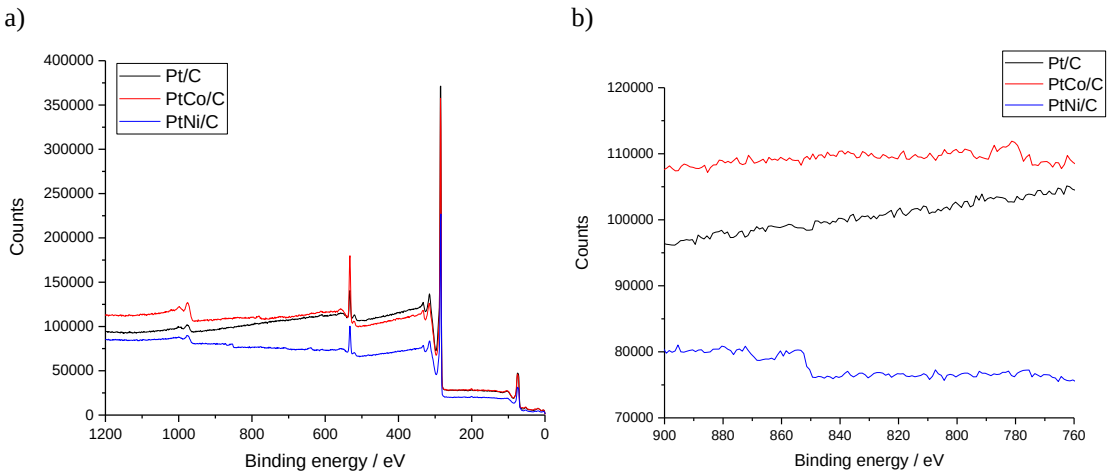

Figure 3 a) XPS survey spectra of the 5 nm Pt/c, PtCo/C and PtNi/C catalyst powders, and b) magnified view of the binding energy region corresponding to where the Co2*p* (785 eV) and Ni2*p* (855 eV) transitions occur.

Peak fitting and composition analysis on the PtCo/C sample for the Pt4*f* and Co2*p* peaks indicated a Pt/Co atomic ratio of 2.16, which is low compared to a ratio of 2.55 calculated

from the bulk composition of the catalyst powder. This would indicate that there is more Co near the surface of the Pt nanoparticles. The EXAFS data presented later corroborates this observation as the total Co coordination number is lower than for Pt, indicative of Co presence at or near the surface of the nanoparticles before contact with the electrolyte. The catalyst synthesis procedure is, however, designed to promote a Pt rich outer shell via annealing and acid leaching treatments. Annealing has been shown to result in a Pt rich surface with a base metal rich layer immediately underneath to maintain the overall stoichiometry,[20] whilst subsequent acid treatment selectively leaches the non-Pt metal out of the nanoparticles leaving the outermost layers Pt rich. Incomplete acid leaching could rationalise the observation of Co near the nanoparticle surface.

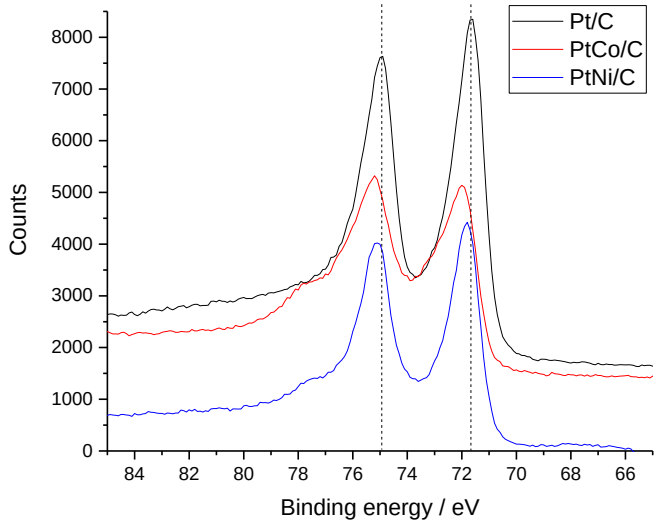

Figure 4 High resolution XPS spectra of Pt4*f* region measured for the catalyst powders. Features on the high binding energy side of the peaks can be observed for the alloy samples, which is indicative of oxidised Pt species. Small features can be observed at lower binding energies that may be assigned to the Co3*p* (59 eV) and Ni3*p* (66 eV) transitions respectively.

Figure 4 shows the Pt4f region of the XPS spectra collected for the catalyst powder samples. Features, at around 78 eV, can be observed for the alloy catalysts, which is indicative of the presence of Pt oxide species. This suggests that there are Pt atoms at the surface of the catalyst particles.

5.3.2.3 XRD

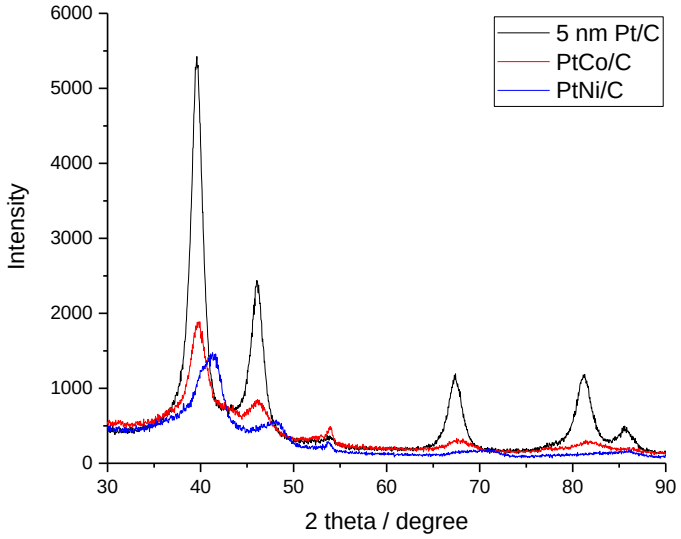

Figure 5 Grazing incidence (2°) XRD patterns for the 5 nm Pt/C, PtCo/C and PtNi/C catalyst powders. The peaks at lower 2θ values attributable to the carbon support material have not been included. The patterns can be indexed to a 3:4:8:11 ratio indicating fcc symmetry, and the general shift of the peaks in the alloy samples to more positive 2θ values indicates a decrease in the lattice parameter for these samples compared to the 5 nm Pt/C standard sample. 2 additional peaks (not shown) at 2θ angles of 18° and 26°, which are not present in the powder samples displayed previously, are attributed to the teflonated carbon paper used as the base of the electrode. The peaks are sharper than observed for the carbon support and are likely caused by graphitic carbon and PTFE from the Teflon treatment. The graphitic carbon peak was used to align the spectra.

Figure 5 shows the XRD spectra collected for the three catalyst coated electrodes at grazing incidence (2°). As observed in a previous chapter, there are two peaks at 2θ angles of 18° and 26° (not shown) caused by the Teflon and graphitic carbon respectively, both of which come from the teflonated carbon paper used as the base of the electrode. These peaks can be used as an internal standard to ensure that peak shifts in the spectra are real. The patterns can again be indexed to an fcc unit cell, however the alloys have much less distinct peaks than the Pt/C sample.

The PtNi/C shows a peak at a 2θ angle of about 42° with a shoulder on the low angle side. This implies that two phases are present, likely Pt rich and Ni rich respectively, although this cannot be clearly seen for any of the other smaller peaks. For the PtCo/C sample, no shoulders or additional features can be seen, although the smaller size of the peaks makes this harder to discern.

All peaks in the PtNi/C pattern are shifted to higher angles, which is expected since the lattice constant for a Pt unit cell will decrease upon addition of the smaller Ni atoms.

However a noticeable shift for the PtCo/C sample is not observed. The PtCo/C sample has a higher Pt content, relative to the base metal, than the PtNi/C – the Pt:M ratios are 2.5 and 1.3 respectively, which will reduce the magnitude of the shift.

Other factors that could explain the peak shift include the presence of faults and defects in the lattice or lattice strain resulting from the incorporation of the base metal into the Pt lattice and its concentration gradient throughout the nanoparticle. These factors are both possible in the system at hand due to the expected segregated and/or core-shell structure of the alloy catalysts. Regardless, the presence of a core-shell structure is unlikely to be detected by XRD without other supporting techniques. Instrumental effects have not been considered as they are expected to be small and will be manifested as a systematic error for all samples as the spectra have been aligned based on the internal standard.

5.3.2.4 XAS

For bimetallic systems, there are a limited number of possible atomic arrangements, which can be separated into 3 categories: a) 2 distinct phases, b) solid solution, random or ordered, and c) non-uniform distribution of elements across the nanoparticle volume. A simplified representation of these structures is given in Figure 6, taken from the paper by Pryadchenko *et al*.,[21] although a real catalyst sample is likely to consist of more than one of these structures due to the variety in particle sizes and composition. For the catalysts studied here, the post-synthesis treatment was designed to selectively produce nanoparticles with a non-uniform arrangement of Pt and the base metal. The metals were simultaneously reduced and attached to the high surface area carbon support forming nanoparticles with a specific ratio of metals governed by the concentration of precursors. An annealing step ensured that the two metals were alloyed, as well as favouring segregation of Pt to the nanoparticle surface with a larger base metal concentration underneath the first Pt monolayer to maintain stoichiometry.[20] The annealed catalyst was then subjected to an acid leaching step whereby the majority of the base metal at or near the nanoparticle surface would be dissolved to leave a Pt rich shell surrounding the alloy core. Any nanoparticles with an incomplete Pt shell would have the base component leached from most of the structure, leaving a pure Pt phase. The ideal structure is the one pictured in Figure 6f, with a core comprised of a non-Pt rich alloy.

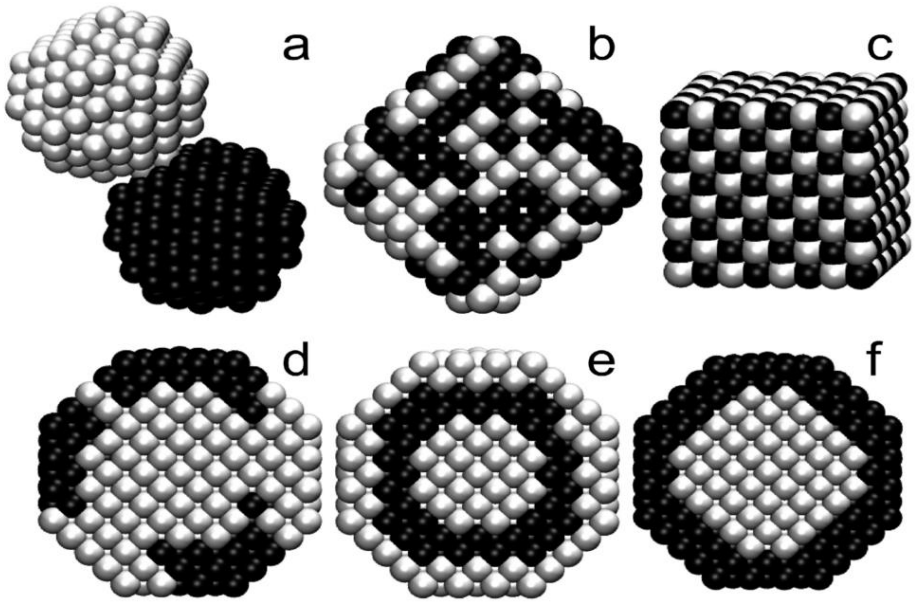

Figure 6 Possible structures that can be assumed in bimetallic particles. Figure reproduced from Pryadchenko *et al.*[21] a) separate phases, b) random solid solution, c) ordered intermetallic compound, d-f) examples of non-uniform distribution of elements within the nanoparticle volume.

In this work, the PtCo/C and PtNi/C samples were assumed to take the fcc structure similar to the monometallic Pt/C samples studied previously. This assumption is validated on the basis of XRD diffraction patterns, which show similar peak positions with the Pt/C patterns that were indexed to this structure. Additionally, alloys of fcc and hcp metals such as Co usually assume the fcc structure.[22] Therefore, the initial guess structure used to generate the scattering paths for the EXAFS fitting is based on that of Pt and modified arbitrarily such that the lattice parameter is 3.72 Å, *i.e.* halfway between that of Pt, 3.92 Å, and Ni, 3.52 Å, with Ni being comparable in size to Co. For these samples, XAS data at the Ni/Co K and the Pt L_3 edges was collected and analysed simultaneously. To fit the data, both monometallic and bimetallic paths were considered, as well as the possibility of oxygen neighbours.

The XAS spectra for the bimetallic catalysts are more difficult to fit than the monometallic samples due to the added disorder in the sample resulting from non-uniform nanoparticle composition, which is likely to vary throughout the range of particle sizes. Cowley's short range order parameter, C, has been shown to effectively characterise order and homogeneity of bimetallic nanoparticles in a quantitative manner,[10] and can be calculated using Equation 3.[23]

$$C = 1 - \frac{N_{AB}/N_{AM}}{f_B}$$

Equation 3

f_B is the molar concentration of element B, N_{AB} is the degeneracy of the A-B scattering path and N_{AM} is the total degeneracy of both the A-B and A-A scattering paths. The Cowley parameter can take values between -1 and +1, where -1 indicates a completely ordered homogeneous system, and +1 shows complete clustering of like atoms, as depicted in Figure 7a) and d) respectively. Thus, for core-shell nanoparticles positive values would be expected. The paper[10] also indicates that analysis of random alloys can also yield small positive values for the Cowley parameter of around 0.2 as an artefact caused by EXAFS being a bulk averaging technique, along with the errors associated with determining the coordination numbers.

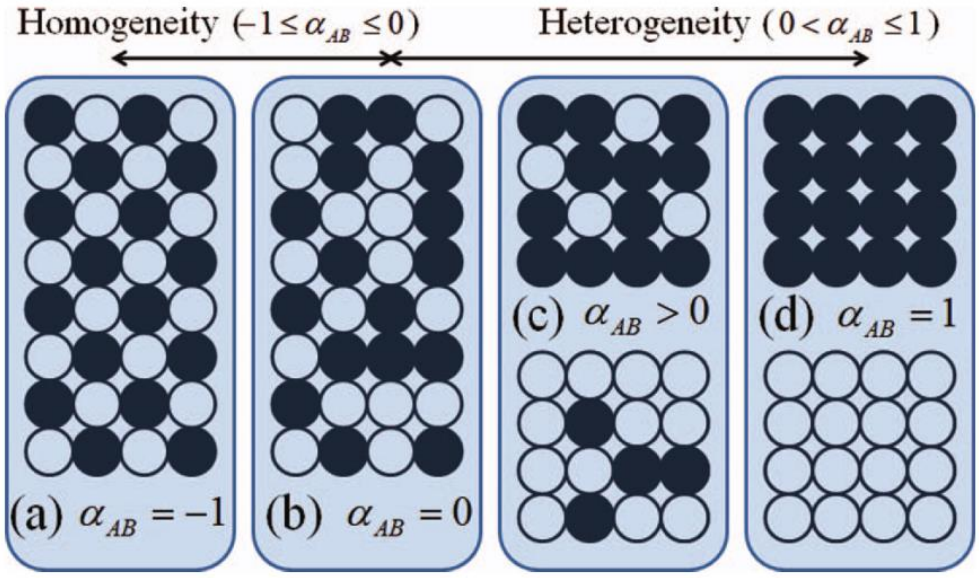

Figure 7 Illustration of cases of homogeneous and heterogeneous atomic packing in a 2D lattice with a 50:50 mix, reproduced from work by Frenkel *et al.*[10] a) and b) show the possible range of homogeneous packing, denoted by a negative value for the Cowley parameter, α, although in the present work, C will be used to avoid confusion. c) and d) show the heterogeneous case indicated by positive values, where clustering of like atoms occurs.

Use of the Cowley parameter has been expanded upon by Beale *et al.*[22] who propose the calculation of this parameter from the points of view of both metals in the alloy. This was postulated as an additional tool for characterisation. Although it is to be noted that there is a problem with the signs of the values calculated in the paper by Beale *et al.*[22] There is also

some confusion between the definition of ordering and clustering of atoms when compared to the explanations given by Frenkel *et al.*[10] The benefit of calculating the Cowley parameter from the point of view of both metals seems unclear unless working with highly ideal samples. All of the Cowley parameters in this work are calculated with Pt denoted as element A and the Co or Ni as element B.

Another measure of atomic distribution in bimetallic nanoparticles is through use of alloying parameters J_A and J_B as done by Hwang *et al.*[11] and is based on ratios of partial and total coordination numbers observed experimentally compared to those expected for a perfectly random alloy. Using the equations and information from this paper,[11] Equation 4 and Equation 5 can be derived for the general alloy $NiPt_x$, where J_A and J_B are the alloying parameters for Ni and Pt respectively, N is the partial or total coordination number and x is the Pt/Ni ratio:

$$J_A = \frac{N_{NiPt}(1+x)}{xN_{NiM}} \times 100$$

Equation 4

$$J_B = \frac{N_{PtNi}(1+x)}{N_{PtM}} \times 100$$

Equation 5

x can be determined experimentally from the EXAFS parameters using Equation 6, as has been done by other authors, *e.g.* Frenkel.[9]

$$x = \frac{N_{NiPt}}{N_{PtNi}} = \frac{f_{Pt}}{f_{Ni}}$$

Equation 6

The values calculated for J_A and J_B and comparison of the relative sizes of the homo- and heteroatomic partial coordination numbers can be used to assign the nanoparticle structure based on the categories shown in Figure 8.

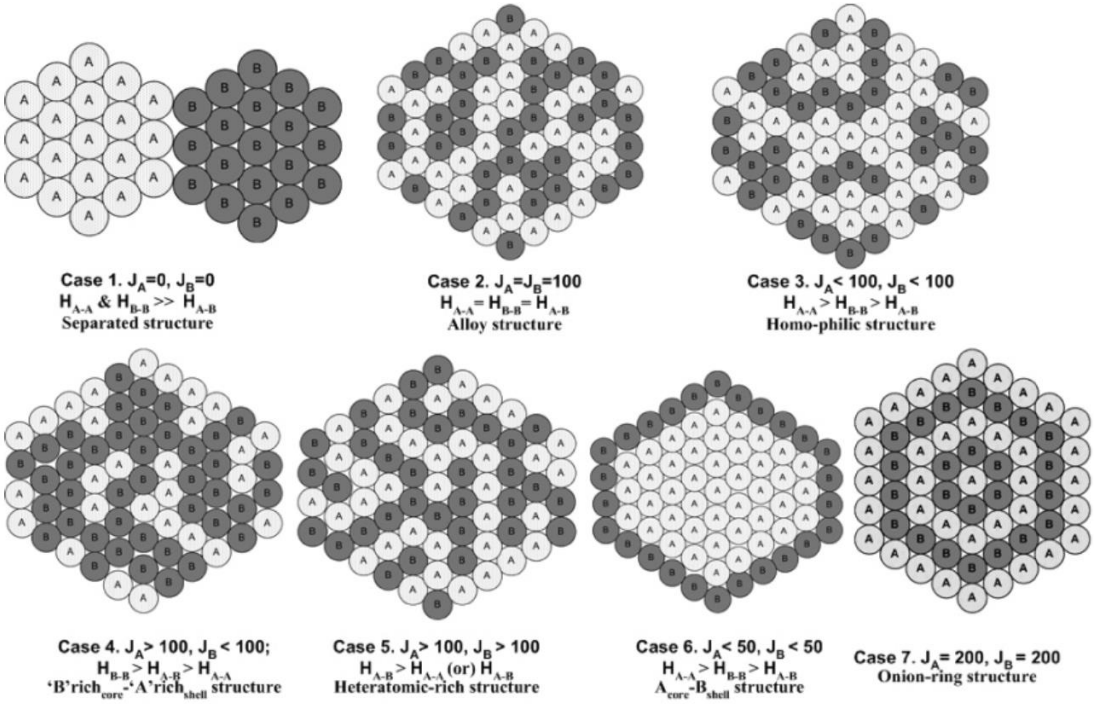

Figure 8 Diagram taken from the paper by Hwang *et al.*[11] indicating the parameters calculated for bimetallic nanoparticles at various degrees of alloying. H_{AA}, H_{BB}, and H_{AB} denote partial coordination numbers for homo- and heteroatomic interactions respectively.

Several of the fits involved metal-oxygen scattering paths, which indicates that the metal is present at the nanoparticle surface. Whilst the Cowley parameter and the alloying parameters J_A and J_B do not account for the presence of O neighbours specifically, they should have relatively little impact on the results. This is based on the fact that they are most likely to be species formed at the surface of the nanoparticles, and, as a result, do not prevent or compete with other metallic neighbours. Subsurface Pt oxide formation via place exchange is a possibility, however Baroody *et al.,*[24] who have thoroughly reviewed and modelled the Pt oxide formation and growth processes, suggest that potentials above 1.1 V *vs.* RHE and oxygen surface coverages of more than 50% are required. Additionally, it was noted that place exchange could occur at potentials as low as 0.75 V *vs.* RHE, but only in the presence of O_2.[25] In this work, the upper limit of the potential window is below 1.1 V *vs.* RHE, and O_2 was removed from the system.

These studies were typically based on polycrystalline or single crystal Pt, but the resulting model has been used to reproduce data from experiments on nanoparticles. Differences are to be expected for the Pt alloy nanoparticles in particular, but since these samples have generally been acid leached, the surface is expected to be Pt rich. Also, the electronic effect of the Ni/Co is to decrease the oxygen adsorption strength, so any differences to the model

should be minimal. Sub-surface oxygen would be anticipated to affect the observed interatomic distances, although due to the inherently high disorder in the systems under study, this may be infeasible to probe.

5.3.2.4.1 PtNi/C

Similar to with the Pt/C, the first step in the EXAFS fitting process was to break the correlation between the amplitude reduction factor, S_0^2, and N, the degeneracy. S_0^2 was calculated by fitting the spectra for a Ni foil, where the degeneracy values can be assumed to be the same as in bulk Ni metal. The value for S_0^2 determined from a 4-shell fit was 0.87, which will be used in each of the fits for the sample data, allowing the unknown degeneracy to be determined.

Figure 9 shows the first attempt at a simultaneous fit for both Pt L_3 and Ni K edges for the EXAFS spectra obtained for the PtNi/C pellet. The pellet was reduced under $H_{2(g)}$, and measured in inert (N_2) atmosphere to minimise O neighbours. The fits were calculated simultaneously and parameterised such that the Pt-Ni bond distances and disorder were the same from the point of view of both edges. The Ni-Pt degeneracy was constrained to be a fixed multiple, x, of the relevant Ni-Pt shell, where x was a fitted value representing the Pt:Ni atomic composition of the alloy, and, based on the fit, was calculated to be 1.4 ± 0.5. Similar constraints have been used previously when fitting bimetallic nanoparticles.[26,27] The expected value according to bulk analysis of the sample using ICP-MS was 1.3, which is consistent with the fitted value obtained here. The other values obtained in the fit are presented in Table 1.

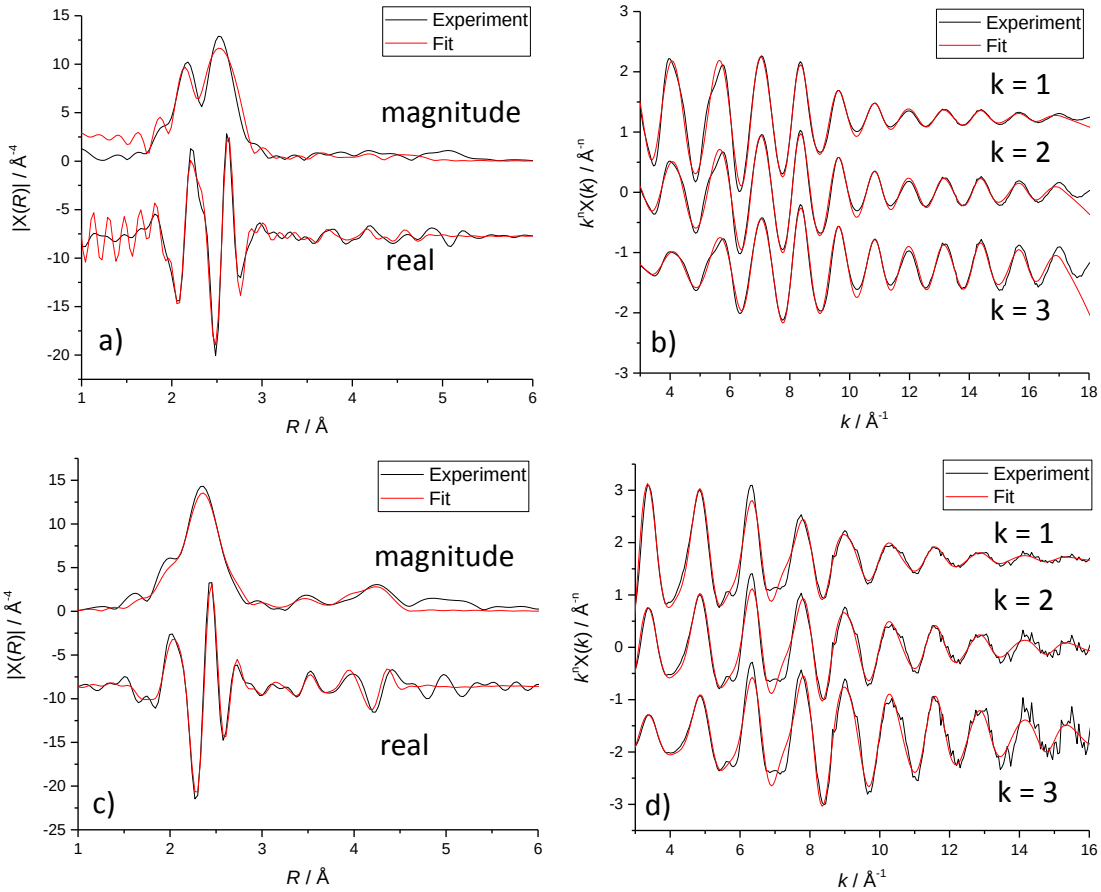

Figure 9 Simultaneous 3 shell EXAFS fit for the PtNi/C catalyst pellet. a) k^2 weighted Fourier transform, and b) k^n weighted data for the Pt L_3 edge c) k^2 weighted Fourier transform, and d) k^n weighted data for the Ni K edge. Plots are not phase corrected.

The deviations between the calculated and experimental *R*-space plots, along with some unusual values for degeneracy and disorder, indicate that there are problems with this model. The fit for the Pt edge data, shown in Figure 9a, does not work well at around 1 – 1.5 Å, and changing the lower limit of the fitting range has no effect, so this might be a problem with the background subtraction process. At high *R*-values, there appears to be little EXAFS present to analyse, unlike previously seen in Chapter 4 for the Pt/C catalysts, and is therefore attributed to the addition of Ni. The magnitude of the EXAFS oscillations is less than half of that seen for the 5 nm Pt/C samples, shown in Figure 10. The imposed restraints between the Pt-Ni and Ni-Pt degeneracies meant that the Ni edge data was also poorly fit at high R values, but EXAFS can still be observed.

Table 1 Values derived from the fits shown in Figure 9. The parameters for the Ni-Pt shells have been linked. *N* is x times the value for the Pt-Ni shell, where x is a fitted value representing the Pt:Ni atomic ratio, evaluated to be 1.4 ± 0.5. The values and errors for *R* and σ^2 are the same as the respective values for the Pt-Ni shells. ICP-MS analysis at JM established the Pt:Ni atomic ratio as 1.3. The r-factor for the fit was 0.036.

Shell	*N*	*R* / Å	σ^2 / Å^2	E_0 / eV
Pt_1-Pt_1	6.8 ± 0.5	2.700 ± 0.003	0.0069 ± 0.0003	6.25 ± 0.48
Pt_1-Pt_2	1.2 ± 1.9	3.819 ± 0.005	0.009 ± 0.009	
Pt_1-Pt_3	2.1 ± 2.3	4.672 ± 0.006	0.008 ± 0.005	
Pt_1-Ni_1	3.3 ± 0.5	2.608 ± 0.005	0.008 ± 0.001	
Pt_1-Ni_2	4.3 ± 7.6	3.689 ± 0.008	0.03 ± 0.03	
Pt_1-Ni_3	0.9 ± 1.4	4.517 ± 0.009	0.007 ± 0.01	
Ni_1-Ni_1	4.3 ± 2.1	2.60 ± 0.02	0.009 ± 0.005	7.1 ± 1.5
Ni_1-Ni_2	1.2 ± 4.6	3.68 ± 0.03	0.008 ± 0.03	
Ni_1-Ni_3	14 ± 23	4.51 ± 0.03	0.02 ± 0.02	
Ni_1-Pt_1	4.6	2.609	0.03	
Ni_1-Pt_2	5.9	3.670	0.007	
Ni_1-Pt_3	1.3	4.519	0.009	

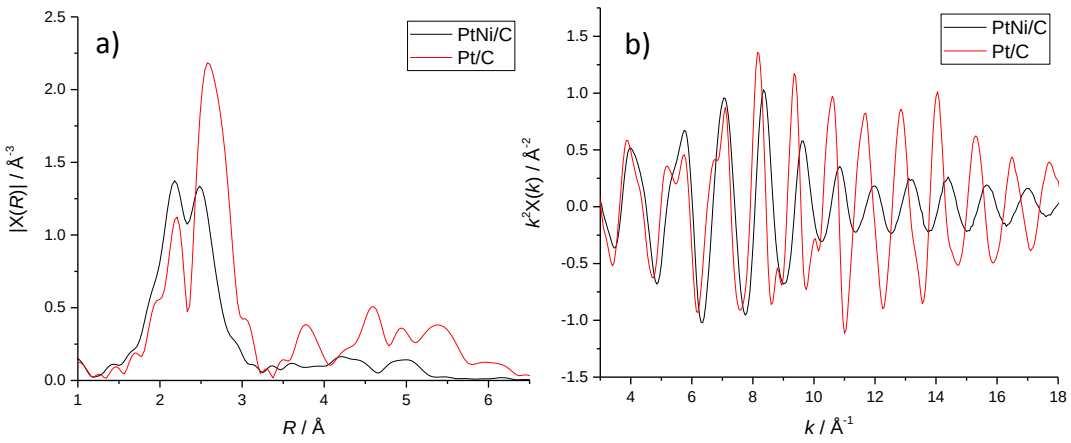

Figure 10 Pt L_3 edge EXAFS data for the PtNi/C and Pt/C pellet samples shown in a) *R*-space, (not phase corrected) and b) k^2 weighted *k*-space to illustrate the effect of adding a second metal to the nanoparticulate sample.

Figure 10 shows Pt L_3 edge EXAFS data for the monometallic and bimetallic nanoparticle samples. The presence of a second metal in the alloy sample results in splitting of the first shell peak (1.7 – 3.2 Å). This is because there are, in effect, two nearest neighbour distances, *i.e.* the Pt-Pt and Pt-Ni interactions, which cause the EXAFS to contain sine waves

of different periodicities, illustrated in Figure 11b. When the Fourier transform is taken, two peaks are observed, as shown in Figure 11a. The EXAFS of the alloy will be the sum of both of these contributions, leading to the observation of 'beats' in the *k*-space data, where the amplitude of the oscillations is small, leading to a split peak in *R*-space and suppression of signal at higher *R* values.

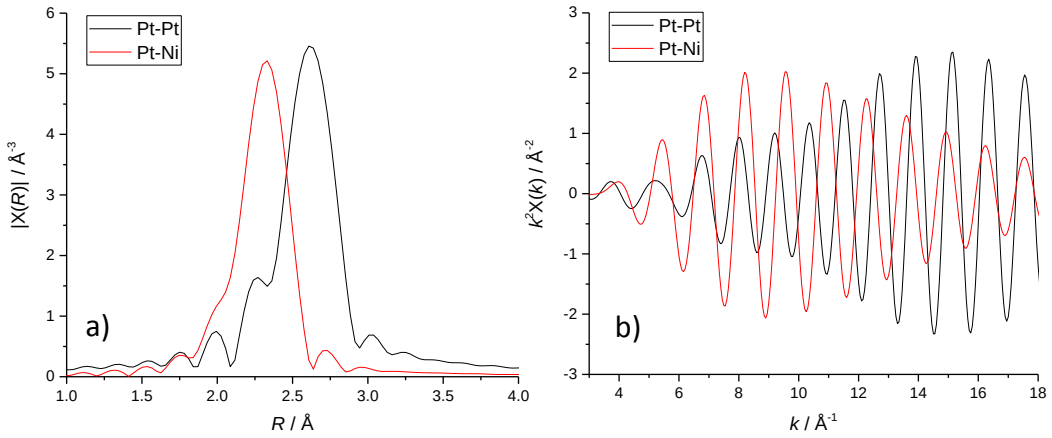

Figure 11 Simulated spectra for the Pt-Pt and Pt-Ni first shell scattering paths in a) *R* and b) *k*-space (k^2 weighted). Simulation based on bulk Pt lattice, and a bulk Ni lattice where a single Ni atom has been replaced with a Pt atom as the absorber.

As a result, fitting of the EXAFS data for the alloys was restricted to a first shell model only. Again, the Pt-Ni distances calculated from the Pt and Ni edge data were forced to be equal, as well as the associated disorder parameter. Two different fits for each sample were modelled, one where the ratio of Ni-Pt to Pt-Ni degeneracy was forced to be 1.3 based on the atomic composition, and the other where this constraint was removed. Both options resulted in acceptable fits and physically reasonable values, along with r-factors <0.02, and addition of O containing scattering paths did not improve the fits. Thus the 'no constraint' model was used in all further analyses thereby allowing independent determination of the atomic composition. The fit for the PtNi/C pellet is shown in Figure 12 and the associated values are shown in Table 2.

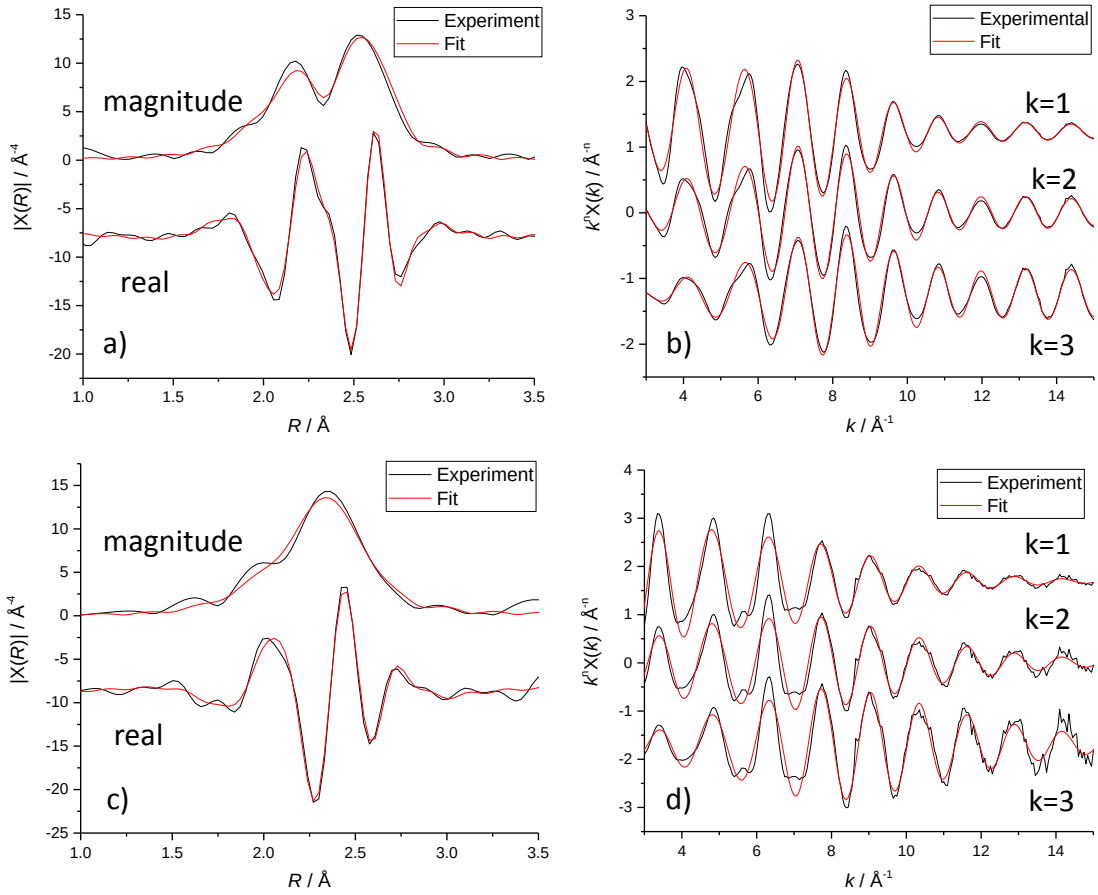

Figure 12 Simultaneous 1 shell EXAFS fit for the PtNi/C catalyst pellet. a) k^2 weighted Fourier transform, and b) k^n weighted data for the Pt L_3 edge, c) k^2 weighted Fourier transform, and d) k^n weighted data for the Ni K edge. No constraint was applied based on atomic composition, and no O neighbours were required in the fit. Plots are not phase corrected. R-factor was 0.0095.

Table 2 Values obtained from the fit to the EXAFS of the PtNi/C pellet, shown in Figure 12.

	N	***R* / Å**	**σ^2 / Å^2**	***E_0* / eV**	**R_f**
Pt-Pt	6.0 ± 0.5	2.699 ± 0.002	0.0065 ± 0.0003	6.0 ± 0.4	0.0095
Pt-Ni	3.7 ± 0.4	2.606 ± 0.004	0.0084 ± 0.0007		
Ni-Pt	4.3 ± 1.3	2.607 ± 0.004	0.0084 ± 0.0007	6.1 ± 1.4	
Ni-Ni	4.0 ± 1.4	2.59 ± 0.02	0.008 ± 0.003		

The values, presented Table 2, have then been used to calculate the Pt:Ni ratio, x, and both the Cowley parameter, C, and the alloying parameters, J_A and J_B. x was calculated to be 1.2, C was evaluated as 0.18, and J_A (Ni) and J_B (Pt) were calculated as 96 and 82 respectively, although the errors in the coordination numbers make these values relatively uncertain.

The Cowley parameter was found to be positive, which corresponds to a degree of clustering of like atoms within the alloy nanoparticles, although the magnitude is small, so any conclusions drawn should be treated with caution.

For this sample, both J_A and J_B are less than 100 indicating that these samples have a 'homophilic' structure indicated by Case 3 in Figure 8. The total coordination number for Ni is less than that of Pt, which indicates that there is Ni present at or near the surface of the nanoparticles. This is due to atoms near the core inherently having more neighbouring atoms than those at the surface.

The presence of Ni atoms at the surface of the nanoparticles is unexpected from the catalyst synthesis procedure, the final step of which involved aggressive chemical leaching in acid designed to remove the less noble component from the near surface region.

It is noted that bond distances are contracted relative to the value obtained for bulk Pt. EXAFS measures the mean bond distance of the sample and as a result the contraction is caused by both the incorporation of smaller Ni atoms into the close-packed Pt structure as well as the relaxation of atoms at the surface. The variation in bond distance manifests itself in the fit as a larger mean squared disorder (σ^2) value or a systematic error, as some of the assumptions behind the EXAFS fitting procedure break down. The anisotropic disorder in bond length can be addressed to some extent by utilising a distortion function.[28] Although this work largely revolves around estimation of errors introduced as a result of the bond length disorder, it may be possible to adapt this further to allow estimation of the strain present in the nanoparticle, but would likely require ideally homogeneous and well-characterised samples.

Several catalyst samples taken at intermediate points during the synthesis process were also analysed using XAS, and are denoted as samples A, B, and C. Sample A is taken after the initial reduction of the metal precursors onto the carbon support, B is a sample from after the annealing step, and C is the same acid leached catalyst as analysed previously. The expected structures based on the synthetic steps are illustrated in Figure 13. Initial arrangement of elements within the nanoparticles from a solution containing both metal precursors is random, and successive treatments lead to segregation and ordering of the individual components. Annealing promotes alloy formation, but also favours segregation to the surface of the species with the larger radius, although other factors like surface energy, and adsorbates can also affect this process.[29] This typically results in Pt segregation

to the surface and an oscillating elemental profile amongst the top few monolayers whilst the bulk stoichiometry is maintained over the whole nanoparticle.[30] Treatment with strong acid such as H_2SO_4 or HNO_3 at temperature results in dissolution of the base metal from the near surface region of the particle, leaving a thicker Pt rich shell.

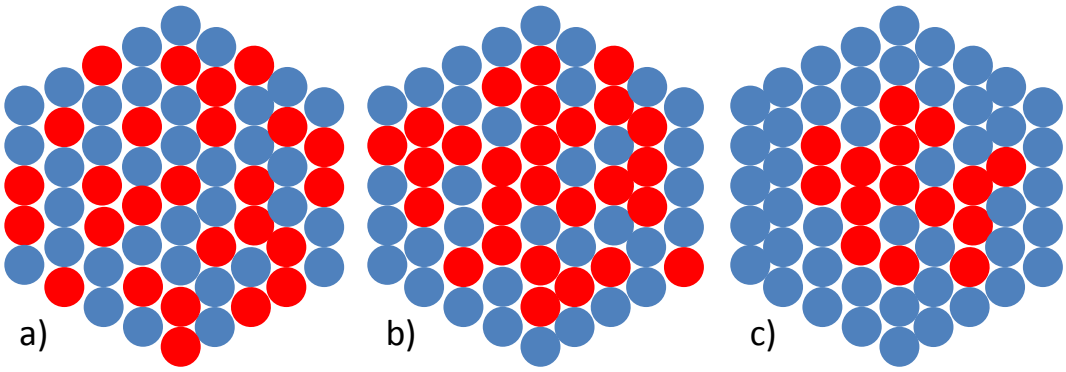

Figure 13 Proposed structures of nanoparticles that have been a) freshly deposited from solution simultaneously onto carbon support, b) annealed at temperature for an extended period of time, and c) chemically de-alloyed using strong acid. The steps lead to progressively more ordered and segregated particles. Porosity is also possible, particularly after acid leaching, but this has not been included in this diagram.

XANES data and corresponding *R*-space plots of the data collected for these samples are shown in Figure 14. The Pt edge data does not reveal many differences between the nanoparticle catalysts apart from a slightly larger signal just above 2 Å in *R*-space, probably due to Pt-Ni scattering paths. Larger differences can be observed in the Ni edge data, *e.g.* the XANES white line intensity, along with the large signal at 1.5 Å in *R*-space for sample B implies Ni oxidation.

As a result of these observations, the use of O scattering paths is justified when looking at the Ni EXAFS data. Although these paths will introduce further variables into the fit, they all have justifiable physical meanings. 15 variables are used in the typical fits, and the spectra contained 30 independent points (26 for sample B due to noise), as calculated from the Nyquist theorem explained in chapter 3.

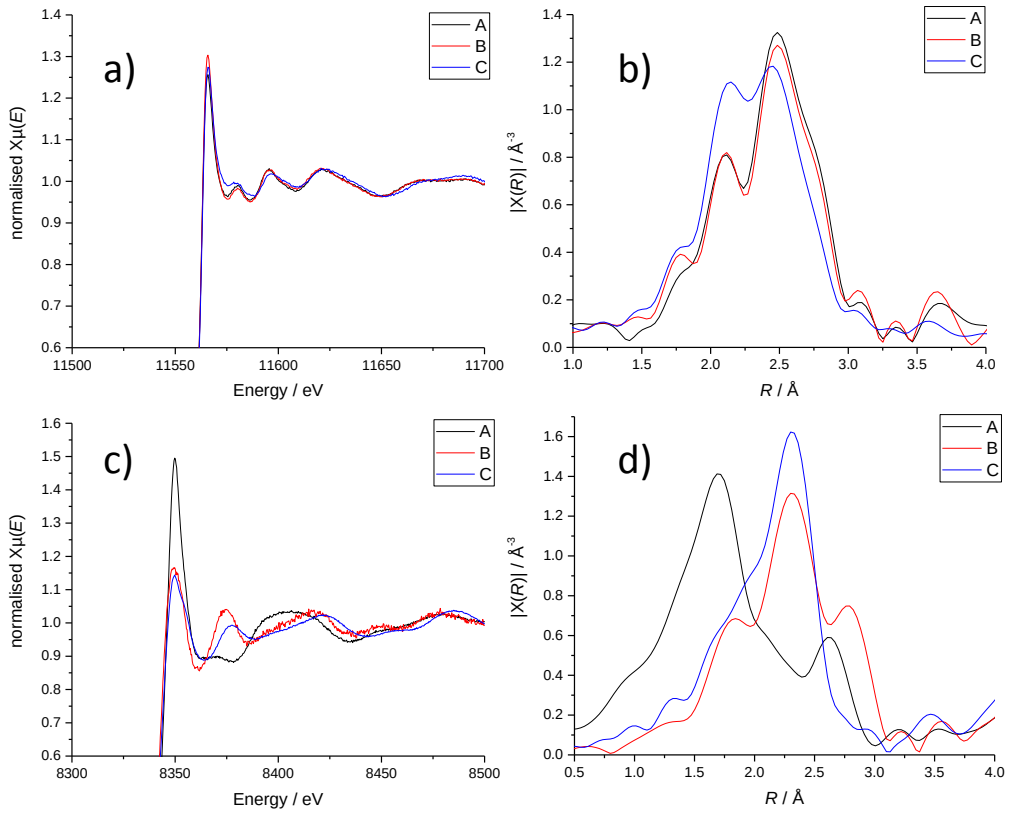

Figure 14 a) XANES and b) *R*-space data at the Pt L_3 edge, and c) XANES and d) *R*-space data at the Ni K edge for three different PtNi/C samples taken at various points during the synthesis process. A – the catalyst after reduction of metal precursors, B – catalyst after annealing and C – the finished, de-alloyed catalyst. Figures c) and d) show that Ni atoms are more oxidised in sample A compared to B and C, whilst the Pt environments are similar as shown by a) and b).

The fit for sample B is shown in Figure 15 as an example and a similar quality of fit was obtained for the other samples.

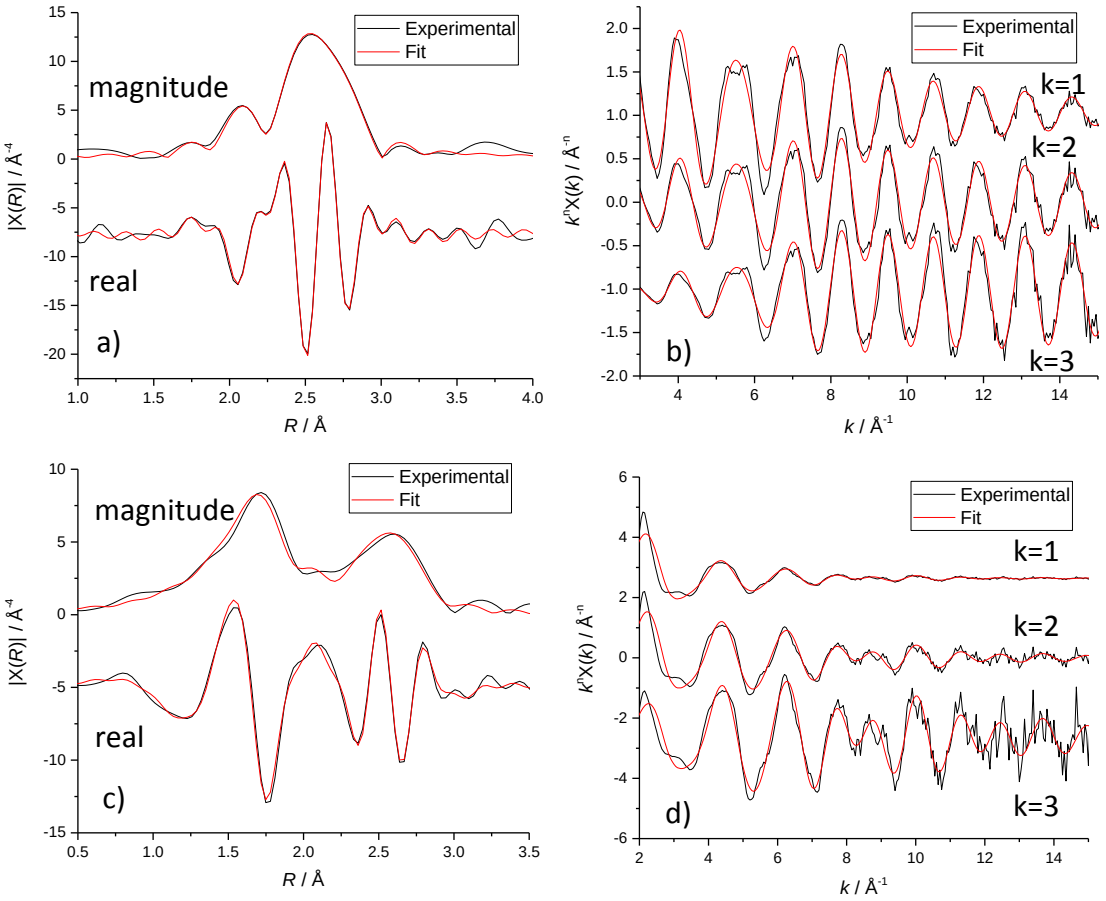

Figure 15 Simultaneous 1 shell EXAFS fit for the PtNi/C pellet sample B. a) k^2 weighted Fourier transform, and b) k^n weighted data for the Pt L_3 edge c) k^2 weighted Fourier transform, and d) k^n weighted data for the Ni K edge. No constraint was applied based on atomic composition. The Ni-O scattering path was included in the fit, with separate degeneracy, bond length and disorder parameters. Plots are not phase corrected. *R*-factor was 0.0069 with the Ni-O path and 0.0274 without.

From these fits, the partial coordination numbers were determined for each of the possible combination of atoms – Pt-Pt, Pt-Ni, Ni-Pt, Ni-Ni and Ni-O. Inclusion of Pt-O scattering paths was also tested, but did not improve the fits. These partial and total coordination numbers are displayed in Table 3.

Table 3 Coordination numbers derived from the EXAFS spectra for three different PtNi/C BN-based pellets. The PtNi/C samples are taken after important steps in the synthesis process. Despite reduction under 5% H_2/N_2 for 30 minutes, Ni-O scattering paths improved the fits universally – the improvement in the fits is reflected by the r-factor. The Pt:Ni ratio, x, the Cowley parameter, C, and the alloying parameters J_A and J_B have also been given. For the fits containing Ni-O scattering paths, denoted as A + O, B + O and C + O, the uncertainty in the coordination numbers is ±0.5 for N_{PtNi} and N_{NiPt}, and ±1 for N_{PtM} and NC_{oM}. When oxygen neighbours were not considered, the r-factors were larger, and the error in the coordination numbers was at least twice as large. The highlighted fit yielded non-physical values.

Sample	N_{PtNi}	N_{PtM}	N_{NiPt}	N_{NiM}	x	C	J_A (Ni)	J_B (Pt)	r-factor
A + O	1.4	9.0	4.0	4.5	2.8	0.39	121	61	0.007
A	-0.8	8.7	3.5	24.0	-4.3	0.69	11	31	0.064
B + O	1.8	8.7	8.8	9.8	4.8	-0.21	107	121	0.007
B	0.9	8.3	4.7	8.6	5.4	0.32	65	68	0.027
C + O	2.9	8.3	3.4	7. 5	1.2	0.25	84	75	0.005
C	1.8	8.1	1.3	5.7	0.7	0.62	54	38	0.042

During the catalyst synthesis procedure, the first sample to be taken was A followed by B and the final catalyst is C, where the procedure consists of initial reduction, annealing then acid leaching steps. Several overall trends in the various parameters can be observed. Firstly, the Pt-Pt bond distance decreases from the value in the bulk, whilst the Ni-Ni bond distances decrease towards the normal bulk value in the order A > B > C. N_{PtPt} decreases and both N_{NiNi} and N_{PtNi} increase in the same order. The values for N_{NiPt} and the total Ni-M coordination reach a maximum for sample B, but the total Pt coordination number decreases. Ni-O coordination decreases in the same order. These changes are consistent with the movement of Pt atoms towards the surface, with clustering of Ni atoms in the core, although evidence from other techniques would add strength to these conclusions. The necessity of Ni-O scattering paths suggests that exposed Ni atoms remain.

The N_{NiPt}:N_{PtNi} ratio, *i.e.* the Pt:Ni atomic composition initially increases, before decreasing as expected after the acid treatment. This initial increase cannot be rationalised by these conclusions, but may be caused by the oscillatory behaviour of the composition anticipated after the annealing step.

5.3.2.4.2 PtCo/C

As before, the first step was to fit the Co foil reference sample where the degeneracies of each of the scattering paths can be assumed to be the same as in a bulk sample thus

breaking the correlation with S_0^2. For Co, the value for S_0^2 was found to be 0.80 from a multi-shell fit out to 5.7 Å in *R*-space. The main difference with Co is that as a pure metal, it takes the hcp structure as opposed to the fcc structure like Ni or Pt. When fitting the foil, this meant that isotropic expansion of the lattice could not be assumed. Instead, the two parameters used to constrain the change in bond distance were based on the lattice parameters of the hcp unit cell, a and c. The interatomic distances and consequently the scattering path lengths can be expressed in terms of these values. When considering the PtCo/C alloy structure however, the structure can be considered as fcc.

Similar to with the PtNi/C samples, only a simple one shell fit of the PtCo/C pellet was attempted, however for this catalyst, an acceptable fit to the EXAFS data could not be found because the Co K edge data was very noisy due to the low concentration and small edge jump.

5.4 Conclusions

The TEM-EDX suggested that there was depletion of Co in the outermost ~0.5 – 1 nm of the nanoparticle. No depletion in Ni content of the surface region was measured for the PtNi nanoparticle; instead possible hollowing of the particle was observed. However, due to the fact that only a single nanoparticle was analysed, these conclusions may not be representative of the whole sample. Fast Fourier transforms of the TEM images of single nanoparticles showed no difference in the lattice spacing between core and shell regions of the particle, although the images were obtained close to the resolution limit of the equipment.

The XRD patterns obtained for the samples confirmed the assumption that both of the alloy catalysts had an fcc unit cell, which was useful for directing the EXAFS.

The results from the EXAFS analysis and XPS both suggest that the initial catalyst nanoparticles have residual base metal atoms at the surface rather than the expected core-shell structure. EXAFS data for catalyst samples taken after important steps in the synthesis was also analysed and rationalised. Structural information was generated from the EXAFS fits by comparing the ratios and relationships between the number of homometallic and heterometallic neighbours, as well as total coordination numbers, to theoretical models. The EXAFS technique struggled somewhat with the high disorder in the real-world catalyst systems, which arose based on the particle size distribution as well as the variation in particle composition.

Overall, this chapter has shown how the initial catalyst structure of the Pt alloy nanoparticles can be established using a combination of techniques. Similar methods will be used in the following chapter to characterise and analyse catalyst samples that have been subjected to the stability testing procedure. It would have been interesting and useful to investigate the two precursor PtNi/C catalysts using several of the techniques other than XAS to further elucidate their structure, potentially allowing for further optimisation of the synthesis process. If these methods were applied *in situ* on samples during the preparation of the de-alloyed catalysts, more homogeneous core-shell structures could result as the treatment could be continued until the desired outcome of a Pt-rich shell was achieved. Carrying out catalytic activity measurements for ORR on the three PtNi/C catalysts would also allow relationships between the surface structure, composition and activity to be established.

5.5 References

(1) Nørskov, J. K.; Rossmeisl, J.; Logadottir, A.; Lindqvist, L.; Kitchin, J. R.; Bligaard, T.; Jónsson, H. Origin of the Overpotential for Oxygen Reduction at a Fuel-Cell Cathode. *J. Phys. Chem. B* **2004**, *108*, 17886–17892.

(2) Stamenkovic, V.; Mun, B. S.; Mayrhofer, K. J. J.; Ross, P. N.; Markovic, N. M.; Rossmeisl, J.; Greeley, J.; Nørskov, J. K. Changing the Activity of Electrocatalysts for Oxygen Reduction by Tuning the Surface Electronic Structure. *Angew. Chemie Int. Ed.* **2006**, *45*, 2897–2901.

(3) Stamenkovic, V. R.; Mun, B. S.; Mayrhofer, K. J. J.; Ross, P. N.; Markovic, N. M. Effect of Surface Composition on Electronic Structure, Stability, and Electrocatalytic Properties of Pt-Transition Metal Alloys: Pt-Skin versus Pt-Skeleton Surfaces. *J. Am. Chem. Soc.* **2006**, *128*, 8813–8819.

(4) Ramírez-Caballero, G. E.; Ma, Y.; Callejas-Tovar, R.; Balbuena, P. B. Surface Segregation and Stability of Core–shell Alloy Catalysts for Oxygen Reduction in Acid Medium. *Phys. Chem. Chem. Phys.* **2010**, *12*, 2209.

(5) Strasser, P.; Koh, S.; Anniyev, T.; Greeley, J.; More, K.; Yu, C.; Liu, Z.; Kaya, S.; Nordlund, D.; Ogasawara, H.; Toney, M. F.; Nilsson, A. Lattice-Strain Control of the Activity in Dealloyed Core–shell Fuel Cell Catalysts. *Nat. Chem.* **2010**, *2*, 454–460.

(6) Wang, X.; Orikasa, Y.; Takesue, Y.; Inoue, H.; Nakamura, M.; Minato, T.; Hoshi, N.;

Uchimoto, Y. Quantitating the Lattice Strain Dependence of Monolayer Pt Shell Activity toward Oxygen Reduction. *J. Am. Chem. Soc.* **2013**, *135*, 5938–5941.

(7) Stamenkovic, V. R.; Mun, B. S.; Arenz, M.; Mayrhofer, K. J. J.; Lucas, C. A.; Wang, G.; Ross, P. N.; Markovic, N. M. Trends in Electrocatalysis on Extended and Nanoscale Pt-Bimetallic Alloy Surfaces. *Nat. Mater.* **2007**, *6*, 241–247.

(8) Hammer, B.; Nørskov, J. K. Electronic Factors Determining the Reactivity of Metal Surfaces. *Surf. Sci.* **1995**, *343*, 211–220.

(9) Frenkel, A. Solving the 3D Structure of Metal Nanoparticles. *Zeitschrift für Krist. - Cryst. Mater.* **2007**, *222*, 605–611.

(10) Frenkel, A. I.; Wang, Q.; Sanchez, S. I.; Small, M. W.; Nuzzo, R. G. Short Range Order in Bimetallic Nanoalloys: An Extended X-Ray Absorption Fine Structure Study. *J. Chem. Phys.* **2013**, *138*, 64202-1-64202–64207.

(11) Hwang, B. J.; Sarma, L. S.; Chen, J. M.; Chen, C. H.; Shin, S. C.; Wang, Q. R.; Liu, D. G.; Lee, J. F.; Tang, M. T. Structural Models and Atomic Distribution of Bimetallic Nanoparticles as Investigated by X-Ray Absorption Spectroscopy. *J. Am. Chem. Soc.* **2005**, *127*, 11140–11145.

(12) Jia, Q.; Li, J.; Caldwell, K.; Ramaker, D. E.; Ziegelbauer, J. M.; Kukreja, R. S.; Kongkanand, A.; Mukerjee, S. Circumventing Metal Dissolution Induced Degradation of Pt-Alloy Catalysts in Proton Exchange Membrane Fuel Cells: Revealing the Asymmetric Volcano Nature of Redox Catalysis. *ACS Catal.* **2016**, *6*, 928–938.

(13) Stassi, A.; Gatto, I.; Monforte, G.; Baglio, V.; Passalacqua, E.; Antonucci, V.; Aricò, A. S. The Effect of Thermal Treatment on Structure and Surface Composition of PtCo Electro-Catalysts for Application in PEMFCs Operating under Automotive Conditions. *J. Power Sources* **2012**, *208*, 35–45.

(14) Jayasayee, K.; Veen, J. A. R. Van; Manivasagam, T. G.; Celebi, S.; Hensen, E. J. M.; de Bruijn, F. A. Oxygen Reduction Reaction (ORR) Activity and Durability of Carbon Supported PtM (Co, Ni, Cu) Alloys: Influence of Particle Size and Non-Noble Metals. *Appl. Catal. B Environ.* **2012**, *111–112*, 515–526.

(15) Frenkel, A. I. Applications of Extended X-Ray Absorption Fine-Structure Spectroscopy to Studies of Bimetallic Nanoparticle Catalysts. *Chem. Soc. Rev.* **2012**,

41, 8163–8178.

(16) Bandyopadhyay, P.; Segre, C. U. Mucal on the web http://www.csrri.iit.edu/mucal.html (accessed Jul 31, 2017).

(17) Dubau, L.; Durst, J.; Maillard, F.; Guétaz, L.; Chatenet, M.; André, J.; Rossinot, E. Further Insights into the Durability of Pt_3Co/C Electrocatalysts: Formation of "hollow" Pt Nanoparticles Induced by the Kirkendall Effect. *Electrochim. Acta* **2011**, *56*, 10658–10667.

(18) Chen, S.; Ferreira, P. J.; Sheng, W.; Yabuuchi, N.; Allard, L. F.; Shao-Horn, Y. Enhanced Activity for Oxygen Reduction Reaction on "Pt_3Co" Nanoparticles: Direct Evidence of Percolated and Sandwich-Segregation Structures. *J. Am. Chem. Soc.* **2008**, *130*, 13818–13819.

(19) Oezaslan, M.; Heggen, M.; Strasser, P. Size-Dependent Morphology of Dealloyed Bimetallic Catalysts: Linking the Nano to the Macro Scale. *J. Am. Chem. Soc.* **2012**, *134*, 514–524.

(20) Stamenkovic, V. R.; Fowler, B.; Mun, B. S.; Wang, G.; Ross, P. N.; Lucas, C. A.; Markovic, N. M. Improved Oxygen Reduction Activity on Pt_3Ni (111) via Increased Surface Site Availability. *Science* **2007**, *315*, 493–497.

(21) Pryadchenko, V. V.; Srabionyan, V. V.; Mikheykina, E. B.; Avakyan, L. A.; Murzin, V. Y.; Zubavichus, Y. V.; Zizak, I.; Guterman, V. E.; Bugaev, L. A. Atomic Structure of Bimetallic Nanoparticles in PtAg/C Catalysts: Determination of Components Distribution in the Range from Disordered Alloys To "Core-Shell" structures. *J. Phys. Chem. C* **2015**, *119*, 3217–3227.

(22) Beale, A. M.; Weckhuysen, B. M. EXAFS as a Tool to Interrogate the Size and Shape of Mono and Bimetallic Catalyst Nanoparticles. *Phys. Chem. Chem. Phys.* **2010**, *12*, 5562.

(23) Cowley, J. M. An Approximate Theory of Order in Alloys. *Phys. Rev.* **1950**, *77*, 669–675.

(24) Baroody, H. A.; Jerkiewicz, G.; Eikerling, M. H. Modelling Oxide Formation and Growth on Platinum. *J. Chem. Phys.* **2017**, *146*, 144102-1-144102–144111.

(25) Kongkanand, A.; Ziegelbauer, J. M. Surface Platinum Electrooxidation in the

Presence of Oxygen. *J. Phys. Chem. C* **2012**, *116*, 3684–3693.

(26) Nashner, M. S.; Frenkel, A. I.; Somerville, D.; Hills, C. W.; Shapley, J. R.; Nuzzo, R. G. Core Shell Inversion during Nucleation and Growth of Bimetallic Pt/Ru Nanoparticles. *J. Am. Chem. Soc.* **1998**, *120*, 8093–8101.

(27) Frenkel, A. I. Applications of Extended X-Ray Absorption Fine-Structure Spectroscopy to Studies of Bimetallic Nanoparticle Catalysts. *Chem. Soc. Rev.* **2012**, *41*, 8163–8178.

(28) Yevick, A.; Frenkel, A. I. Effects of Surface Disorder on EXAFS Modeling of Metallic Clusters. *Phys. Rev. B - Condens. Matter Mater. Phys.* **2010**, *81*, 1–7.

(29) Cui, C.; Ahmadi, M.; Behafarid, F.; Gan, L.; Neumann, M.; Heggen, M.; Cuenya, B. R.; Strasser, P. Shape-Selected Bimetallic Nanoparticle Electrocatalysts: Evolution of Their Atomic-Scale Structure, Chemical Composition, and Electrochemical Reactivity under Various Chemical Environments. *Faraday Discuss.* **2013**, *162*, 91–112.

(30) Gauthier, Y.; Baudoing-Savois, R.; Bugnard, J. M.; Hebenstreit, W.; Schmid, M.; Varga, P. Segregation and Chemical Ordering in the Surface Layers of $Pt_{25}Co_{75}$ (111): A LEED/STM Study. *Surf. Sci.* **2000**, *466*, 155–166.

Chapter 6: Degradation of PtCo/C and PtNi/C

6.1 Introduction

A vital remaining challenge for supported Pt nanoparticle catalysts is their durability in the harsh fuel cell conditions, particularly in the highly oxidising environment present at the cathode. As a result, catalysts are subjected to an accelerated stress test (AST) in an attempt to mimic the stresses experienced during operation over a short period of time and determine whether the performance of the catalyst can be maintained over a reasonable lifetime. The US Department of Energy has covered this topic extensively, with much of the information summarised by authors such as Kocha[1] and Garsany[2], including standard protocols for performing ASTs for thin film catalyst layers in RDE experiments.

The DOE recommended AST protocol for the RDE consists of 30000 cycles between 0.6 and 1.0 V *vs.* RHE at 50 mV s^{-1}, at 25 ^{o}C in 0.5 M H_2SO_4 or 0.57 M $HClO_4$, with the ECSA and ORR activity measured after 10, 100, 1000, 3000, 10000, 20000, and 30000 cycles. In this work, the DOE protocol was modified to reduce the length of the experiments by increasing the harshness of the conditions used. Here, the protocol used involved 1000 cycles over the same potential window and at the same scan rate, carried out in 1 M $HClO_4$ at 80 ^{o}C, and the work aimed to establish the effect of this altered procedure on the catalysts. Various other protocols have been used in previously published studies, employing temperatures ranging from 25 – 75 ^{o}C, typically in 0.1 M $HClO_4$, and employing both potential holds and cycling treatments.[3,4,5,6] Sheng *et al.*[7] in particular, have used a similar procedure *i.e.* 1200 scans of 0.6 – 1.0 V *vs.* RHE at 20 mV s^{-1} in N_2 saturated 0.5 M $H2SO_4$ at 80 ^{o}C. Pt is expected to be stable under this potential regime,[8,9] however the 3rd row transition metal is not and will gradually leach out from the catalyst particles, *e.g.* Rudi *et al.*[10] used 200 cycles 0.06-1.0 V *vs.* RHE at 500 mV s^{-1} in N_2 saturated 0.1 M $HClO_4$ to dealloy PtNi/C samples. Antolini *et al.*[11] also showed that the most significant dissolution of Co, Ni and Fe from the respective Pt alloy occurred within the first 500 cycles or 2-3 hours after immersion in electrolyte.

The ensemble of literature, including the references above, has highlighted several degradation mechanisms for the Pt/C catalyst family, primarily Pt dissolution and carbon

corrosion, which are closely linked to, or cause, Otswald ripening, particle agglomeration and detachment. The main degradation pathway varies wildly depending on the exact catalyst preparation and experimental procedure, particularly whether high temperature treatment was employed, as well as metal loading, nanoparticle size, temperature and potential cycling protocol.

When studying Pt-based catalysts, the ECSA is a key parameter for measuring the activity and performance of the material. The ECSA is commonly measured using either the charge required for specific adsorption of under potential deposited H monolayer and/or its subsequent desorption, or the charge required to oxidise an adsorbed CO monolayer, although other surface probes can be used. The charge is then converted to an area based on established conversion factors for 1 and 2 e^- processes on Pt, 210 and 420 μC cm^{-2} respectively. Discussion commonly arises about the suitability and reliability of the methods, particularly when nanostructured and nanosegregated Pt-alloys are to be studied.

The key considerations for the H_{upd} method revolve around the reduction in coverage observed on Pt alloys due to the electronic effect of the non-Pt element on the adsorption properties of the surface. Other discrepancies can arise due to selection of the potential window used for integration, the charge to area conversion factor, and other experimental variables including electrolyte.[12]

When using CO adsorption, common concerns include whether monolayer coverage is achieved, and bonding configuration of the CO molecule, which both affect the charge-area conversion factor, along with probable restructuring or surface annealing of the catalyst. This has been evidenced for both Pt[12] and PtNi/C electrodes,[13] where it was also shown that the order of ECSA determination and other potential treatments had a significant impact on the obtained values. In this chapter, the H_{upd} method is favoured, primarily due to the likelihood of surface reconstruction when using CO.[14]

This chapter will look at the effect of the AST on the de-alloyed PtNi/C and PtCo/C catalysts using TEM/EDX, XPS and XAS as characterisation techniques. These catalysts have a similar particle size and have been subjected to a similar heat treatment to the 5 nm Pt/C catalyst analysed previously, which will be used for comparison purposes. The analysis presented in chapter 5 has shown that the initial structure is partially core-shell like for the Co, although there are still Co atoms present at or near the nanoparticle surface. The PtNi/C was shown

to have a segregated structure, with atoms of the same element tending to cluster together, but could not be classed as core-shell nanoparticles.

The growth of oxide species on the catalyst surfaces will also be examined as various studies have indicated that OH_{ads} and other intermediate oxygen-containing species act as poisons on the catalysts.[15,16] Fitting EXAFS data of Pt alloy nanoparticles is also undertaken.

6.2 Experimental

Samples and experiments were carried out as described in chapters 4 and 5 replacing the Pt/C catalysts with PtNi/C and PtCo/C, however additional samples were prepared for *in situ* XAS analysis. More details of the atomic composition and de-alloying treatments are given in the experimental chapter.

The accelerated stability testing procedure was carried out, as before, on PtNi/C and PtCo/C coated electrodes, at a Pt loading of 0.2 mg cm^{-2}, with numerous cycles of 0.6 – 1.0 V *vs.* RHE at 50 mVs^{-1}. Additional sets of electrodes for both catalysts were subjected to the same number of cycles, but using limits of 0.6 – 0.9 V *vs.* RHE and 0.6 – 1.1 V *vs.* RHE and at the higher Pt loading of 0.5 mg cm^{-2} to allow for *in situ* XAS measurements. These procedures should be respectively less and more severe than the previous procedure.

The amount of oxide formed on polycrystalline Pt RDE and the Pt/C, PtCo/C and PtNi/C thin film modified GC RDE was measured using the following procedure. The addition of the catalyst layer, and the conditioning procedures were carried out as described previously for the activity measurements. The ECSA was determined and then the 'oxide growth' procedure was performed, which consisted of a linear sweep from 0.05 V up to the anodic limit for the experiment (0.8, 0.9, 1.0, 1.1, or 1.2 V *vs.* RHE) at 20 mV s^{-1}, followed by a potential hold for 15 minutes at the anodic limit and then a linear sweep down to 0.05 V *vs.* RHE at 20 mV s^{-1}. 3 CVs were then obtained to re-measure the ECSA. All measurements were done in N_2 purged 0.1 M $HClO_4$. O_2 purging during the potential hold was found to have no impact on the amount of oxide formed, similar to experiments carried out by others.[17] The RDE was rotated at 1600 RPM during the potential hold to prevent any effects due to local concentration changes.

6.3 Results and Discussion

6.3.1 Thin film Electrodes

Thin films of the catalyst sample were freshly deposited on the polished GC RDE tip before each measurement.

6.3.1.1 Ink Characterisation

As before, the particle size distribution of the catalyst inks themselves was characterised in order to provide an estimate of the catalyst layer thickness. There is a significant difference between the 2 catalysts. It can be seen from Figure 1 and Figure 2 that the PtCo/C ink contains a larger proportion of particles of around 0.1 µm in diameter as compared to the PtNi/C catalyst ink that contains a large amount of 10 µm particles. This is likely to result in a thicker PtNi/C catalyst layer, which may also be less uniform. There also seems to be less agglomeration occurring than with the Pt/C catalyst, particularly compared to the PtCo/C sample. A summary of the particle sizes is shown in Table 1. The diffusion layer thickness when using the RDE at 1600 RPM is about 15 µm, which is close to the measured particle size of both the Pt/C and PtNi/C catalysts and three times that of the PtCo/C catalyst. This should have a negligible impact on the established RDE theory provided that the films are relatively even. If the roughness of the catalyst layer is similar in scale to the diffusion layer thickness, the theory will break, and experimentally, turbulence and additional currents will be observed.

Table 1 Descriptive values for the liquid phase particle size distribution of the 3 catalysts. A D(0.1) value of 0.097 indicates that 10% of the particles have a diameter less than or equal to 0.097 µm. Likewise, for D(0.5) and D(0.9) values, 50 and 90% of the particles, respectively, are at or below the indicated diameter.

Catalyst	D(0.1) / µm	D(0.5) / µm	D(0.9) / µm
Pt/C	0.097	3.66	11.41
PtCo/C	0.078	0.95	4.72
PtNi/C	0.174	6.43	14.21

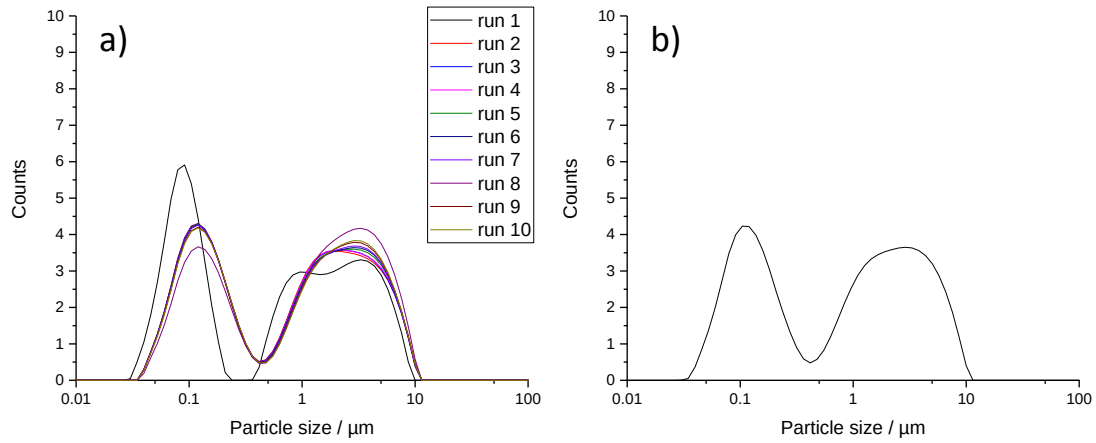

Figure 1 Liquid phase particle sixe distribution of the PtCo/C ink measured using laser light reflectivity, a) the 10 consecutive measurements, b) the average distribution. The measurements were taken whilst stirring the catalyst ink in dispersant at 800 RPM.

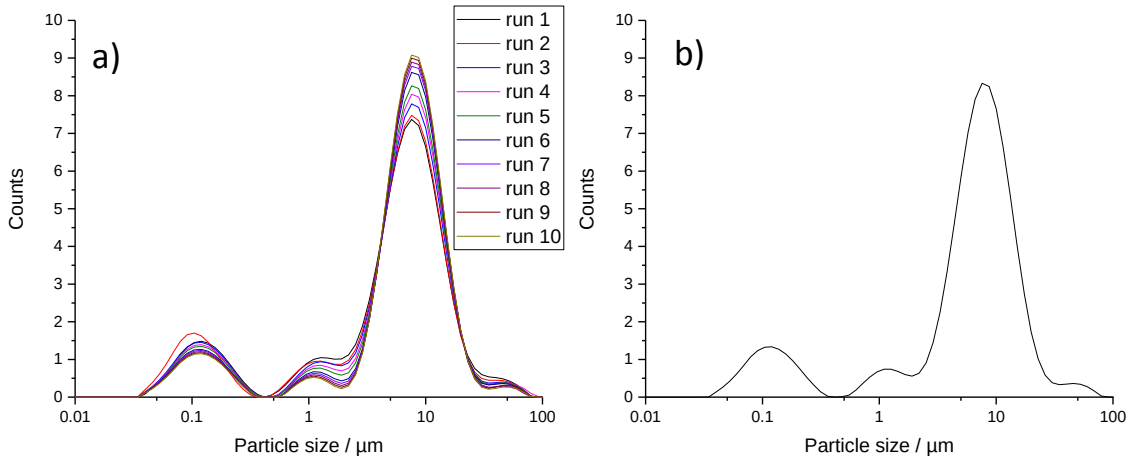

Figure 2 Liquid phase particle size distribution of the PtNi/C ink measured using laser light reflectivity, a) the 10 consecutive measurements, and b) the average distribution. The measurements were taken whilst stirring the catalyst ink in dispersant at 800 RPM.

6.3.1.2 Film Characterisation

The PtCo/C thin film, shown in Figure 3a is the most uniform of the 3 catalysts used, with a relatively consistent film covering the majority of the electrode surface, although some gaps through to the GC surface are still evident. The film reaches to an average of 121.7 µm from the electrode edge, equating to 90.5% of the total electrode surface. The uniformity of this film is likely linked to the significantly smaller particles making up the ink. As shown in Table 1, the PtCo/C ink had significantly lower D(0.1), D(0.5) and D(0.9) values than either of the other catalysts.

The PtNi/C thin film, Figure 3b, looks similar to the Pt/C film shown previously, with larger clumps of catalyst powder at the centre of the electrode surrounded by a region where the ink has dried, but left little catalyst material. It may have been possible to alleviate the non-uniformity of the films by either applying a larger amount of the ink as 1 or more drops or by investigating alternate drying methods that encourage more consistent layers, such as drying in an ethanol or IPA rich environment.[18] Additional sonication or other methods of homogenising the ink may also have helped disperse and break up the larger catalyst particles further. The coverage is estimated to be 50%. The contrast in Figure 3b is affected by the light reflecting off the uncovered GC surface.

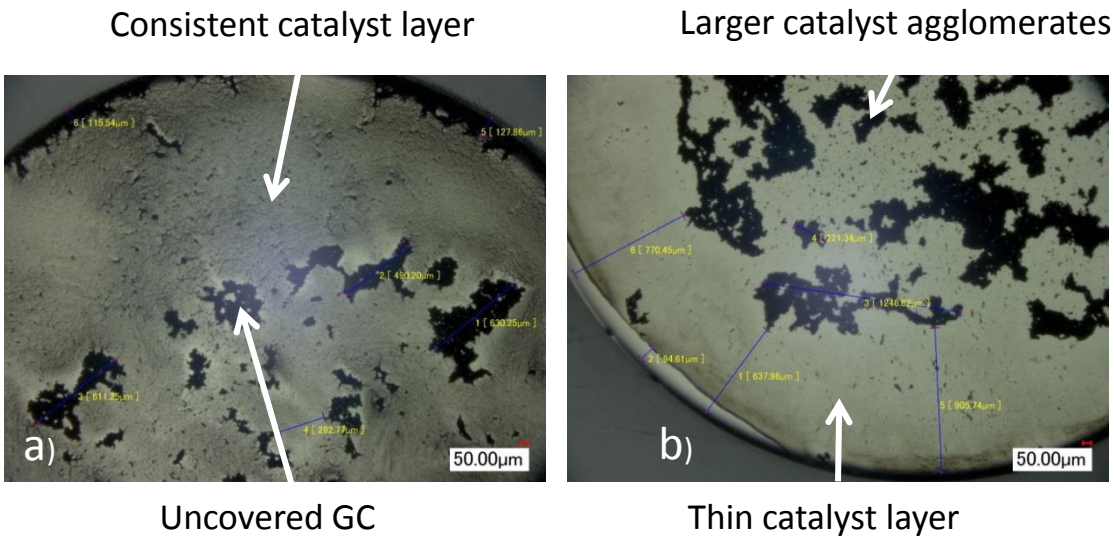

Figure 3 Optical microscope images taken of a) PtCo/C and b) PtNi/C thin films on a GC RDE.

6.3.1.3 Activity

As with the Pt/C catalyst, the activity of the PtCo/C and PtNi/C catalysts was measured using the RDE method, and the resulting potential sweeps are displayed in Figure 4. The measurements for the PtCo/C films are reproducible, more so than either of the other catalysts, whereas the measurements for the PtNi/C films are much less so, and take a different shape to the PtCo/C due to the poorer film quality. This result fits well with the optical microscope images displayed earlier in Figure 3, the PtNi/C film is patchy with significant gaps in the layer, whilst the PtCo/C film is more uniform and covers electrode surface.

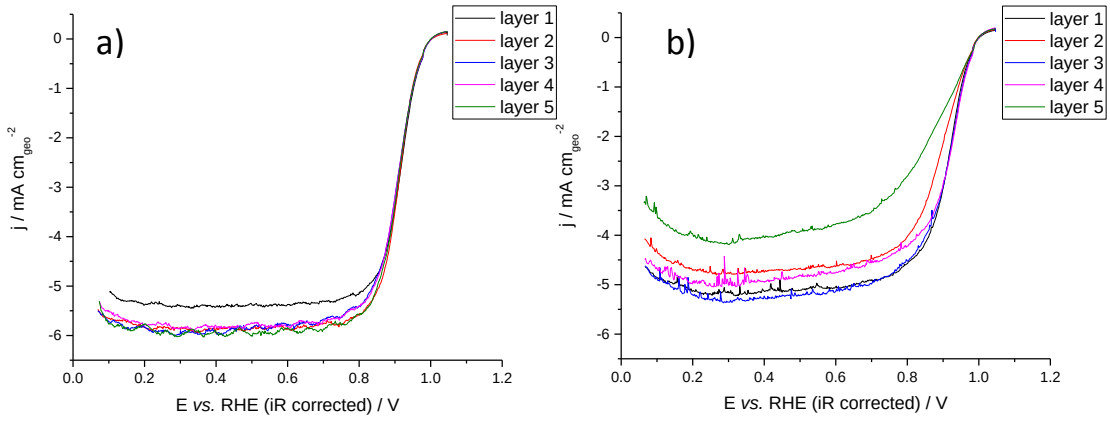

Figure 4 Positive going potential sweeps in O_2 purged 0.1 M $HClO_4$ at 20 mV s^{-1} recorded at 1600 RPM for a) PtCo/C and b) PtNi/C coated GC RDEs. Each measurement was conducted 5 times on a freshly polished and cleaned GC RDE tip. The resistance, determined by the high frequency x-intercept of a Nyquist plot, was accounted for and a background CV in N_2 purged electrolyte was collected and subtracted from the raw data to produce these plots.

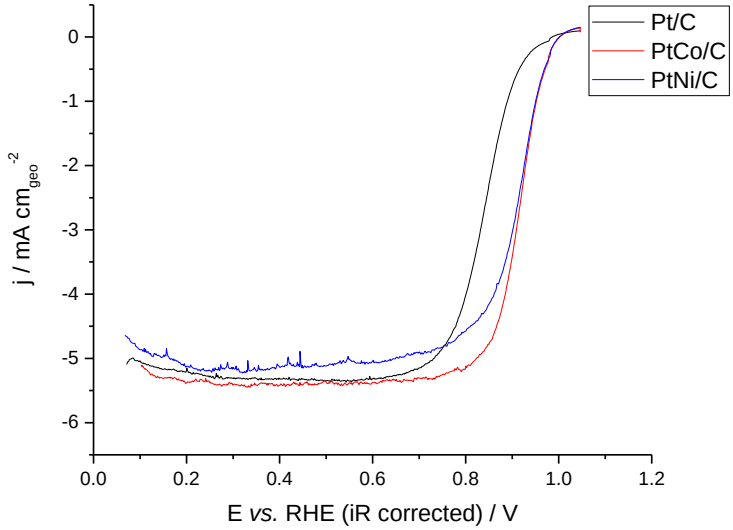

Figure 5 Comparison of the positive going potential sweeps obtaining when measuring the activity for the ORR using thin film coated GC RDE in O_2 purged 0.1 M $HClO_4$ at 20 mV s^{-1}.

Figure 5 shows a comparison of the potential sweeps obtained for each of the 3 catalysts, and it is clear from the onset potential that both of the alloy catalysts show a significant improvement over Pt/C. The magnitude of the mass transport limited current agrees with the theoretical value calculated based on the assumption that 4 electrons are transferred. This was calculated using the Levich equation, shown in Equation 1, with values for the diffusion coefficient of O_2 in 0.1 M $HClO_4$, the kinematic viscosity, and the concentration of O_2 taken from the paper by Wang *et al.*[19]

$$I_L = 0.62nFAD^{2/3}\omega^{1/2}\nu^{-1/6}C$$

Equation 1

Table 2 Mass transport limited currents of the potential sweeps for the catalyst coated GC RDEs and the polycrystalline Pt RDE compared to the theoretical value calculate using the Levich equation. The limited current was taken at 0.5 V *vs.* RHE at a rotation rate of 1600 RPM, which was converted to 167.6 rad s^{-1}. The number of electrons transferred was taken as 4. n is the apparent number of electrons transferred calculated from the average of the limiting currents measured in the experiments.

Experiment number	Pt/C / mA	PtCo/C / mA	PtNi/C / mA	Poly-Pt RDE / mA
1	-1.05	-1.05	-1.00	-1.08
2	-1.14	-1.15	-0.92	-1.16
3	-0.95	-1.14	-1.02	-1.17
4	-0.98	-1.13	-0.94	-1.18
5	-1.12	-1.18	-0.77*	-1.16
6	-	-	-	-1.16
7	-	-	-	-1.16
average	-1.05	-1.13	-0.97	-1.15
theoretical	-1.18	-1.18	-1.18	-1.18
n	3.55	3.85	3.3	3.9

* Outlier excluded from average.

Table 2 shows the mass transport limited currents taken at 0.5 V vs. RHE for each of the RDE values in comparison with the theoretically value calculated using the Levich equation. Of the 3 catalysts, the PtCo/C comes closest to the theoretical value followed by the Pt/C, then the PtNi/C. As seen from the optical microscope images and the liquid phase PSD measurements, the PtCo/C produced the best films with even coverage. Some production of hydrogen peroxide is expected,[20] leading to an apparent electron transfer of less than 4.

Table 3 details the ECSA, specific and mass activity measured for the PtCo/C and PtNi/C catalysts. Both catalysts have improved activity over the standard Pt/C sample, with the PtCo/C having the much higher activity than PtNi/C, which may in part be down to the lower PtNi/C film quality. The values determined here follow the same trend as in previously published work,[20] bearing in mind that the experiments reported in this paper were carried out at higher temperature and on slightly different catalysts.

Table 3 ECSA, specific and mass activities for the PtCo/C and PtNi/C catlaysts at 25°C. The ECSA was caluculated from the H_{upd} region of the CV in N_2 purged 0.1 M $HClO_4$ at 20 mV s^{-1} using the mass of Pt determined by XRF measurements. The specific and mass activities were calculated from the positive going, background subtracted, iR corrected sweep from 0.1 – 1.05 V vs. RHE in O_2 saturated 0.1 M $HClO_4$ at 20 mV s^{-1}, based on the current at 0.9 V and 0.5 V, the ECSA and the mass of catalyst used. For reference the average ECSA, specific and mass activity for the 5 nm Pt/C catalyst were 45.7 ± 7.0 m^2 g_{Pt}^{-1}, 299 ± 16 µA cm^{-2}, and 137 ± 24 A g_{Pt}^{-1} respectively.

RDE type	ECSA / m^2 g_{Pt}^{-1}	Specific activity / µA cm^{-2}	Mass activity / A g_{Pt}^{-1}
PtCo/C (layer 1)	37.5	2807	1054
PtCo/C (layer 2)	33.5	2832	949
PtCo/C (layer 3)	41.6	2027	844
PtCo/C (layer 4)	32.6	2548	832
PtCo/C (layer 5)	28.7	3027	869
PtCo/C average	34.8 ± 4.4	2648 ± 346	909 ± 83
PtNi/C (layer 1)	55.1	2063	1136
PtNi/C (layer 2)	53.3	918	409
PtNi/C (layer 3)	56.9	1511	859
PtNi/C (layer 4)	58.3	1480	862
PtNi/C (layer 5)*	41.8*	482*	202*
PtNi/C average	53.1 ± 5.9	1291 ± 543	709 ± 327
PtNi/C average*	55.9 ± 1.9	1493 ± 405	836 ± 230

* Outlier excluded from average.

ORR activity was also measured periodically throughout the accelerated stability test, although these results proved to be unreliable as several problems were encountered. The measurements were performed at the same temperature as the AST, *i.e.* 80 °C, with the cycling procedure and ECSA measurement carried out in N_2 purged 1 M $HClO_4$, and the ORR activity measured in O_2 purged 0.1 M $HClO_4$. This affected both the ECSAs measured by the H_{upd} method due to changes in surface coverage, as well as the activity by decreasing the amount of dissolved O_2. A key problem was the introduction of thermal convection, most noticeable when attempting to measure the ECSA due to the low scan rate (20 mV s^{-1}), which resulted in a slow periodic oscillation in current throughout the potential window. Build-up of contamination on the electrode surface over the course of the experiment, despite rigorous cleaning, was also a slight issue. The contamination was likely compounded by the frequent exposure of the electrode to the atmosphere when

transferring from one solution to the other. A flow cell type experiment designed to facilitate changing between solutions may have been more appropriate for these measurements.

6.3.1.4 Oxide Growth

The presence of oxygenated species on the catalyst surface may act as a poison and inhibit the ORR as well as provide a driving force for the segregation of the base metal to the surface.[21,22] Whilst the catalysts under study here have been de-alloyed via acid treatment to form core-shell structures during the synthesis process, the base metal still constitutes roughly 30% of the atoms present in the nanoparticles.

Experiments were performed on thin film catalyst layers on a GC RDE, and on a polycrystalline Pt RDE for comparison, where the potential was held at various anodic limits for 15 minutes in N_2 purged 0.1 M $HClO_4$ whilst rotating at 1600 RPM. Saturating the solution with O_2 was found to have no impact on the charge required to reduce the oxide layer.

Figure 6 depicts the potential sweeps showing the reduction of the oxide layers. No oxide is produced on any of the catalysts during the potential hold at 0.8 V *vs.* RHE, with successively more at each of the higher anodic limits, which cover the typical operating window of a H_2-O_2 fuel cell. The peak shape for the Pt/C catalyst is notably different from the others, with a tail reaching to about 0.4 V *vs.* RHE. This is attributed to the broader particle size distribution (see Figure 1 in Chapter 5), since the binding energy for O will increase on smaller particles due to the increase in the number of under coordinated Pt atoms,[23] although it is noted that other factors, such as the exposed crystal facets and interparticle difference, may also have an important effect.

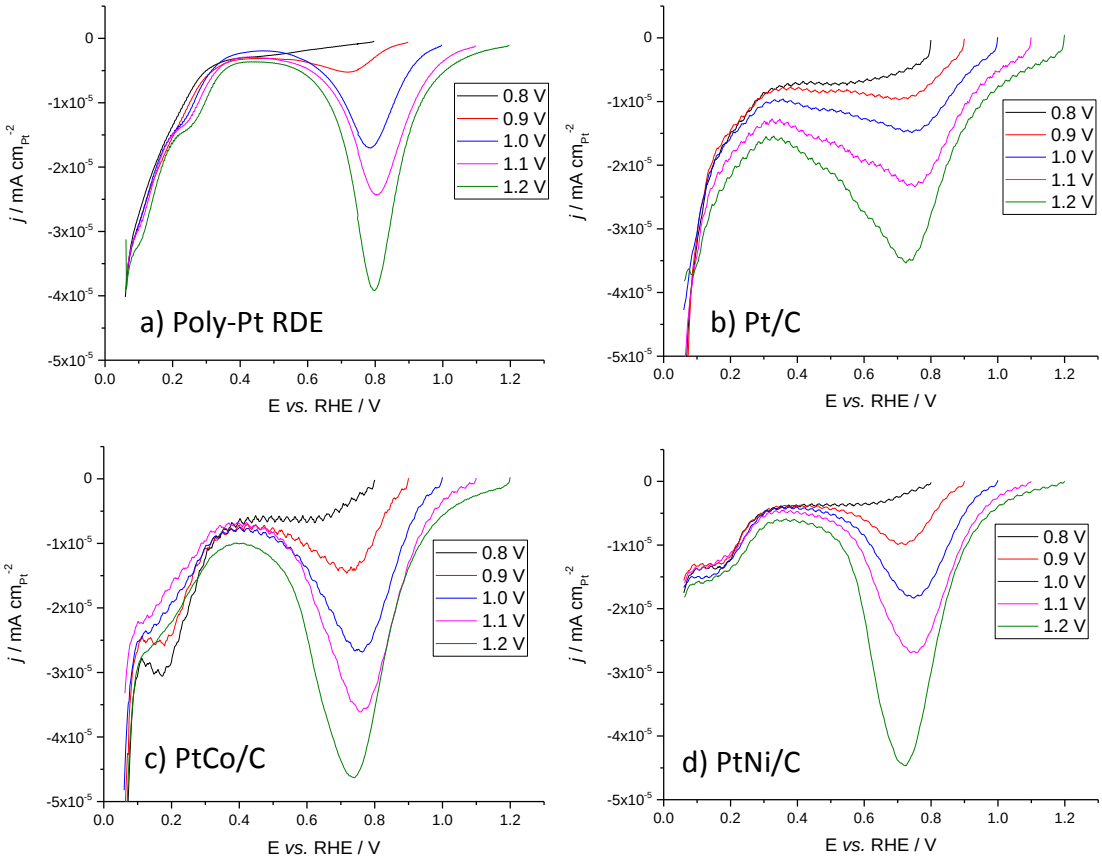

Figure 6 Linear sweeps at 20 mV s^{-1} in N_2 purged 0.1 M $HClO_4$ at 25 °C showing the reduction of an oxide layer grown on a) a Pt RDE, b) Pt/C c) PtCo/C and d) PtNi/C modified GC RDE. The ECSAs of the electrodes were determined (after conditioning scans), the potential was held at the indicated anodic limit for 15 minutes, and then the potential sweeps shown here were recorded.

The integrals of the reduction peaks are plotted against the anodic limit used in Figure 7. The charge has been normalised by the ECSA of the catalyst layer and thus is proportional to the number of oxidised Pt atoms. The polycrystalline Pt and Pt/C measurements indicates that whilst particle size has an effect on the shape of the reduction wave, there is a very similar amount of oxide produced, once the surface area has been accounted for, which suggests that the electronic structure is broadly comparable. Theoretical calculations on Au[24] have shown that the finite size effects observed in nanoparticles diminish and tend towards bulk-like properties for particles larger than around 3 nm, which is in keeping with the results here.

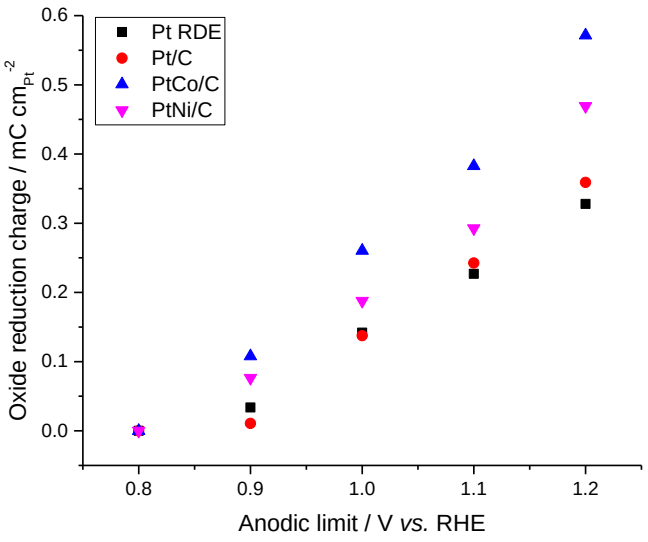

Figure 7 Charge required to reduce the oxide produced during the potential at the anodic limit. The charge has been normalised by the ECSA of the electrode determined by H_{upd}, and is representative of the number of oxidised Pt atoms.

Both of the alloy catalysts formed more oxide than either of the Pt samples, which is unexpected based on the rationale behind the use of alloys *i.e.* the effect of the 3*d* metals on the electronic structure of the Pt alloy surface. The *d*-electron structure will be studied using *in situ* XAS measurements at the Pt L_2 and L_3 edges later. The electronic structure of the alloys is designed to weaken the O binding strength by increasing the occupancy of the antibonding orbitals,[25] despite the fact that as pure metals both Co and Ni adsorb O more strongly.[26] By a similar mechanism – filling of the antibonding orbitals – the H binding strength on the catalyst surfaces will also be affected. As a result, the observed difference could be linked with underestimation of the catalyst ECSA when using H_{upd} as the surface probe. Use of CO monolayer oxidation as a way of determining the ECSA would have provided an additional comparison less susceptible to the electronic effect of alloying Pt with other metals, but this method has other problems as discussed, such as causing reconstruction of the Pt surface. Presence of the base metal at the nanoparticle surface is not anticipated due to the conditioning treatment in the highly oxidising and acidic environment.

6.3.2 Catalyst Coated Button Electrodes

These electrodes are all consist of carbon paper discs loaded with a known amount of Nafion coated PtNi/C or PtCo/C catalyst samples. These electrodes were hot pressed and flooded with purified water (18 MΩ cm) before use.

6.3.2.1 TEM

Figure 8 depicts the PSDs for the PtCo/C catalyst powder compared to the as-prepared and aged electrode samples. There is little change in the PSD over the course of the stability testing. There might be some increase in the number of particles with a diameter of 10 nm or more, although analysing a larger number of particles would add more confidence as for some of the histograms, fewer than 100 particles were counted. The RDE measurements, however, also showed that the ECSA of the catalyst layer was unaffected by the cycling treatment.

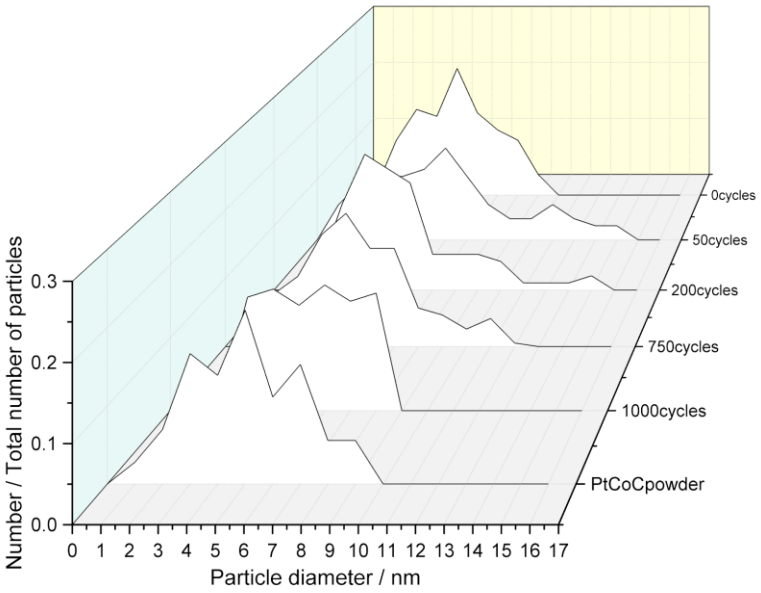

Figure 8 PSD of the PtCo/C powder compared to catalyst samples scraped off of the aged catalyst coated carbon paper electrodes. Number of particles counted: 72 for 'PtCo/C', 180 for '1000 cycles', 195 for '750 cycles', 90 for '200 cycles', 86 for '50 cycles', and 168 for '0 cycles.' The number of particles at each diameter is expressed as a fraction of the total number of particles imaged.

The PtNi/C samples look to be following a similar trend *i.e.* insignificant differences between aged samples, although several data points are missing as they were damaged or altered during other analytical techniques. This data is shown in Figure 9.

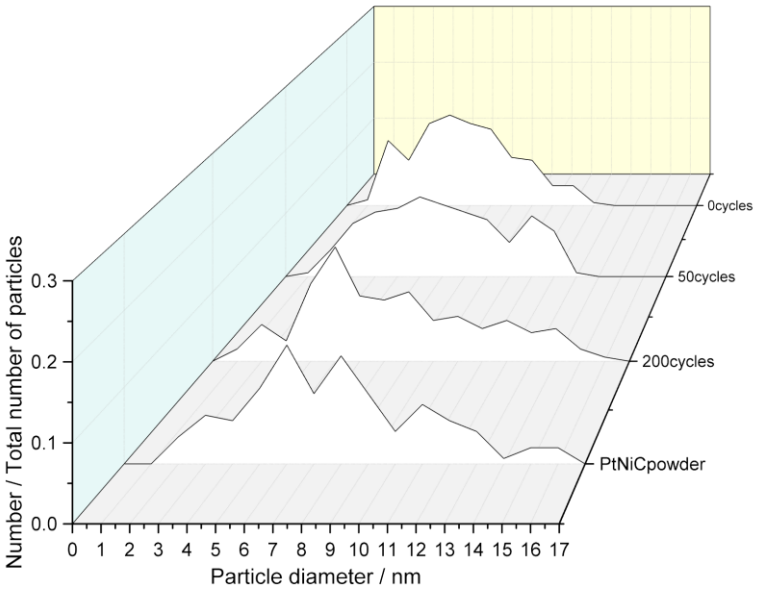

Figure 9 PSD of the PtNi/C powder compared to catalyst samples scraped off of the aged catalyst coated carbon paper electrodes. Number of particles counted: 142 for 'PtNi/C', 170 for '200 cycles', 167 for '50 cycles', and 206 for '0 cycles.' The number of particles at each diameter is expressed as a fraction of the total number of particles imaged.

TEM-EDX linescans across individual particles were also possible and were carried out for the PtCo/C and PtNi/C for the powders as well as several of the catalyst coated electrode samples, and was done by monitoring the emission at the Pt L, and the Ni and Co K edges. Ideally this analysis would be done for a number of particles within each sample to ensure that they are well represented, however only single particles were analysed due to time constraints. As these measurements were nearing the spatial resolution of the microscope and detectors, typically, nanoparticles towards the upper end of the size range were chosen. Measurement accuracy and precision were also limited by nanoparticles drifting, or becoming charged as a result of the electron beam, low x-ray photon counts and deliberate selection of isolated nanoparticles.

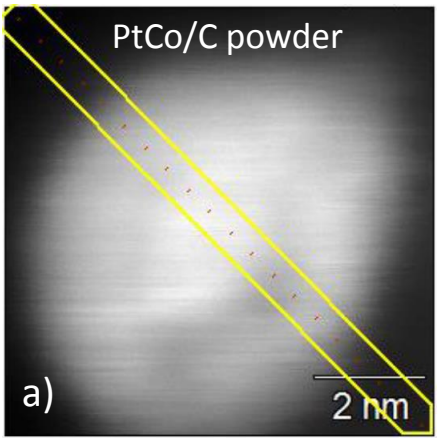
PtCo/C powder
a)
2 nm

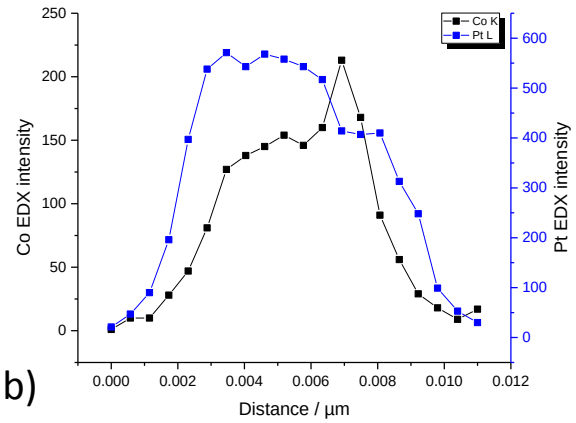
b)
Co K
Pt L
Co EDX intensity
Pt EDX intensity
Distance / µm

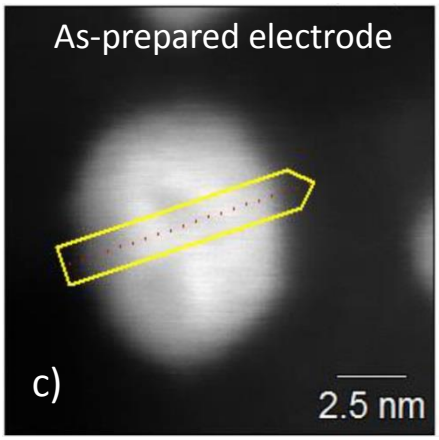
As-prepared electrode
c)
2.5 nm

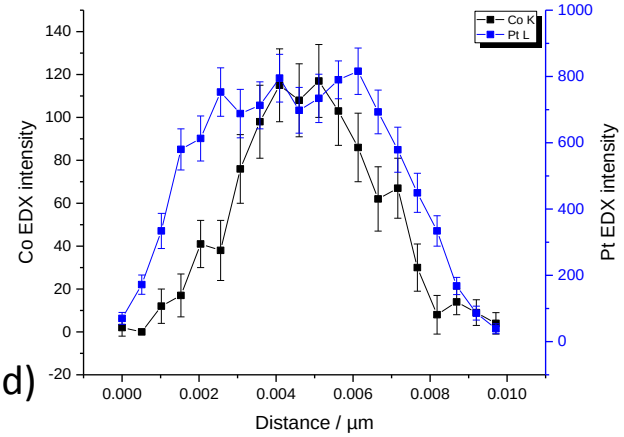
d)
Co K
Pt L
Co EDX intensity
Pt EDX intensity
Distance / µm

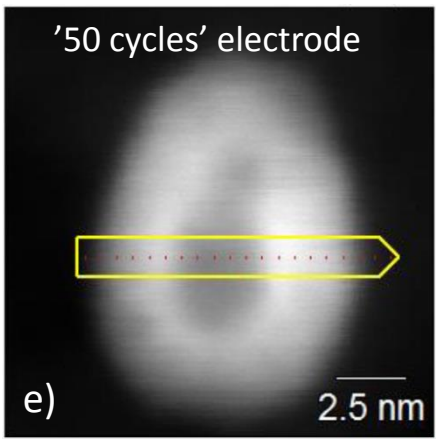
'50 cycles' electrode
e)
2.5 nm

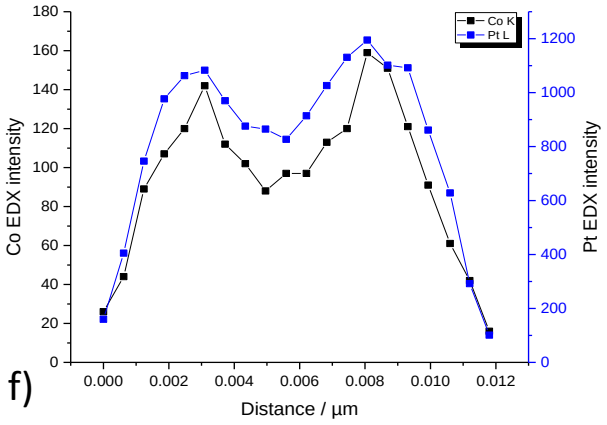
f)
Co K
Pt L
Co EDX intensity
Pt EDX intensity
Distance / µm

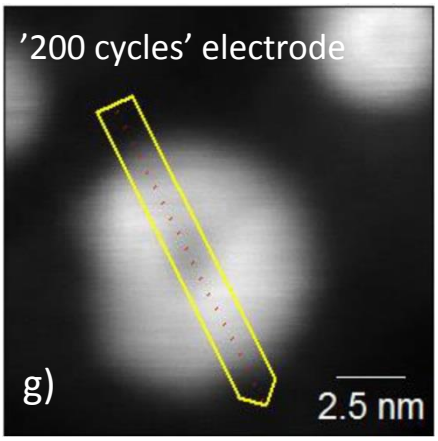
'200 cycles' electrode
g)
2.5 nm

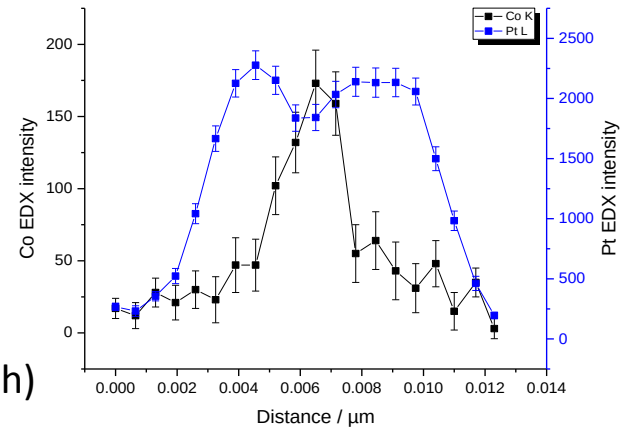
h)
Co K
Pt L
Co EDX intensity
Pt EDX intensity
Distance / µm

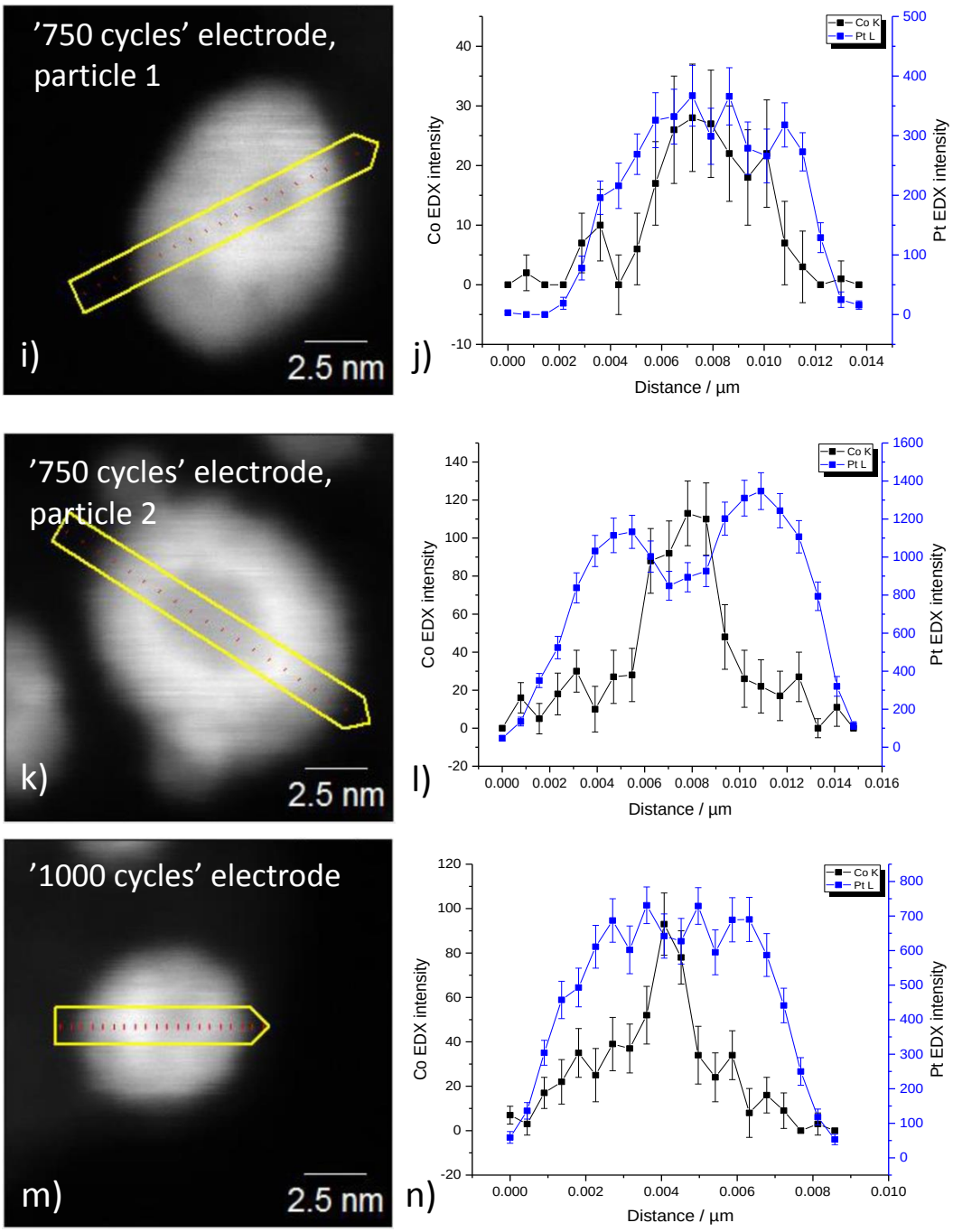

Figure 10 Dark field TEM images of the PtCo/C nanoparticle analysed are shown on the left hand side and the composition, as measured by EDX, is displayed on the right. The samples are as follows: a+b) PtCo/C powder, c+d) as-prepared PtCo/C electrode sample, e+f) PtCo/C electrode after 50 cycles, g+h) PtCo/C electrode after 200 cycles i - l) two nanoparticles from the PtCo/C electrode after 750 cycles, and m+n) the PtCo/C electrode after 1000 cycles.

Dark field TEM images along with EDX linescans across example nanoparticles in each of the PtCo/C powder and electrode samples are shown in Figure 10. In several of the images, *e.g.* in Figure 10e and k, darker patches can be seen in the centre of the bright PtCo nanoparticles, which is qualitatively indicative of variation in elemental distribution. The

EDX linescans confirm that there is a decrease in the amount of Pt present over the centre of the particle. However, in Figure 10f, there is also a dip in the emitted intensity at the Co K edge, which could suggest that particles are changing shape or becoming hollow (seen previously[27]). Figure 10l is a good example of the expected intensity profile expected for a core-shell particle. The EXAFS data, presented later in the chapter, suggests that there is a change in elemental distribution, which occurs once the catalyst has been exposed to the acidic electrolyte. This agrees with the linescans shown here. The samples taken at an earlier point in the stability test show either a thin Pt rich shell or non-core-shell like distributions, *e.g.* Figure 10d or f, whereas the later samples, such as Figure 10l or m, show a thicker region of Pt at each edge of the nanoparticle.

As these alloy catalysts have been acid-leached and annealed, it is possible that multiple structures exist, especially considering the range of particle sizes in the sample, which affects the leaching process.[28] This is shown by the electrode sample taken after 750 cycles, for which two nanoparticles were analysed, shown in Figure 10j and l. Both of these linescans can be explained based on a core-shell structure, although the second particle has a more defined, thicker Pt rich shell.

The same analysis was carried out on the PtNi/C powder and electrodes, however as mentioned previously, some electrodes were unavailable for testing. These images and results are presented in Figure 11.

The linescans generally show an increase at the Ni edge near the centre of the particle, with less intensity towards the nanoparticle surface. Figure 11b and f show relatively high Pt:Ni atomic ratios, from compositional analysis of the bulk catalyst powder, the expected ratio is 1.3 Pt atoms per Ni atom, which suggests a Pt rich outer layer. The EDX linescan in Figure 11f shows a lopsided distribution with multiple maxima at the Ni edge and could indicate multiple regions of high Ni content. Alternatively, there may be two or more particles that are overlapping.

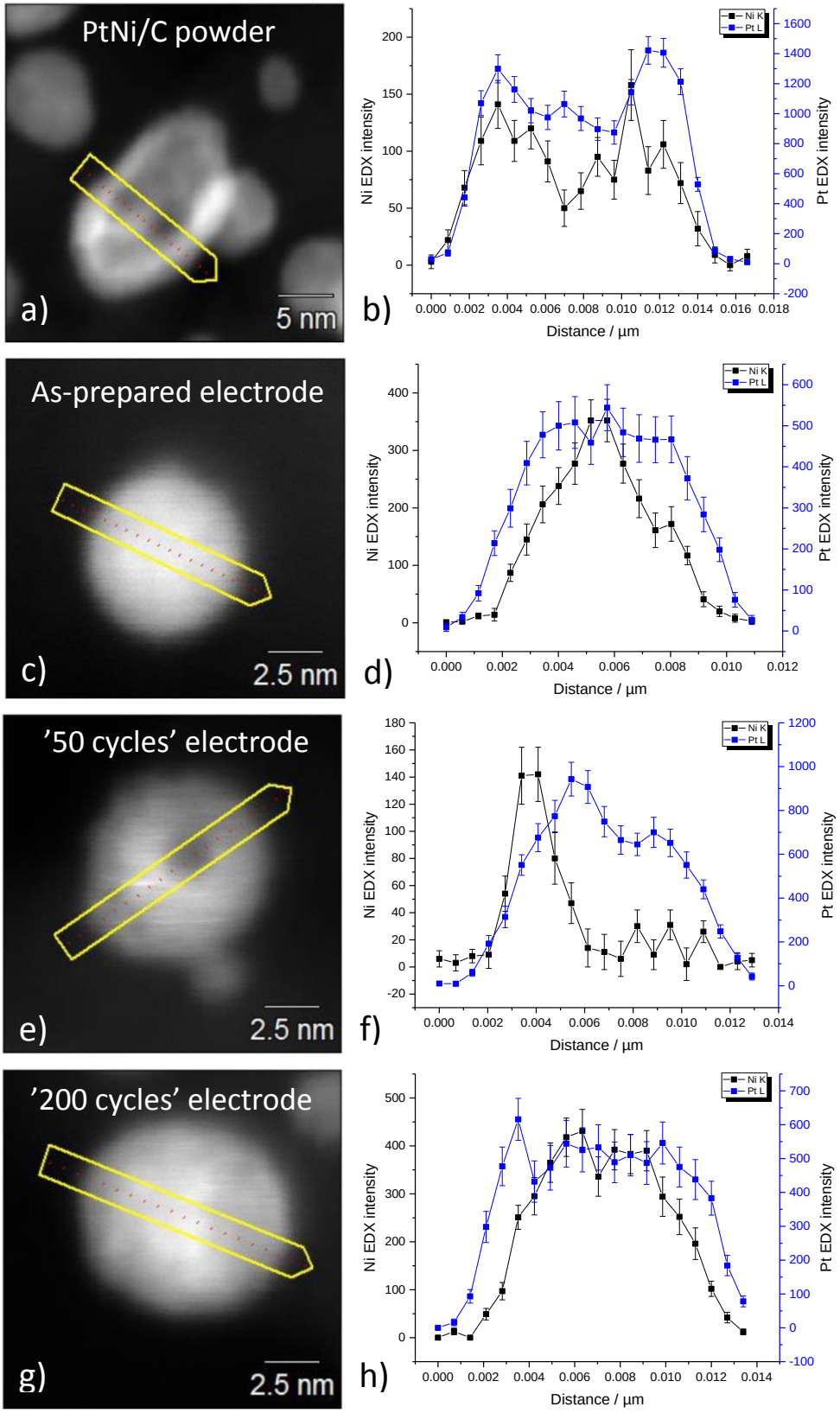

Figure 11 Dark field TEM images of the PtCo/C nanoparticle analysed are shown on the left hand side and the composition, as measured by EDX, is displayed on the right. The samples are as follows: a+b) PtNi/C powder, c+d) as-prepared PtNi/C electrode sample, e+f) PtNi/C electrode after 50 cycles, and g+h) the PtNi/C electrode after 200 cycles.

6.3.2.2 XPS

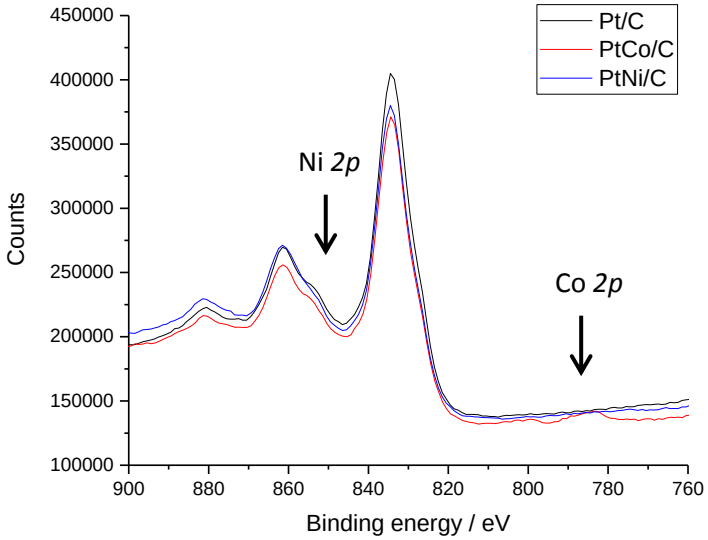

Figure 12 XPS spectra of the Pt/C, PtCo/C and PtNi/C coated electrodes in the Co2*p* and Ni2*p* region. The addition of Nafion results in large F Auger electron peaks, which strongly overlap with the Ni2*p* region and may cause problems when looking at the Co2*p* peaks.

The fluorine content of the Nafion that was added to the catalyst ink as a binding agent caused problems when looking at the XPS spectra for the electrode materials. Figure 12 shows the binding energy region expected for the Ni2*p* and Co2*p* transition peaks in high resolution. The broad multiplet from the fluorine Auger electron processes overlaps with and swamps the Ni2*p* peak, and due to the large size difference, deconvolution of the peaks becomes inaccurate. Due to differences in the catalyst and Nafion loading on the electrode samples, the Ni2*p* peak can't be determined via subtraction of the Pt/C spectrum as a background.

a) Pt4*f* region, catalyst powders

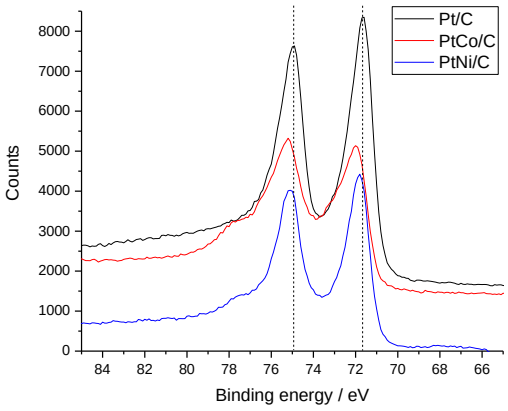

b) Pt4*f* region, as-prepared electrodes

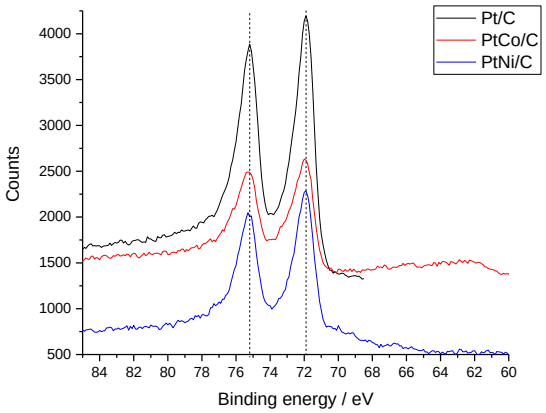

c) Pt4*f* region, cycled PtCo/C electrodes

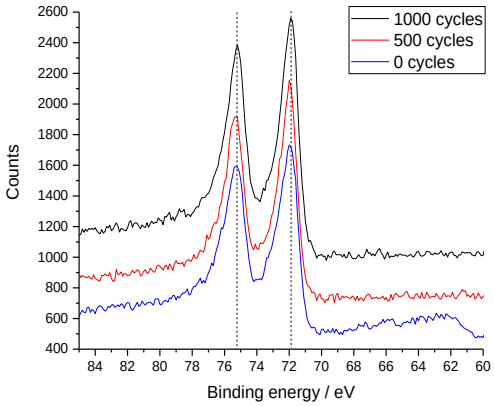

d) Co2*p* region, cycled PtCo/C electrodes

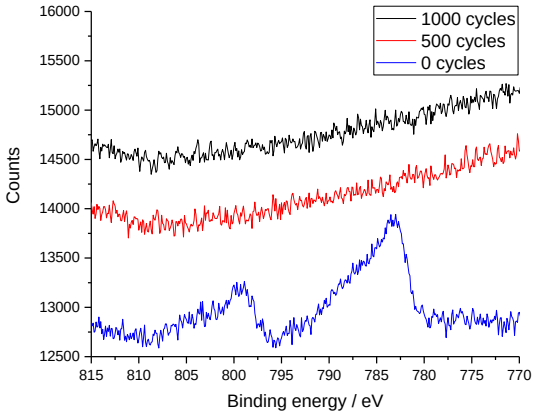

e) Pt4*f* region, cycled PtNi/C electrodes

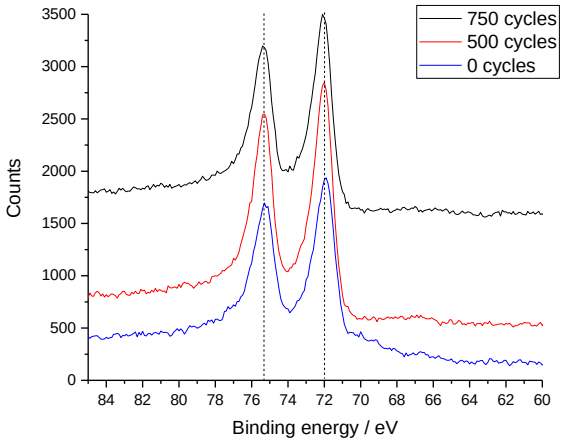

Figure 13 XPS spectra of the 5 nm Pt/C, PtCo/C and PtNi/C catalyst powders and coated electrode samples. a) and b) show the catalyst powders and electrode samples. The tail at higher binding energies for the alloy samples is indicative of oxidised Pt species, whilst small features at low binding energies may be assigned to the Co3*p* and Ni3*p* at 59 and 66 eV respectively. c) and d) show the Pt4*f* and Co2*p* transition regions for the PtCo/C coated electrode samples. The peak at 63 eV for the as-prepared sample may be assigned to the Co3*p* transition. Peaks in the Co2*p* region can only be observed for the as-prepared sample. Finally, e) shows the Pt4*f* region for the PtNi/C coated electrode samples. A shoulder, which could be caused by the Ni3*p* transition, can be identified at around 70 eV for the freshly prepared electrode sample only.

Peak fitting and composition analysis were performed for the alloy catalysts, however the presence of Nafion strongly overlaps with the Ni2*p* peaks, whilst the small Ni3*p* peak overlaps with the Pt4*f* transition. The Co2*p* and 3*p* peaks don't overlap with anything else, but, as can be seen in Figure 13d, can only be observed for the catalyst powder and the as-prepared sample. As mentioned previously and covered in more detail further on, there is evidence based on EXAFS derived coordination numbers that, before contact with the electrolyte, some Co atoms remain at the surface.

6.3.2.3 XAS

The Pt alloy samples were analysed as explained in the previous chapter, although care must be taken to consider whether Co-O, Ni-O and Pt-O scattering paths should be included in the fits. Again, only first shell fits were used.

6.3.2.4.1 PtNi/C

Unlike with the PtNi/C pellet, the freshly prepared/untreated electrode sample required scattering paths involving O neighbours in the fit. These paths were included by adding separate degeneracies and bond distances, and a single disorder parameter for both Pt-O and Ni-O scattering paths. Inclusion of O neighbours is reasonable as this sample was not reduced under H_2(g) and some oxidation is expected from the catalyst synthesis and coating processes. This fit is shown Figure 14 and the extracted parameters are shown in Table 4.

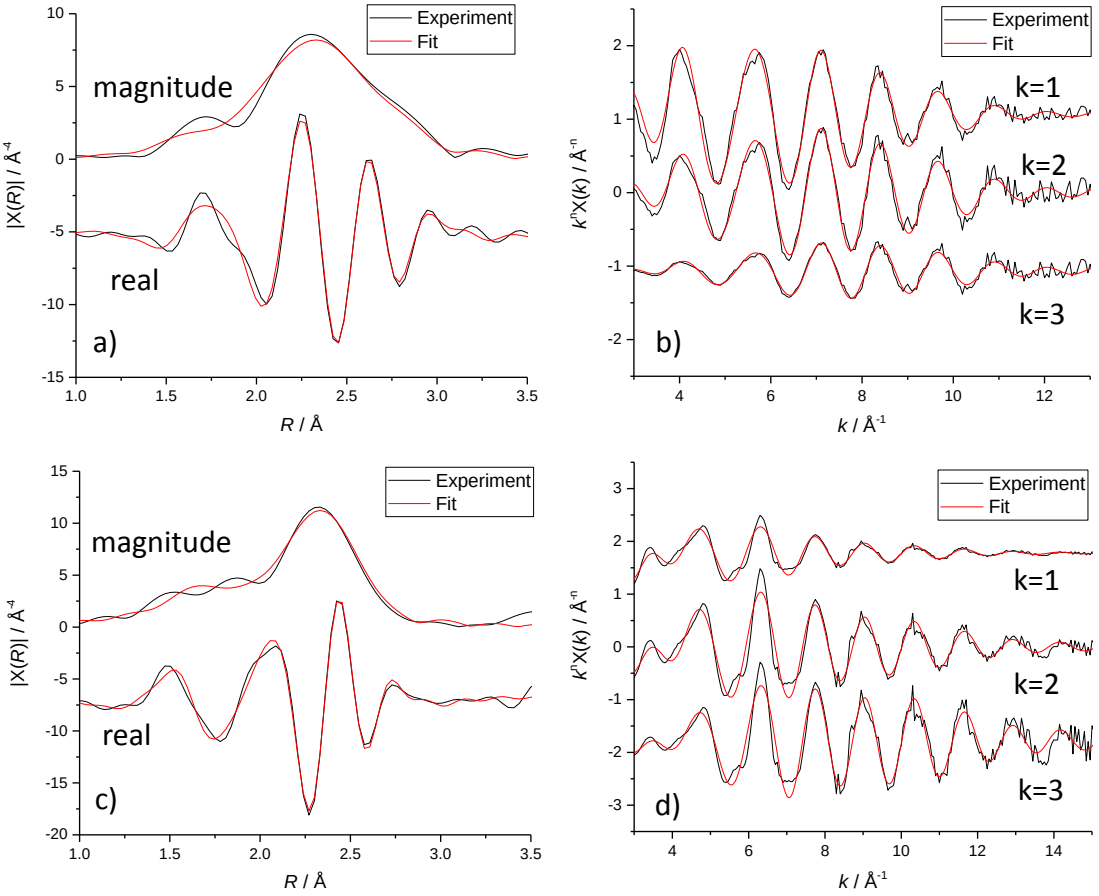

Figure 14 Simultaneous 1 shell EXAFS fit for the untreated PtNi/C electrode sample. a) k^2 weighted Fourier transform, and b) k^n weighted data for the Pt L_3 edge c) k^2 weighted Fourier transform, and d) k^n weighted data for the Ni K edge. No constraint was applied based on atomic composition. Pt-O and Ni-O scattering paths were included in the fit, with separate degeneracy and bond length parameters, but an equal disorder parameter. Plots are not phase corrected. R-factor was 0.0091.

Table 4 Values obtained from the fit to the EXAFS of the untreated PtNi/C electrode sample, shown in Figure 14.

	N	***R* / Å**	**σ^2 / Å^2**	**E_0 / eV**	**R_f**
Pt-Pt	8.0 ± 1.9	2.69 ± 0.02	0.01 ± 0.002	6.9 ± 1.3	0.0091
Pt-Ni	2.9 ± 0.7	2.604 ± 0.008	0.008 ± 0.002		
Pt-O	0.6 ± 0.3	2.00 ± 0.05	0.006 ± 0.003		
Ni-O	1.6 ± 0.3	2.01 ± 0.01	0.006 ± 0.003	5.8 ± 0.9	
Ni-Pt	3.0 ± 0.8	2.605 ± 0.008	0.008 ± 0.002		
Ni-Ni	3.5 ± 0.5	2.580 ± 0.008	0.008 ± 0.001		

Table 5 shows the coordination numbers calculated from the fits to each of the *ex situ* PtNi/C samples. The as-prepared electrode was also measured after being reduced in the

same way as the pellet sample, and these results are included along with the values for the pellet sample. Addition of O scattering paths to the other fits returned negative degeneracy values, and did not improve the r-factor.

The coordination numbers are denoted as N_{PtNi} and N_{PtM} for the Pt-Ni and total Pt-metal (Pt-M, *i.e.* the total number of Pt and Ni neighbours, excluding oxygen neighbours) coordination numbers respectively. The coordination numbers involving Ni are defined as N_{NiPt} and N_{NiM} using the same system. These values have then been used to calculate the Pt:Ni ratio, x, and both the Cowley parameter and the alloying parameters. The errors on the values for the partial coordination numbers, N_{PtNi} and N_{NiPt} is on the order of 0.5, leading to an error of around 1 on the total metal coordination number, denoted by N_{PtM} and N_{NiM} respectively.

Table 5 Coordination numbers derived from the EXAFS spectra for the series of aged PtNi/C electrode samples, alongside the pellet sample and an as-prepared electrode that had been chemically reduced with H_2. x, the Pt/Ni ratio of the sample, C, the Cowley parameter and the alloying parameters, J_A and J_B, are also shown for each sample. The number of 0.6 – 1.0 V *vs.* RHE potential cycles that each sample has undergone is also shown. Errors are on the order of ±0.5 and ±1 for the partial and total coordination numbers respectively. The as-prepared electrode sample required 0.5 and 1.5 Pt-O and Ni-O neighbours respectively. The oxygen neighbours are not included in the N_{PtM} value.

Cycles	N_{PtNi}	N_{PtM}	N_{NiPt}	N_{NiM}	x	C	J_A (Ni)	J_B (Pt)
Pellet	3.7	9.7	4.3	8.3	1.2	0.18	96	82
0, reduced	3.3	9.4	3.8	7.8	1.1	0.24	91	76
0, as-prep	2.9	10.9	3.0	6.5	1.1	0.46	90	54
50	2.8	8.8	4.6	9.6	1.6	0.17	76	83
100	2.9	8.9	4.6	9.6	1.6	0.15	78	85
200	2.9	8.3	4.6	9.6	1.6	0.10	77	90
500	2.7	9.1	4.7	9.9	1.8	0.19	75	81
750	3.3	8.5	4.9	10.0	1.5	0.03	82	97
1000	2.7	8.6	4.7	9.7	1.7	0.15	76	85

For all of the values, there is an observable difference between the samples that have been exposed to a number of cycles in the 80 ^{o}C 1 M $HClO_4$ electrolyte and those that have not, *i.e.* the pellet sample and the two '0 cycles' samples. x increases from 1.1-1.2 to 1.6 or higher upon cycling in acid, indicating that there is still some Ni present at or near the

surface able to be dissolved. Less coordinated Ni atoms at the surface have been removed by the cycling leading to an increase in both Ni-Ni and Ni-M coordination, as Ni atoms within the particle core are more fully coordinated.

The Cowley parameter, C, was found to be positive for all samples, which corresponds to a degree of clustering of like atoms within the alloy nanoparticles, although the magnitudes are small, so any conclusions drawn should be treated with caution. The untreated sample has a much larger value for C than the others, which could be due to the ~0.5 Pt-O and ~1.5 Ni-O neighbours required in the fit as the parameter is based on a bimetallic alloy and doesn't account for surface oxides.

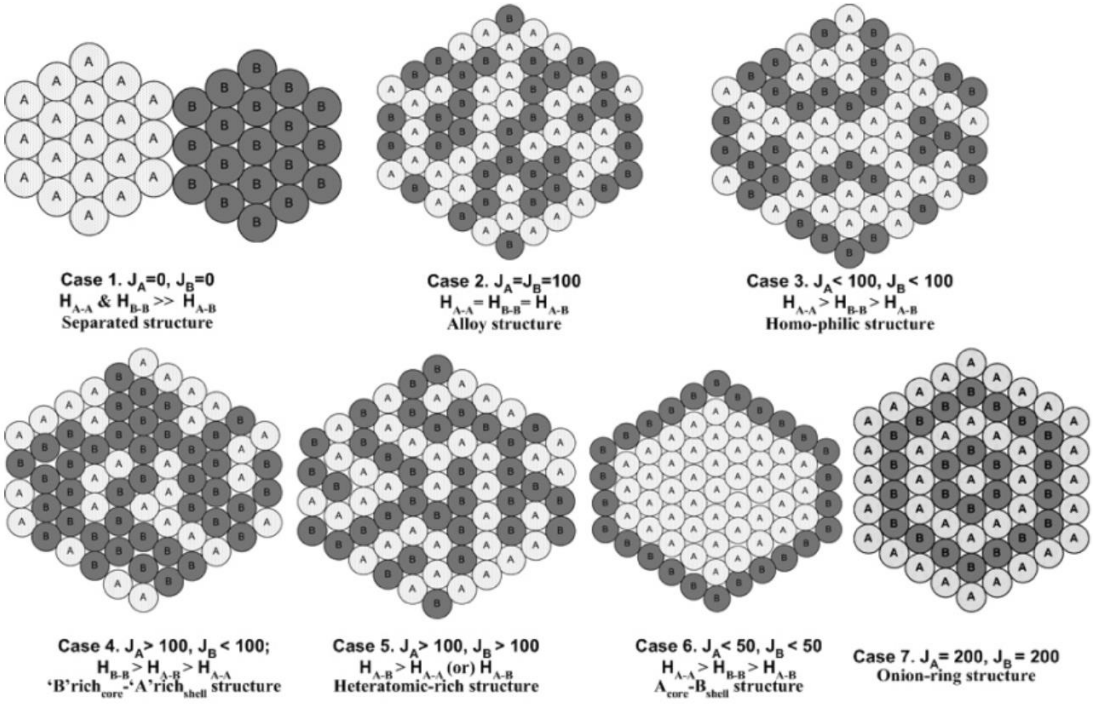

Figure 15 Diagram taken from the paper by Hwang *et al.*[29] indicating the parameters calculated for bimetallic nanoparticles at various degrees of alloying. H_{AA}, H_{BB}, and H_{AB} denote partial coordination numbers for homo- and heteroatomic interactions respectively.

For all samples, both J_A and J_B are less than 100 indicating that these samples have a 'homophilic' structure indicated by Case 3 in Figure 15. Again, there is a difference when looking at the acid exposed samples. For the samples that had not come into contact with the acid, $J_A > J_B$ and $N_{PtM} > N_{NiM}$ whilst for those that had been exposed to electrolyte $J_B > J_A$ and $N_{NiM} > N_{PtM}$. These differences are indicative of which element is most prevalent near the surface as opposed to deeper within the particle. This is due to atoms near the core having inherently having more neighbouring atoms than those at the surface. The results

suggest that initially Ni is present near the surface, but once exposed to the acidic electrolyte and potential cycling, Ni is dissolved leaving Pt at the surface.

The presence of Ni atoms at the surface of the nanoparticles is unexpected from the catalyst synthesis procedure, the final step of which involved aggressive chemical leaching in acid designed to remove the less noble component from the near surface region. These surface Ni atoms are quickly removed after fewer than 50 cycles of the AST. Both the absence of Ni-O scattering paths and the alloying parameters suggest that Ni surface species are no longer present, as well as a significant decrease in white line intensity in the Ni XANES region. An example of this can be seen in Figure 14c in the previous chapter, which compares the XANES regions measured for PtNi/C powder samples taken at several points during the synthesis process.

6.3.2.4.2 PtCo/C

Similar to with the PtNi/C samples, only a simple one shell fit will be considered and used to determine the partial and total coordination numbers, along with the alloying parameters. Unlike the previous samples, Pt-O scattering paths were required in the fits for several samples, and Co-O paths were needed for the 2 untreated samples. Inclusion of the O neighbours improved the r-factors of the fits, but in one case led to an infeasible coordination number, which has been highlighted in red. In general, the data for these samples was noisier than for previous samples, and the errors are larger. The partial coordination numbers determined in these fits are shown in Table 6. The pellet sample for this catalyst could not be analysed because the Co K edge data was very noisy.

Table 6 Partial and total coordination numbers derived from the EXAFS spectra for the series of aged PtCo/C electrode samples. The number of 0.6 – 1.0 V *vs.* RHE potential cycles that each sample has undergone is also shown. Errors in the coordination numbers are on the order of ±1 and ±2 for the total metal coordination numbers, N_{PtM} and N_{CoM}. Two fits were made for several samples; one fit was done without including Pt-O or Co-O neighbours, and the second fit included scattering paths to oxygen (denoted with + O) where necessary.

Cycles	N_{PtPt}	N_{PtCo}	N_{PtO}	N_{PtM}	N_{CoCo}	N_{CoPt}	N_{CoO}	N_{CoM}
0, reduced	9.1	1.1	0	10.2	2.8	3.2	2.9	6.0
0, as-prep	8.2	0.4	1.0	8.6	2.3	1.3	3.2	3.6
50 (+O)	8.1	1.1	-6.7	9.2	5.2	4.8	0	10.1
50	6.8	1.9	0	8.7	5.3	4.8	0	10.1
100 (+O)	7.7	1.3	1.3	9.0	5.2	4.8	0	10.0
100	6.6	2.2	0	8.9	5.2	4.8	0	10.0
200 (+O)	6.5	1.3	0.7	7.8	5.2	4.8	0	10.0
200	6.0	2.5	0	8.6	5.4	4.8	0	10.2
500	7.4	1.9	0	9.3	5.3	4.8	0	10.2
750	8.3	1.4	0	9.7	5.4	4.6	0	10.0
1000	7.1	2.0	0	9.1	5.2	5.5	0	10.7

Example fits showing samples which require O neighbours (Figure 17), may require O neighbours (Figure 18) and the case where no O neighbours are required (Figure 19) are provided below.

In Figure 17, there is a significant low R component of the EXAFS signal at both the Co and Pt absorption edges, which can't be removed as a part of the background, and is in the expected range for metal-oxygen scattering paths. Oxidation is also indicated by the white line intensity in the XANES region for these materials. These spectra are shown in Figure 16. As a result and in combination with the significant improvement in the fit, inclusion of O neighbours is justified. The presence of O neighbours also implies that both Co and Pt species are present at the surface of the catalyst nanoparticles.

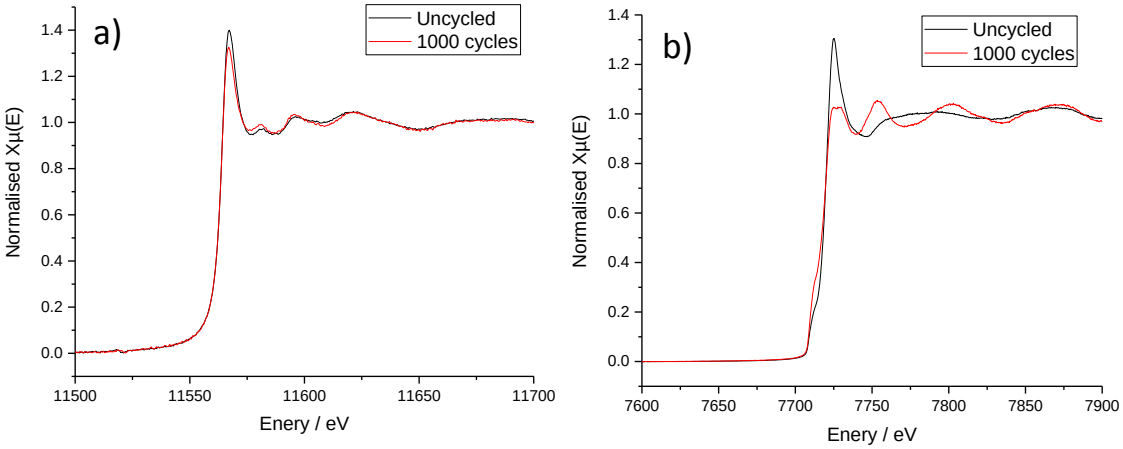

Figure 16 a) Pt L_3 and b) Co K EXAFS regions for the uncycled electrode (*i.e.* heavily oxidised) and the oxide free electrode that had been cycled 1000 times from 0.6-1.0 V *vs.* RHE in 1 M $HClO_4$ at 50 mV s^{-1} at 80 °C. The increased intensity of the white line is indicative of oxidation.

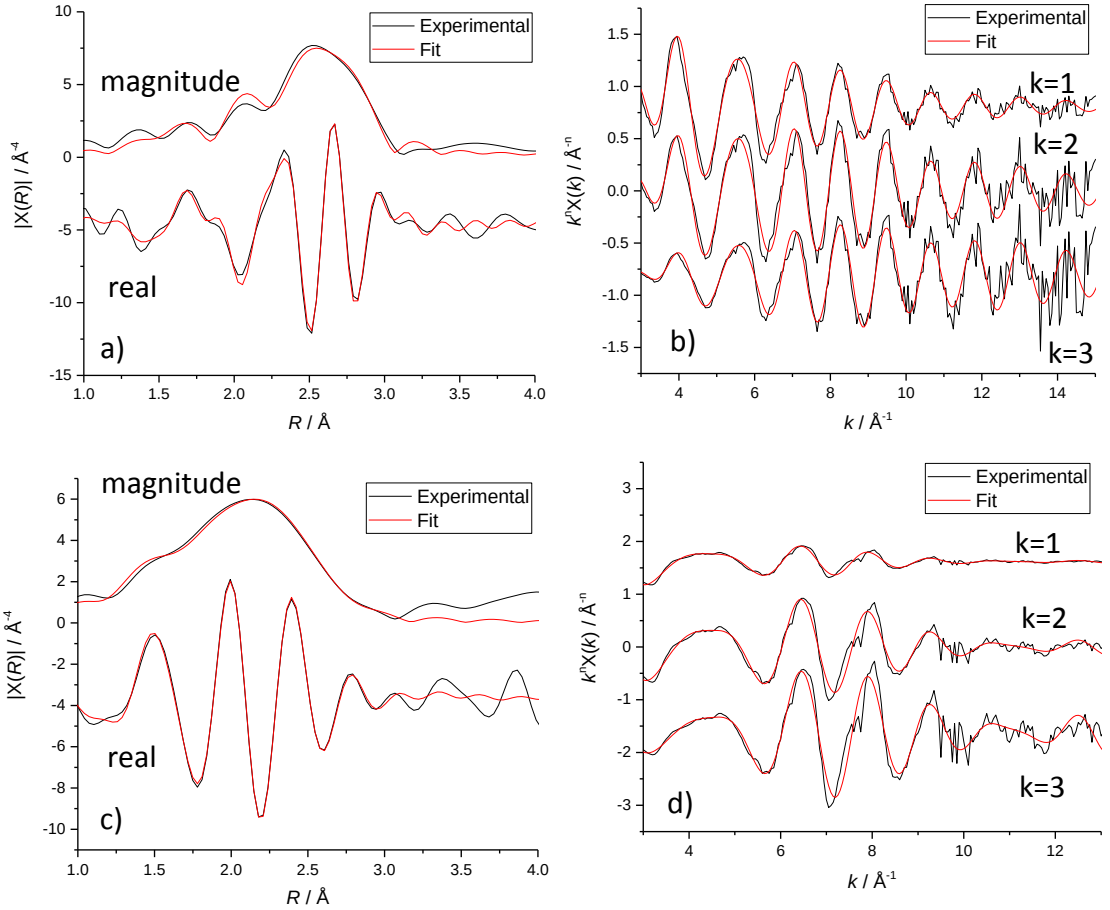

Figure 17 Simultaneous 1 shell EXAFS fit for the uncycled PtCo/C electrode sample. a) k^2 weighted Fourier transform, and b) k^n weighted data for the Pt L_3 edge c) k^2 weighted Fourier transform, and d) k^n weighted data for the Co K edge. No constraint was applied based on atomic composition. Pt-O and Co-O scattering paths were included in the fit, with separate degeneracy, bond length and disorder parameter. Plots are not phase corrected. The *R*-factor was 0.0065.

For some of the electrode samples that had been exposed to the acidic electrolyte, Pt-O neighbours can potentially still be observed, but the Co coordination environment is metallic and no Co-O interactions can be seen. This can be seen visually from the *R*-space EXAFS in Figure 17a and c compared to Figure 18a and c respectively. The fit statistics are improved by the addition of the Pt-O scattering path, but it is worth noting that incorrect or incomplete background subtraction may also give rise to signal in the low *R* region.

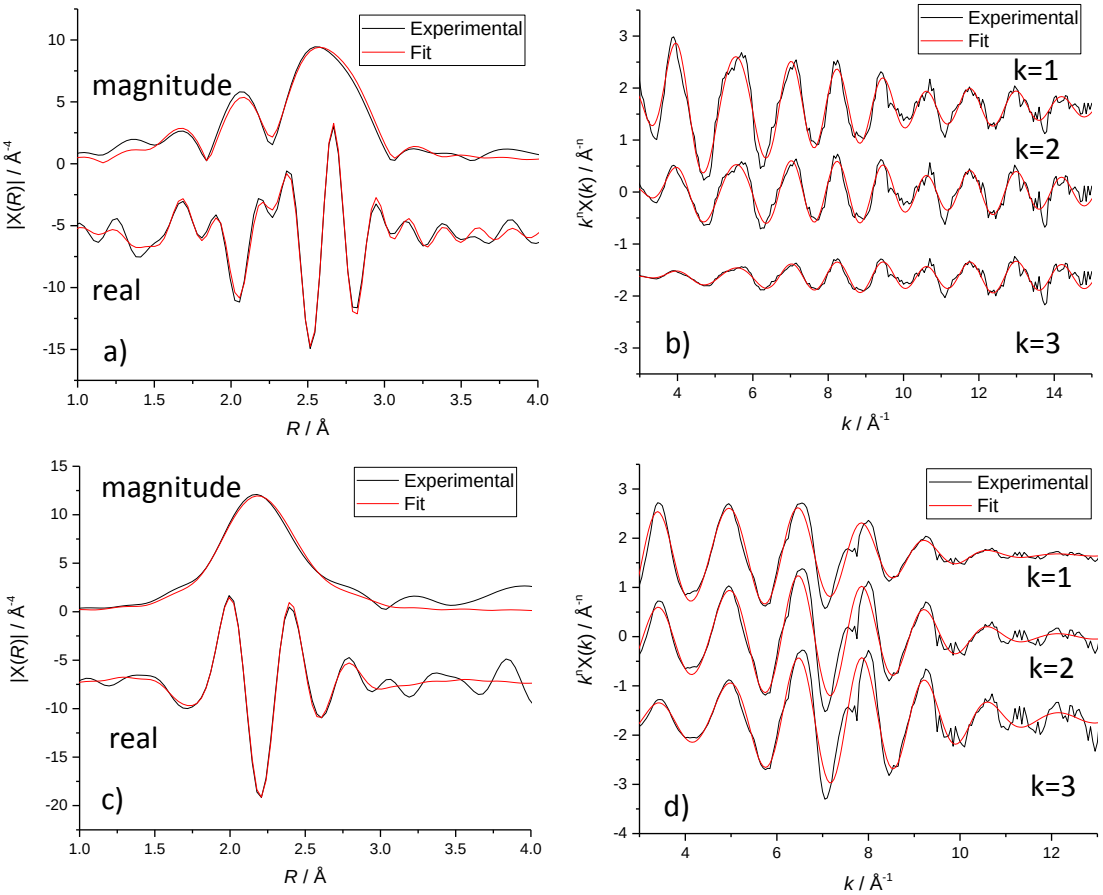

Figure 18 Simultaneous 1 shell EXAFS fit for the PtCo/C electrode sample that had been cycled 200 times from 0.6-1.0 V *vs.* RHE, at 50 mVs^{-1} in 1 M $HClO_4$ at 80 °C. a) k^2 weighted Fourier transform, and b) k^n weighted data for the Pt L_3 edge c) k^2 weighted Fourier transform, and d) k^n weighted data for the Co K edge. No constraint was applied based on atomic composition. The Pt-O scattering path was included in the fit, with separate degeneracy, bond length and disorder parameters. Plots are not phase corrected. *R*-factor was 0.0076 when including O neighbours, but 0.0294 without.

The most cycled PtCo/C electrode sample did not require scattering pathways involving O neighbours, and the fit is shown Figure 19.

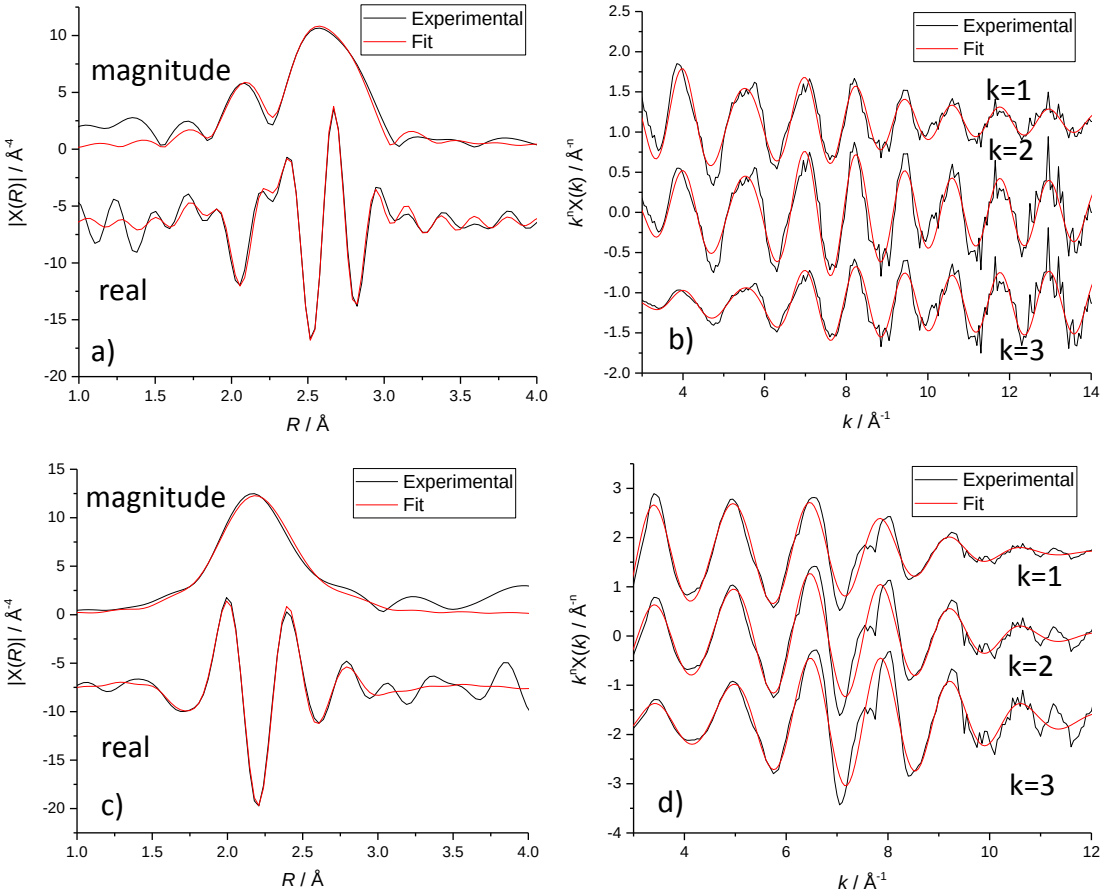

Figure 19 Simultaneous 1 shell EXAFS fit for the PtCo/C electrode sample that had been cycled 1000 times from 0.6-1.0 V *vs.* RHE, at 50 mVs^{-1} in 1 M $HClO_4$ at 80 °C. a) k^2 weighted Fourier transform, and b) k^n weighted data for the Pt L_3 edge c) k^2 weighted Fourier transform, and d) k^n weighted data for the Ni K edge. No constraint was applied based on atomic composition, and no O neighbours were required in the fit. Plots are not phase corrected. *R*-factor was 0.0280.

From the total metal coordination numbers for Pt and Co, see Table 7, it can be inferred that initially there is some Co present at the nanoparticle surface, as, for the two uncycled electrodes, $N_{PtM} > N_{CoM}$. After the potential cycling treatment in 1 M $HClO_4$ however, the situation is reversed implying that there is now a Pt shell and the Co is located towards the core. The Cowley parameter for the PtCo/C samples has, in general, a more positive value than for the PtNi/C electrodes, which indicates a greater heterogeneity of the alloy meaning that clustering of like atoms tends to occur.

The alloying parameters tell a different story. Since both J_A and $J_B < 100$, the implied structure is similar to that shown as case 3 in Figure 15. As $J_A > J_B$, the nanoparticles supposedly have a Pt (B) rich core and Co (A) rich shell, which contradicts chemical intuition and evidence from the TEM-EDX results. In addition, this does not fit well with the fact that the total coordination number for Co is larger than that of Pt. This situation might be

caused by the larger errors in the obtained values for the coordination numbers than for the PtNi/C samples. The mean square disorder terms for the mixed metal scattering paths are also relatively large at 0.012 Å^2.

Table 7 Partial and total coordination numbers derived from the EXAFS spectra for the series of aged PtCo/C samples, one of which was reduced under H_2 before analysis. x, the Pt/Co ratio of the sample, C, the Cowley parameter and the alloying parameters, J_A and J_B, are also shown for each sample. The number of 0.6 – 1.0 V *vs.* RHE potential cycles that each sample has undergone is also shown. Errors are on the order of ±1 and ±2 for the partial and total coordination numbers respectively.

Cycles	N_{PtCo}	N_{PtM}	N_{CoPt}	N_{CoM}	x	C	J_A (Co)	J_B (Pt)
0, reduced	1.1	10.2	3.2	6.0	2.9	0.58	71	31
0, as-prep	0.4	8.6	1.3	3.6	2.9	0.80	48	15
50 (+O)	1.1	9.2	4.8	10.1	4.5	0.36	59	53
50	1.9	8.7	4.8	10.1	2.6	0.23	66	55
100 (+O)	1.3	9.0	4.8	10.0	3.7	0.32	61	54
100	2.2	8.9	4.8	10.0	2.2	0.21	70	54
200 (+O)	1.3	7.8	4.8	10.0	3.6	0.22	61	61
200	2.5	8.6	4.8	10.2	1.9	0.14	71	56
500	1.9	9.3	4.8	10.2	2.5	0.28	67	52
750	1.4	9.7	4.6	10.0	3.4	0.38	60	48
1000	2.0	9.1	5.5	10.7	2.7	0.17	71	60

Table 7 shows the degeneracy parameters generated from the fits displayed in Figure 17-Figure 19. The addition of Pt-O scattering paths improves the r-factor of the fit by about 0.01 in each case, although also increases the number of variables to 15 compared to approximately 26 independent points. The inclusion of Pt-O scattering paths leads to slight decrease in Pt-Pt and an increase in the Pt-Co coordination numbers, whilst the total Pt-M coordination, the Cowley and alloying parameters remain roughly the same.

Figure 20 shows the average Pt-Pt bond distances in the catalyst coated electrodes as determined from the EXAFS fits. It has been shown that this bond distance correlates with strain effects observed in PtM/C nanoparticles,[30] which in turn has been linked with increased activity for the ORR.[31] However in this instance, no other evidence for lattice strain can be provided *e.g.* use of Fourier transforms of TEM images in the 'core' and 'shell' regions did not show a change in lattice parameter. Additionally no correlation between

coordination numbers and the bond length was observed, which suggests that variations that can be seen in Figure 20 are unlikely to be as a result of progressive leaching of either Co or Ni.

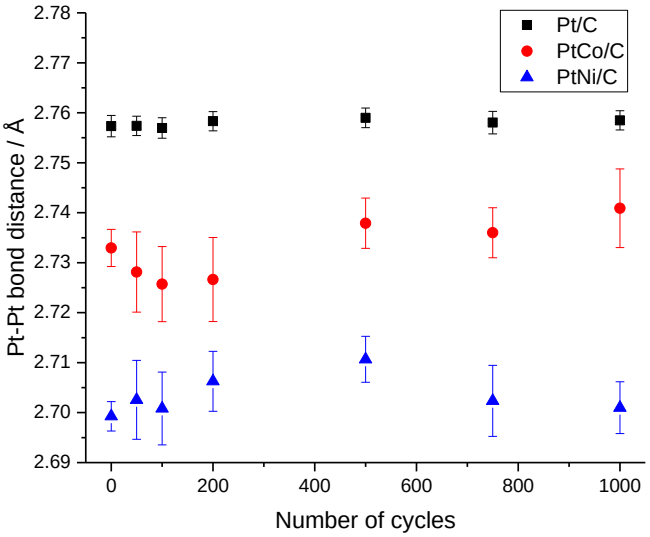

Figure 20 Average Pt-Pt bond distances in the three sets of catalyst coated electrodes as determined from the EXAFS fits. The typical bond distance in bulk Pt is 2.775 Å.

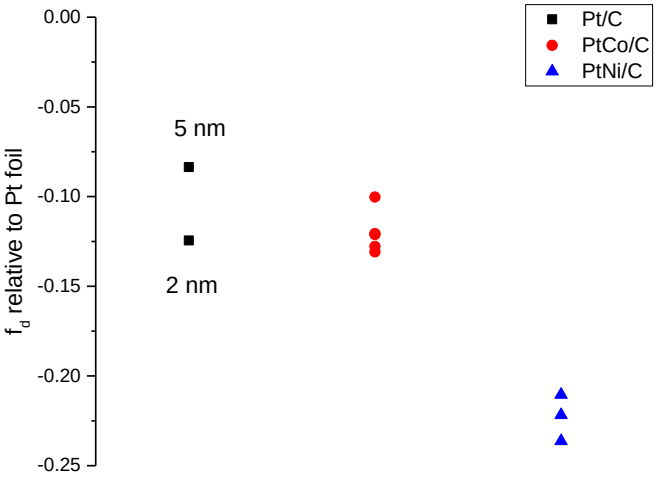

Figure 21 F_d values for the PtCo/C and PtNi/C catalyst coated electrodes relative to the Pt foil measured *in situ* at 0.6 V *vs.* RHE. The AST had no consistent effect on these values, so the data points are grouped according to composition.

Figure 21 shows a comparison of the calculated values for f_d relative to Pt foil for the catalyst samples. Five PtCo/C and three PtNi/C samples were measured *in situ* in N_2 purged 1 M $HClO_4$ at 0.6 V *vs.* RHE, including a freshly prepared electrode and electrode samples

taken at various points throughout the AST. No clear trend could be observed, considering an error of approximately 10%, so the data points are instead grouped by composition.

6.4 Conclusions

In this chapter, it has been shown that the accelerated stability testing was not harsh enough to result in significant changes in the catalyst structure pre- and post-treatment. This is contrary to previous work such as that by Colón-Mercado *et al.,*[32] and Yu *et al.*,[33] where significant dissolution of Co, Ni and other 3rd row transition metals was observed. In hindsight, the use of stagnant electrolyte decreases the ECSA loss due to redeposition of Pt.[34] As a result, the ensemble of techniques employed here revealed few differences in structure due to the insignificant effect of the stability treatment. If the work were to be repeated, the stability testing regime must be altered such that enough degradation occurs as to be observable. This could be done most simply by increasing the number of cycles used in the procedure, although higher acid concentrations, or more positive potential limits could also be used. However it should be noted that this will affect the degradation mechanism, as carbon corrosion will be become dominant at high potential rather than dissolution of Pt or the alloying metal. This may mean that other characterisation techniques would better suited to study the changes, for example identical location TEM images would facilitate the observation of support degradation and particle detachment,[4,35] which is not possible using x-ray based spectroscopy techniques.

The RDE technique yielded the expected increase in activity for the two alloy catalysts over the pure Pt sample. A combination of optical microscopy, XRF and liquid phase particle size analysis allowed accurate quantification of catalyst loading, and assessment of the thin films deposited on the RDE tip. Various problems arose when incorporating evaluation of ORR activity into the stability testing regime, but better cell configuration could ameliorate these difficulties. Key features would include improvements in thermal insulation of the cell to remove convection, and full enclosure of the system to prevent electrolyte evaporation, which ultimately limited the timescale of the experiments. Alternatively, the system could be cooled to room temperature for certain measurements, but this would considerably lengthen the measurement time.

Results from the EXAFS analysis and XPS both suggest that the initial catalyst nanoparticles have residual base metal atoms at the surface that are quickly removed upon immersion in the acidic electrolyte. The EXAFS technique struggled somewhat with the high disorder in

the real-world catalyst systems, which arose based on the particle size distribution as well as the variation in particle composition. XPS was not found to be useful once the catalyst samples had been incorporated into Nafion containing inks because the high fluorine content of the ionomer dominates the signal in the expected binding energy region for the Co2p and Ni2p transitions. Future work could investigate the possibility of using Nafion-free catalyst inks[36] or a different ionomer which does not contain fluorine, for example, a liquid form of a polybenzimidazole type compound, which has previously been suggested as a substitute for Nafion in high temperature fuel cells.

In contrast, the TEM-EDX suggested that in most cases there was significant depletion of Ni or Co in the outermost ~0.5 – 1 nm of the nanoparticles. The shell thickness estimated from the EDX linescans also grew slightly to 3 nm over the course of the AST for the PtCo/C electrode samples. This was not observed for the PtNi/C samples, although fewer samples were available for testing.

On balance, the techniques used in this work to analyse the PtCo/C and PtNi/C nanoparticle samples suggest that a Pt rich shell was formed, particularly after the samples had been exposed to the acidic electrochemical environment. Based on these results, it is however unlikely that the nanoparticle sample consists of true core-shell particles. The broad size distribution of the particles is most likely a key contributing factor that results in differences in behaviour when the nanoparticles are acid-leached.

In comparison with the performance of the pure Pt/C catalysts, the alloy catalysts were more stable than the 2 nm Pt/C sample, most likely due to the inherent stability granted by the larger particle size as the 5 nm Pt/C sample was also stable against the degradation procedure used in this work. Consequently, in order to confirm whether Pt alloys show increased stability, it is suggested that either more cycles are carried out, or the acid concentration is increased. Care must be taken when selecting the potential window used for the cycles, as increasing the upper limit further will also degrade the carbon support material thereby affecting the degradation pathway. The DOE lists a separate protocol for durability testing of the support using a potential window of 1.0 to 1.6 V *vs.* RHE rather than the upper limit of 1.0 V *vs.* RHE used for the catalyst itself. The temperature used in this work is comparable to that used in PEMFCs and raising it further will add complications in terms of evaporation of electrolyte as well as safety.

6.5 References

(1) Takahashi, I.; Kocha, S. S. Examination of the Activity and Durability of PEMFC Catalysts in Liquid Electrolytes. *J. Power Sources* **2010**, *195*, 6312–6322.

(2) Garsany, Y.; Baturina, O. A.; Swider-Lyons, K. E.; Kocha, S. S. Experimental Methods for Quantifying the Activity of Platinum Electrocatalysts for the Oxygen Reduction Reaction. *Anal. Chem.* **2010**, *82*, 6321–6328.

(3) Jackson, C.; Smith, G. T.; Inwood, D. W.; Leach, A. S.; Whalley, P. S.; Callisti, M.; Polcar, T.; Russell, A. E.; Levecque, P.; Kramer, D. Electronic Metal-Support Interaction Enhanced Oxygen Reduction Activity and Stability of Boron Carbide Supported Platinum. *Nat. Commun.* **2017**, *8*, 15802.

(4) Meier, J. C.; Galeano, C.; Katsounaros, I.; Topalov, A. A.; Kostka, A.; Schüth, F.; Mayrhofer, K. J. J. Degradation Mechanisms of Pt/C Fuel Cell Catalysts under Simulated Start-Stop Conditions. *ACS Catal.* **2012**, *2*, 832–843.

(5) Schlögl, K.; Mayrhofer, K. J. J.; Hanzlik, M.; Arenz, M. Identical-Location TEM Investigations of Pt/C Electrocatalyst Degradation at Elevated Temperatures. *J. Electroanal. Chem.* **2011**, *662*, 355–360.

(6) Gan, L.; Heggen, M.; O'Malley, R.; Theobald, B.; Strasser, P. Understanding and Controlling Nanoporosity Formation for Improving the Stability of Bimetallic Fuel Cell Catalysts. *Nano Lett.* **2013**, *13*, 1131–1138.

(7) Sheng, W.; Chen, S.; Vescovo, E.; Shao-Horn, Y. Size Influence on the Oxygen Reduction Reaction Activity and Instability of Supported Pt Nanoparticles. *J. Electrochem. Soc.* **2012**, *159*, B96.

(8) Topalov, A. A.; Cherevko, S.; Zeradjanin, A. R.; Meier, J. C.; Katsounaros, I.; Mayrhofer, K. J. J. Towards a Comprehensive Understanding of Platinum Dissolution in Acidic Media. *Chem. Sci.* **2014**, *5*, 631–638.

(9) Topalov, A. A.; Katsounaros, I.; Auinger, M.; Cherevko, S.; Meier, J. C.; Klemm, S. O.; Mayrhofer, K. J. J. Dissolution of Platinum: Limits for the Deployment of Electrochemical Energy Conversion? *Angew. Chemie - Int. Ed.* **2012**.

(10) Rudi, S.; Gan, L.; Cui, C.; Gliech, M.; Strasser, P. Electrochemical Dealloying of Bimetallic ORR Nanoparticle Catalysts at Constant Electrode Potentials. *J.*

Electrochem. Soc. **2015**, *162*, F403–F409.

(11) Antolini, E.; Salgado, J. R. C.; Gonzalez, E. R. The Stability of Pt–M (M=first Row Transition Metal) Alloy Catalysts and Its Effect on the Activity in Low Temperature Fuel Cells. *J. Power Sources* **2006**, *160*, 957–968.

(12) Chen, D.; Tao, Q.; Liao, L. W.; Liu, S. X.; Chen, Y. X.; Ye, S. Determining the Active Surface Area for Various Platinum Electrodes. *Electrocatalysis* **2011**, *2*, 207–219.

(13) Rudi, S.; Cui, C.; Gan, L.; Strasser, P. Comparative Study of the Electrocatalytically Active Surface Areas (ECSAs) of Pt Alloy Nanoparticles Evaluated by Hupd and CO-Stripping Voltammetry. *Electrocatalysis* **2014**, *5*, 408–418.

(14) Avanesian, T.; Dai, S.; Kale, M. J.; Graham, G. W.; Pan, X.; Christopher, P. Quantitative and Atomic-Scale View of CO-Induced Pt Nanoparticle Surface Reconstruction at Saturation Coverage via DFT Calculations Coupled with in Situ TEM and IR. *J. Am. Chem. Soc.* **2017**, *139*, 4551–4558.

(15) Zhang, J.; Mo, Y.; Vukmirovic, M. B.; Klie, R.; Sasaki, K.; Adzic, R. R. Platinum Monolayer Electrocatalysts for O 2 Reduction: Pt Monolayer on Pd(111) and on Carbon-Supported Pd Nanoparticles. *J. Phys. Chem. B* **2004**, *108*, 10955–10964.

(16) Stamenković, V.; Schmidt, T. J.; Ross, P. N.; Marković, N. M. Surface Composition Effects in Electrocatalysis: Kinetics of Oxygen Reduction on Well-Defined Pt 3 Ni and Pt 3 Co Alloy Surfaces. *J. Phys. Chem. B* **2002**, *106*, 11970–11979.

(17) Kongkanand, A.; Ziegelbauer, J. M. Surface Platinum Electrooxidation in the Presence of Oxygen. *J. Phys. Chem. C* **2012**, *116*, 3684–3693.

(18) Deegan, R. D.; Bakajin, O.; Dupont, T. F.; Huber, G.; Nagel, S. R.; Witten, T. A. Capillary Flow as the Cause of Ring Stains from Dried Liquid Drops. *Nature* **1997**, *389*, 827–829.

(19) Wang, D.; Xin, H. L.; Hovden, R.; Wang, H.; Yu, Y.; Muller, D. a.; DiSalvo, F. J.; Abruña, H. D. Structurally Ordered Intermetallic Platinum–cobalt Core–shell Nanoparticles with Enhanced Activity and Stability as Oxygen Reduction Electrocatalysts. *Nat. Mater.* **2012**, *12*, 81–87.

(20) Stamenkovic, V.; Mun, B. S.; Mayrhofer, K. J. J.; Ross, P. N.; Markovic, N. M.; Rossmeisl, J.; Greeley, J.; Nørskov, J. K. Changing the Activity of Electrocatalysts for

Oxygen Reduction by Tuning the Surface Electronic Structure. *Angew. Chemie Int. Ed.* **2006**, *45*, 2897–2901.

(21) Ramírez-Caballero, G. E.; Ma, Y.; Callejas-Tovar, R.; Balbuena, P. B. Surface Segregation and Stability of Core–shell Alloy Catalysts for Oxygen Reduction in Acid Medium. *Phys. Chem. Chem. Phys.* **2010**, *12*, 2209.

(22) Jia, Q.; Li, J.; Caldwell, K.; Ramaker, D. E.; Ziegelbauer, J. M.; Kukreja, R. S.; Kongkanand, A.; Mukerjee, S. Circumventing Metal Dissolution Induced Degradation of Pt-Alloy Catalysts in Proton Exchange Membrane Fuel Cells: Revealing the Asymmetric Volcano Nature of Redox Catalysis. *ACS Catal.* **2016**, *6*, 928–938.

(23) Shao, M.; Peles, A.; Shoemaker, K. Electrocatalysis on Platinum Nanoparticles: Particle Size Effect on Oxygen Reduction Reaction Activity. *Nano Lett.* **2011**, *11*, 3714–3719.

(24) Kleis, J.; Greeley, J.; Romero, N. A.; Morozov, V. A.; Falsig, H.; Larsen, A. H.; Lu, J.; Mortensen, J. J.; Dułak, M.; Thygesen, K. S.; Nørskov, J. K.; Jacobsen, K. W. Finite Size Effects in Chemical Bonding: From Small Clusters to Solids. *Catal. Letters* **2011**, *141*, 1067–1071.

(25) Hammer, B.; Norskov, J. K. Theoretical Surface Science and Catalysis — Calculations and Concepts. *Adv. Catal.* **2000**, *45*, 71–129.

(26) Nørskov, J. K.; Rossmeisl, J.; Logadottir, A.; Lindqvist, L.; Kitchin, J. R.; Bligaard, T.; Jónsson, H. Origin of the Overpotential for Oxygen Reduction at a Fuel-Cell Cathode. *J. Phys. Chem. B* **2004**, *108*, 17886–17892.

(27) Dubau, L.; Durst, J.; Maillard, F.; Guétaz, L.; Chatenet, M.; André, J.; Rossinot, E. Further Insights into the Durability of Pt_3Co/C Electrocatalysts: Formation of “hollow” Pt Nanoparticles Induced by the Kirkendall Effect. *Electrochim. Acta* **2011**, *56*, 10658–10667.

(28) Oezaslan, M.; Heggen, M.; Strasser, P. Size-Dependent Morphology of Dealloyed Bimetallic Catalysts: Linking the Nano to the Macro Scale. *J. Am. Chem. Soc.* **2012**, *134*, 514–524.

(29) Hwang, B. J.; Sarma, L. S.; Chen, J. M.; Chen, C. H.; Shin, S. C.; Wang, Q. R.; Liu, D. G.; Lee, J. F.; Tang, M. T. Structural Models and Atomic Distribution of Bimetallic

Nanoparticles as Investigated by X-Ray Absorption Spectroscopy. *J. Am. Chem. Soc.* **2005**, *127*, 11140–11145.

(30) Jia, Q.; Caldwell, K.; Strickland, K.; Ziegelbauer, J. M.; Liu, Z.; Yu, Z.; Ramaker, D. E.; Mukerjee, S. Improved Oxygen Reduction Activity and Durability of Dealloyed PtCo X Catalysts for Proton Exchange Membrane Fuel Cells: Strain, Ligand, and Particle Size Effects. *ACS Catal.* **2015**, *5*, 176–186.

(31) Strasser, P.; Koh, S.; Anniyev, T.; Greeley, J.; More, K.; Yu, C.; Liu, Z.; Kaya, S.; Nordlund, D.; Ogasawara, H.; Toney, M. F.; Nilsson, A. Lattice-Strain Control of the Activity in Dealloyed Core–shell Fuel Cell Catalysts. *Nat. Chem.* **2010**, *2*, 454–460.

(32) Colón-Mercado, H. R.; Popov, B. N. Stability of Platinum Based Alloy Cathode Catalysts in PEM Fuel Cells. *J. Power Sources* **2006**, *155*, 253–263.

(33) Yu, P.; Pemberton, M.; Plasse, P. PtCo/C Cathode Catalyst for Improved Durability in PEMFCs. *J. Power Sources* **2005**, *144*, 11–20.

(34) Kocha, S. S.; Garsany, Y.; Myers, D. Testing Oxygen Reduction Reaction Activity with the Rotating Disc Electrode Technique http://energy.gov/eere/fuelcells/downloads/testing-oxygen-reduction-reaction-activity-rotating-disc-electrode (accessed Sep 14, 2016).

(35) Perez-Alonso, F. J.; Elkjær, C. F.; Shim, S. S.; Abrams, B. L.; Stephens, I. E. L.; Chorkendorff, I. B. Identical Locations Transmission Electron Microscopy Study of Pt/C Electrocatalyst Degradation during Oxygen Reduction Reaction. *J. Power Sources* **2011**, *196*, 6085–6091.

(36) Shinozaki, K.; Pivovar, B. S.; Kocha, S. S. Enhanced Oxygen Reduction Activity on Pt/C for Nafion-Free, Thin, Uniform Films in Rotating Disk Electrode Studies. *ECS Trans.* **2013**, *58*, 15–26.

Chapter 7: Activity Measurements in the GDE

7.1 Introduction

Various methods for determining catalytic activity exist, including the RDE,[1] floating electrode,[2] and gas diffusion electrode (GDE)[3] techniques as well as testing in fuel cell stacks and MEAs,[4,5] which result in a range of recorded values for mass and specific activities. A comparison of the activity of a variety of Pt catalysts measured using RDE and MEA type experiments is presented in work by Debe.[6]

The work and discussion presented in this chapter arose when comparing the catalytic activity measured using the typical RDE method and the less frequently used GDE. The motivation for this was to explore the observed differences between activities measured using the RDE and under true fuel cell conditions in a membrane electrode assembly (MEA), see Figure 1, and to find a suitable lab scale method that could reproduce these results.

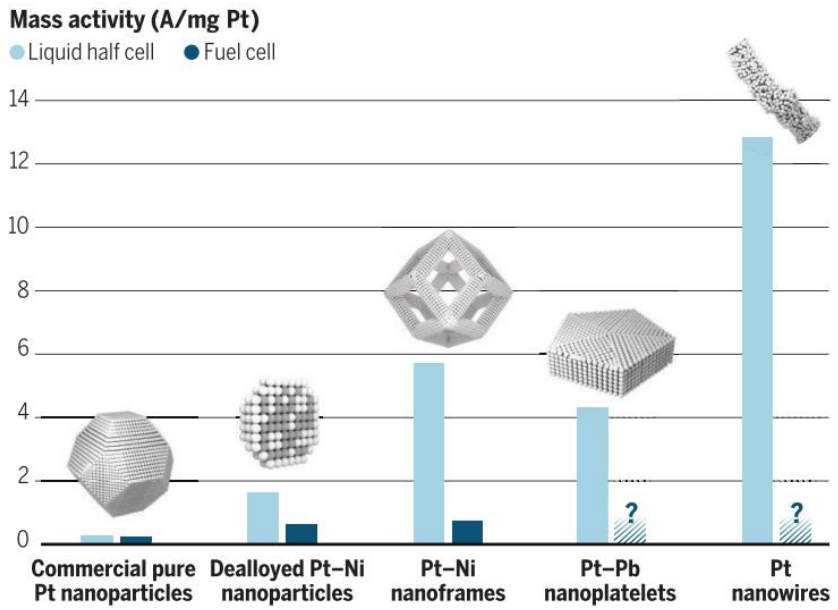

Figure 1 Comparison of the activities of several Pt based electrocatalysts measured using liquid half cell experiments, typically the RDE technique, in comparison to performance in a fuel cell stack. Figure reproduced from work by Stephens *et al.*[7]

This discrepancy between activity measurements, along with an apparent limiting surface-specific current density at around 0.1 A cm^{-2},[8] has been linked with mass transport of reactants through the Nafion ionomer. When the Pt loading is reduced, or at higher current density, more protons and O_2 are required to reach the Pt surface. The supply of O_2 in particular has been shown to be problematic and has led to the coining of the term 'local O_2 resistance.' This resistance has been identified as a way of reconciling the high activity achieved in liquid half cells with the fuel cell performance.

An alternative hypothesis proposed by Stephens *et al.*[7] is that at increasingly high overpotentials, the electrode kinetics are only negligibly improved, thus the presence of a limiting current density is observed. Consequently, more active catalysts should reach this overpotential sooner, and when operating above this overpotential, the surface-specific activity of different catalysts become equivalent.

The GDE was chosen because this configuration contains a three phase interface, allowing gaseous O_2 to be used rather than relying on the solubility and diffusion of O_2 in the electrolyte, making the technique more comparable to real world operating conditions *i.e.* operation at high power, high overpotentials and high current density. It is also operated in a three electrode system as a half cell thereby avoiding some of the complications that arise in a MEA in a fuel cell such as parasitic currents from H_2 crossover, less precise knowledge of electrode potentials, and concentration gradients across the electrode.

Other half cell configurations are also able to access the high current density regime relevant to fuel cell operation. For example, Zalitis *et al.*[2] have presented a floating electrode design capable of achieving current densities two orders of magnitude greater than in the RDE. The main advantage of the GDE system used in this work over the floating electrode is the similarity of the ink composition and electrode structure to that used in fuel cell tests *i.e.* in both cases the catalyst ink is applied to a wet-proofed carbon paper gas diffusion layer to a Pt loading on the order of 0.2 mg_{Pt} cm^{-2}. In contrast, the floating electrode employs PCTE substrates, which allows an ideal configuration with catalyst particles situated close to straight gas channels as opposed to the thicker (0.205 mm) and more tortuous carbon paper. A comparison of these configurations is shown in Figure 2. The primary difference between the GDE is the absence of the Nafion polymer membrane typically used in MEAs to separate the anode and cathode.

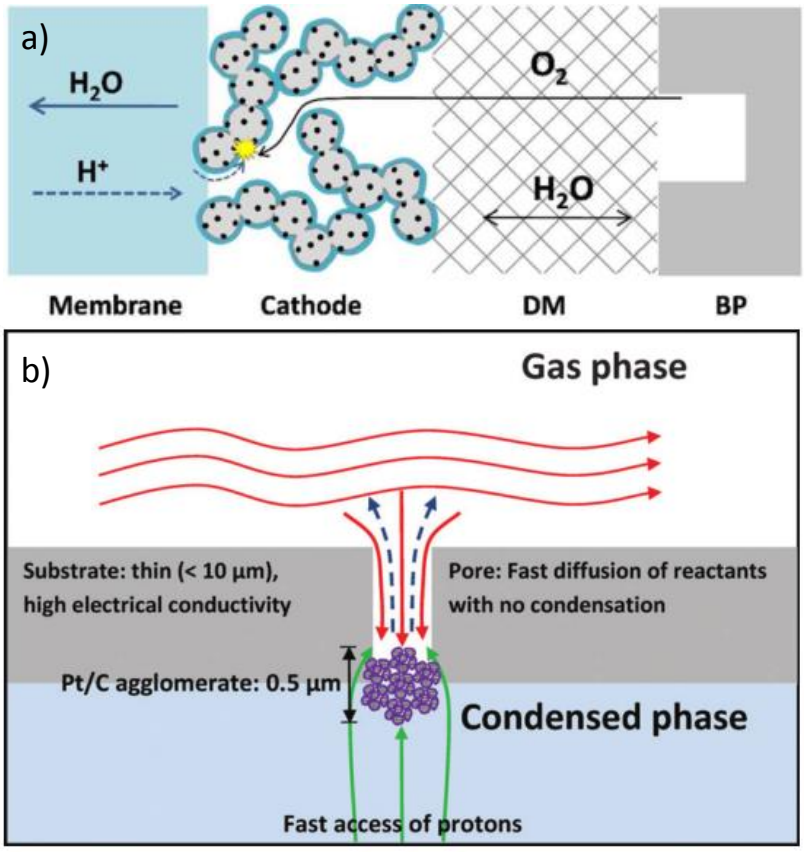

Figure 2 Depictions of the electrode structure in a) an MEA, taken from Kongkanand and Mathias,[8] and b) the floating electrode by Zalitis et al.[2] DM stands for diffusion media, and BP is the bipolar plate current collector. The GDE used here is comparable to the a), the MEA, with the main difference being the replacement of the membrane with liquid electrolyte. The current collector structure is also different, but of no importance.

An important parameter to be measured when studying electrocatalytic activity is the electrochemically active surface area (ECSA). On Pt, this can be done easily using the H adsorption and desorption features observed via cyclic voltammetry or by adsorbing and subsequently oxidising a monolayer of CO from the surface. By integrating the charge representing any of these features, the surface area can be calculated by assuming that the charge required for the single electron process, adsorption or desorption of a monolayer of H on atop sites is 210 µC cm^{-2}, and double that for the oxidation of CO molecules adsorbed on atop sites. CO adsorption is often preferred to H adsorption/desorption when studying Pt nanoparticles, and in particular for segregated Pt alloys, due to the altered electronic structure of the surface.[9] Other methods are also possible, such as utilising the underpotential deposition of Ag,[10] and Cu,[11] CO displacement, $PtOH/PtO_x$ adsorption and double layer charging capacitance.[11] Common drawbacks of these techniques include uncertainties over the bonding mode or site *e.g.* whether CO bonds in atop or bridging configuration, and whether monolayer coverage is achieved, which is particularly relevant

for the underpotential deposition methods. The CO monolayer oxidation and H adsorption and desorption methods are the most common, and both will be used in this chapter. Use of these two methods was discussed in a previous chapter.

In a fuel cell system, the ECSA could be considered as dynamic due to the changing humidity and water content in the MEA. The gas supplies to the MEA are humidified, and water is also produced at the cathode by the ORR, however the operating temperature of the fuel cell leads to evaporation and as a result must be carefully managed as the optimal three phase interface is disrupted by the build-up of water obstructing gas channels. Catalyst layer flooding is apparent for some of the results obtained using the GDE and presented in this chapter. Methods by which this can be quantified in the GDE are postulated and may further understanding of the flooding process in the fuel cell MEA.

7.2 Experimental

As a result of observations made in preliminary experiments, the catalysts analysed in this chapter were restricted to carbon supported Pt nanoparticles, Pt/C.

The results displayed here were collected with assistance from undergraduate project students Peter Mardle, and Jake Lawrie-Ashton.

7.2.1 RDE

Thin film modified GC RDE tips are commonly used to analyse the performance of catalysts. The methodology has been outlined in previous chapters. In brief, a 3 µL drop of ink (~10 mg catalyst powder, 6.00 mL water:IPA mix, 25:75 ratio, 30 µL 5.77% Nafion solution in IPA) was dropped onto a polished (sequentially 1, 0.3, and 0.05 µm alumina, 0.196 cm^2) GC RDE tip whilst rotating the tip at 100 RPM. The thin film was dried at 600 RPM in air. Characterisation of the thin film and catalyst ink has been presented previously. As before conditioning scans (100 scans at 500 mV s^{-1}, 0.0 – 1.0 V *vs.* RHE) in N_2 purged 0.1 M $HClO_4$, before the ECSA and catalytic activity were determined.

7.2.2 Button electrodes

Large teflonated carbon paper discs (32 mm diameter) were coated with the catalyst to a loading of 0.2 mg_{Pt} cm^{-2}. The ink used consisted of ~0.5 g catalyst powder and ~2.9 g of Nafion solution (11.92% solids in alcohol) such that equivalent amounts by mass of both carbon and Nafion were used. This was then mixed using an anticyclone planetary ball mixer for 7 minutes total, with time allowed for cooling after 2 and 5 minutes. The catalyst

ink was brush coated onto the carbon paper disks, where each layer was dried on a hotplate at 85 ^{o}C before addition of the next. The loading was calculated based on the mass of catalyst added, remembering to account for the ionomer weight. The electrodes were hot pressed at 177 ^{o}C under a 4 kg weight. The temperature was chosen to be close to the glass transition point for Nafion. Multiple disks (11 mm diameter) were cut out from each of the larger disks for use as electrodes to improve the consistency of Pt loading.

Before any electrochemical experiments were done, the button electrodes were first immersed in high purity water whilst under vacuum to forcefully hydrate the catalyst layer thereby ensuring all of the catalyst is in contact with the electrolyte. Full hydration was assumed once the electrode sunk rather than floated to the surface. The carbon paper disks were held in a loop of gold wire and used as the working electrode in a conventional water jacketed 3 necked cell alongside a Pt gauze counter electrode and a homemade MMS reference electrode. All potentials are reported against the RHE, and the temperature was typically maintained at 25 ^{o}C.

Conditioning scans (25 scans, 0.0 – 1.0 V *vs.* RHE, 50 mV s^{-1}) were carried out in N_2 purged 1 M H_2SO_4 until reproducible cyclic voltammograms were obtained. The ECSA was determined using the H_{upd} method as well as CO monolayer oxidation. For both methods, a scan rate of 10 mV s^{-1} was used, and CO was adsorbed at 0.15 V *vs.* RHE whilst bubbling CO through the solution for 15 minutes. Excess CO was removed by purging with N_2 for at least 30 minutes.

7.2.3 GDE

The same catalyst coated electrodes were also used in the GDE setup, the schematic for which is presented in Figure 3, although the wire used to make electrical contact was changed from nickel to platinum such that work in acidic environments could be performed.

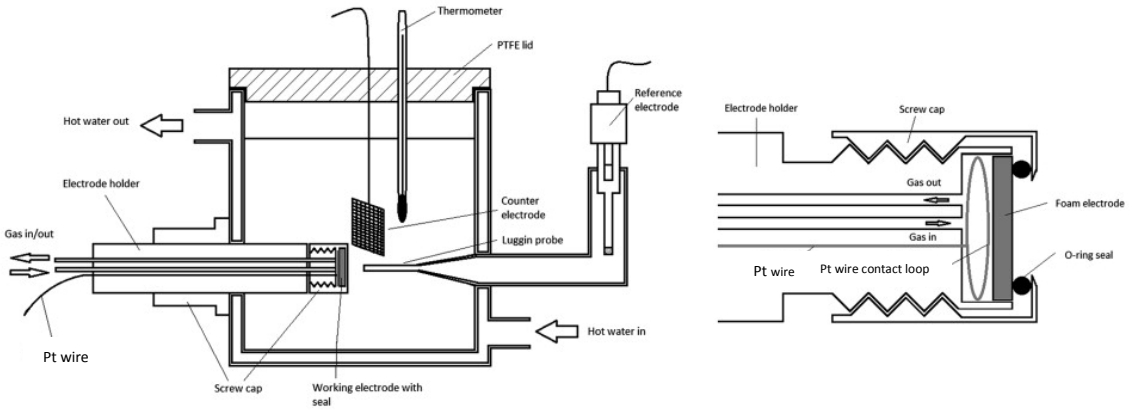

Figure 3 Schematic showing an example of the design for the cell employed when performing experiments with the gas diffusion electrode. This design in particular has been used to study bifunctional oxygen electrodes for use in alkaline secondary batteries, and is taken from the paper by Price *et al.*[12]. The cell was modified for work in acidic environments by swapping the Ni wire for Pt. a) the full cell diagram, and b) close up view of the gas diffusion electrode insert.

Care must be taken when assembling the gas diffusion electrode cell to ensure that the O-ring, electrode and the contact loop are aligned to prevent electrolyte leakage and ensure good electrical contact. Overtightening of the cap resulting in damage to the electrode must also be avoided.

Conditioning treatment was carried out in the same way as done for the button electrodes in the three necked cell, with the temperature again maintained at 25 ^{o}C. Typically, 1 M $HClO_4$ was used as the electrolyte, although some preliminary experiments were performed in H_2SO_4 and using different acid concentrations.

When determining the ECSA using CO, two methods of supplying CO to the electrode are explored. Firstly, the gas can be bubbled through the electrolyte for a period of time as done in the RDE and button electrode studies. For the GDE, N_2 was also passed through the gas channels behind the electrode to avoid the effects of exposure to atmospheric O_2. Alternatively, CO can be directly supplied to the reverse side of the electrode through the gas channels in the insert, whilst the electrolyte solution is purged with N_2 to avoid O_2 dissolution. These methods will be referred to as CO (sol) and CO (gas) respectively. The potential treatment is otherwise identical. Both the electrolyte and the gas channels are thoroughly purged with N_2 for at least 30 minutes before the adsorbed CO monolayer was electrochemically oxidised.

Unlike the RDE, a mass transport limited current is not reached for the ORR under the typical potential window used due to the fact that O_2 is supplied in the gas phase and is

therefore at higher effective concentration than O_2 dissolved in the electrolyte. Gas diffusion electrodes are designed to operate with a high limiting current such that the current measured at potentials of interest in fuel cell applications is close enough to the kinetic current such that mass transport corrections can be neglected.

The RDE method relies on the ability to control and define the limiting current by altering rotation rate. The measured limiting current must be corrected for mass transport, thereby yielding the kinetic current, which can be normalised by the ECSA or mass of Pt used.

The dissolved O_2 concentration in 0.1 M $HClO_4$ (O_2 purged) is around $1.26*10^{-6}$ mol cm^{-3} (value taken from a paper by Wang *et al.*[13]), whilst as a pure gas at atmospheric pressure and temperature, it is estimated to be two orders of magnitude greater at $2*10^{-4}$ mol cm^{-3}. The diffusion coefficient of O_2 in the electrolyte is $1.93*10^{-5}$ cm^2 s^{-1}. In the GDE, the diffusion coefficient is affected by the properties of the gas diffusion layer, *i.e.* the teflonated carbon paper, and the effective diffusion coefficient can be calculated based on Equation 1, where δ is the constrictivity, τ is the tortuosity, ϕ is the pore fraction, and D is the diffusion coefficient in air in cm^2 s^{-1}. The values used in the calculation were D = 0.226 cm^2 s^{-1}, δ = 0.028 (assuming the mean pore diameter to 2631 nm and the diameter of O_2 molecules to be 0.12 nm), τ = 2.76 and ϕ = 0.6306, and were found in papers by Zalitis *et al.*[2] and El-Kharouf *et al.*[14]

$$\boldsymbol{D_{eff} = \frac{\phi\delta}{\tau} D}$$

Equation 1

Based on this, D_{eff} for this GDE was estimated to be 0.0014 cm^2 s^{-1}. The O_2 will also have to diffuse through the acid/ionomer layer surrounding the Pt/C catalyst, which is likely to be thicker than in typical thin film catalyst layers drop cast onto RDE tips due to the composition of the ink.

Zalitis *et al.*[2] devised an equation for determining the limiting current in their floating electrode and found that for ORR, the limiting current was 448 A cm^{-2} based on the geometric surface area of the catalyst layer. The limiting current for the gas diffusion electrode is expected to be lower than this based on the increased thickness and tortuosity of the gas diffusion layer compared to the floating electrode.

Gas flow for all gases to the back of the electrode was maintained at 3 cm^3 s^{-1}. The effect of gas flow was investigated, but found to have no impact on the measured current over the studied range in potentials and gas flow (1 – 6 cm^3 s^{-1}). This suggests that the limiting step is the dissolution and diffusion of O_2 into the acid film and ionomer layer surrounding the catalyst particles.

A typical decrease in current when using compressed air in place of pure O_2 is observed due to the lower O_2 partial pressure. Humidification of the gas flow to the reverse face of the electrode was achieved by flowing the gas through a Dreschel bottle containing ultra-pure water. Humidification was beneficial in terms of the activity, but caused other problems due to contamination of the system with dissolved metal ions originating from the flow meter.

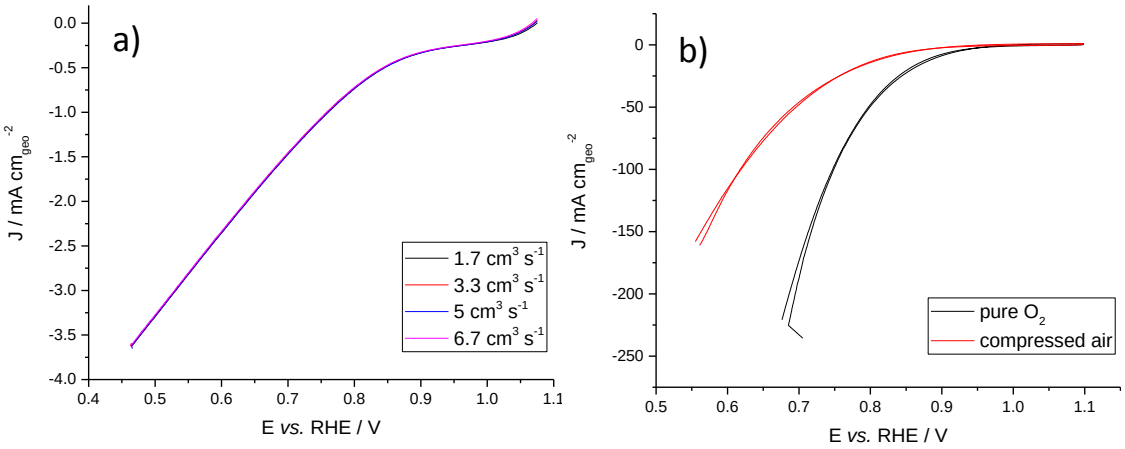

Figure 4 The effect of changing a) the flow rate (2 nm Pt/C in 0.1 M $HClO_4$) and b) the partial pressure of O_2 (5 nm Pt/C in 1 M $HClO_4$) on the electrochemical response of Pt/C in the GDE. The four measurements at different flow rates were carried out on the same electrode, and a separate electrode was used for the two measurements involving O_2 partial pressure. The data has been iR corrected using the resistance determined via impedance.

Due to the high currents involved, correction for iR drop is important. The high frequency intercept of the Nyquist impedance plot was used to determine the resistance as done with the RDE measurements earlier. To minimise the uncompensated resistance and any errors introduced when calculating the correction, higher concentrations of $HClO_4$ were investigated. These results are presented in Figure 5.

The measured response is highly dependent on the concentration; even after correcting for iR drop, much higher current densities are accessible when using higher concentrations of acid. The final experiments will be conducted in 1 M $HClO_4$, which represents a compromise between minimising the uncompensated resistance, catalyst degradation (particularly for

the alloys) and any effects due to anion adsorption blocking active sites. The resistance is only marginally decreased when increasing the concentration to higher than 1 M. However, other published work employs higher concentration electrolyte when using similar electrode configurations.[2,15]

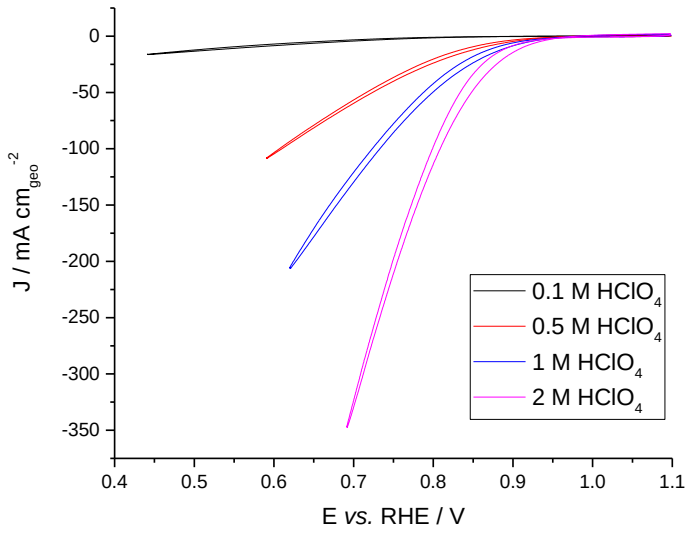

Figure 5 CVs at 10 mV s^{-1} in $HClO_4$ of varying concentration whilst supplying O_2 gas to the electrode. The Pt loading was 0.2 mg_{Pt} cm^{-2}, and the exposed geometric area was 0.502 cm^2. The resistance was measured using the high frequency intercept of the impedance Nyquist plot, and ranged from 17.5 Ω in 0.1 M $HClO_4$ to 2.5 Ω in 2 M $HClO_4$.

The effect of Pt loading on the electrochemical response observed in the GDE was recorded and the results are shown in Figure 6, with the measured ECSAs displayed in Figure 7. As would be expected, larger H_{upd}, double layer capacitance and oxide regions can be observed at higher loadings. The amount of Pt on the carbon support was kept constant at 30% by weight, so the thickness of the layers will also increase. This is probably offset to some extent by hot pressing the electrodes.

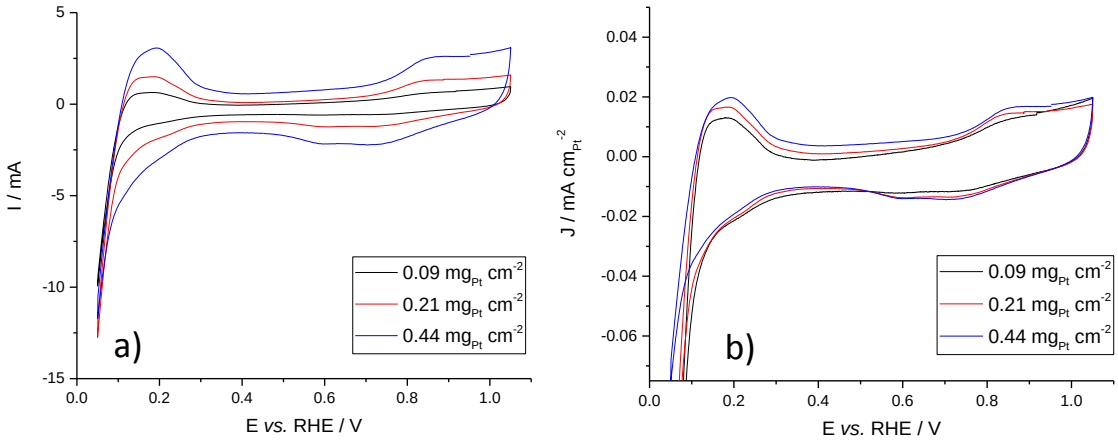

Figure 6 Loading study for the 2 nm Pt/C coated electrodes in the GDE with an exposed geometric area of 0.502 cm^2. CVs carried out in N_2 purged 1 M $HClO_4$ at 10 mV s^{-1}, whilst flowing N_2 to the back of the electrode. CVs presented a) as measured, and b) normalised by ECSA, which was determined form the hydrogen desorption region.

There is a lack of definition of the strong and weak hydrogen ads/desorption peaks in these CVs, and while broader peaks are to be expected for Pt/C compared to ideal Pt surfaces due to both the particle size distribution and the absence of extended crystal faces, these peaks typically can still be observed. This can be seen in Figure 13, which shows a CV of an electrode, coated with the same catalyst, where the catalyst layer has been forcefully flooded and immersed in the electrolyte.

Figure 7 shows the ECSA that has been calculated from the H desorption peaks. A linear fit to the experimental data points yields a gradient of 300 ± 16 cm^2 mg$_{Pt}^{-1}$ and an intercept of 24 ± 4 cm^2. The intercept is not due to either the Pt wire used to make electrical contact, as it is not exposed to the electrolyte, or the electrochemical response of the carbon paper used as the base of the electrode, which has a negligible response.

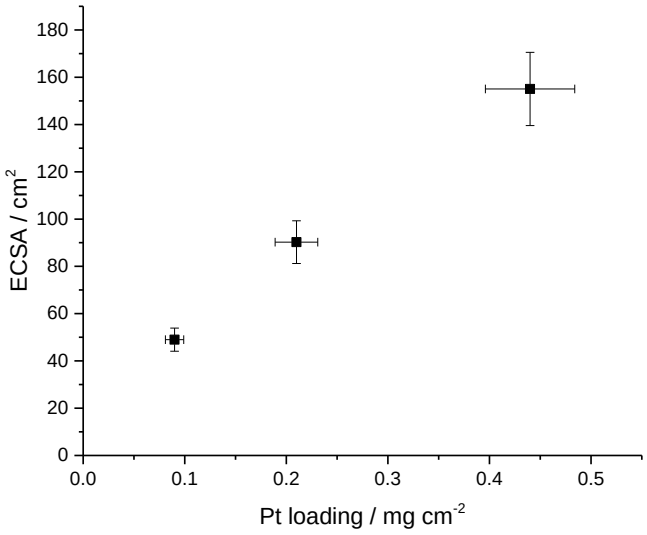

Figure 7 Plot of the change in ECSA, measured using the H desorption region, when the electrode loading is increased. Error bars have been (arbitrarily) set at 10% of both the x and y values. The biggest errors likely arise from the possibility of uneven coating of the electrode and the difficulty in estimating the charge associated with H desorption. Extrapolation of the points yields a y-intercept of 24 cm^2. However, control experiments (not shown here) have shown that this is not due to the carbon paper or Pt wire contact.

The electrochemical response of the Pt/C in the GDE when supplying O_2 through the gas channels to the back of the electrode is displayed in Figure 8. The currents have been normalised by the geometric area and mass of Pt respectively.

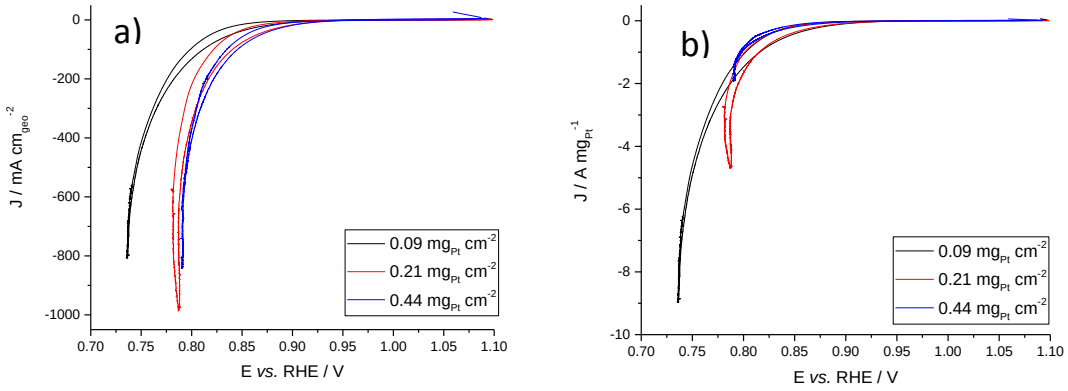

Figure 8 CVs, performed at 10 mV s^{-1} in 1 M $HClO_4$ whilst supplying O_2 gas to the electrode, for 2 nm Pt/C coated electrodes at several Pt loadings. Data normalised by a) exposed geometric area, 0.502 cm^2, and b) mass of Pt. Mass of Pt was calculated from mass of catalyst applied to the carbon paper to make the electrode. IR correction has been applied based on the resistance determined using impedance.

Table 1 Performance of the 2 nm Pt/C catalyst as evaluated by the GDE method. Potentials are referenced to the RHE.

Loading / mg_{Pt} cm^{-2}	ECSA / m^2 g_{Pt}^{-1}	-J @ 0.9 V / µA cm_{Pt}^{-2}	-J @ 0.9 V / A mg_{Pt}^{-1}
0.09	110	25.1	0.027
0.21	86	25.4	0.027
0.44	70	49.6	0.020

7.3 Results and Discussion

7.3.1 Catalyst Activity

7.3.1.1 MEA

The data were provided by JMTC, and are presented as received since the individual data points are unavailable. The measurements were carried out in a purpose built fuel cell test stand using an MEA incorporating teflonated carbon paper disks coated with commercially available Pt/C and the ORR catalyst of interest as the anode and cathode respectively. The cathode loading is several times higher than the anode loading due to the difference in reaction kinetics for H_2 oxidation and O_2 reduction. Electrodes were placed at either side of a sheet of Nafion (117) and hot-pressed. The activity was determined using pure, humidified (relative humidity = 100%) H_2 and O_2 in a 1.5:10 molar ratio with an initial pressure of 50 kPa and measured at 80 ^{o}C. The specific and mass activities for the 2 nm Pt/C (denoted Pt/C), 5 nm Pt/C (denoted AN-Pt/C), PtNi/C and PtCo/C catalysts are displayed in Figure 9 and Figure 10. The potential is reported against the RHE, and the resistance was measured using the current interrupt method to allow for iR correction.

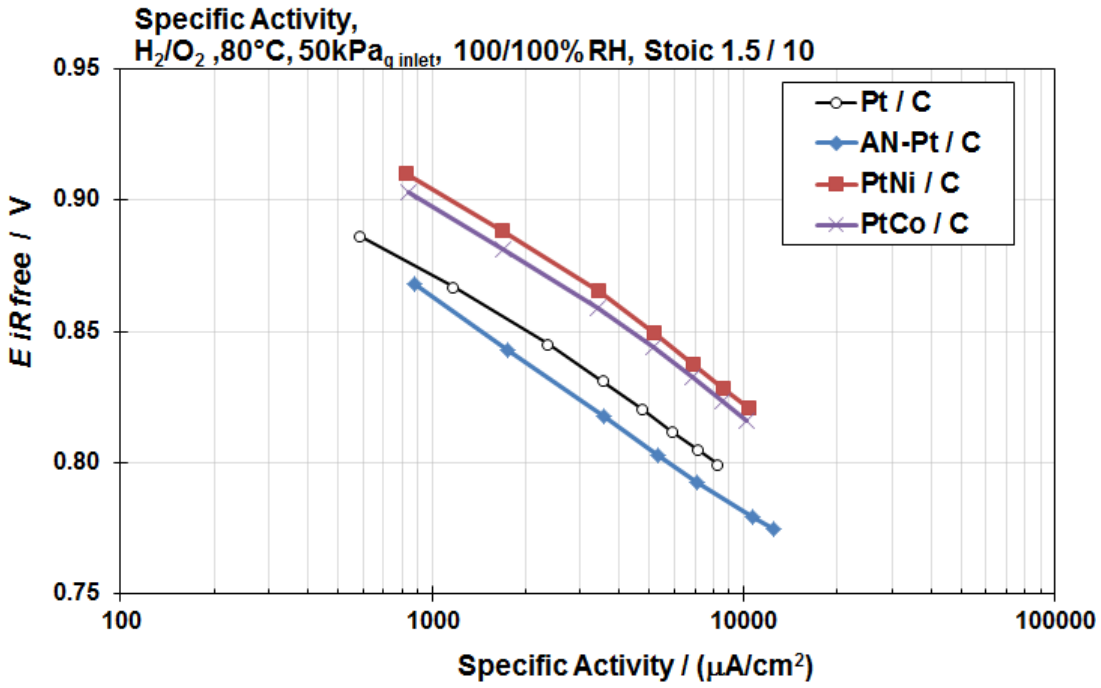

Figure 9 Specific activity measured using an MEA in a fuel cell test stand. The catalyst denoted AN-Pt/C is the 5 nm Pt/C samples, whilst the catalyst denoted Pt/C is the 2 nm sample.

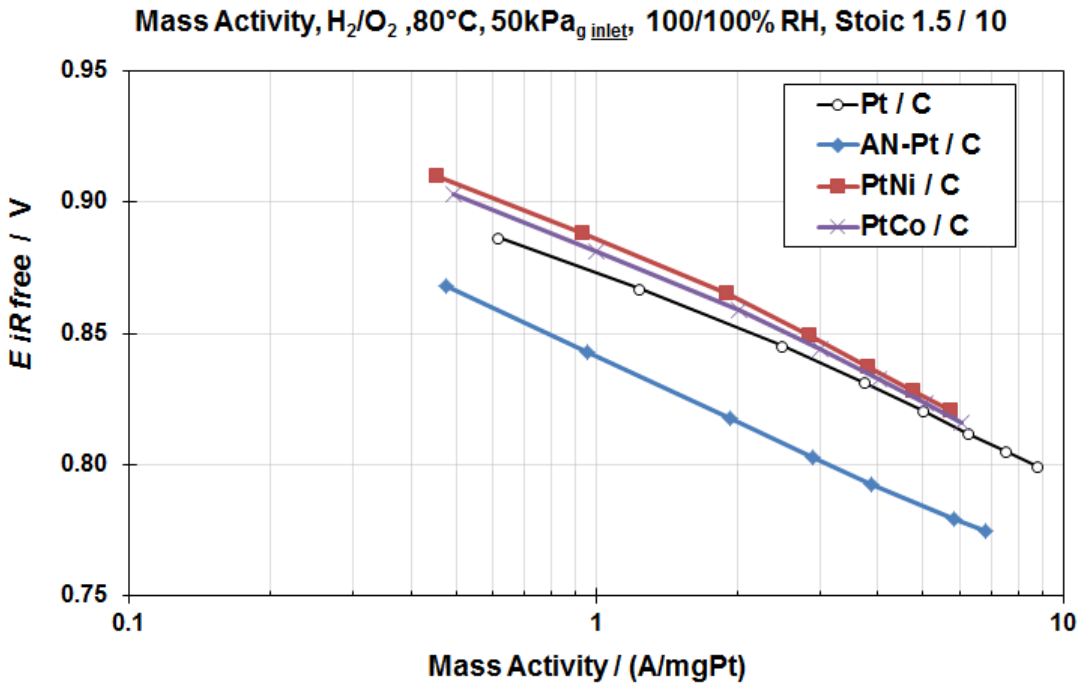

Figure 10 Mass activity measured using an MEA in a fuel cell test stand. The catalyst denoted AN-Pt/C is the 5 nm Pt/C samples, whilst the catalyst denoted Pt/C is the 2 nm sample.

The ECSA was measured using gas phase CO adsorption on the catalyst powders rather than as electrodes. A full summary of the results is shown in Table 2.

7.3.1.2 RDE

The measurements of the ECSA and catalytic activity for the various samples are shown in Figure 11. The measurements were carried out at 25 °C in N_2 or O_2 purged 0.1 M $HClO_4$ using a scan rate of 20 mV s^{-1} and the resulting activities are shown in Table 2. This data is also presented in a previous chapter.

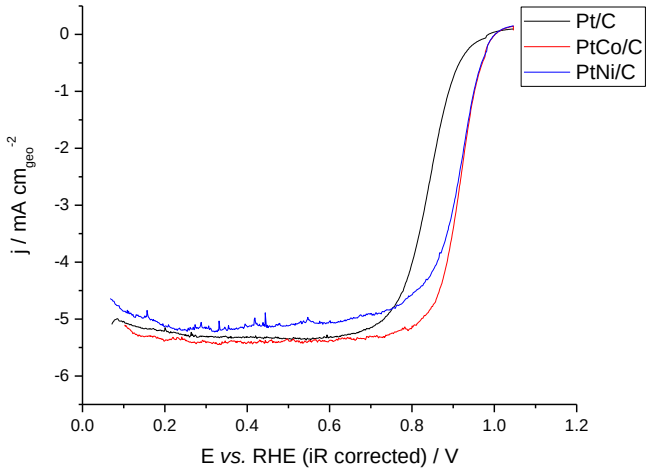

Figure 11 Comparison of the positive going potential sweeps obtaining when measuring the activity for the ORR using thin film coated GC RDE in O_2 purged 0.1 M $HClO_4$ at 20 mV s^{-1}. Repeated from previous chapter.

7.3.1.3 GDE

The activity results obtained in the GDE are displayed in Figure 12 and shown alongside the results from the other methods in Table 2. In each case the Pt loading was 0.2 mg_{Pt} cm^{-2}, the electrolyte was 1 M $HClO_4$, pure O_2 was supplied at 3.3 cm^2 s^{-1} and the voltammetry was collected at 10 mV s^{-1}.

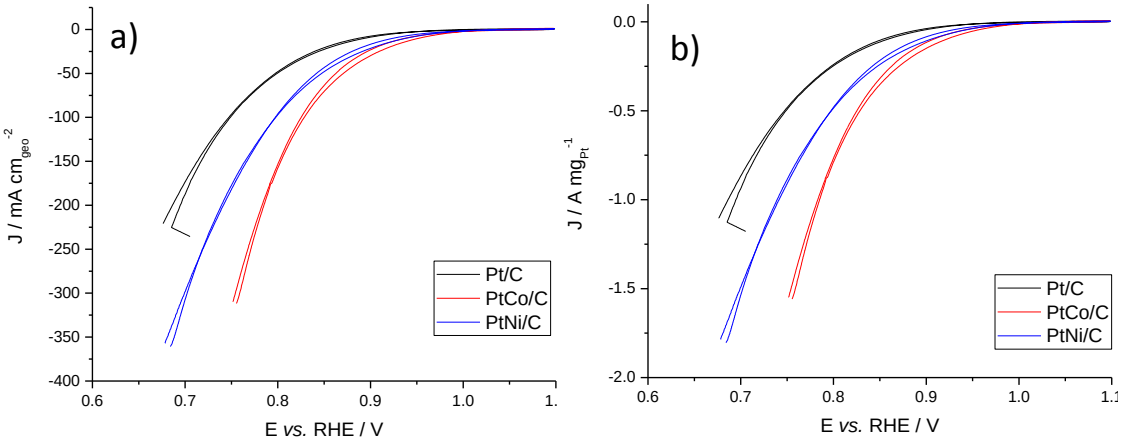

Figure 12 Comparison of the ORR activity of the 5 nm Pt/C, PtCo/C and PtNi/C catalysts measured using the GDE in 1 M $HClO_4$ at 10 mV s^{-1} whilst supplying O_2 gas to the electrode. In each case the Pt loading was 0.2 mg cm^{-2}, the exposed geometric electrode area was 0.502 cm^2, and the ECSA was determined using the CO(sol) method.

7.3.1.4 Discussion

A summary of the activities and ECSAs measured for each catalyst using the three techniques is presented in Table 2 below.

The ECSA measured electrochemically in both the RDE and the GDE are comparable, and are also consistent with the value obtained by CO chemisorption. The main differences are with the measured activities that sometimes vary by up to several orders of magnitude. The reasons for this will be discussed. For comparison, the floating electrode work by Zalitis *et al.*[2] achieved a geometric activity of ~80 mA cm_{geo}^{-2} at 0.7 V vs. RHE with a 60% Pt/C catalyst, approximately half of the measured activity in the GDE used in this work for a 30% Pt/C sample.

Table 2 Summary of the performance of the 5 nm Pt/C, PtNi/C and PtCo/C catalysts as measured in an MEA, using the RDE and using the GDE. The activities are measured at 0.9 V *vs.* RHE. ECSA listed as the MEA technique where measured by CO chemisorption rather than via electrochemistry.

Catalyst	Type	ECSA / $m^2\ g_{Pt}^{-1}$	Specific activity / µA cm_{Pt}^{-2}	Mass activity / A mg_{Pt}^{-1}
Pt/C	RDE	46 ± 7	299 ± 16	137 ± 24
Pt/C	GDE	40	110	0.044
Pt/C	MEA	37.4	350	0.37
PtNi/C	RDE	56 ± 2	1493 ± 405	836 ± 230
PtNi/C	GDE	48	221	0.107
PtNi/C	MEA	50.2	1150	0.63
PtCo/C	RDE	35 ± 4	2648 ± 346	909 ± 83
PtCo/C	GDE	49	303	0.150
PtCo/C	MEA	44.1	950	0.54

There are several factors that contribute to the observed differences in the specific and mass activities as a function of the testing method. The electrochemical procedure used for the testing, the way in which the catalyst layers and inks were prepared, and finally the electrode environment during the procedure.

The electrochemical treatment in both the GDE and RDE measurements is identical with the exception of the scan rate used: 20 mV s^{-1} was used for the RDE whilst 10 mV s^{-1} was used for the GDE measurements. Whilst the Levich equation and the theory behind the

RDE shows that scan rate does not affect the limiting current there will be an impact in the low overpotential region controlled by electrode kinetics. This is due to the fact that the system at hand is not a highly reversible reaction so there will be some lag between the change in potential and achieving equilibrium. The same is true for the GDE in that preliminary experiments showed that cathodic linear sweeps, starting at 1.1 V *vs.* RHE and taken at different scan rates differ until ~0.6 V *vs.* RHE, where they converge. By using the positive going sweeps for both techniques, this effect should be minimised, as well as effects due to the presence of an oxidised Pt surface. In the MEA, a polarisation curve was used instead of voltammetry, where current is drawn from the cell and the drop in cell voltage is monitored. The response from the anode and cathode, as well as the overall potential difference between the two electrodes can be obtained. The observed voltage drop can be assigned to activation losses, Ohmic resistance from *e.g.* the Nafion membrane, and finally mass transport at high currents. Figure 9 shows the region where Ohmic losses dominate the response.

The preparation of the catalyst layer and the electrodes was also different for each technique. In the RDE, ~3 µL of dilute ink containing a small amount of Nafion and ~10 µg of catalyst powder was dropped onto the polished RDE tip and dried in air whilst rotating. This results in a thin film catalyst layer that is of a similar thickness to the carbon particles that make up the catalyst ink, the largest of which were measured to be around 10 µm in diameter. For the electrodes used in both the MEA and the GDE, carbon paper (teflonated, carbon baselayer) acting as a gas diffusion layer was coated with a thick ink containing a significant proportion of Nafion (11.92% in alcohol) and 0.5 – 1 mg of catalyst powder. These catalyst layers contain approximately 30-40 times the amount of Nafion as the thin films used for the RDE. Several layers were added until the desired loading was achieved. This leads to a layer approximately 0.2 mm thick, although once hot pressed, this probably decreases. SEM images would help to quantify this. In the MEA, the electrode is hot pressed to a Nafion membrane with a second Pt/C coated electrode on the opposite side.

The three methods each provide a unique electrode environment, which is a significant reason for the differences in the activity measured for the same catalysts.

The simplest case is in the RDE, where the low catalyst loading leads to a thin catalyst layer, which is completely hydrated by the electrolyte. The entire catalyst layer is accessible to the electrolyte, which allows fast diffusion and transfer of protons to the catalyst particles, all of which are in close proximity to the electrode surface so electrical resistance is also

minimal. The reproducible and controllable limiting step results from the concentration of dissolved O_2 and the forced convection created by electrode rotation. The measurements were carried out at room temperature (25 ^{o}C).

In the MEA, the electrolyte is completely replaced by the Nafion ionomer, which introduces a trade-off between availability of protons to the catalyst particles, potential blockage of the active Pt surface, and increasing the electrical resistance within the thicker catalyst layer. The sulfonate groups present in Nafion are likely to be adsorbed more strongly on Pt than the perchlorate anions used in the RDE measurements.[16] The Nafion membrane separating the two electrodes in the MEA must also be thick enough to physically prevent crossover of O_2 and H_2 to the opposite electrode. For the MEA measurements, the gas flows are humidified to maintain hydration of the Nafion at the operating temperature (80 ^{o}C) and the electrodes are made hydrophobic with PTFE to prevent flooding of the serpentine gas channels and the gas diffusion layer. This configuration creates the three phase interface between O_2 gas, the hydrated Nafion polymer electrolyte and the solid Pt nanoparticles, which is optimal for fast rates of ORR.

The GDE incorporates aspects from both designs. Similar to in the MEA, electrodes with thicker catalyst layers with Pt loadings ($mg_{Pt}\ cm_{geo}^{-2}$) several orders of magnitude greater than in the RDE are used. Similar to the RDE, only weakly adsorbing perchlorate anions are present in the electrolyte, although there is a large amount of Nafion incorporated into the catalyst layer itself. The electrolyte provides fast mass transfer of protons, while O_2 can be supplied directly via the gas channels. Like the RDE, the measurements were carried out at room temperature (25 ^{o}C). A small benefit was realised by humidifying the inlet gas stream, although this also increased the potential for contamination; commonly a redox couple was observed in the double layer region of the Pt CV, which was eventually attributed to the use of the flow meter in combination with the humidified gas.

When measured using the RDE the ECSA is larger for two of the catalysts than when the same catalysts are measured in the GDE, although the difference in the values is close to the experimental error and the ECSA determined for PtCo/C was higher in the GDE. Higher ECSAs are likely in the RDE experiments because of the high catalyst utilisation allowed by the thin catalyst layer, the weakly adsorbing anions present in the electrolyte and the smaller amount of Nafion present compared to the GDE. In the GDE, as will be discussed further, the amount of catalyst that is electrochemically available is somewhat uncertain. Compared to the values measured using CO chemisorption, the electrochemically

determined values are generally greater, which is somewhat surprising. One explanation for this is that a stronger driving force is applied in terms of the potential used to adsorb the CO monolayer, which may allow greater surface coverages to be achieved in the electrochemical environment.

The specific activity measured by the RDE method is generally highest, followed by the MEA and finally the GDE method, although it is important to remember that the MEA was operated at 80 ^{o}C, whilst the other measurements were taken at 25 ^{o}C. It has been suggested that when extracting the kinetic current from the raw data from the RDE, extrapolation is sometimes performed to one or more orders of magnitude away from the measured current density, which may lead to inaccuracies.[17] This arises because the measured current in the RDE reaches a mass transport limited value so, as a result, the measured current at lower overpotentials where electron transfer kinetics can be observed must be extrapolated to higher potentials. In the GDE, like in an MEA, the mass transport limited current occurs at much higher overpotentials so no extrapolation is required. For the GDE used in this work, the applied iR correction is considerable, 200-300 mV at the higher currents, although at 0.9 V *vs.* RHE the potential of interest, the correction is only 5 mV. Use of higher acid concentrations might need to be considered to minimise the uncompensated resistance. Higher acid concentrations also resulted in dramatically increased currents, as shown in Figure 5.

The GDE measurements have only been carried out in full once for each catalyst, although the preliminary experiments showed that the voltammetric response of each electrode at the same loading was comparable. Some variation between Pt loading on the electrodes is expected due to possible uneven coating. Part of the reason that the activity measured in the MEA is lower than that measured with the RDE is that due to the electrochemical procedure used, the Pt surface is oxidised in the MEA. A better comparison would be with the cathodic going sweeps measured in the RDE and GDE.

In the GDE there are perhaps some issues with accessing the entirety of the catalyst layer, for example, in Table 1 the results for the 2 nm Pt/C catalyst show that at half the Pt loading and with likely a thinner catalyst layer, the same specific activity was achieved. However the results also showed that the highest loading resulted in an increased specific activity, but decreased mass activity and ECSA. This suggests that perhaps there is a factor that was not explicitly controlled for in the experiments, possibly related to the timescale over which the experiments were performed. A longer conditioning period would help to

minimise these effects. In this work 25 CVs were used as the conditioning treatment, whereas often much longer treatments are used, *e.g.* for the RDE work 100 conditioning cycles were completed before any measurements were made, and for the work published by Koh *et al.*,[18] 200 cycles from 0.06 – 1.2 V *vs.* RHE at 100 mV s^{-1} were used.

The mass activity measured in the GDE and MEA are of a similar order of magnitude for all catalysts, with the MEA measuring slightly higher activity, although accounting for the temperature of the measurements may resolve this difference. This suggests that GDE measurements could well provide a more realistic alternative to the RDE. A thorough optimisation process including conditioning protocol, catalyst layer thickness and loading should be carried out as there are some questions remaining about how much of the catalyst layer is accessed in the GDE. Standard conditions and operating procedure similar to the existing protocols for the RDE, *e.g.* by the DOE, should also be established.

7.3.2 ECSA determination in the GDE

During the course of the activity measurements, several interesting observations regarding the electrochemical response of the Pt/C catalyst in the GDE were observed.

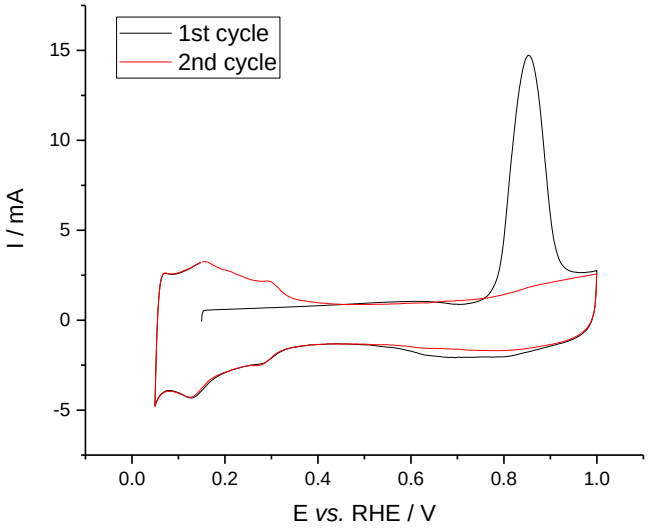

Figure 13 CO adsorbed monolayer oxidation at 10 mV s^{-1} carried out on a fully immersed Pt/C coated electrode in the three neck cell. Monolayer adsorbed by purging the electrolyte with CO whilst holding the potential at 0.15 V *vs.* RHE. The first scan showing the oxidation of the monolayer as well as the second scan both in N_2 purged 1 M $HClO_4$ are displayed. The second scan (and all following scans) shows a decrease in the area of the oxide reduction peak. The electrode was previously conditioned by potential cycles until reproducible behaviour was observed. This observation is made regardless of cell configuration.

Oxidation of an adsorbed monolayer of CO was used to determine the ECSA. An example of the typical behaviour is shown in Figure 13, in this case for a fully flooded catalyst layer, but

is also seen in the GDE measurements as well. It is interesting to note that the second, and all further, scans have a smaller oxide reduction peak than the first scan during which the CO monolayer was oxidised. The CV is otherwise identical in the hydrogen and double layer regions. The same observation can be made for CO monolayer oxidation CVs in a number of published papers,[15,19,20] but not included in any resulting discussion. A possible explanation for the additional oxide reduction charge is that the Pt surface in part is blocked by CO until higher potentials when the CO is oxidatively removed. As a result, the bare Pt surface is then exposed to a high potential allowing fast oxidation whereas during a normal CV the Pt surface is already covered with OH_{ads} or other oxide species, passivating the surface to a certain extent. Alternatively, CO may cause cleaning and reconstruction of the surface, which facilitates oxide formation leading to a larger reduction peak. Then, once the oxide has been reduced, the surface is destabilised and reconstructs to more energetically favourable crystal faces.

The method by which CO was supplied to the electrode was also found to have an impact on the calculated ECSA. If CO was flowed directly to the reverse face of electrode through the gas channels a larger surface area was recorded than if the CO was bubbled through the electrolyte. This can be seen in Figure 14.

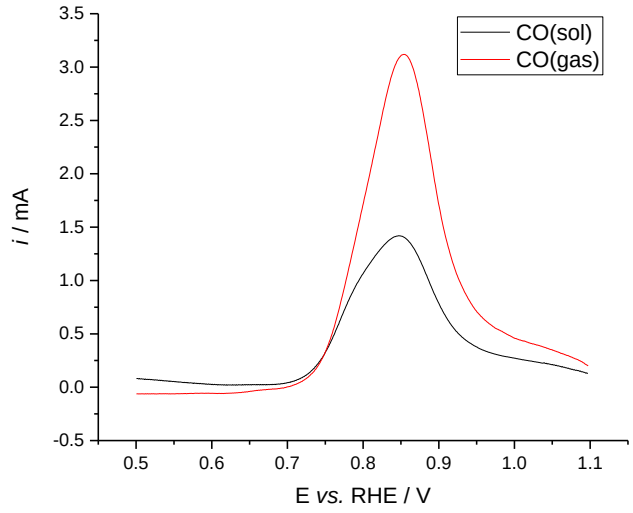

Figure 14 Oxidation, at 10 mV s^{-1}, of the adsorbed monolayer generated by purging the electrolyte (1 M $HClO_4$) with CO and by supplying CO gas to the reverse of the electrode respectively in the GDE. The electrochemical response in N_2 purged electrolyte has been subtracted. The Pt loading of the electrodes is the same, 0.2 mg_{Pt} cm^{-2}.

The more restricted electrolyte access to the electrode and catalyst layer in the GDE may have been a factor, therefore the length of time for which CO was supplied was varied for

both modes. The results when the CO(gas) method was used are shown in Figure 15, which shows that saturation levels are achieved even on the sub-minute time frame. The full set of results is presented in Figure 16. In each case the same catalyst, nominal Pt loading, and potential treatment were used.

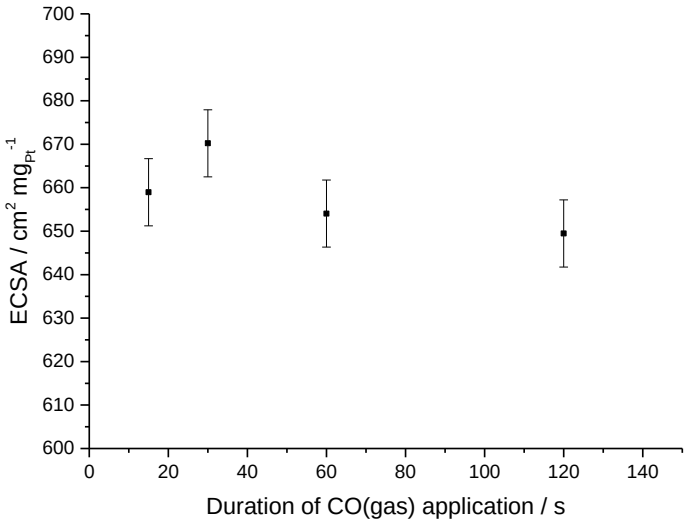

Figure 15 ECSA of the Pt/C catalyst (Pt loading 0.2 mg_{Pt} cm^{-2}) measured using the CO(gas) method, i.e. direct gaseous supply of CO through the gas channel to the electrode. The time for which the CO was supplied was varied, whilst maintaining the flow rate at 3 cm^3 s^{-1}. The error bars are taken as the standard deviation of the results: 8 cm^2 mg_{Pt}^{-1}.

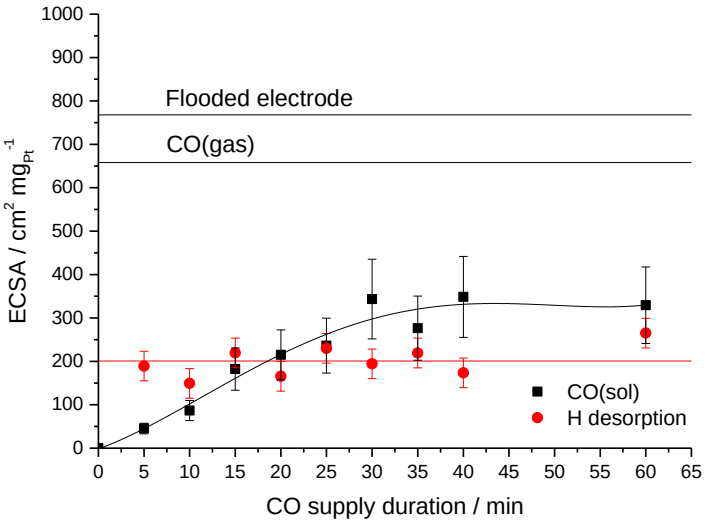

Figure 16 The ECSA of a Pt/C coated electrode determined via several methods. The maximum ECSA, 768 ± 9 cm^2 mg_{Pt}^{-1}, was measured when the electrode (A = 0.950 cm^2) was fully immersed in electrolyte in the 3 neck cell setup, denoted as 'flooded electrode'. The other measurements were obtained using the GDE where CO was supplied as both a gas and dissolved in the electrolyte for the indicated period of time. The average ECSA for the CO(gas) method was determined from Figure 15 as 658 ± 8 cm^2 mg_{Pt}^{-1} and found to be invariant with time. Lines have been added to guide the eye. The errors associated with the GDE method are largely caused by the uncertainty in the exposed geometric area (A = 0.502 cm^2) as the O-ring prevents electrolyte access to the outermost region of the electrode.

Figure 16 shows the normalised ECSA measured by each method in the GDE, alongside the values determined from the H desorption region, and the value calculated when the electrode was forcefully flooded and fully immersed in the electrolyte.

The largest area is returned from the measurement in the fully flooded and immersed state as might be expected as the catalyst layer is fully accessible. The CO(gas) methods results in a slightly decreased ECSA, whilst the CO(sol) and H desorption methods yield much smaller areas. The ECSAs have been normalised by mass to remove the differences due to the exposed geometric area. There were some concerns that the O-ring, used to seal the GDE, would allow seepage of electrolyte leading to erroneously high ECSAs, thus the diameter of O-ring used was varied. Figure 17 shows that the O-ring diameter does affect the ECSA regardless of the method (CO(gas) or CO(sol)), and, assuming a linear trend, would result in a negative intercept value and the non-physical notion of a negative ECSA. An exponential trendline might be more appropriate, although further data points would be necessary to fit the line accurately. Either way, this does suggest that a good seal is formed, and that there is a real difference in ECSA measured in the case of a flooded electrode and in the GDE.

If normalised by mass of Pt, the ECSA decreases slightly for the smaller diameter O-rings. An explanation for this could be that the size of the O-ring affects the depth or shape of the region of the catalyst layer that is electrochemically accessible, whereas the amount of Pt is assumed to be equal to the exposed area multiplied by the loading. A cartoon diagram of this is shown in Figure 18.

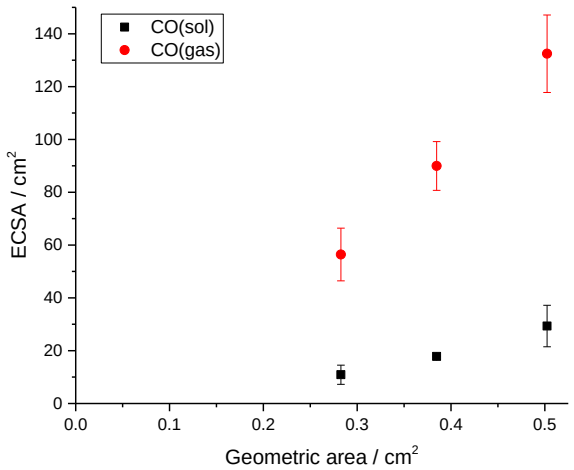

Figure 17 Plot of the ECSA measured via CO monolayer oxidation at 10 mV s^{-1} in 1 M $HClO_4$ when changing the diameter of the O-ring used to seal the GDE.

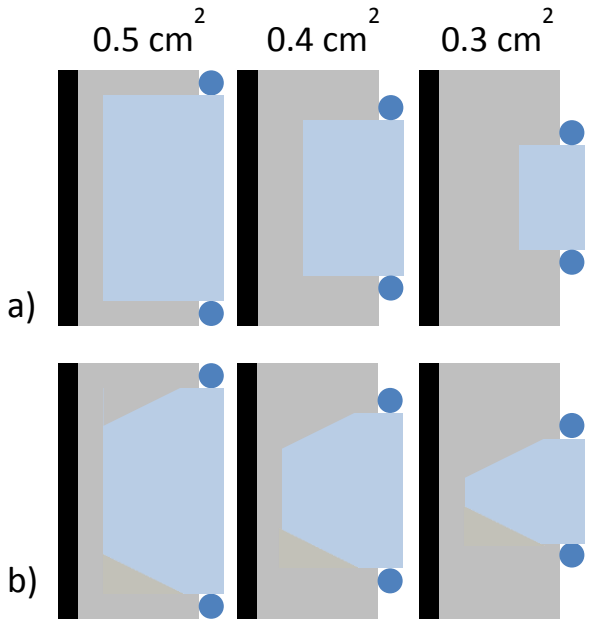

Figure 18 Cartoon illustration of the cross section of the electrode in the GDE showing how the region accessible by electrolyte changes when the O-ring size is decreased. a) Depth of electrolyte penetration into the catalyst layer is affected or b) shape of the electrochemically accessible area changes with the O-ring area. The black region indicates the carbon paper current collector, the dark blue circles are the O-ring, the grey region is the dry catalyst layer not in contact with electrolyte, and the light blue region is the electrolyte filled catalyst layer.

The data presented in Figure 16 shows that the various methods for determining the ECSA of the catalyst yield different values, and as a result suggests that a different proportion of the catalyst layer is accessible in each case. A detailed impression of the catalyst layer in the GDE holder is displayed in Figure 19 and will be referred to when discussing the ECSA measurements.

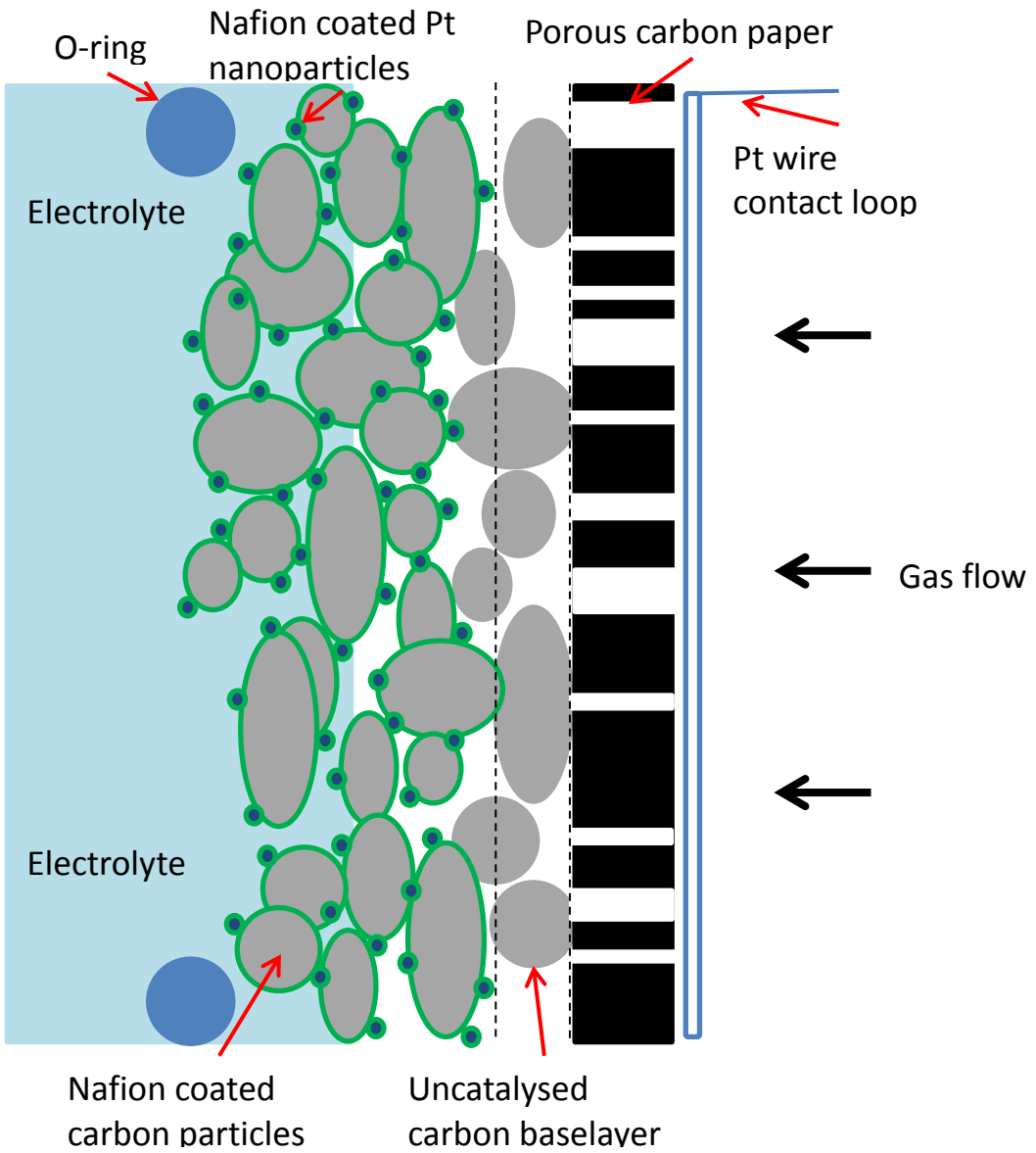

Figure 19 Detailed cartoon showing a cross section of the catalyst coated electrode in the GDE. The carbon paper gas diffusion layer is in contact with the Pt wire used to make electrical connection, has a thin layer of carbon powder (5% by weight), and has been treated with PTFE to increase hydrophobicity. The catalyst powder ink is coated onto the carbon baselayer and the screw cap applying pressure on the O-ring is used to create a watertight seal and to ensure good electrical contact. The catalyst powder consists of porous carbon particles on the 50 µm scale coated with Pt nanoparticles, which, when incorporated into the ink, will be encapsulated in a layer of the Nafion ionomer.

When the catalyst coated electrode has been forcefully filled with electrolyte and is measured whilst fully immersed in the electrolyte *i.e.* in the three necked cell, the entire catalyst layer is accessible to both the electrolyte and the dissolved CO. The areas determined using either the CO oxidation, H adsorption or H desorption peaks yield very similar results *e.g.* for the data shown in Figure 13, values of 246, 250 and 248 cm^2 are

obtained for the CO oxidation, H_{ads} and H_{des} peaks respectively. CO was dosed for 15 minutes before purging with N_2 for a further 30 minutes. Shorter dosing times will reduce the Pt surface area covered with CO, although this was not investigated in detail.

In the GDE on the other hand, significant differences in the ECSAs are measured. When dosing CO into the electrolyte solution, diffusion of the dissolved CO to the catalyst surface is hindered by the electrode holder and the restricted pathway to the catalyst as only the front face of the electrode is accessible. As a result, the CO must be supplied for a longer period of time before saturation of the surface is attained. The results from Figure 16 suggest that 30-40 minutes of CO dosing is required. The ECSA determined by this method is around 50% of the value obtained in the fully immersed case, once the exposed geometric area was considered. It is thought that electrolyte can access a fraction of the catalyst layer, which then allows diffusion of CO to the contacted Pt nanoparticles. Some amount of additional Pt surface area is accessible through hydration of the Nafion film surrounding the catalyst beyond the penetration depth of the electrolyte. Diffusion of CO through the hydrated ionomer may be possible, but the diffusion distance to additional Pt nanoparticles is large.

Negligible vapour pressure of CO above the electrolyte surface inside the electrode holder is expected based on the low concentration of dissolved CO in the saturated electrolyte - approximately 1 mM in pure water.[21] Based on Raoult's law, this leads to a vapour pressure of around 0.1 bar, which is likely to be an overestimate as electrolyte solutions containing charged species cause negative deviations to the expected behaviour from Raoult's law. The negative deviations are caused by strong attractive interactions between ions and solvation effects. The free space behind the electrode is also continually purged with N_2.

When supplying CO as a gas to the back of the electrode, there is a short diffusion path through to any Pt surfaces covered by hydrated ionomer, whilst dissolution into the electrolyte can also occur due to the high CO partial pressure, and the CO molecules are already in close proximity to the catalyst. As a result, a larger Pt ECSA is measured by this method, although not as large as when the electrode is fully immersed presumably due to some of the ionomer coating the catalyst layer remaining dry over the timescales of these experiments.

To test these hypotheses further, a lower concentration of CO gas was used for the gas phase dosing to the back of the electrode. A full sequence of CO monolayer dosing and

subsequent oxidation experiments are presented in Figure 20, including experiments with dilute (3% CO by volume, balance N_2) and pure CO. 3% CO was chosen in an attempt to mimic the estimated concentration of dissolved CO. When dosing the dilute CO into the electrolyte in either the fully immersed case or via the electrolyte in the GDE, monolayer coverage of CO was not achieved in a reasonable period of time, only a negligible oxidation peak is observed. As a result these data were omitted.

The first experiment was carried out on a fully flooded electrode immersed in electrolyte. This electrode was washed (with ultrapure H_2O) and then dried in an oven at 50 ^{o}C overnight to remove any water, and was then used in the GDE for the set of three experiments using each mode of CO supply, liquid and gas phase, as well as the dilute CO source. The electrode was then forcefully flooded and retested in the immersed configuration to ensure that the original experiment was reproducible. In each case the CO was supplied for 15 minutes.

The same order of the magnitude of the ECSA was obtained as with the previous set of experiments, with the dilute CO resulting in marginally lower coverage than the pure CO gas source, but higher than when the pure CO was purged through the electrolyte. No significant decrease in ECSA was observed when using the dilute CO. Further dilution or shorter timescale dosing times are therefore necessary. The idea was that at sufficiently low partial pressures of CO over a short enough time, negligible dissolution into the electrolyte would occur. This would allow both the ECSA of the flooded and the electrolyte-free regions to be independently measured and compared to the total ECSA. This information would be of interest in order to maximise catalyst utilisation and avoid unnecessarily thick catalyst layers.

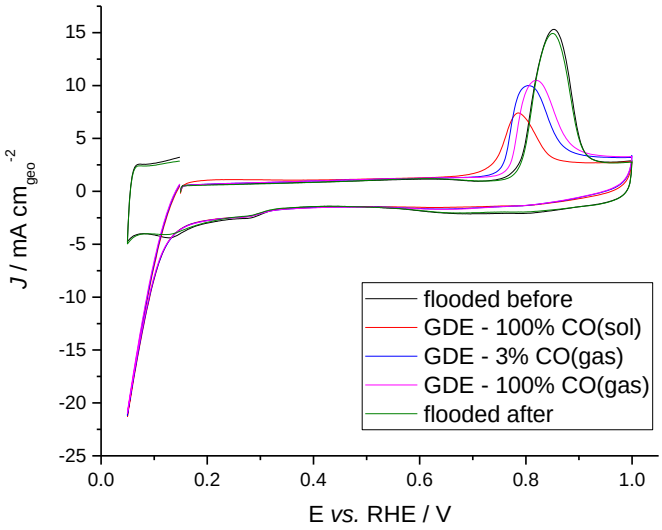

Figure 20 CO monolayer oxidation profiles for the same Pt/C (0.2 mg_{Pt} cm^{-2}) coated electrode. First measurement was taken under flooded conditions in the three neck cell in CO purged 1 M $HClO_4$. The electrode was then oven dried at 50 °C, and placed in the GDE. Sequentially, CO stripping experiments were carried out where CO was purged through the electrolyte and supplied directly as a gas, respectively. Both pure CO gas and a 3% CO mixture in N_2 were used. The method by which the CO is supplied to the catalyst layer affects the resulting ECSA. The exposed geometric area has been taken into consideration.

A final observation is that there is a noticeable difference in the hydrogen region between when the electrode is immersed and when it is held in the GDE. There is an apparent shift to more positive potentials in the onset for H_2 evolution in the GDE. In the three neck cell, the onset of H_2 evolution is at 0.05 V or below, whereas in the GDE, H_2 evolution starts at around 0.1 V. Kinetically, the rate of desorption into the continuously purged gas channels may be higher than desorption into the electrolyte solution; however this does not explain the apparent shift in potential. This shift could be caused by a difference in the anion adsorption blocking active sites, as the onset of adsorbed CO oxidation is also affected. In the flooded state, the catalyst is completely immersed in the electrolyte, whereas in the GDE, the electrolyte is in contact with a fraction of the catalyst layer. Perchloric acid is chosen primarily due to the fact that the perchlorate anion is weakly adsorbing on Pt, although the hydrogen oxidation reaction (HOR) is very surface sensitive. One way to investigate this further would be to vary the concentration of $HClO_4$ used as the electrolyte through adding additional acid or a salt such as $KClO_4$, or to change the supporting anion itself and use H_2SO_4, for example.

Alternatively, the activity of water could have an impact. In the flooded case, the activity is approximately 1, whilst in the GDE, the activity will be proportional to the partial pressure of water, which may vary throughout the catalyst layer and was not controlled for in these

experiments. The gas supplied to the gas diffusion electrode was not humidified. The activity of H_2O, and H_3O^+, will affect the formation of the H_{ads}, and OH_{ads}, species involved as intermediates in the HOR and CO oxidation reactions. By humidifying the N_2 gas supply and controlling the relative humidity either through temperature or by bubbling the gas through specific salt solutions, this hypothesis could be tested.

7.4 Conclusions

The activity of three comparable oxygen reduction catalysts was measured in GDE, RDE and MEA type experiments. The ECSAs measured in each case were comparable, whereas the specific and mass activities differed by up to several orders of magnitude. The RDE yielded the highest activity, likely because of the relative simplicity of the system and some of the assumptions made when extrapolating the raw data to determine kinetic currents free of mass transport limitations. The GDE and MEA methods returned activities of a similar order of magnitude, with the catalysts showing higher activity in the MEA. This in part was due to the higher operating temperature of the MEA/fuel cell test stand, but also due to issues regarding catalyst utilisation in the GDE. In comparison with results in floating electrode experiments, the GDE set-up used in this work is both more similar in terms of electrode structure to the MEA used in commercial fuel cells and was shown here to have superior activity to the floating electrode.[2] The activity measured in the GDE is also comparable to that measured during fuel cell testing. Currently, the floating electrode system has been defined more precisely than the GDE in terms of describing the mass transport and consequently the expected behaviour of the electrode. Further measurements supported by computer modelling of the GDE system would address this and would result in a more practical and realistic method for activity measurements.

The loading study carried out in the GDE with a test catalyst (2 nm Pt/C) showed a decreasing ECSA when normalised by the mass of Pt used, as well as lower mass activity. This suggests that the entire catalyst layer is not available for oxygen reduction.

The issue of measuring the ECSA in the GDE was investigated further by changing the way in which the CO surface probe was supplied to the electrode. CO was supplied in the typical fashion by purging the electrolyte solution as well as directly as a gas. Different surface areas were measured by each method, both of which were lower than if the electrode was forcefully filled with electrolyte and immersed in the electrolyte completely.

It was hypothesised that when using dissolved CO, only the region of the catalyst layer in direct contact with the electrolyte was poisoned. When gaseous CO was used, a proportion of the catalyst layer further away from the electrolyte, but still in contact with hydrated ionomer, was also poisoned, as well as the catalyst in the electrolyte filled region. This can be used to explain the somewhat lower oxygen reduction activities observed in the GDE than by the other methods. Several other interesting results in the GDE are also briefly discussed.

Overall the results presented in the chapter suggest that the GDE configuration is a promising alternative to the RDE as it can provide more realistic values for the activity of ORR catalysts. However, clearly some further optimisation is required, particularly the development of a reliable, reproducible conditioning protocol that facilitates the wetting of the hydrophobic catalyst layer and electrode without exposing the catalysts to high potentials, especially important for the alloy nanoparticles. The effect of catalyst layer thickness should also be addressed.

7.5 References

(1) Shinozaki, K.; Zack, J. W.; Richards, R. M.; Pivovar, B. S.; Kocha, S. S. Oxygen Reduction Reaction Measurements on Platinum Electrocatalysts Utilizing Rotating Disk Electrode Technique. *J. Electrochem. Soc.* **2015**, *162*, F1144–F1158.

(2) Zalitis, C. M.; Kramer, D.; Kucernak, A. R. Electrocatalytic Performance of Fuel Cell Reactions at Low Catalyst Loading and High Mass Transport. *Phys. Chem. Chem. Phys.* **2013**, *15*, 4329–4340.

(3) Stassi, A.; Modica, E.; Antonucci, V.; Aricò, A. S. A Half Cell Study of Performance and Degradation of Oxygen Reduction Catalysts for Application in Low Temperature Fuel Cells. *Fuel Cells* **2009**, *9*, 201–208.

(4) Gasteiger, H. A.; Kocha, S. S.; Sompalli, B.; Wagner, F. T. Activity Benchmarks and Requirements for Pt, Pt-Alloy, and Non-Pt Oxygen Reduction Catalysts for PEMFCs. *Appl. Catal. B Environ.* **2005**, *56*, 9–35.

(5) Williams, M. V; Kunz, H. R.; Fenton, J. M. Analysis of Polarization Curves to Evaluate Polarization Sources in Hydrogen/Air PEM Fuel Cells. *J. Electrochem. Soc.* **2005**, *152*, A635–A644.

(6) Debe, M. K. Electrocatalyst Approaches and Challenges for Automotive Fuel Cells. *Nature* **2012**, *486*, 43–51.

(7) Stephens, I. E. L.; Rossmeisl, J.; Chorkendorff, I. Toward Sustainable Fuel Cells. *Science (80-.).* **2016**, *354*, 1378–1379.

(8) Kongkanand, A.; Mathias, M. F. The Priority and Challenge of High-Power Performance of Low-Platinum Proton-Exchange Membrane Fuel Cells. *J. Phys. Chem. Lett.* **2016**, *7*, 1127–1137.

(9) Garrick, T. R.; Moylan, T. E.; Carpenter, M. K.; Kongkanand, A. Electrochemically Active Surface Area Measurement of Aged Pt Alloy Catalysts in PEM Fuel Cells by CO Stripping. *J. Electrochem. Soc.* **2017**, *164*, F55–F59.

(10) Watt-Smith, M. J.; Friedrich, J. M.; Rigby, S. P.; Ralph, T. R.; Walsh, F. C. Determination of the Electrochemically Active Surface Area of Pt/C PEM Fuel Cell Electrodes Using Different Adsorbates. *J. Phys. D. Appl. Phys.* **2008**, *41*, 174004–174011.

(11) Chen, D.; Tao, Q.; Liao, L. W.; Liu, S. X.; Chen, Y. X.; Ye, S. Determining the Active Surface Area for Various Platinum Electrodes. *Electrocatalysis* **2011**, *2*, 207–219.

(12) Price, S. W. T.; Thompson, S. J.; Li, X.; Gorman, S. F.; Pletcher, D.; Russell, A. E.; Walsh, F. C.; Wills, R. G. A. The Fabrication of a Bifunctional Oxygen Electrode without Carbon Components for Alkaline Secondary Batteries. *J. Power Sources* **2014**, *259*, 43–49.

(13) Wang, D.; Xin, H. L.; Hovden, R.; Wang, H.; Yu, Y.; Muller, D. a.; DiSalvo, F. J.; Abruña, H. D. Structurally Ordered Intermetallic Platinum–Cobalt Core–Shell Nanoparticles with Enhanced Activity and Stability as Oxygen Reduction Electrocatalysts. *Nat. Mater.* **2012**, *12*, 81–87.

(14) El-kharouf, A.; Mason, T. J.; Brett, D. J. L.; Pollet, B. G. Ex Situ Characterisation of Gas Diffusion Layers for Proton Exchange Membrane Fuel Cells. *J. Power Sources* **2012**, *218*, 393–404.

(15) Pozio, A.; De Francesco, M.; Cemmi, A.; Cardellini, F.; Giorgi, L. Comparison of High Surface Pt/C Catalysts by Cyclic Voltammetry. *J. Power Sources* **2002**, *105*, 13–19.

(16) Kolics, A.; Wieckowski, A. Adsorption of Bisulfate and Sulfate Anions on a Pt (111)

Electrode. *J. Phys. Chem. B* **2001**, *105*, 2588–2595.

(17) Neyerlin, K. C.; Gu, W.; Jorne, J.; Gasteiger, H. A. Determination of Catalyst Unique Parameters for the Oxygen Reduction Reaction in a PEMFC. *J. Electrochem. Soc.* **2006**, *153*, A1955–A1963.

(18) Koh, S.; Leisch, J.; Toney, M. F.; Strasser, P. Structure-Activity-Stability Relationships of Pt−Co Alloy Electrocatalysts in Gas-Diffusion Electrode Layers. *J. Phys. Chem. C* **2007**, *111*, 3744–3752.

(19) Sui, X.; Wang, Z.; Xia, Y.; Yang, M.; Zhao, L.; Gu, D. A Rapid Synthesis of TiO 2 Nanotubes in an Ethylene Glycol System by Anodization as a Pt-Based Catalyst Support for Methanol Electrooxidation. *RSC Adv.* **2015**, *5*, 35518–35523.

(20) Maillard, F.; Eikerling, M.; Cherstiouk, O. V.; Schreier, S.; Savinova, E.; Stimming, U. Size Effects on Reactivity of Pt Nanoparticles in CO Monolayer Oxidation: The Role of Surface Mobility. *Faraday Discuss.* **2004**, *125*, 357–377.

(21) Jauregui-Haza, U. J.; Pardillo-Fontdevila, E. J.; Wilhelm, A. M.; Delmas, H. Solubility of Hydrogen and Carbon Monoxide in Water and Some Organic Solvents. *Lat. Am. Appl. Res.* **2004**, *34*, 71–74.

Chapter 8: Conclusions and Future Work

8.1 Original Aims

One of the aims of the project was to use x-ray based techniques including XPS, XRD and primarily XAS to study the structure of the Pt/C, PtCo/C and PtNi/C catalysts. The idea was to subject the catalysts to a shorter accelerated stability testing protocol, rather than that proposed by the US DOE,[1] which takes more than 100 hours, and use the various techniques in combination with TEM imaging to build up a picture of the evolution of the structure over the lifetime of the catalysts. The catalysts were characterised *ex situ* at intermediate points throughout the protocol with the intention of also recording ORR activity. This would enable any changes in activity to be correlated with any changes in structure. The catalysts used in this work were shown to be largely unaffected by the stability test, so the procedure used here is not a suitable model for the degradation experienced in fuel cells.

A secondary part of the project was to look at whether the adsorption of molecules, in this case iodine was used, at the surface of the Pt nanoparticles would aid in the characterisation of the surface using EXAFS. The idea behind this being that the iodine would strongly adsorb to the exposed Pt surfaces and allow them to be distinguished from the bulk Pt atoms in the core of the nanoparticle. This was shown to be possible, although was limited by the lack of degradation caused by the stability test. When looking at pure Pt nanoparticles, this method is unlikely to add benefit without further testing, since the particle size can be determined relatively easily via the Pt coordination. On the other hand, when looking at alloy nanoparticles this methodology may be useful as the Pt-Pt and Pt-M coordination numbers are affected by both changes in particle size as well as compositional and structural changes.

The final aim was to compare and contrast several methods for measuring the electrocatalytic activity for the ORR of Pt and Pt alloy nanoparticles as currently there is a large discrepancy between activities measured in laboratory based half cell measurements and in fuel cells.[2] In this work, activities measured using the laboratory based techniques of

the RDE and the more unusual GDE and were compared to measurements made in the less commonly available MEA in a commercial fuel cell test stand. The results presented here show that the GDE set up is a viable replacement for the RDE and provides activity measurements and conditions that are more similar to those found in the fuel cell cathode.

8.2 Conclusions

8.2.1 Characterisation

The techniques used in this work were all shown to provide some useful information about the samples, although they inevitably had some limitations. The full capabilities of the techniques were also hindered by the lack of degradation caused by the stability testing.

Firstly, the electrochemical techniques suggested that the samples were very much Pt-like. All samples exhibited the typical Pt features including adsorption and desorption of H, double layer region and oxide formation and reduction. They also showed high activity for the ORR, with the expected improvement in activity for the Pt alloy materials, as well as the ability to adsorb CO, which only occurs to a much lesser extent, if at all, on Ni and Co. No additional oxidation and reduction peaks that could be assigned to redox couples of Ni or Co species were observed. Although, electrochemistry alone is not enough to fully characterise the materials, the results suggest that the active surface is dominated by Pt rather than Co or Ni atoms. Measurements made in alkaline solution particularly during the initial cycling of the alloy samples could allow the observation of Co and Ni redox couples, which would help to support the conclusions drawn from the EXAFS analysis.

As the surface of the nanoparticles is of primary interest and importance to its activity for the ORR, XPS was used as a surface sensitive technique to analyse this. However, when looking at nanoparticles, it is likely that much of the surface sensitivity granted by the limited mean free path length of the ejected photoelectrons in solids, typically on the order of 1-5 nm, is not as relevant for nanoparticles as it is for more bulk like samples. This is because the diameter of the nanoparticles is close to the mean free path length, meaning that photoelectrons will be able to escape from a larger portion of the nanoparticle not just the surface region. For the catalyst powder samples, small peaks can be observed in the binding energy region expected for the Co2*p* and Ni2*p* transitions. Fitting, integrating and comparing the various peaks in the spectra and accounting for the relative sensitivity factors, the ratio of Pt:Co was calculated to be 2.15 as compared to 2.55 from the bulk

analysis. This however suggests that the near surface composition is richer in Co relative to the bulk composition. In the electrode samples, the presence of Nafion presented significant problems and to resolve this alternative ionomers, such as PBI, or removal of the ionomer entirely could be explored. The high fluorine content and the Auger transitions associated with the element obscured the regions required for observation of the Co2*p*, and particularly the Ni2*p* transitions as can be seen in Figure 1. It may be possible to analyse the 3*p* transitions, as they are in a similar region to the Pt4*f* transitions, which can be easily observed.

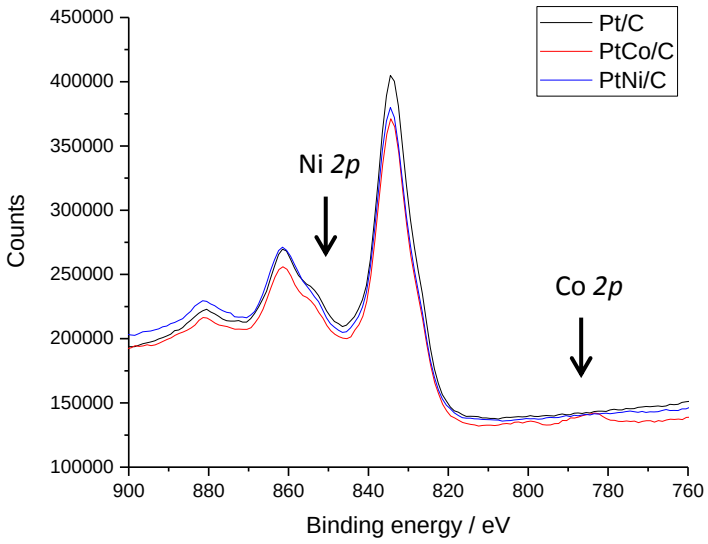

Figure 1 XPS spectra of the Pt/C, PtCo/C and PtNi/C coated electrodes in the Co2*p* and Ni2*p* region. The addition of Nafion results in large F Auger electron peaks, which strongly overlap with the Ni2*p* region and may cause problems when looking at the Co2*p* peaks.

XRD patterns were collected for the majority of the electrode samples, although some were damaged during other spectroscopic techniques, as well as for the powder samples. In each case, the peaks could be indexed to the face centred cubic structure, which was useful information, particularly to confirm the unit cell for the PtCo/C samples. The lattice parameter was also calculated for the Pt/C samples and found to be similar to literature values. The nanoparticle samples were not in the size regime where use of Scherrer equation for determining crystallite size would be accurate or useful. XRD, as a bulk averaging technique, also struggles to distinguish core-shell or other segregated structures from random alloys so no differences were observed across the range of aged electrode samples.

TEM provided direct evidence for particle shapes and sizes, which provided a useful comparison for the particle sizes estimated from the XAS analysis. The shell and core sections of the nanoparticles could not be distinguished based on fast Fourier transforms of the images due to insufficient resolution or image processing used. Use of annular dark field STEM could allow the quantification of strain and direct imaging of catalyst nanoparticles, for example, work done by Jones *et al*.[3] on aluminium precipitates has highlighted how much information can be gained from high quality, atomic resolution TEM images. When combined with EDX measurements, elemental profiles consistent with core-shell nanoparticles were obtained for both the PtCo/C and PtNi/C samples *e.g.* Figure 2. The width of the shell compared to the core can be estimated from these results, although it would be wrong to say that the few particles studied are necessarily representative of the entire sample. Particle selection was undoubtedly biased to some extent by the need to find isolated particles and the selection of larger than average particles to facilitate the measurements.

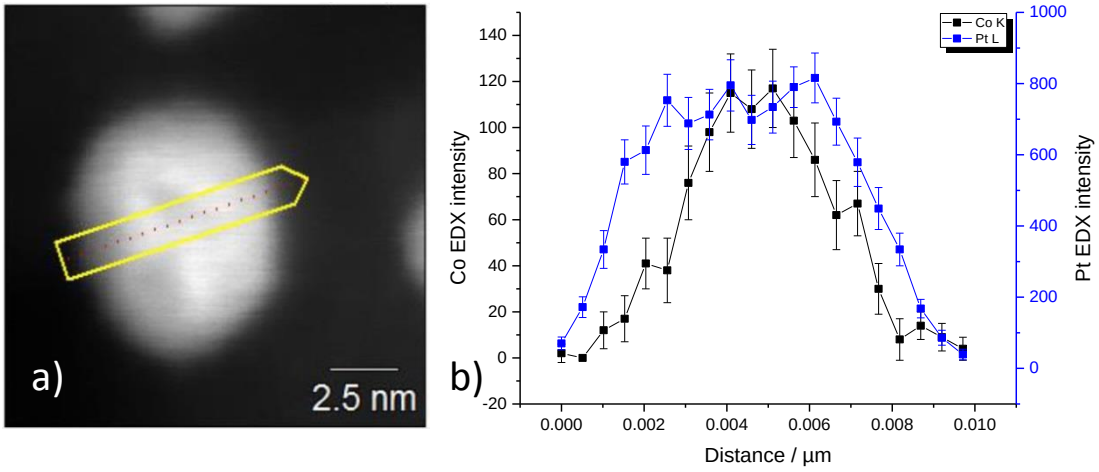

Figure 2 a) Dark-field TEM image of the analysed nanoparticle in the as-prepared PtCo/C electrode sample with arrow showing the measurement positions, and b) the composition, measured by EDX, across the nanoparticle.

The EXAFS data for the monometallic Pt samples were successfully fit using a model incorporating up to four atomic shells, achieving similar results to previously published models, whilst requiring fewer fitting parameters. This would be of most use when only a limited amount of information is present in the EXAFS spectrum, typically in low symmetry and highly disordered systems, however this is also where the assumptions used in this model are less relevant and tricky to apply. The model itself builds on ideas and strategies from work such as that by Frenkel *et al.*[4,5] as well as from workshops run by Diamond Light Source.

The coordination numbers obtained during the data analysis were compared to computationally obtained values determined by authors such as Jentys,[6] and Glasner and Frenkel[7] in order to estimate the average particle size in the sample. Due to the way in which the coordination numbers vary with particle size, the method is less sensitive to larger particles where the calculated coordination number is tending slowly towards the bulk value. In the work here, the particle size measured using TEM and EXAFS for the 2 nm Pt/C sample gave similar values, around 124 and 183 atoms, corresponding to diameters of 1.53 nm and 1.74 nm respectively, although the error for the EXAFS determined size is larger due to the uncertainty in the fitting process. For the 5 nm Pt/C sample, there was a much larger discrepancy, with the EXAFS predicting a much smaller particle size than TEM. This has been attributed to the failure of the EXAFS theory to account for the increased disorder in nanoparticle samples due to the relaxation of atoms at surfaces leading to a breakdown in some of the assumptions involved.[8]

For the alloy samples, analysis of the XAS was more difficult due to the extra disorder caused by the second metal because of the combination of both the range of particle sizes in the sample as well as the likely variation in elemental composition of the particles. This restricted the analysis to a first shell model only. In chapter 5, the untreated catalysts were characterised in order to provide a baseline to which the samples subjected to the AST could be compared. Unfortunately, the 5 nm catalysts, both pure Pt and the alloy samples, proved more resistant to the test than anticipated and as a result, the initial structure was affected minimally. The partial and total coordination numbers determined from the model were used to estimate the degree of clustering and segregation in the model by employing the Cowley short range order parameter[9,10] and another similar method by Hwang *et al*.[11] The total coordination number for each species was used as an indicator for the metal present at the surface in the shell of the nanoparticle. In the models, scattering pathways containing O atoms were also required, which was also indicative of which metal was at the surface. The results showed that initially, there were Ni or Co atoms remaining at or near the surface, but after exposure to the electrochemical environment, these were dissolved leaving a Pt rich shell.

8.2.2 Activity Measurements

The electrocatalytic activity and the ECSA of three carbon supported Pt nanoparticles of comparable particle size were measured using three different methods and the expected increase in activity granted by alloying Pt with Ni and Co was observed in each case.

The ECSAs measured in each case were comparable, although the electrochemical measurements returned a slightly higher value than those obtained chemically through CO adsorption at JMTC. When measured using the RDE, the activity of the catalysts were much higher than when the same experiments were carried out using the same catalyst in either the GDE or the MEA. Potential reasons for this difference were discussed such as electrical and electrolyte access to catalyst layers of different thicknesses, the assumptions involved for the corrections in the RDE, the influence of the large amount of Nafion ionomer, and the presence of the three phase interface. The results from the experiments in the MEA compared to the GDE were similar, with slightly higher activities measured in the MEA most likely due to the fact that the experiments were carried out at higher temperature. Some of the results in the GDE also suggested that the electrolyte was not able to access the entire catalyst layer. In comparison to similar experiments using alternative electrode configurations, the GDE compared favourably both in terms of the activity measured and the relative simplicity of the system. Phenomena, such as flooding, observed in fuel cells were also exhibited in the GDE experiments, which as a result presents a useful method by which these effects can be studied, although the origin is different, methods and observations may be transferable and applicable to catalyst behaviour in fuel cells.

In the GDE, the results from the loading study indicated that once the mass of catalyst used was accounted for, the ECSA was actually decreasing at higher loadings. This was interpreted in terms of utilisation of the catalyst layer with the supposition that due to the thickness of the layer the electrolyte would only be able to penetrate to a certain depth. The penetration depth being limited by the hydrophobicity of the PTFE treated carbon paper used as the gas diffusion layer, current collector and base of the electrode. In initial experiments, untreated carbon paper was used, but in the GDE, the electrolyte leaked through into the gas channels very quickly and electrochemical behaviour was dramatically affected. Varying the mode by which the CO surface was supplied to the surface either by dissolving the gas in the electrolyte or by suppling it directly to the electrode surface as gas showed potential as a way of measuring the flooded and electrolyte free regions in the

catalyst layer. The results presented in Figure 3 illustrate the differences in ECSA measured for the same electrode and accounting for the differences in exposed catalyst.

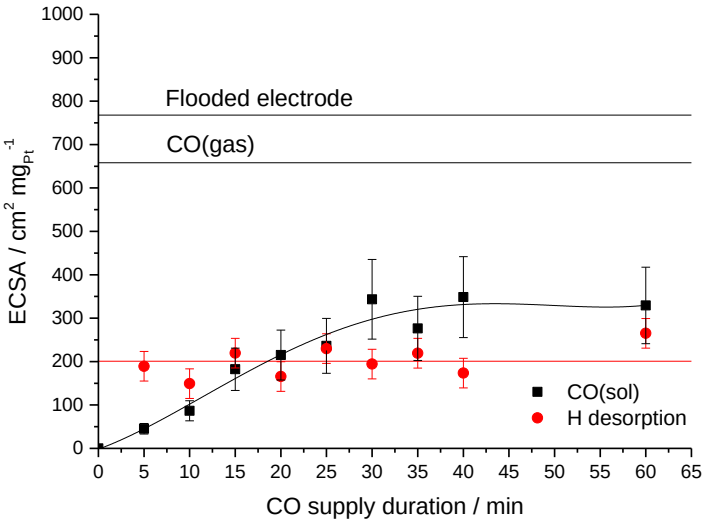

Figure 3 The ECSA of a Pt/C coated electrode determined via several methods. The maximum ECSA, 768 ± 9 cm^2 mg_{Pt}^{-1}, was measured when the electrode (A = 0.950 cm^2) was fully immersed in electrolyte in the 3 neck cell setup, denoted as 'flooded electrode'. The other measurements were obtained using the GDE where CO was supplied as both a gas and dissolved in the electrolyte for the indicated period of time. The average ECSA for the CO(gas) method was determined from Error! Reference source not found. **as 658 ± 8 cm^2 mg_{Pt}^{-1} and found to be invariant with time. Lines have been added to guide the eye. The errors associated with the GDE method are largely caused by the uncertainty in the exposed geometric area (A = 0.502 cm^2) as the O-ring prevents electrolyte access to the outermost region of the electrode.**

Several other observations made during the experiments were also discussed. Firstly, additional oxide reduction charge after oxidation of the adsorbed CO monolayer was observed both in the GDE experiments as well as when the electrode was fully immersed in electrolyte. The hypothesis proposed for this observation was that the presence of the CO monolayer shields the Pt surface until higher potentials where it would normally be covered/passivated by adsorbed OH species. Once the CO is oxidatively removed, the bare Pt surface is exposed to higher potentials than it would normally see. On subsequent cycles, the oxide reduction peak is the same size as observed before the adsorption of the CO monolayer. An alternative explanation could invoke surface reconstruction by the CO results in surfaces with more undercoordinated atoms and hence slightly larger roughness factors. These could be relatively stable whilst O containing species are adsorbed, but quickly rearrange once the oxide has been reduced. This would explain the observation of the larger reduction peak on the first cycle only.

It was also observed that there was an apparent shift in the potential of the H_2 evolution reaction in the GDE compared to when the same catalyst and electrode was fully immersed in the electrolyte.

Overall the results from the GDE suggest that with a little further work, such as a more thorough conditioning protocol and optimisation of the catalyst layer thickness, the technique would provide an easily accessible alternative to the RDE or fuel cell test stand for obtaining realistic catalytic activities.

8.3 Future Work

Due to the complexity and disorder present in nanoparticle systems, their characterisation is trickier than that of bulk materials and requires a variety of techniques to fully interpret their structure.

This work showed that XPS is of limited use when Nafion ionomer or PTFE is incorporated into the electrode or ink composition. Nafion free inks have been previously used[1] in RDE studies, which would allow XPS analysis to be carried out on catalyst samples that had been exposed to the electrochemical environment rather than just restricting the analysis to the as-prepared catalyst powder itself. Alternatively, rather than using the normal Ni2*p* and Co2*p* transitions, the 3*p* region could be studied more closely instead. However, this region still overlaps with the Pt4*f* region, the peaks are smaller in intensity and the sensitivity factor is less than for the 2*p* transitions.

Similarly, XRD patterns provided limited information primarily due to the size range of the sample of interest in this work.

The XAS analysis, one of the principle techniques used in this work, was useful in terms of characterising the Pt nanoparticle samples. The technique can be used to estimate the average particle size, particularly so for the smaller nanoparticles. Although the uncertainty in the measurement is higher than that for TEM particle size analysis, it has the benefit of allowing *in situ* analysis and also as bulk averaging technique removes any human bias towards regions in the sample that are 'nicer' or show the desired result. The main areas for improvement lie in decreasing the error in the numbers determined in the fitting process. Much of the uncertainty results from the nature of the sample itself, *i.e.* the range of particle sizes and the inevitable presence of very large particles that may significantly influence the resulting coordination number, as well as termination effects inherent to

nanoparticles. The disorder could perhaps be reduced by the incorporation of molecular dynamics simulations into the analysis,[8] which better account for the distribution in bond lengths present in nanoparticles.

The use of iodine as a surface probe to allow a measure of surface sensitivity in EXAFS analysis was explored, and Pt-Pt and Pt-I 1st shell coordination were found to be negatively correlated, albeit with a relatively large scatter as can be seen in Figure 4. Rather than starting immediately with commercially relevant catalysts, the use of more ideal, monodisperse particles, over a range of particle sizes would provide a better starting point for developing the method. Ultimately, the methodology will be of more use for alloy samples since changes in Pt-Pt and Pt-M coordination numbers are caused by changes in the particle size, structure and composition of the nanoparticles.

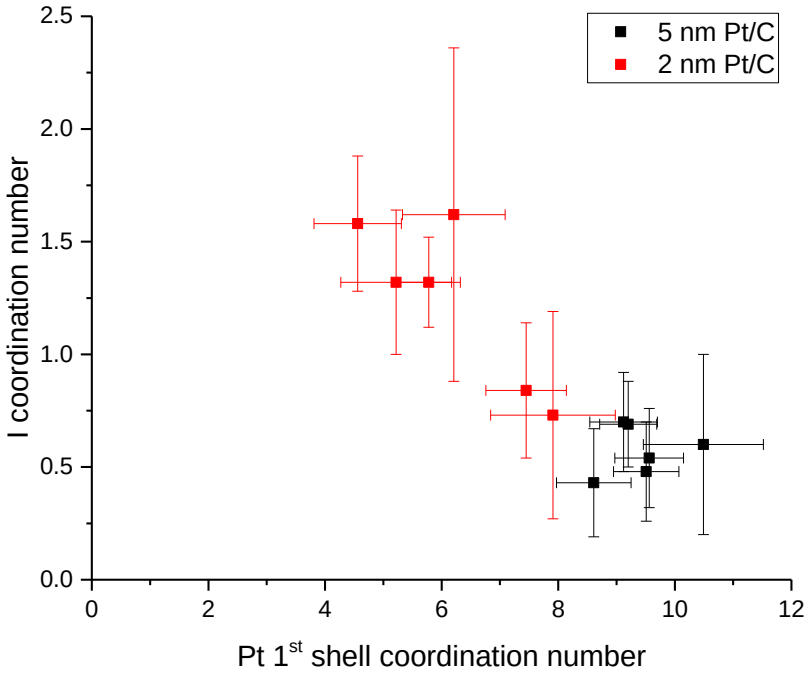

Figure 4 I coordination numbers plotted against the 1st shell Pt coordination numbers obtained from the EXAFS spectra for each of the KI poisoned electrodes. The as prepared samples (0 cycles) were not included due to the inhibition of iodine adsorption by the presence of significant surface oxides. The Pt/C samples were fitted using the same model as used previously with the addition of a Pt-I scattering path.

8.4 References

(1) Kocha, S. S.; Garsany, Y.; Myers, D. Testing Oxygen Reduction Reaction Activity with the Rotating Disc Electrode Technique http://energy.gov/eere/fuelcells/downloads/testing-oxygen-reduction-reaction-

activity-rotating-disc-electrode (accessed Sep 14, 2016).

(2) Stephens, I. E. L.; Rossmeisl, J.; Chorkendorff, I. Toward Sustainable Fuel Cells. *Science (80-.).* **2016**, *354*, 1378–1379.

(3) Jones, L.; Wenner, S.; Nord, M.; Ninive, P. H.; Løvvik, O. M.; Holmestad, R.; Nellist, P. D. Optimising Multi-Frame ADF-STEM for High-Precision Atomic-Resolution Strain Mapping. *Ultramicroscopy* **2017**, *179*, 57–62.

(4) Frenkel, A. I. Solving the Structure of Nanoparticles by Multiple-Scattering EXAFS Analysis. *J. Synchrotron Radiat.* **1999**, *6*, 293–295.

(5) Frenkel, A. I.; Hills, C. W.; Nuzzo, R. G. A View from the Inside: Complexity in the Atomic Scale Ordering of Supported Metal Nanoparticles. *J. Phys. Chem. B* **2001**, *105*, 12689–12703.

(6) Jentys, A. Estimation of Mean Size and Shape of Small Metal Particles by EXAFS. *Phys. Chem. Chem. Phys.* **1999**, *1*, 4059–4063.

(7) Glasner, D.; Frenkel, A. I. Geometrical Characteristics of Regular Polyhedra: Application to EXAFS Studies of Nanoclusters. In *AIP Conference Proceedings*; AIP, 2007; 882, 746–748.

(8) Price, S. W. T.; Zonias, N.; Skylaris, C. K.; Hyde, T. I.; Ravel, B.; Russell, A. E. Fitting EXAFS Data Using Molecular Dynamics Outputs and a Histogram Approach. *Phys. Rev. B - Condens. Matter Mater. Phys.* **2012**, *85*, 1–14.

(9) Cowley, J. M. An Approximate Theory of Order in Alloys. *Phys. Rev.* **1950**, *77*, 669–675.

(10) Frenkel, A. I.; Wang, Q.; Sanchez, S. I.; Small, M. W.; Nuzzo, R. G. Short Range Order in Bimetallic Nanoalloys: An Extended X-Ray Absorption Fine Structure Study. *J. Chem. Phys.* **2013**, *138*, 64202-1-64202–64207.

(11) Hwang, B. J.; Sarma, L. S.; Chen, J. M.; Chen, C. H.; Shin, S. C.; Wang, Q. R.; Liu, D. G.; Lee, J. F.; Tang, M. T. Structural Models and Atomic Distribution of Bimetallic Nanoparticles as Investigated by X-Ray Absorption Spectroscopy. *J. Am. Chem. Soc.* **2005**, *127*, 11140–11145.